UNIVERSITAT POLITÈCNICA DE VALÈNCIA
Departamento De Química

Metal-Organic Hybrid Materials with Catalytic and Photocatalytic Applications

Doctoral Thesis

Submitted by:
Arianna Melillo

Supervisors:
Dra. Belén Ferrer Ribera
Dra. Mercedes Alvaro Rodríguez

Valencia, March 2022

Belén Ferrer Ribera, PhD in Chemistry and Professor at the Universitat Politècnica de València and Mercedes Álvaro Rodríguez, PhD in Chemistry and Professor at the Universitat Politècnica de València.

CERTIFY:

That the work "Metal-Organic Hybrid Materials with Catalytic and Photocatalytic Applications" has been developed by Arianna Melillo under their supervision at the Departamento de Química of the Universitat Politècnica de València, as a Thesis Project to obtain the degree of PhD in Sustainable Chemistry at the Universitat Politècnica de València.

Dra. Belén Ferrer Ribera Dra. Mercedes Álvaro Rodríguez

A mio padre, luce guida del mio cammino

There is no royal road to science, and only those who do not dread the fatiguing climb of its steep paths have a change of gaining its luminous summits.

K. Marx

Acknowlegments:

Ho sempre creduto che la personalità di un individuo dipenda fortemente dall'intorno nel quale cresce e si sviluppa ed è, dunque, proprio a partire da questo pilastro delle mie credenze che sento l'esigenza di ringraziare tutte le persone che in questo lungo ed intenso percorso hanno lasciato un "granito de arena" nella mia crescita scientifica e personale.

Antes de todo quiero agradecer al profesor Hermenegildo García por ser mi mentor no solo en estos cuatros años si no que en todos los que vendrán, porque sin duda sin su ayuda esta tesis doctoral no hubiera visto la luz. Gracias por todo el tiempo que me has dedicado y las enseñanzas que me has dejado.

Quiero también agradecer a la Profesora Mercedes Álvaro y a la Profesora Belén Ferrer, mis directoras de tesis, no solo por haberme dado esta enorme oportunidad sino también por apoyarme y ayudarme a levantar todas las veces que he caído.

Sin duda he de agradecer al Profesor Sergio Navalón, por todo el tiempo que me ha dedicado, por todas las ayudas que me ha dado, pero sobre todo por enseñarme que el trabajo duro siempre es compensado.

Sento l'esigenza di ringraziare il Professor Gaetano Guerra per avermi insegnato tanto, tutto; per aver creduto in me mostrandomi il cammino più adatto, per essere senza dubbio alcuno uno dei ricercatori che mi ha insegnato l'amore per la chimica ma ancor di più la passione per la ricerca; allo stesso tempo non posso non ringraziare la "mia madrina", la Dottoressa Rosaria Acocella per essere stato un faro nella notte, non solo una tutor ma piuttosto una maestra di vita.

Sin embargo, estos largos cuatros años se han hecho mucho más llevadero gracias a mis compañeros de laboratorio:

A Andrea, mi queen, por estar siempre tan disponible y ser tan abierta y sincera conmigo.

A Juan Carlos por ser el compañero de trabajo que cualquiera quisiera en su vida.

A Cristina por enseñarme a seguir siempre mis sueños, aunque puedan parecer locos.

A María Cabrero por todas las risas y los buenos momentos.

A Herme junior por sus consejos de hermano, por todas las posibilidades que me ha dado y por todas las veces que me ha tendido sus manos.

A Eva por su dulzura y apoyo incondicional, por ser siempre una amiga y no solo una compañera de trabajo.

A Celia por recordarme que la verdad de las cosas no es una si no que hay millones de verdades según quien mire; por ser tan cristalina y buena.

A María Novoa, mi loqui, una de las personas con las cuales más he compartido en estos años, con la esperanza de encontrarnos siempre en cualquier lugar que la vida nos mande.

A Antón por su bondad y por todas las venganzas de padel que han venido y que vendran.

A Maykel por su extrema disponibilidad.

A Fatima per essere arrivata in uno dei momenti più bui di questo lungo cammino ed avermi aiutato a vedere il finale del tunnel.

A Ana Primo por todo su apoyo y sus preciosos consejos.

A Pedro por toda la ayuda que me ha dado en estos años.

A todos los compañeros del ITQ, en particular a Esther Y Amparo por ayudarme y escucharme siempre que lo he necesitado y a Rubén por todos los buenos momentos vividos juntos.
Quiero agradecer con todo mi corazón a los chicos de Lab 2.2:
A Jorge por sus grandes historias; a Dani por todos sus magníficos discursos y sus consideraciones sobre la vida; a Alejandro por ser mi amigo y mi gran apoyo; a Raúl por ayudarme siempre.
A tutte le persone che ho avuto il piacere di conoscere qui a Valencia; senza dubbio a Marco per essere il mio fratellino minore, per esserci sempre, nelle gioie e nei dolori, perché i momenti belli vissuti qui hanno il tuo nome. Se oggi sono quella che sono è anche grazie a Francesca ed Espedito per avermi fatto conoscere il lavoro divertente ed insegnato tanto, tantissimo, é soprattutto grazie a voi e grazie a quella esperienza che oggi posso contare su persone splendide: Martina, Simona ed Alessandra, perché con voi ho vissuto momenti indimenticabili.
A Stefania, per tutto il bello che la vita ci ha dato, per aver condiviso i migliori anni della nostra vita insieme, per esserci sempre.
A mi media pera, Lorena, por ser tan yo, tan dulce, sensible y fuerte, por estar siempre allí en los buenos y en los malos momentos, sé que nunca podré estar muy lejos de ti.
A Maria, mia sorella chimica, per tutte le tachicardie condivise prima, durante e dopo gli esami, per tutte le risate e i pianti, per tutti i momenti nostri e di nessun altro, a te devo una parte di questo lavoro.
Alla famiglia che si sceglie, a Vissia a Mario a Esther e Wanda perche' siete il mio punto fisso, una delle poche consapevolezze della vita.

A Vissia per la sua dolcezza incondizionata, a Mario per la sua pazzia, ad Esther per avermi mostrato che la determinazione è alla base dei grandi traguardi personali. A Wanda, per esserci sempre. La tua amicizia incondizionata non è cambiata né con la distanza, né in assenza di tempo; la tua presenza è uno dei regali più belli che ho avuto dalla vita.

A la familia Herrera porque he aprendido que familia no es solo cuestión de sangre, gracias por todo lo que me habéis dado, por todas las risas, los buenos momentos, y por ser personas tan excepcionales.

A Nicole, per essere amica, sorella, confidente ed amore puro, per tanto, per tutto e per la gioia immensa di conoscere Hera.

A Zia Antonietta per essere una delle poche persone di cui mi fido ciecamente, per essere una seconda mamma e per credere in me come pochi.

A mamma per avermi dato tutte le possibilità di questa vita; per tutte le volte che mi hai insegnato il cammino da seguire, per avermi dato la possibilità di essere tua figlia e di imparare in ogni momento.

A papà perché anche se la vita ci ha separati troppo presto sei stato il miglior maestro che potessi desiderare. Ogni successo e traguardo raggiunto spero siano per te motivo di gran orgoglio, tu lo sei per me, sempre.

A Mattia, fratello e confidente, per la tua testardaggine, per essere tanto tanto diverso da me seppure tanto simile. Spero di essere per te la stella che illumina il cammino; sappi che in ogni momento, in qualsiasi luogo, se ne avrai bisogno la mia mano sarà sempre disposta ad abbracciare la tua.

A Jorge, el amor de mi vida, por apoyarme, abrirme los ojos y enseñarme a ser yo en cualquier momento, por ser certeza en cualquier instante.

A Zoey mía, grande y estupenda sorpresa.

Abbreviations and Acronyms

°C Degrees celsius

λ Wavenumber

3D Tridimensional

4 NP 4-Nitrophenol

4 AP 4-Aminophenol

ACN Acetonitrile

ATR-FTIR Attenuated total reflection-Infrared spectroscopy Fourier transform

H_2BDC Terephthalic acid or benzene dicarboxylate

BET Brunauer-Emmett-Taller

CB Conduction band

DMF Dimethylformamide

e^- Electron

$E_{1/2}$ Halfwave potential

Ea Activation energy

EDX Energy dispersive X-Ray

FESEM Field emission scanning electron microscope

FID Flame ionization detector

FT-IR Infrared spectroscopy Fourier transform

GC Chromatography

h Hour

h^+ Hole

HER Hydrogen Evolution Reaction

HRTEM High resolution transmission electron microscopy

HRSEM High resolution scanning electron microscopy

ICP Inductively coupled plasma

ICP-AES Inductively coupled plasma-atomic emission spectroscopy

IR Infrared spectroscopy

MeOH Methanol

MIL Materiaux de l'Institute Lavoiser

MOF Metal-organic frameworks

MV^{2+} Methyl viologen

NHE Normal hydrogen electrode

nm Nanometer

NMR Nuclear magnetic resonance spectroscopy

NP Nanoparticle

OER Oxygen Evolution Reaction

PL Photoluminescence

ppm Parts per million

PSE Post synthetic exchange

PXRD Powder X-Ray diffraction

R^2 Regression coefficient

SBU Secondary building units

SEM Scanning electron microscopy

SI Supplementary information

STH Solar-to-Hydrogen

TGA Thermogravimetric analysis

TEM Transmission electron microscopy

TEOA Triethanolamine

THF Tetrahydrofuran

TMPDA N, N, N’, N’-tetramethyl-p-phenylene-diamine

TAS Transient absorption spectroscopy

UiO University of Oslo

UV Ultraviolet

UV-Vis Ultraviolet-Visible

VB Valence band

XP X-ray photoelectron

XPS X-ray photoelectron spectroscopy

XRD Powder X-ray diffraction

Style

This Doctoral Thesis is written in a journal article compilation style format constituted by eight chapters in which the main features of the developed work are described. In Chapter 1 is detailed a literature review to synthesize the state of the art of the main characteristics of MOFs and their application in the photo-catalytic and catalytic fields, raising the issues addressed during the course of this doctoral thesis. Chapter 2 collects the objectives of the work. Chapters 3, 4, 5 and 6 show the research results of this thesis. Chapter 7 summarizes the conclusions of the work, while Chapter 8 presents the abstract. Annex I collects the publications and participation in conferences.

Index

1. Introduction……1

1.1 Definition of MOFs……...1

1.2 Versatility of MOFs ……..4

1.3 Stability of MOFs……..8

1.4 UiO66(Zr)……...10

1.4.1 MOFs as heterogeneous catalysts……..….12

1.5 MIL-125 (Ti)……...16

1.6 Photocatalysis…….18

1.6.1. MOFs as photocatalysts……24

1.6.1.1. Core shell type MOFs……..27

1.6.2. Photocatalytic hydrogen generation…….29

2. Aim of the Work……37

3. Enhancing visible-light photocatalytic activity for overall water splitting in UiO-66 by controlling metal node composition

3.1 Abstract……..45

3.2 Introduction……45

3.3 Materials preparation……..48

3.4 Results and discussion……58

3.5 Conclusions……73

3.6 References……..75

3.7 Supporting information……...79

4. Solar-driven photocatalytic overall water splitting using MOF-on-MOF heterojunctions based on UiO-66 topology

4.1. Abstract……...117

4.2. Introduction……118

4.3. Experimental section……...120

4.4. Results and discussion……125

4.5. Conclusions…….147
4.6. References……...149
4.7. Supporting information……...151
5. Bifunctional metal–organic frameworks for the hydrogenation of nitrophenol using methanol as the hydrogen source
5.1. Abstract……...169
5.2. Introduction…….170
5.3. Experimental section……...……171
5.4. Results and discussion…….…...….173
5.5. Conclusions…….183
5.6. References……...184
5.7. Supporting information……...187
6. Metal Nodes of Metal Organic Frameworks Can Activate Molecular Hydrogen
6.1 Abstract……201
6.2 Discussion……202
6.3 Conclusions……..211
6.4 References……213
6.5 Supporting information……215
7. Conclusions…….221
8. Abstracts of the Thesis…….223
8.1 Abstract……223
8.2 Resumen……224
8.3 Resum……225
Annex I Research articles and conferences
I.1 Publications related with the Thesis report……..227
I.2 Other publications……227
I.3 Participation in conference……...229

Chapter 1. Introduction

1.1 Definition of MOFs

Metal organic frameworks (MOFs) are three-dimensional materials that, due to their versatility, have become well established in the scientific world over, the last decade. MOFs can be classified as coordination polymers. The IUPAC definition of a coordination polymer is: "A coordination compound continuously extending in 1, 2 or 3 dimensions through coordination bonds". [1,2] These cross-linked materials were developed almost simultaneously by research groups at Arizona State University by led Omar Yaghi, Versailles University led by Gerard Ferey, and at the Japanese University of Kyoto led by Kitagawa. [3-7] The first MOF with interesting chemical-physical characteristics was MOF-5 as synthesized by Omar Yaghi's group in 1999.[3] This material immediately became famous in the scientific community because it was possible to completely remove the solvent molecules from its pores. Moreover, it reported a surface area of 3000 m^2/g, an aspect that made it similar to the renowned zeolites.[5]

Starting from the initial definition of an MOF it is possible to describe the main characteristics of these species. In detail, an MOF has high levels of crystallinity and porosity and a large surface area. In the literature, there are reports of surface area values reaching some 6000 m^2/g.[8] It is interesting to note that the three-dimensional network depends on the presence of strong metal-ligand coordination bonds.[3, 6, 7, 9-14]

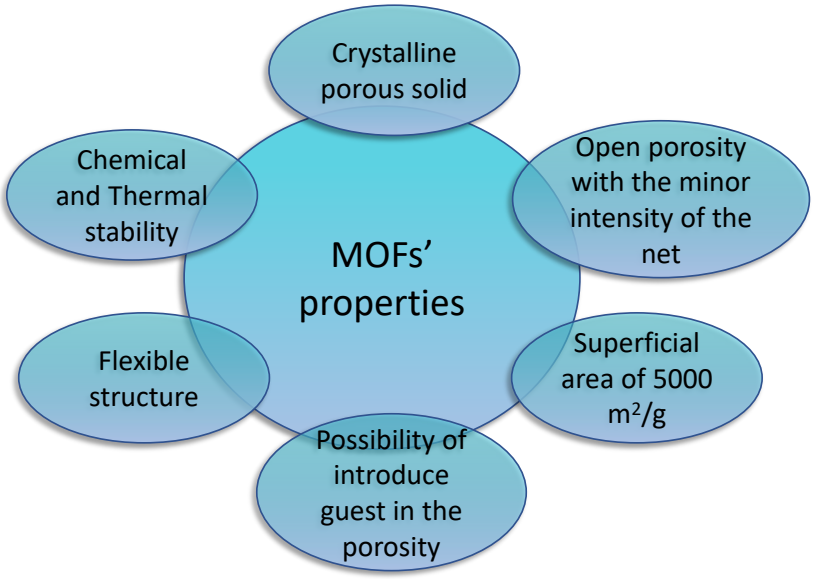

Scheme 1.1. Structural properties shown by MOFs

The crystalline structure of an MOF is built from a metallic cationic cluster and organic ligands that connect the various clusters to each other. [3,6,14] Such organic ligands have a rigid structure with two or more coordination positions (bi or multipodal). Typical organic ligands are mono or polycyclic aromatic compounds that possess substituents capable of coordinating with metal clusters. Among the substituents present on the ligand, a key role is represented by the carboxylate functional group. In this case, the anion interacts with the cations of the metal atoms to construct the MOF through coordination bonds and by generating strong anion-cation electrostatic bonds. [6, 15-18]

Other basic ligands capable of generating bridges between clusters that define the three-dimensional structure are the nitrogen anions present in imidazole and benzyl imidazole units.

Regarding the nature of the metal cation present in the cluster of an MOF, metal cations of almost all transition metals have been used – as well as metal cations from rare earth metals. [15, 18-20]

Strongly connected to the nature of the transition metal constituting an MOF and its affinity for the oxygen atom of the organic ligand, is the possibility of defining clusters consisting of a single metal ion as in the case of $Al_2(BDC)_3$; while, for example, in the case of $Cu_3(BTC)_2$ (H-KUST), the node consists of a pair of Cu^{2+} ions bonded to three carboxylate groups and forming a paddle wheel pattern.[21]

In the case of MOF-5, the node is formed by a central oxygen atom coordinated with four Zn^{2+} ions and these clusters of Zn_4O are then connected to the carboxylate groups. The molecular formulae are $Zn_4O(BDC)_3$, where BDC represent the 1,4-benzodicarboxylate ligand.

Among the most interesting structural characteristics, a key role is certainly defined by the high specific surface area and respective porosity observed for these materials. The large surface area is directly related to the open structure of MOFs and this enables both high porosity and an occupation of only a small proportion of the space (which can be so low as to cover less than 20% of all the space defined by the crystalline unit formula). It follows that MOFs are characterized by a very low reticular density.[6]

This parameter refers to the mass contained in the volume of the crystalline unit, and therefore, the reticular density is so small that these materials are the least dense so far described. [15,18,22-27]

Previously, it was shown that an MOF is prepared starting from a metal cluster and an organic ligand; it is therefore worthwhile underlining that one of the most interesting aspects for this type of material is the high percentage of metal that an MOF often contains.

The metal content is usually approximately 30% and there are reported cases of metal contents higher than 50%.

It is precisely the high metal content of MOFs that allows these materials to be used as catalysts to a greater extent than well-known materials such as zeolites or activated carbon in which the presence of metal is less than 10%. [22-27]

1.2 Versatility of MOFs

In the previous section we have enumerated and described the main characteristics of MOFs, such as high crystallinity, porosity, metal content, and large surface area. Strongly related to these properties are the areas of applicability of these materials. For example, the high surface area is such as to allow the use of MOFs in processes of absorption of both simple gases and species with larger dimensions such as hydrocarbons. [28-29]

Similarly, MOFs, due to their high porosity, can be used for the separation of ethylene/propylene mixtures in residues derived from the thermal cracking of crude oil. Yaghi and Ferey described the H_2 and O_2 sorption properties of some MOFs. [30-31]

Among the most interesting properties of these materials is the ability to design the final structure of the material by evaluating both the nature and the coordination of the metal nodes and the direction of the organic ligands.[32] This ability is unique when compared with other porous materials, in particular with respect to zeolites (for which the choice of the template is the only parameter that can be varied when designing the size and geometry of the pore).

In a preliminary work, Yaghi showed that by keeping the nature of the metal cation and the directionality of the organic ligand fixed, but modifying the size of the latter, it is possible to prepare a series of isostructural crystalline solids in which the dimensions of the cavities increase according to the size of the organic ligand. [33,34] Figure 1.1 illustrates this concept.

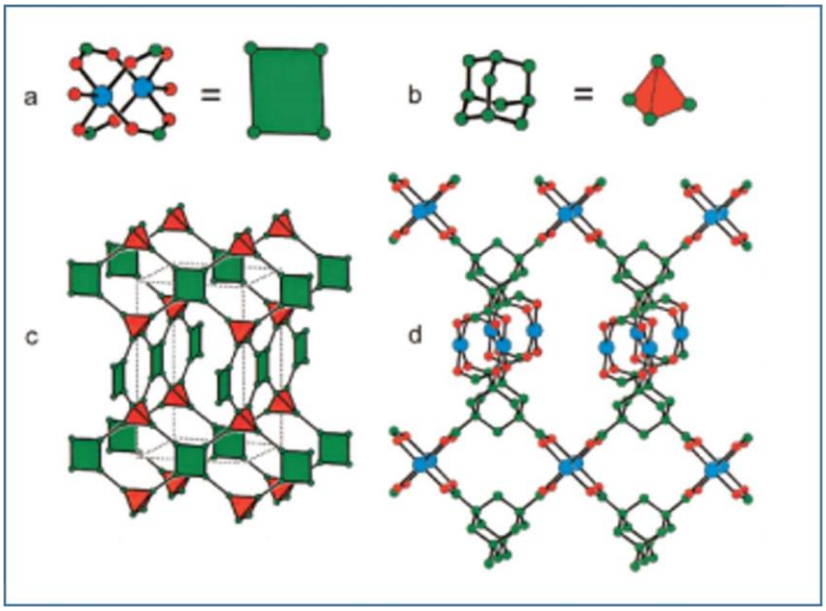

Figure 1.1. Prediction of the structure of MOFs based on the consideration of the direction of coordination of the metallic nodes and the structure of the organic ligands.[33,34]

However, it is possible to observe that by changing the directionality and multipodality of the ligand, the structure of the MOF totally changes.

An obvious example of the versatility of MOFs is found in the synthetic process and lies in the reversibility of the metal-ligand bond. This bond, in fact, is susceptible to reaction conditions such as a concentration of the reactants and temperature of the medium. [35, 36]

Starting from these premises, two complementary lines of research have been developed to assess the versatility of MOFs. In one line, the crystallinity of an MOF was analyzed during synthesis: a monopodal ligand is used to slow down the kinetic of the process, thus improving the crystallinity of the material (as it is known to depend on the reaction time). Generally, these ligands are monodentate carboxylic acids defined as modulators. Among those most used are benzoic acid and trifluoro acetic acid.[37]

In the other research line, the lability of the metal-ligand bond can be used to perform an interchange process that can be produced both at the ligand or metal cation level.[38]

In the case of the metal cation, the interchange can take place in two distinct forms: firstly, the literature reports cases in which the cluster consists of at least two metal cations and is obtained through a synthetic process using a mixture of metal salts as precursors: this is the case of the synthesis of the material UiO66(Zr/Ce) reported in Chapter 3.[39,40] Secondly, it is possible to obtain an interchange of the metal cation in a post-synthetic step as will be described and expanded in Chapter 3 and where the efficient post-synthetic interchange of Zr^{4+} and/or Ce^{4+} cations by Ti^{4+} in the structure of UiO66(Zr/Ce) is reported.[41] These materials are generally defined in terms of "mixed metal MOFs".

The possibility is also reported of interchanging the organic ligand, both during the synthetic process, or in a post-synthetic step, using for example, the correct proportions of terephthalate and substituted terephthalate as ligand. [42]

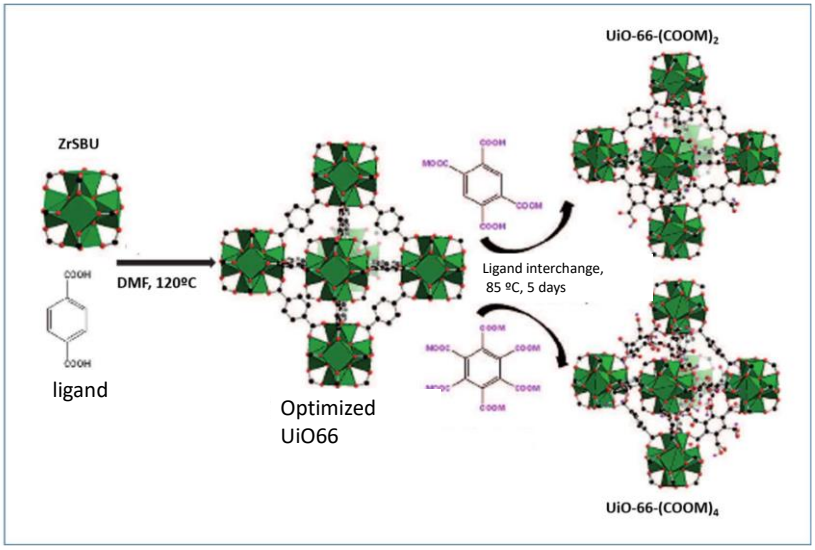

Figure 1.2. Post-synthetic ligand exchange process in UiO-66 that enables obtaining samples of UiO-66 with mixtures of different ligands.[42]

Both strategies – the introduction of one or more metal cations in the crystalline structure of the MOF, as well as the introduction of auxochromic and bathochromic units in the organic ligand – improve the photocatalytic activity of these materials. The introduction of a new metal in the cluster enables a more appropriate alignment of the metal atomic orbitals with those of the ligand, meanwhile with the introduction of a new ligand it is possible to observe how the substituent present on it enables a shift of the absorption to regions closer to the visible range of the spectrum. [38-41]

Recent studies have shown that the introduction of a co-catalyst positioned either on the crystal's external surface, or preferably inside the pores, increases the efficiency of the catalytic process by at least one order of magnitude.[43] In the specific case of MOFs, it is clearly possible to introduce a co-catalyst such as metal nanoparticles (NPS) inside the pores due to their high porosity. The co-catalytic activity will, thus, depend on numerous factors such as the experimental synthesis procedure, the size of the particles, and their location within the solid. The metal nanoparticles can be deposited in the internal or the external part of the MOF and may act differently depending on their location. Specific studies have reported that the photocatalytic efficiency of an MOF material is enhanced when the metal nanoparticles are arranged inside the pores of the material.[44] These co-catalysts are prepared through a photo-deposition method (a green procedure that enables obtaining an improved material and demonstrates one of the most interesting aspects of MOFs as semiconductors – such as the photo-generation of electrons and positive holes on light irradiation).

The process foresees that a metal or a metal oxide is precipitated on the photocatalyst through the irradiation of the MOF in the presence of a solution containing the precursor metal salt in an oxidation state that is soluble in the medium.[43] Scheme 1.2 is a general illustration of the generation of NPS or metal oxides by the photo-deposition method.

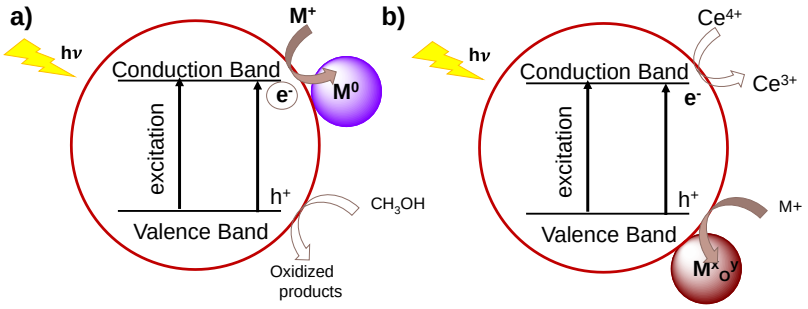

Scheme 1.2. Photodeposition of metal NPs on the catalyst surface through reduction (a) or (b) oxidation of the metal salt precursors. Methanol and Ce^{4+} are frequently employed as sacrificial electron and hole donors, respectively.

Previous works reported the photo-deposition of Ru^{4+} NPS inside the MOF cavities starting from Ru^{3+} species and so promoting their oxidation to Ru^{4+} through photo-irradiation. The reaction takes place in water where the Ru^{4+} cations form insoluble oxides of RuO_2 which are photo-deposited in the form of NPS in the crystalline structure of the MOF near the positive holes that are photo-generated on irradiation. [43]

1.3 Stability of MOFs

With the term stability, in the specific case of MOFs, three different criteria are evaluated:

i) chemical stability

ii) thermal stability

iii) mechanical stability.

In the case of MOFs, stability generally refers to structural resistance to degradation under experimental working conditions.[46-52]

Therefore, it is noteworthy that thermal stability is strongly related to chemical stability, because when the system is heated, thermal energy can alter the chemical structure of the MOFs and give rise to an initial degradation of the corresponding crystalline structure.[51,53-54] Depending on the type of application, the stability

required for the MOF material differs. Chemical stability is fundamental for applications in aqueous medium and/or at different pH value, as observed in molecular separation or drug delivery applications, while both chemical and thermal stability are fundamental parameters for catalytic processes carried out in extreme conditions such as in fuel production applications. [22, 55-58]

The main objective in the synthesis of these materials has changed from focusing on achieving extensive surface area and pore volume to achieving strong and robust materials able to resist extreme pH and corrosive conditions. [38, 45, 59-62]

The stability of MOFs generally increases as the cationic node charge increases, and consequently, the materials that have the greatest stability correspond to structures that possess positive tri and tetra metals, and this is especially true when considering materials whose structure is made up of divalent cations that are more labile (as in the case of HKUST-1, whose metallic element is Cu^{2+} or the MOF-5 consisting of Zn^{2+}).

It is known that the structure of MOF-5 changes with prolonged exposure to humidity, even at room temperature, and a species defined as MOF-5' is produced. [51,53,54] Similarly, it has been shown that HKUST-1 is not particularly stable when the material is suspended in solutions containing amines, thiols, or other agents capable of complexing the Cu^{2+} cation.[54]

Nevertheless, materials that are extremely stable to both chemical and physical treatments have been described. Among them are the MOF materials that will be studied in this PhD work. We focus our attention on UiO66, MIL-125 and UiO66(Zr)-NH_2@UiO66(Ce) structures. [1,59-64]

1.3 UiO66(Zr)

The structure of the UiO66(Zr) material was first described in 2008 by Lillerud,[1] and it has since shown incredible chemical, physical, and thermal stability.

The term UiO indicates Universitet i Oslo which represents the university where the material was discovered.

It is a general rule to denote each MOF with a three-letter code followed by numbers. Due to its stability the MOF has shown tremendous potential in industrial applications and scientists from all over the world have actively analyzed its structure.

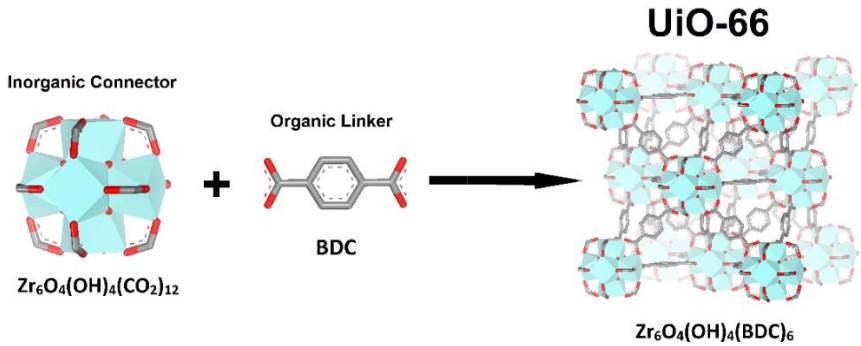

Figure 1.3. Structure of the UiO-66. Hydrogen atoms are omitted for clarity.[58]

The crystalline cell formula of this material is $Zr_6O_4(OH)_4(C_8H_4O_4)_6$.

The structure of the material is built from metallic nodes containing 6 atoms of Zr^{4+} forming an octahedron in whose faces it is positioned, with a coordination μ3, an oxygen atom or an OH^- group. Such metal nodes are thus coordinated with 6 terephthalic ligands defining cells having a size about of 1.2 nm. [65]

As previously described, one of the main characteristics of UiO66 is its high thermal and chemical stability. It is reported that heating at 400 °C does not cause the collapse of the crystalline structure, even if a redeposition at the atomic level is observed at these temperatures (which causes the elimination of a certain percentage of the ligand units).

Structural collapse starts at 500 °C and where a complete decomposition of the UiO66 structure begins.

The decomposition temperature is considerable and, as experimentally demonstrated, higher than the decomposition temperature or systematic structural change of most homogeneous and heterogeneous catalysts. [1]

In addition to its great stability, all the structural characteristics previously mentioned are extremely relevant; in detail, the studies related to UiO66 report surface area values of 1150 m^2/g and pore volumes of 0.43 cm^3/g. [1, 65, 66]

Fundamental for this thesis work is a recent study that describes the presence of structural defects that affect both the stability of the material and the catalytic properties, an aspect that will be discussed in Chapters 3 and 6.

Related to this last point, it is important to highlight that some synthetic processes use trifluoro acetic acid and/or other additives as modulating agents, favoring the controlled growth of the crystalline structure, and thus obtaining a material whose crystallinity and coordination can be considered almost free of structural defects.[37]

However, it has been observed that in the absence of modulators, a material with an improved catalytic activity can be obtained. The structural analysis of this material shows a discrepancy between the experimental and theoretical Zr content, indicating that there is an excess or a defect of ligand with respect to the Zr content. Thus, the presence of these defects implies free Zr^{4+} coordination positions which could play an active role in the catalysis carried out by the material. [67, 68]

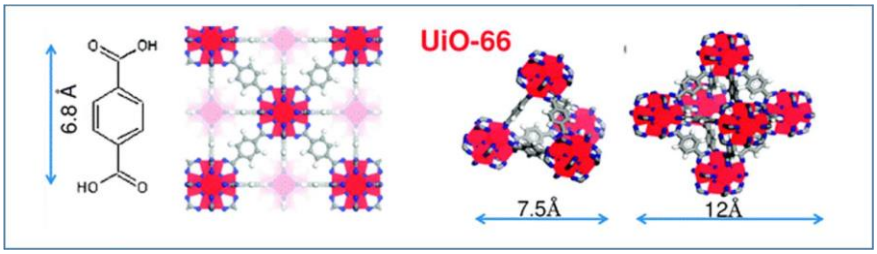

Figure 1.4. Structure of UiO66 where the dimensions of the terephthalate, the cubic structure of the unit cell and the presence in its structure of supertetrahedra and superoctahedra defined by four and six nodes, respectively, are indicated. [100]

1.4.1 MOFs as heterogeneous catalysts

As already discussed in the previous sections, one of the most promising applications of MOFs is their use as catalysts due to features such as pore size – which is in the order of 0.3/0.5 nm.

Numerous applications for MOFs as heterogeneous catalysts are reported in literature; in this chapter we will report only those strictly connected with the objective of the doctoral thesis, the use of MOFs as heterogeneous catalysts for reduction reactions of organic substrates. [38,59-62]

Different positions of the MOF structure can function as active centers for heterogeneous catalysis as defined in Figure 1.5.

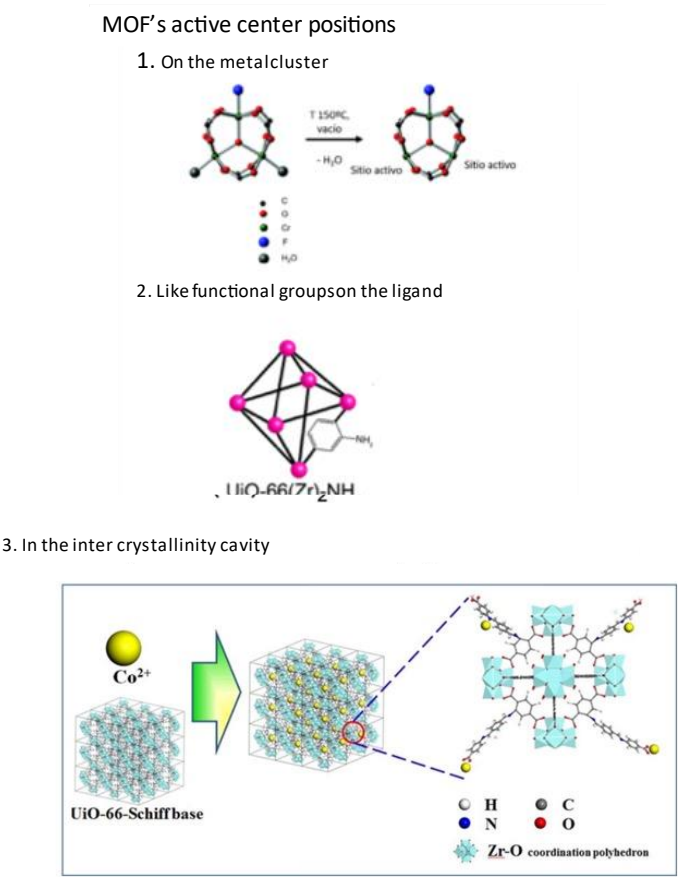

Figure 1.5. Possible location of the active centers in an MOF.[101,102]

From the analysis of the figure, it emerges that the metal centers (generally transition metals) can have interchangeable coordination positions which can easily react with the substrate. The transition metal center can behave as a Lewis acid (coordinating with the reactant), or as an oxidant.[62]

In the last case, an electronic transfer process is observed between the reactant and the metal which may not involve a coordination phenomenon.

For stable MOF structures, such as UiO66(Zr) or MIL-53, the presence of defects in the structure at the metallic center position, due to a deficit of ligand, enables the

MOF to function as the Lewis acid's center and as a heterogeneous catalyst for different type of reactions.

Thus, structural defects play a very important role in heterogeneous catalysis in materials such as MOFs, as well as zeolites (for which, for example, it is assumed that the octahedral aluminum that is positioned outside a crystalline structure behaves as the Lewis acid's center).[69]

It is known that the UiO66(Zr) material can present a variable number of structural defects in relation to the synthesis process employed.[37,67,68] These defects emerge during crystal formation due to the strong metal-ligand coordination.

It has been shown that when the metal has a high positive charge density, a thermodynamically stable structure is generated, corresponding to a perfect and defect-free crystalline structure. Structural defects occur when certain positions of the Zr^{4+} coordination sphere are incomplete.[70]

The organic reactions that have been studied using MOFs as solid Lewis catalysts include aldol condensation reactions, esterification, multiple bond additions, epoxide opening, and heterocycle formation. [38,51,56,62,65,71,72]

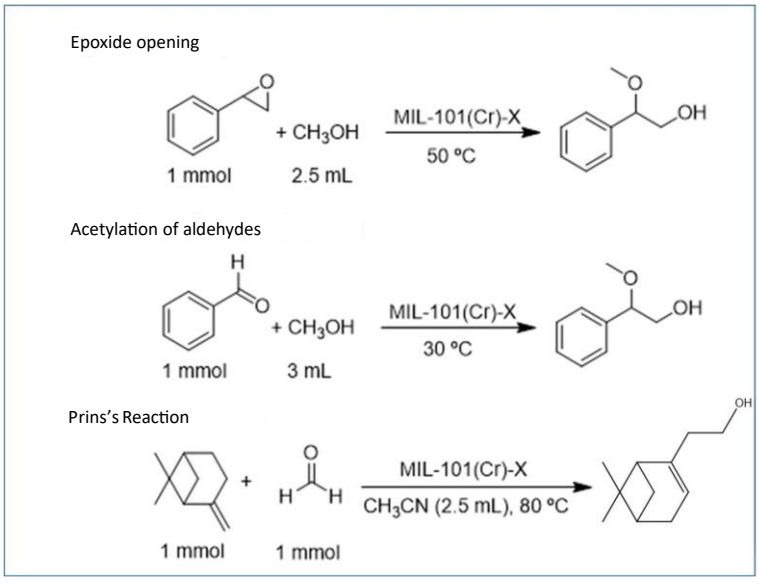

Figure 1.6. Reactions catalyzed by Lewis acid centers.

Figure 1.6 illustrates examples of reactions promoted by Lewis acid centers catalyzed by the metal nodes characterizing MOFs. Other examples discussed in the literature demonstrate how the organic ligand of the MOF structure can also function as a catalytic center.[38,61,62] In these cases, the metal centers can be perfectly coordinated and define the crystalline structure of the material. [62] Typical examples of functional groups with catalytic activity are the amino and sulfonic acid groups of the terephthalic acid ligand.[38,61,62] Although the basicity of anilines is very weak, generally much lower than that of aliphatic amines, numerous condensation reactions catalyzed by the amino groups of the terephthalate ligands in heterogeneous catalysts such as MOFs have been described.[38, 61, 62,65,73]

The third position of the MOF structure that could function as an active center are the crystalline cavities and pores where it is possible to house a guest that can function as a catalytic center of the process. Reported examples of this catalytic strategy include the formation of metal complexes in satellite positions with respect to the structure as occurs in the case of shift bases, such as phthalocyanines and metal oxides.

MOFs can function as heterogeneous catalysts of reduction reactions. Recent studies by Tang [74] have shown that MOFs can selectively reduce double bonds present in α–β unsaturated systems in specific contexts. In general, for thermodynamic reasons, in the presence of hydrogen, the reduction reaction in α–β unsaturated systems is preferably carried out at the C-O aldehyde double bond. However, when the MOF used as a catalyst has structural defects (such as Lewis acid centers and Lewis base centers obtained by the lack of a coordinated ligand in the metallic sphere of the cluster), the Lewis acid-base pair is spatially separated and this makes possible the thermodynamically unfavorable mechanism that enables the reduction of the unsaturated α–β double bond in α–β unsaturated aldehyde compounds.

Starting from all the premises described so far, Chapter 6 shows the effective reduction of unsaturated organic substrates in the presence of hydrogen and catalyzed by stable MOFs. This shows, can be justified by computational calculations, that frustrated Lewis acid-base pairs are responsible for the catalytic activity.

1.5 MIL-125 (Ti)

The term MIL indicates Material from Institute Lavoisier in reference to the university where MOF was first synthesized in 2009 by a group led by Gerard Ferey.[64]

Scientific research has long investigated the potential of titanium oxides and derivatives, especially in relation to the peculiarities of these materials in photocatalysis, but only thanks to the work developed by Ferey was it possible to isolate a highly crystalline material starting from a reaction mixture containing methanol and dimethyl formamide in the presence of titanium tetraisopropoxide at 150 °C.

The structural analysis showed that the crystalline cell is formed by $Ti_8O_8(OH_4)$-$(O_2C$-C_6H_4-$CO_2)$ units capable of generating body-centered cubic structures in which the atoms are replaced by cyclic octamers which are indicated with SBU-8 of $TiO_5(OH)$. These octamers are linked by 1,4-benzoyl dicarboxylate (BDC) linkers to generate the final 3D structure.

As happens in a CC-packed structure, each octamer has 12 neighboring SBUs, connected by BDC ligands. The 3D arrangement involves the generation of two octahedral cages corresponding to the vacant and tetrahedral octahedral positions in a typical CC package.

The heart of the SBU subunit consists of the bone and hydroxy groups in the μ2 position (Figure 1.7).

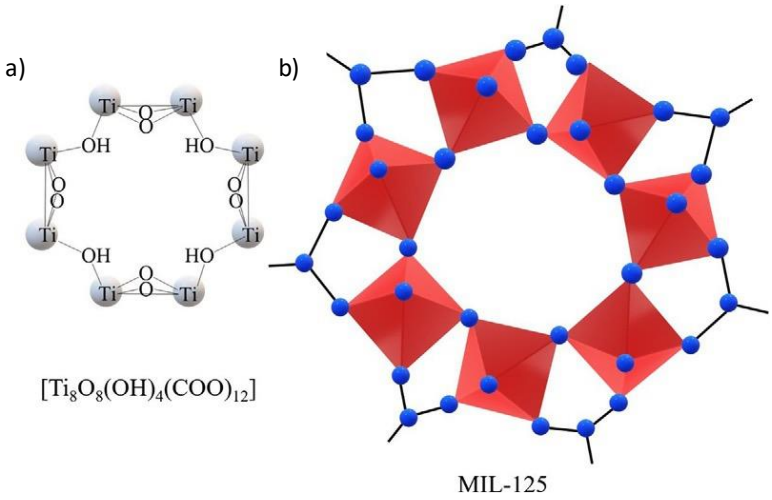

Figure 1.7. Metal nodes/clusters and primary structures of MIL-125(Ti) (a and b) solids.

MIL-125 material is extremely robust as demonstrated by thermogravimetric analysis that shows crystallinity is maintained up to 200 °C; and between 290 °C and 350 °C there is a change in the structural characteristics and a decrease in crystallinity and a structural collapse only starts at 360 °C. The structural reorganization observed at 300 °C is probably due to the loss of some hydroxyl groups as evidenced by the small weight loss in this area.

The surface area is moderately high. Ferey reports a value of 1550 $m^2\ g^{-1}$ and a pore volume of 0.65 $cm^3\ g^{-1}$. Ultraviolet analysis demonstrated the presence of absorption bands in the visible region at 500 and 596 nm; this phenomenon can be associated with the electron transition process occurring in the d-d orbitals of the titanium cluster allowing oxidation from Ti (III) to Ti (IV).

The electronic transition of d-d type favors the use of MIL-125(Ti) as a photocatalyst. It has been shown that the introduction of an amino terephthalic ligand ensures a better alignment of the HOCO-LUCO (HOCO: high occupied crystal orbital; LUCO: lower unoccupied crystal orbital) frontier orbitals as is observed by the shift of the UV absorption band in the visible region.[43]

Hence, it appears evident that the resulting MIL-125(Ti)-NH_2 material has improved photocatalytic applicability.[43] This aspect will be taken up and expanded in Chapter 5 where the photocatalytic activity of MIL-125(Ti)-NH_2 will be compared with the materials of the UiO66(Zr)-Y series.

1.6 Photocatalysis

Catalytic is defined as a process in which the presence of a species, identified as a catalyst, enables or accelerates the transformation of a substrate into the respective product, making the transition state of the aforementioned process accessible and lowering the activation energy.

A catalyst generally promotes the thermal activation of a reaction when the energy required for the transformation of the substrate is provided by heat.

However, chemistry is not only interested in thermal type reactions and there are many examples of reactions that develop using other types of energy. For this reason, attention has been increasingly focused, in recent decades, on the implementation of other types of catalysts.

In photocatalysis, a photocatalyst is defined as a molecule or a material species able to use the energy of light to promote the transformation of a substrate into a product. Most of the molecules that function as photocatalysts are organic molecules, metal complexes, or semiconductors (i.e., predominantly insoluble organic solids).

Inorganic photocatalysts, specifically metal oxides, are considered durable and perfectly stable when irradiated, but they are more difficult to modify than organic photocatalysts.

Fujishima and Honda reported that a TiO_2 photoelectrode could generate H_2 from H_2O.[75-76] From this moment, TiO_2 was used in various contexts due to its ability to combine different properties such as a lack of toxicity, durability, robustness, and an aspect of considerable importance, a high level of photocatalytic activity when irradiated with ultraviolet light. The photo response of TiO_2 is observed at

wavelengths of about 380 nm and this prevents the use of the semiconductor to expand the photo response of the photocatalysts in the visible region (the solar radiation that reaches the Earth's surface contains only a small portion of ultraviolet equal to about 4%).[77]

Scheme 1.3 illustrates the process that occurs when TiO_2 is excited by light irradiation.

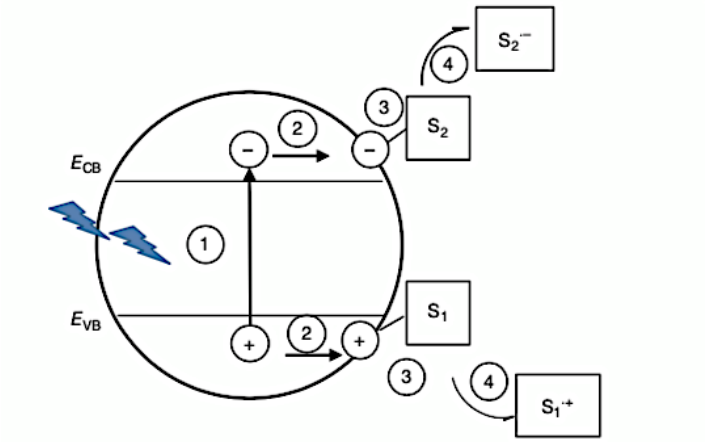

Scheme 1.3. Photocatalytic events occurring in a TiO_2 particle upon excitation with photons of appropriate wavelength. Legend: (1) Excitation; (2) charge migration to the surface; (3) molecular adsorption; (4) charge transfer.

In recent years the scientific world has focused attention on the use of renewable sources due to global warming and the scarcity of fossil sources. It is preferable to use the sun's radiation as an energy source; this implies that although TiO_2 plays a key role in the photocatalytic context, it cannot be used efficiently to promote reactions that directly convert sunlight into chemical energy. The most common strategies that have led to limited success in reducing the band gap for inorganic semiconductors include the doping of metals and non-metals and the amorphization of the outermost layer of the crystals. A continuing challenge in photocatalysis is the search for other types of inorganic and solid photocatalysts that include metal and

chalcogenic sulfides, oxalides, and metal-free materials (such as carbon nitrides or defective graphene).

The greatest limitation in the use of organic photocatalysts is the ease with which they degrade and lose their catalytic activity. Nevertheless, these organic compounds have several advantages: they are easy to synthesize, and, at the same time, it is simple to modify their photocatalytic and photochemical characteristics by introducing chromophores as substituents. An alternative for avoiding their decomposition is to support or adsorb them in solid porous materials such as zeolites or MOFs.

A particular case is the photochemical behavior shown by the metal-organic complex ruthenium tris bipyridine which, in the homogeneous phase, shows a maximum absorption band at 460 nm with a shoulder in the blue region that is responsible for its characteristic orange color.

Upon photoexcitation, an intermolecular electron transfer process takes place from the donor metal ion to the acceptor organic ligand which generates an extremely long-lived triplet excited state that decays in the microsecond time scale through an intersystem crossing from the triplet excited state to a singlet state.

Electronic decay occurs with a phosphorescence emission characterized by a high level of quantum energy at room temperature with a value of 540 nm. This is only one of the possible charge separation mechanisms induced by light absorption at a specific wavelength in a metal-organic complex. Extrapolating this behavior to a solid material suggests that another possibility to implement this type of mechanism is to excite the metal cluster of a semiconductor such as an MOF. [55, 78, 79]

As has already been extensively described in the initial part of this doctoral thesis, an MOF is a hybrid material consisting of a metal cluster and an organic linker. The metal cluster is generally formed by transition metal cations and most of the absorption visible bands in the UV-visible absorption spectra of the transition metals

are due to the presence of electrons in the d-type orbitals, hence, these absorptions are related to the electronic d-d transitions of the metal ions.[79]

The absorption of photons and the excitation of d-d electrons generally cause a rapid decay to the ground state that prevents electron transfer between the metal node and the linker.

Nevertheless, there are some exceptions, and reference is made to the electronic transitions of metal clusters that have an external electronic configuration d^{10}. In this case, it is shown that the excitation of the metal allows an effective electron transfer process from the metal node, as the electron donor, to the organic linker, as the electron acceptor.

Transient absorption spectroscopy is an extremely useful technique for detecting photochemically generated transient states while simultaneously evaluating their kinetics.[55,80] These analyses predict that a short laser pulse can generate a high concentration of transient species that is sufficient to be detected through a change in the transient absorption spectrum recorded during laser analysis.[81,82]

At the same time, it is possible to determine the kinetics of a photogenerated transient species by evaluating a signal at a specific wavelength.

It is quite common to observe that the transient signal, recorded for an MOF at a given wavelength upon laser excitation, decays in long time scales (generally in the order of milliseconds). However, this lifetime is longer than that observed for an organic molecule dispersed in solution.

The transient species observed during laser analysis can actively interact with reactants defined as quenchers, marking significant changes in the recorded transient absorption spectra.[81,83] Quenchers that are generally used to determine the nature of the photogenerated transient species are electron donors, such as methanol and amines, or electron acceptors such as oxygen and dichloromethane.

Thus, for example, the transient signal generated upon removal of an electron and corresponding to positive holes (h^+) can be quenched by the presence of an electron donor quencher such as methanol.

A parallel behavior occurs when the transient signals recorded correspond to the presence of electrons. In this case, the lifetime of the transient species decreases in the presence of electron acceptor species such as dichloromethane.

It has been observed that the typical quenchers employed are gaseous or liquid molecules with a low boiling point that facilitates diffusion through the solid during signal recording.

The experimental protocols have enabled determining the nature of the photogenerated species upon laser excitation of MOF-type materials and are the basis of the general mechanism of the metal-to-ligand type photoinduced electron transfer process.

In many cases, both e^-/h^+ species are detected during transient absorption spectroscopy studies.

Steady state measurements using electron-donor and acceptor compounds are also useful to determine the photo-generation of the e^-/h^+ charge separated state.

Some experiments are particularly convincing as they enable visually determining the photo-generation of the charge separated state upon MOF excitation by employing electron donor or acceptor molecules able to donate or accept one electron from the photo-generated charge separated state. Aromatic molecules such as viologen or 2,2'-bipyridine, as is the case of paraquat, are typically used.[81] These heterocyclic cations are strong electron acceptors, and the resulting radical cation, generated in the acceptance of an electron, exhibits an intense blue or green color.[84] Besides being brightly colored, these radical cations are particularly stable in the absence of oxygen or metals. Their molecular absorbance can be evaluated by spectroscopic analysis, and this provides a quantitative value of the concentration of the radical produced. In this way, it is possible to estimate the quantum efficiency of

the photo-generated charge separated state. Equation 1.1 shows this electron transfer process.

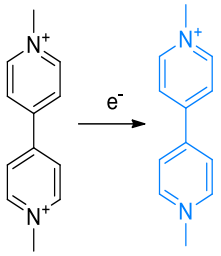

Equation 1.1

Depending on what happens when using methyl viologen as an electron acceptor, a series of aromatic heterocycles, such as phenyl diamines, can be used as electron donor molecules that are useful to demonstrate the photo-generation of positive holes on excitation of the MOF.[84]

The methyl or alkyl substituted nitrogen atoms of these organic molecules donate electrons to stabilize the photo-generated radical cations in the presence of an MOF. In this case, colorimetry can be used to quantitatively determine the concentration of the photo-generated species.

Equation 1.2 describes this process in detail.

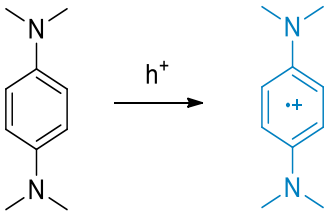

Equation 1.2

1.6.1 MOFs as photocatalysts

A key point in photophysical processes is that only photons absorbed by the material during the process (thus generating electronic states) can promote photochemical reactions.[80]

Starting from this concept, the absorption spectrum of an MOF determines which wavelengths can lead to efficient photocatalytic events. [83]

Optical spectra are defined by the absorption bands of the organic ligand (due to its rigid aromatic structure) and the absorption bands corresponding to the electronic ligand-to-metal or metal-to-ligand transitions. These latter transitions are less intense and are accompanied by the d-d electronic transitions localized on the metal ions orbitals constituting the nodes. [85]

It has already been pointed out that in the case of an MOF the allowed d-d transitions are observed for d^0 and d^{10} type metal ions. In general, the d-d type transitions localized in the metal node are defined too quickly and decay rapidly without allowing for any photochemical reaction.

In contrast, the excitation of the organic ligands occurs at the level of the π electrons. This allows electronic transitions that can generate a singlet excited state, and subsequently, a triplet excited state of the ligand that can facilitate an electronic ligand-to-metal type transfer and so generate a charge separated state. [83,86]

Thus, following the excitation of the terephthalate units of an MOF in water at a neutral pH, it is possible to record a transient signal decaying in the microsecond time scale.

By using O_2 as quencher it is possible to assess whether the decay of the electron occurs via a triplet excited state.

Similarly, the photoinduced charge separation mechanism can be verified using a metal cluster as a quencher. In the homogeneous phase, it has been experimentally demonstrated that in the presence of a Zr^{4+} cluster (which constitutes the nodes of

the UiO66(Zr) MOF) the transient signal relating to the triplet excited state of the ligand is immediately quenched.[41]

This type of quenching is defined as dynamic quenching and corresponds to all those cases in which the triplet excited state of the terephthalate unit is generated in the first instance, but due to the interaction with the Zr^{4+} cluster, its lifetime is drastically reduced.

The transient absorption spectrum of an MOF recorded a few microseconds after the laser pulse generally evolves into the formation of transient species with a very long lifetime (more than 100 microseconds). [86]

This aspect drastically contrasts with what has been observed for the transient absorption spectra recorded for organic molecules. In this second case, the lifetime of the transient species is shorter.

This change in the spectrum recorded for an MOF-like material compared to that observed for an organic ligand in solution is considered as evidence of the relocation of electrons and positive holes that have not undergone geminal recombination and thus give rise to the state of charge separation.

A further phenomenon of interest, connected to photocatalytic efficiency, emerges when evaluating the efficiency of the electronic transfer from the organic linker to the metal node. [83]

Theoretical calculations can be used to determine the superposition of the molecular orbitals LUCO of the metal and HOCO of the organic linker. [83,86,87,88] If there is no overlap and the distance between the energy clouds of neighboring species is too great, the electron transfer from the metal to the ligand will be ineffective.

This is what happens in the case of UiO66(Zr) and this lack of electron transfer from the terephthalate linker to the $Zr_6O_6(OH)_6$ cluster has been proposed to rationalize the poor photocatalytic efficiency generally observed for this MOF.

Starting from these premises, a current trend in the preparation of MOFs consists in the synthesis of mixed metal MOFs in which the metal cluster is made up of two or more metals in variable proportions. [83]

A preliminary work of great scientific interest was carried out by Li and his collaborators in which the photocatalytic efficiency of UiO66(Zr/Ti), obtained starting from UiO66(Zr), was shown to be improved following the interchange of the Zr^{4+} cation with Ti^{4+}.[89]

In this case, the Ti^{4+} cation is positioned in the hexameric nodes and acts as an electronic mediator facilitating the electronic transfer in an excited state from the terephthalate ligand to the metal node and so improving the efficiency of the photogeneration of the charge separated state with e^- and h^+.

The direct comparison of the transient absorption spectra obtained for UiO66(Zr) with those relating to UiO66(Zr/Ti) experimentally demonstrates the active role of Ti^{4+} as a mediator. A very long lifetime for the charge separated state is obtained if Ti^{4+} is present.[90]

Furthermore, the presence of a substituent in the organic ligand can facilitate the charge transfer process to the metal node by acting as an electron donor substituent. Undoubtedly, the case of the amino group is noteworthy as this functional group introduces an absorption band in the visible region (at about 400 nm) that is attributed to the free electron pair located on the nitrogen atom that provide the electron density to the π cloud of the aromatic ring. [78,79]

In this way, the amino group introduces a response in the visible region of the spectrum. This is shown in Figure 1.8.

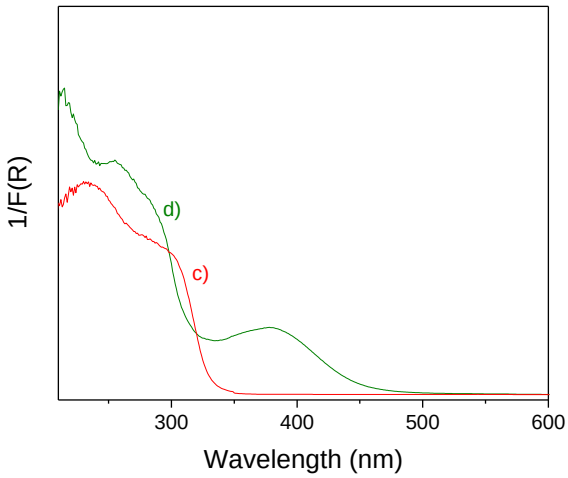

Figure 1.8. Diffuse reflectance UV-vis of MIL-l25(Ti) (b') and MIL-125(Ti)-NH_2 (b'').

The introduction of a second amino group on the aromatic ring allows a greater response of the material synthesized starting from this ligand – as proven by a shift towards the red regions in the absorption spectrum.

Similarly, the use of anthracene or naphthalene units as chromophores positioned on the organic linker can increase the response of the material in the visible region and thus could be used to promote the photoexcitation of the MOF.

1.6.1.1 Core shell type MOFs synthesis

The photocatalytic activity of MOFs can be modified and often improved by the introduction of functional groups in the ligand with auxochromic and bathochromic characteristics.

There are numerous ways to introduce a functionalized ligand into an MOF. There are some examples of direct synthesis, in which the organic functionalized ligand is introduced in the synthesis step, and there are other examples in which the functionalized ligand is introduced after the synthesis in a post-synthetic interchange

(PSE or its equivalent solvent-assisted exchange). The last procedure was found to be interesting due to the simplicity of the exchange process. The PSE protocol involves the incubation of an already formed crystal of the MOF in a solution of a pure ligand dissolved in a suitable solvent such as DMF or water.

The amount of ligand used in the post-synthetic step changes relative to what the desired product is: thus, it emerged from experimental analysis, that when complete replacement of the starting ligand is required, it is necessary to use more than four equivalents of the new ligand.[77, 91, 92]

When a lesser quantity of ligand is required to be incorporated in the post synthetic step, a 1:1 exchange: parent MOF ratio or less is used. [93-96]

This synthetic process has been widely used for the production of substituted MOFs and has shown a high degree of compatibility between ligand and MOF.

There are only few studies on the reaction mechanism and the way in which the ligand is distributed within the MOF is unknown.

In 2017, Matzger[92] proved that the distribution of the ligand within the MOF strictly depends on the diffusion process and it has been shown that if the diffusion process of the ligand is fast then it is possible to generate core shell species of the ligand positioned inside the pores of the material as shown in Figure 1.9.

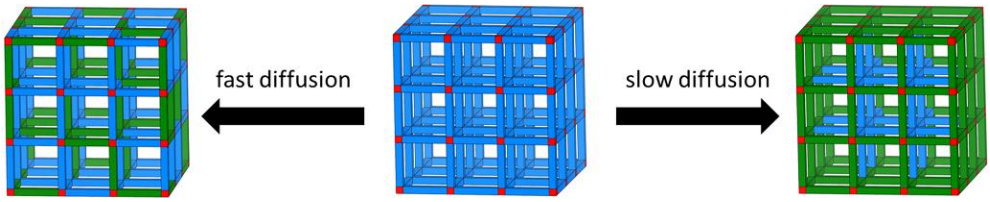

Figure 1.9. Two different ligand incorporation models: (left) a uniform distribution associated with fast diffusion relative to the exchange process, and (right) a core-shell distribution associated with slow diffusion relative to the exchange process.[92]

In other cases, in which the diffusion of the ligand inside the MOF is sluggish, as in the case of the MOF-5,[92] a structure with fewer defects is obtained which provides a homogeneous and uniform distribution of the ligand.

It emerges that both species obtained have interesting characteristics and that due to the greater number of defects generated, the core shell type species has an improved catalytic and photocatalytic level of activity.

Starting from these premises, various studies have been developed with the aim of generating core shell MOFs consisting of the heterojunction of two types of MOFs. One of the techniques developed for the synthesis of new core shell MOFs involves a seed induced growth procedure whose characteristics are like those described previously. In this case, an already synthesized MOF will be present as the core on which a second MOF will be grown by generating a structure of the MOF@MOF type.[97]

The synthesis of these hierarchical structures enables obtaining catalysts with a higher surface area; and the presence of a greater number of defects can lead to obtaining a greater number of active sites (a parameter directly related to the photocatalytic activity).

In addition, a pore-rich structure allows for the rapid and easy transmission of electrons and the diffusion of water molecules.

It can be concluded that core shell type catalysts not only maintain the excellent performance of both core and shell materials but overcome some of the disadvantages of single MOFs and exhibit properties different from single core or shell MOFs.

It should also be noted that there is an interface between the core and the shell in the MOF@MOF type structure which favors the electronic transfer process and can increase the degree of interfacial charge transfer if the material is used as a photocatalyst.

1.6.2 Photocatalytic hydrogen generation

Due to the scarcity of fossil materials used as primary energy source, the scientific world is focusing more and more attention on obtaining energy from renewable

sources. One of the possibilities that arises is to generate hydrogen from water using sunlight as a primary energy source.[85] The use of sunlight in combination with a photocatalyst to produce reduced chemical species (as is the case of H_2, methane, or formate) is a field generally known as the production of solar fuels.

For the H_2 production process, Garcia and co-workers were the first to report the photocatalytic generation of H_2 using UiO66(Zr)-NH_2 as a photocatalyst in the presence of a sacrificial electron-donor. [98] Scheme 1.4 shows the elementary reactions triggered by light which result in the reduction of an H^+ of H_2O resulting in H_2.

$$H_2O \xrightarrow[\text{photocatalyst}]{h\nu} H_2 + 1/2\ O_2 \qquad \Delta G^0 = 237.2\ KJ \cdot mol^{-1} \quad \text{(Eq. 1)}$$

$$2\ H^+ + 2\ e^- \longrightarrow H_2 \qquad \text{Reduction half-reaction (Eq. 2)}$$

$$H_2O + 2\ h^+ \longrightarrow 2\ H^+ + 1/2\ O_2 \qquad \text{Oxidation half-reaction (Eq. 3)}$$

Scheme 1.4. Photocatalytic Overall Water Splitting.

The process is similar to what occurs in the presence of traditional metal oxide photocatalysts.[78] The research area appears to be relatively new. The current goal is to increase the efficiency of the process in the presence of sunlight as an energy source and using the characteristics of MOFs in terms of synthesis flexibility. [41, 78]

One of the problems connected to the preliminary studies on the production of H_2 from water is related to the use of electron donor species which have the role of sacrificial agents and make the process industrially scalable. The next step is to use MOFs as photocatalysts which are able to convert water into H_2 and O_2 in stoichiometric quantities in the presence of light radiation (as defined in previous scheme 1.4).

From a thermodynamic point of view, the electrochemical potential required for the oxidation of water to O_2 is high and corresponds to +1.23 eV under standard

conditions with respect to the SHE electrode. This oxidation reaction represents a challenge for the scientific world.

It should also be noted that kinetically, the process requires 4 electrons and the elimination of 4 protons. Therefore, for both thermodynamic and kinetic reasons, the obtaining of H_2 and O_2 from water through an Overall Water Splitting reaction, in stoichiometric quantities, is far less documented than the evolution of H_2. [78]

Recent studies have shown the use of stable MOFs, such as MIL-125 NH_2[43,99] or even MIL-101 [43,99] to promote Overall Water Splitting reactions.

The study conducted by Garcia and a co-worker [43] showed that like inorganic oxides, the photocatalytic activity of these materials is increased by at least one order of magnitude by the use of a co-catalyst that can be incorporated on the surface or in the pores of the semiconductor.

From the experimental studies it emerged that the photocatalytic activity of the MOF improves if the co-catalyst is photo-deposited in the pores of the semiconductor and not only on the surface. It is thus clear that the photocatalytic activity of an Overall Water Splitting process depends on numerous factors – including the position of the NPS as co-catalysts, the size of the co-catalyst, and the interfacial contact between them. The preparation of these co-catalysts, as described in previous paragraphs, is implemented through a green methodology named photo-deposition and uses water and methanol as a reaction medium.

Interestingly for the work proposed in this doctoral thesis is the photo-deposition process of Ru^{4+} in the form of NPS. In this specific context, the oxidation of Ru^{3+} to Ru^{4+} is promoted through the photoirradiation of the system in which the ruthenium salt is dispersed; and in this case the reaction medium is also water and methanol. Ruthenium oxide (RuO_2), which is formed as a result of the photoirradiation process, is insoluble in the medium so that the nanoparticles will be photo- deposited in the position of the MOF in which, upon irradiation, positive holes (h^+) are photo-generated from the removal of an electron.

1.7 References

1. J. C. Hafizovic, S. Jakobsen, U. Olsbye, N. Guillou, C. Lamberti, S. Bordiga, K. P. Lillerud, *J. Am. Chem. Soc.* **2008**, *130*, 13850-13851.
2. S. R. Batten, N. R. Champness, X.-M. Chen, J. Garcia-Martinez, S. Kitagawa, L. Ohrstrom, M. O'Keeffe, M. P. Suh, J. Reedijk, *CrystEngComm.* **2012**, *14*, 3001-3004.
3. H. Li, M. Eddaoudi, M. O'Keeffe, O. M. Yaghi, *Nature*. **1999**, 402, 276-279.
4. M. Eddaoudi, J. Kim, N. Rosi, D. Vodak, J. Wachter, M. O'Keefe, O. M. Yaghi, *Science*. **2002**, 295, 469-472.
5. H. K. Chae, D. Y. Siberio-Perez, J. Kim, Y. B. Go, M. Eddaoudi, A. J. Matzger, M. O'Keeffe, O. M. Yaghi, *Nature*. **2004**, 427, 523-527.
6. J. L. C. Rowsell and O.M. Yaghi, *Microporous Mesoporous Mater.* **2004**, 73, 3-14.
7. J. L. C. Rowsell and O. M. Yaghi, *Angew. Chem.int.ed* **2005**, 117, 4748-4758.
8. O. K. Farha, I. Eryazici, N. C. Jeong, B. G. Hauser, C. E. Wilmer, A. A. Sarjeant, R. Q. Snurr, S. T. Nguyen, A. Ö. Yazaydın, J. T. Hupp, *J. Am. Chem. Soc.* **2012**, *134*, 15016-15021.
9. A. K. Cheetham, G. Férey, T. Loiseau, *Angew. Chem.in.ed* **1999**, 111, 3466-3492.
10. G. Férey, *Chem. Mater*. **2001**, 13, 3084-3098.
11. S. Kitagawa, R. Kitaura, *Comments Inorg. Chem*. **2002**, 23, 101-126.
12. S. Kitagawa, R. Kitaura, S. Noro, *Angew. Chem., Int. Ed*. **2004**, 43, 2334-2375.
13. U. Mueller, M. Schubert, F. Teich, H. Puetter, K. Schierle-Arndt, J. Pastre, *J. Mater. Chem*. **2006**, 16, 626-636.
14. M. Eddaoudi, D. B. Moler, H. Li, B. Chen, T. M. Reineke, M. O'Keeffe, O. M. Yaghi, *Acc. Chem. Res*. **2001**, 34, 319-330.
15. S. L. James, *Chem. Soc. Rev*. **2003,** 32, 276-288.
16. H. Li, M. Eddaoudi, T.L. Groy, O.M. Yaghi, *J. Am. Chem. Soc*. **1998**, 120, 8571-8572.
17. T.M. Reineke, M. Eddaoudi, M. O'Keeffe, O. M. Yaghi, *Angew. Chem. Int. Ed.* **1999**, 38, 2590-2594.
18. O. K. Farha and J. T. Hupp, *Acc. Chem. Res*. **2010**, 43, 1166-1175.
19. T Loiseau and G Férey, *J. Fluorine Chem*. **2007**, 128, 413-422.
20. L. J. Wang, H. Deng, H. Furukawa, F. Gandara, K. E. Cordova, D. Peri and O. M. Yaghi, *Inorg. Chem*. **2014**, 53, 5881−5883.
21. D. Britt, D. Tranchemontagne, O. M. Yaghi, *PNAS*, **2008,** 105, 11623–11627.
22. G. Férey, *Chem. Soc. Rev*. **2008**, 37, 191-214.
23. S. Bordiga, F. Bonino, K. P. Lillerud and C. Lamberti, *Chem. Soc. Rev*. **2010,** 4885-4927
24. Y. J. Colon and R. Q. Snurr, *Chem. Soc. Rev*. **2014**, 43, 5735-5749.

25. Q.L. Zhu and Q. Xu, *Chem. Soc. Rev*. **2014,** 43, 5468-5512.
26. H. Furukawa, N. Ko, Y. B. Go, N. Aratani, S. B. Choi, E. Choi, A. OÈ. Yazaydin, R. Q. Snurr, M. O'Keeffe, J. Kim, O. M. Yaghi, *Science*. **2010**, 329, 424-428.
27. J. J. Perry IV, J. A. Perman, M. J. Zaworotko, *Chem. Soc. Rev*. **2009**, 38, 1400-1417.
28. J.R. Li, J. Sculley, H.C. Zhou, *Chem. Rev*. **2012**, 112 (2) 869–932.
29. L.Zhu, X.Q.Liu, H.L.Jiang, L.B.Sun; *Chem.Rev*. **2017**, 117, 8129–8176,
30. G. Férey, C. Mellot-Draznieks, C.Serre and F. Millange, *Acc. Chem. Res.* **2005** ,38, 217–225.
31. H. Hayashi, A. P. Côté, H.Furukawa, M. O'Keeffe and O. M. Yaghi, *Nat. Mater.* **2007**, 6, 501–506
32. A. Kirchon, L. Feng, H.F. Drake, E.A. Joseph, H.C. Zhou, *Chem. Soc. Rev*. **2018,** 47, 8611–8638,
33. B. Chen, M. Eddaoudi, T. M. Reineke, J. W. Kampf, M. O'Keeffe, and O. M. Yaghi, *J. Am. Chem. Soc*. **2000**, 122, 11559-11560.
34. J. Kim, B. Chen, T. M. Reineke, H. Li, M. Eddaoudi, D. B. Moler, M. O′Keeffe, O. M. Yaghi, *J. Am. Chem. Soc.*, **2001,** 123, 8239-8247.
35. K. J. Gagnon, C. M. Beavers, A. Clearfield, *J. Am. Chem. Soc*., **2013**, 135, 1252-1255.
36. F. Vermoortele, B. Bueken, G. Le Bars, B. V. de Voorde, M. Vandichel, K. Houthoofd, A. Vimont, M. Daturi, M. Waroquier, V. Van Speybroeck, C. Kirschhock, D. E. de Vos, *J. Am. Chem. Soc*. **2013**, 135, 11465-11468.
37. Z. Fang, B. Bueken, D. E. de Vos, R. A. Fischer, *Angew. Chem. Int. Ed.* **2015**, 54, 7234 -7254.
38. A. Santiago-Portillo, S. Navalón, M. Álvaro, H. García, *J. Catal*. **2018**, 365, 450-463.
39. X.-P. Wu, L. Gagliardi, D.G. Truhlar, *J. Am. Chem. Soc*. **2018, 1**40, 7904–7912.
40. X.-P. Wu, L. Gagliardi, D.G. Truhlar, *J. Chem. Phys*. **2019**,150, 041701.
41. A. Melillo, M. Cabrero-Antonino, S. Navalon, M. Alvaro, B. Ferrer; H. Garcia, *Appl. Catal. B. Environ.* **2020,** 278, 119345
42. Z. Hu, S. Faucher, Y. Zhuo, Y. Sun, S. Wang, D. Zhao, *Chem. Eur. J*. **2015**, 21, 17246-17255.
43. S. Remiro-Buenamañana, M. Cabrero-Antonino, M. Martínez-Guanter, M. Álvaro, S. Navalón, H. García, *Appl. Catal. B. Environ*. **2019**, 677–684.
44. J.D. Xiao, Q. Shang, Y. Xiong, Q. Zhang, Y. Luo, S.H. Yu, H.L. Jiang, *Angew. Chem. Int. Ed.* **2016**, 55, 9389–9393.
45. S. Yuan, L. Feng, K. Wang, J. Pang, M. Bosch, C. Lollar, Y. Sun, J. Qin, X. Yang, P. Zhang, Q. Wang, L. Zou, Y. Zhang, L. Zhang, Y. Fang J. Li, H.-C. Zhou, *Adv. Mater.* **2018**, 30, 1704303.

46. S. S.-Y. Chui, S. M.-F. Lo, J. P. H. Charmant, A. G. Orpen, I. D. Williams, *Science*, **1999,** 283, 1148-1150.
47. C. Wang, X. Liu, N. Keser Demir, J. P. Chen, K. Li, *Chem. Soc. Rev*. **2016**, 45, 5107-5134.
48. T. Devic and C. Serre, *Chem. Soc. Rev*. **2014**, 43, 6097-6115.
49. Y. Bai, Y. Dou, L.-H. Xie, W. Rutledge, J.-R. Li, H.-C. Zhou, *Chem. Soc. Rev*. **2016**, 45, 2327-2367.
50. J. Canivet, A. Fateeva, Y. Guo, B. Coasne, D. Farrusseng, *Chem. Soc. Rev*. **2014**, 43, 5594-5617.
51. N. C. Burtch, H. Jasuja, K. S. Walton, *Chem. Rev*. **2014**, 114, 10575-10612.
52. A. J. Howarth, Y. Liu, P. Li, Z. Li, T. C. Wang, J. T. Hupp, O. K. Farha, *Nat. Rev. Mater*. **2016**, 1, 15018-15032.
53. Y. Ming, N. Kumar, D. J. Siege, *ACS Omega*, **2017**, 2, 4921-4928.
54. V. V. Butova, M. A. Soldatov, A. A. Guda, K. A. Lomachenko, C. Lamberti, *Russian Chem. Rev*. **2016**, 85, 280-307.
55. H. Garcia, S. Navalon, *Wiley*, **2018**.
56. G. Ferey, C. Mellot-Draznieks, C. Serre, F. Millange, J. Dutour, S. Surble, I. Margiolaki, *Science*, **2005**, 309, 2040–2042.
57. O. Stroyuk, A. Raevskaya, N. Gaponik, *Chem. Soc. Rev*. **2018**, 47, 5354–5422.
58. J.H. Cavka, S. Jakobsen, U. Olsbye, N. Guillou, C. Lamberti, S. Bordiga, K.P. Lillerud, *J. Am. Chem. Soc*. **2008**, 130, 13850–13851.
59. A. Santiago-Portillo, S. Navalon, F. Cirujano, F. Llabrés i Xamena, M. Alvaro, H. Garcia, *ACS Catal*. **2015**, 5, 3216-3224.
60. A. Gómez-Paricio, A. Santiago-Portillo, S. Navalón, P. Concepción, M. Alvaro, H. Garcia, *Green Chem.* **2016**, 18, 508-515.
61. A. Santiago-Portillo, J. F. Blandez, S. Navalón, M. Álvaro, H. García, *Catal. Sci. Technol*. **2017**, 7, 1351-1362.
62. A. Santiago-Portillo, S. Navalón, P. Concepción, M. Álvaro, H. García, *ChemCat Chem*, **2017**, 9, 2506-2511.
63. Jing, L., Zhou, W., Tian, G., Fu, H. *Chem. Soc. Rev.* **2013**, 42, 9509–9549.
64. D. Hardi, C. Serre, T. Frot, L. Rozes, G. Maurin, C. Sanchez, G. Ferey, *J. Am. Chem. Soc.*, **2009**, 131, 10857–10859.
65. J. F. Blandez, A. Santiago-Portillo, S. Navalón, M. Gimenez-Marques, M. Alvaro, P. Horcajada, H. García, *J. Mol. Catal. A Chem*. **2016**, 425, 332-339.
66. L. Valenzano, B. Civalleri, S. Chavan, S. Bordiga, M. H. Nilsen, S. Jakobsen, K. P. Lillerud, C. Lamberti, *Chem. Mater*. **2011**, 23, 1700-1718.
67. Y. Jiao, Y. Liu, G. Zhu, J. T. Hungerford, S. Bhattacharyya, R. P. Lively, D. S. Sholl, K. S. Walton, *J. Phys. Chem. C*, **2017,** 121, 23471-23479.
68. A. W. Thornton, R. Babarao, A. Jain, F. Trousseletc and F.-X. Coudert, *Dalton Trans.*, **2016**, 45, 4352-4359.

69. M. Vandichel, J. Hajek, F. Vermoortele, M. Waroquier, D. E. de Vos, V. Van Speybroeck, *Cryst. Eng. Comm.* **2015**, 17, 395-406.
70. G. C. Shearer, S. Chavan, S. Bordiga, S. Svelle, U. Olsbye, K. P. Lillerud, *Chem. Mater.* **2016**, 28, 3749-3761.
71. N. V. Maksimchuk, O. V. zalomaeva, I. Y. Skobelev, K. A. Kovalenko, V. P. Fedin, O. A. Kholdeeva, *Proc. R. Soc. A*, **2012**, 468, 2017-2034.
72. X. Li, L. Lachmanski, S. Saf, S. Sene, C. Serre, J. M. Grenèche, J. Zhang, R. Gref, *Scientific Reports*, **2017**, 7, 13142-13153.
73. A. Santiago-Portillo, S. Daliran, S. Navalón, A. R. Oveisi, M. Álvaro, R. Ghorbani-Vaghei, D. Azarifar, H. García, *J. Colloid Interface Sci*., **2018**, 532, 700-710.
74. M. Zhao, K. Yuan, Y. Wang, G. Li, J. Guo, L. Gu, W. Hu, H. Zhao, Z. Tang, *Nature*, **2016,** 19763, 76-80
75. T. Inoue, A. Fujishima, S. Konishi, K. Honda, *Nature*, **1979**, 277 (5698), 637–638.
76. A. Fujishima, K. Honda, *Nature*, **1972**, 238, 37–38.
77. J. Kou, C. Lu, J. Wang, Y. Chen, Z. Xu, R.S. Varma, *Chem. Rev.* **2017**, 117, 1445–1514.
78. A. Dhakshinamoorthy, A.M. Asiri, H. Garcıa, *Angew. Chem. Int. Ed*. **2016**, 18, 5414–5445.
79. J.L. Wang, C. Wang, W. Lin, *ACS Catal*, **2012**, 2, 2630–2640.
80. N.J. Turro, V. Ramamurthy, J.C. Scaiano, *University Science Books*, **2009**.
81. M. Alvaro, E. Carbonell, B. Ferrer, F.X. Llabres I Xamena, H. Garcia, *Chem. A Eur. J*., **2007,** 13, 5106–5112.
82. A. Walsh, J. Gascon, J.G. Santaclara, K. Svane, B. Van Der Linden, S.L. Veber, F. Kapteijn, *Sci. Rep.*, **2016** ,6.
83. A. Santiago Portillo, H.G. Baldovı, M.T. Garcıa Fernandez, S. Navalon, P. Atienzar, B. Ferrer, Z. Li, *J. Phys. Chem. C*, **2017,** 121, 7015–7024.
84. L. Michaelis, M.P. Schubert, S. Granick, *J. Am. Chem. Soc*,**1939**, 6, 1981–1992.
85. Q. Wang, K. Domen, *Chem. Rev*., **2020,** 120, 919–985.
86. D. Sun, W. Liu, M. Qiu, Y. Zhang, Z. Li, *Chem. Commun*., **2015,** 51, 2056–2059.
87. L. Shen, M. Luo, L. Huang, P. Feng, L. Wu, *Inorg. Chem*. **2015**, 54, 1191–1193.
88. D. Wang, J. Albero, H. Garcıa, Z. Li, *J. Catal*., **2017,** 349, 156–162,
89. W. Chong-Chen, L. Jian-Rong, L. Xiu-Liang, Z. Yan-Qiu, G. Guangsheng, *Energ. Environ. Sci*. **2014,** 2831–2867,
90. F.X. Llabres I Xamena, A. Corma, H. Garcia, *J. Phys. Chem. C*, **2007**, 80–85.
91. A. Fujishima, X. Zhang, D.A. Tryk, *Surf. Sci. Rep.*, **2008**, 63, 515–582.
92. J. A. Boissonnault, A. G. Wong-Foy, A. J. Matzger, *J.Am.Chem.Soc*, **2017**, 139, 14841-14844.
93. M. B Lalonde, J. E Mondloch,P. Deria, A.A Sarjeant, S.S Al- Juaid, O.L. Osman, O.K. Farha, J.T. Hupp, *Inorg. Chem*., **2015**, 54, 7142.
94. G. Nickerl, I. Senkovska, S. Kaskel, *Chem. Commun*., **2015**, 51, 2280.

95. S. Pullen, H. Fei, A. Orthaber, S.M. Cohen, S. Ott, *J. Am. Chem. Soc*., **2013**, 135, 16997.
96. X. Yu, S.M. Cohen, *Chem. Commun*. **2015**, 51, 9880.
97. W.Shenjie, Z.Guoxin, W.Jinxin Wei, Z. Zanyong, Y. Yu, *J. of Mater. Chem. A,* **2018,** 6, 18234.
98. C.G. Silva, I. Luz, F.X. Llabres I Xamena, A. Corma, H. Garcıa, *Chem. A Eur. J*., **2010** 16, 11133–11138.
99. Y. An, B. Xu, Y. Liu, Z. Wang, P. Wang, Y. Dai, B. Huang, *Chemistry Open,* **2017**, 6, 701–705.
100. S. M Chavan, J.G. Vitillo, D. Gianolio, O. Zavorotynska, B. Civalleri, S.N. Jakobsen,M. Hansen Nilsen, L. Valenzano, C. Lamberti, K. Petter Lillerud and S. Bordiga, *J.Phys.chem.***2012,**145,1614-26.
101. G. Yuan, Y. Tian, J. Liu, H. Tu, J. Liao, J. Yang, Y. Yang, D. Wang, N. Liu, *J. Chem. Eng.* **2017**, 326, 691-699.
102. S. M. J. Rogge, A. Bavykina , J. Hajek , H. Garcia , A. I. Olivos-Suarez , A. Sepúlveda-Escribano , A. Vimont , G. Clet , P. Bazin , F. Kapteijn , M. Daturi , E. V. Ramos-Fernandez , F. X. Llabrés i Xamena, V. Van Speybroeck and J. Gascon, *Chem.Soc. Rev*. **2017,** 46, 3134-3184.

Chapter 2. Aim of the work

The increasingly scarce availability of energy from fossil fuels has spurred, in the last decade, global research towards the development of processes that generate energy from renewable sources. In this context, the obtaining of stoichiometric hydrogen and oxygen from water using solar light radiation appears very interesting. This photocatalytic process is known under the name of Overall Water Splitting.

Previously literature studies have reported that the complementary oxidation and reduction reactions of water can be catalyzed by metal oxides which have shown high activity when irradiated with ultraviolet light. However, they cannot be easily chemically modified among other disadvantages.

Distinctly, as described in the introductory part, MOFs are materials that can be obtained starting from different combinations of metal clusters and organic ligands. Therefore, our aim is to synthesize new photoactive MOF materials acting as photocatalysts upon visible light irradiation.

The strategies employed are described as the objectives of this doctoral thesis:

1) Design and photophysical study of a new trimetallic UiO66 (Zr/ Ce/Ti) MOF material obtained following a post synthetic interchange of an already synthetized UiO66 (Zr/Ce) which was described for the first time by Thrular.

Thus, five UiO66 (X)-H materials will be synthesized and structurally characterized. The photocatalytic activity of the materials will firstly be analyzed through laser flash photolysis studies and subsequently the solids will be tested in the photocatalytic Overall Water Splitting reaction upon UV-visible and simulated sunlight irradiation.

The reusability of the more active material will be further investigated.

2) The Overall Water Splitting reaction will be further evaluated in the presence of new core-shell structures MOF@MOF as photocatalysts

The aim is to synthesize core-shell type MOFs of UiO66 (Zr) -NH_2 and UiO66 (Ce) which, independently, have given good photocatalytic responses in the visible range, through post-synthetic methodologies that use variable proportions of UiO66 (Zr) -NH_2 and / or UiO66 (Ce).

The structures obtained by heterojunction of UiO66 materials will be, thus, structurally analyzed and, then, photo-catalytically tested as photocatalysts for the Overall Water Splitting reaction upon UV-visible and simulated sunlight irradiation. The most photo-catalytically active material will be reused.

The photophysical study of the materials, including, the study of the transient absorption spectrum of the photogenerated transient species and the measurement of the charge separated lifetime will be reported.

3) The photocatalytic reduction reaction of 4-nitrophenol (4-NP) to 4-aminophenol (4-AP) will be studied through a tandem reaction.

The first step of the reaction will assume the generation of hydrogen from water, employing methanol as electron donor, in the presence of a series of UiO66 (Zr) – X, (X = NH_2; NO_2 and H), materials as photocatalysts. The effect of the substituent in the organic ligand will be studied. The developed hydrogen will be then used for the reduction of 4-NP to 4-AP.

The reaction mechanism will be studied in detail. Analysis in dark will be reported in order to clarify the role of the catalyst.

The photocatalytic activity will be justified both by structural analysis of the materials and by photophysical characterization.

4) Compare the catalytic activity of different UiO66(Zr) MOFs in the reduction reactions of toxic substrates to give products that represent fundamental reagents of the pharmaceutical and / or cosmetic industry which therefore have a low impact on the environment and on human health.

The main objective of this chapter will be developing a catalytic process in the absence of co-catalysts, such as metal nanoparticles, or light radiation sources.
The catalytic activity will, thus, be improved by the presence of structural defects in the MOFs which will be synthesized in the absence of modulators, leading to the formation of a frustrated Lewis acid / base center obtained by the absence of a metallic ligand-cluster bond in the active centers of the synthesized MOFs.

Solo gli occhi aperti possono scoprire che l'Universo è il libro della più alta verità.

Chapter 3.

Enhancing visible-light photocatalytic activity for overall water splitting in UiO-66 by controlling metal node composition.

Arianna Melillo[a], María Cabrero-Antonino[a], Sergio Navalón[a,*], Mercedes Álvaro[a], Belén Ferrer[a,*], Hermenegildo García[a,b,*]

[a] Departamento de Química, Universitat Politècnica de València, Camino de Vera s/n, Valencia 46022, Spain

[b] Instituto Universitario de Tecnología Química, CSIC-UPV, Universitat Politècnica de València, Av. de los Naranjos, Valencia 46022, Spain

Applied Catalysis B: Environmental 278 (2020) 119345

3.1 Abstract

The photocatalytic activity of a series of five UiO-66 (M: Zr, Zr/Ti, Zr/Ce, Zr/Ce/Ti, Ce) materials for Overall Water Splitting with generation of hydrogen and oxygen has been herein measured. The most efficient photo-catalyst for the Overall Water Splitting is the trimetallic MOF UiO-66(Zr/Ce/Ti) which achieves 230 μ mol $\cdot$ g^{-1} of H_2 and 110 μ mol$\cdot$ g^{-1} of O_2, upon UV light irradiation, and 210 μ mol$\cdot$ g^{-1} of H_2 and 70 μ mol$\cdot$ g^{-1} of O_2, under visible light irradiation. These productivity data indicate that a considerable percentage of its photo- catalytic activity derives from the visible region of the spectrum (λ> 450 nm). The photocatalytic activity of trimetallic UiO-66(Zr/Ce/Ti) was maintained upon reuse. Kinetics of the charge separated state monitored by transient absorption spectroscopy shows similar deactivation profiles for the five UiO-66 samples, suggesting that it is the charge separation efficiency the main factor responsible for the differences in the photocatalytic activity. The use of methanol as sacrificial agent during the photocatalytic experiments indicated that the high photocatalytic efficiency for Overall Water Splitting in the case of UiO-66(Zr/Ce/Ti) derives from the favorable kinetics of oxygen evolution. These results show the potential of multimetallic metal-organic frameworks as solar photo-catalysts by tuning light absorption towards the visible region.

3.2 Introduction

Metal-organic frameworks (MOFs) [1–7] in where metal ions or clusters of metal ions are interacting through coordinative bonds with organic linkers in a highly porous, crystalline, solid structure are promising photocatalysts for the production of solar fuels, including hydrogen generation. [8–21] It has been shown that the strong interaction and the rigid environment with a fixed geometry and distance between the metallic node and the organic linkers favor the photoinduced electron transfer from the organic liker to the positively charged metallic nodes, resulting in an

efficient charge separation. [8,22–26] The large diversity of transition metals together with the large number of linkers offer a considerable flexibility in the selection of adequate chromophores to enhance the photocatalytic activity. [8,14,18,24,27–30] Among the main challenges to overcome, one of them is to increase the visible light photo response of MOFs, this property being of particular interest for photocatalytic applications under solar light irradiation. [8,13,15,18,31–40]

One of the strategies that has been well established in the area is the use of amino substituted organic linkers or the use of mixed ligand (amino functionalized and parent linker) MOFs as visible light photo responsive MOFs. [8]

Another alternative and complementary approach to enhance the photo response is the use of mixed metals MOFs, in where more than one transition metal is present in the metallic node. [25,41–45] Electron relay from one metal to another can narrow the effective band gap by introducing intra band gap states that can also facilitate photo- catalytic activity by increasing the charge separation efficiency and the lifetime of the charge separation state. [25,44,46,47]

One case in where the mixed metal approach has shown its benefits is the case of UiO-66(Zr). [44,48–52] Theoretical calculations have suggested that the main of bottleneck of its photocatalytic activity derives from the fact that both the highest unoccupied (LUCO) and the highest occupied crystal orbital (HOCO) in UiO-66 correspond to frontier orbitals mostly located at the organic linker, resulting in a poor efficiency for the linker to metal node charge transfer. [22] Recently, introduction of Ti^{4+} on the node of UiO-66(Zr) has shown that the photocatalytic activity for CO_2 reduction in the presence of sacrificial electron donors of the mixed metal UiO-66 (Zr/Ti) improves in comparison to single metal analogs. [44,50,53]

In a series of papers focused on the calculation of the band gap energies and HOCO/LUCO redox potential in UiO structures, Truhlar and coworkers have proposed that Ce^{4+} based UiO-66 should be an efficient photocatalyst due to the low-laying empty 4f orbitals of Ce^{4+} that would correspond to the HOCO of this UiO-

66(Ce) material. [42] In addition, metal doping in Ce^{4+}-based MOFs should promote visible light photoresponse in UiO-66 structure by narrowing the band gap. [43] These theoretical calculations also indicate that the LUCO and HOCO energies of the resulting metal doped Ce^{4+}-UiO-66(Zr) should still have enough energy to promote water oxidation and hydrogen generation, respectively, but these predictions still require experimental evidence. [42,43]

In connection with the use of MOFs as solar light photocatalysts for Overall Water Splitting, [54–58] our group has shown that besides hydrogen generation in the presence of sacrificial electron donors, [56] MOFs can also generate oxygen photo-catalytically from H_2O in the absence of electron acceptors, a more challenging process than simple hydrogen generation in the presence of electron donors. [56] It is clear that real application of MOFs for the production of solar fuels requires the simultaneous stoichiometric generation of hydrogen and oxygen from water.

Continuing with this line of research and led by the theoretical calculations showing that modification of node composition can result in alteration of the bandgap, [42,43] the present manuscript reports the solar and visible light photocatalytic activity for Overall Water Splitting of mixed-metal UiO-66(Zr/Ce/Ti) solids. Only a few reports have shown that MOFs are able to promote the photocatalytic Overall Water Splitting, but the production rates with simulated sunlight up to now are low, about 100 $\mu mol \times g\ catalyst^{-1}$ [56]. Also, the photo-response was almost exclusively due to the UV light. In contrast to these precedents, the present study reports a high Overall Water Splitting activity mostly in the visible region due to the node composition with the three transition metals with respect to the mono and bimetallic analogs. The present study shows the opportunity that MOFs offer to tune their photocatalytic activity in the visible region and increase the photo- catalytic efficiency by developing sites that favor four electrons/four protons required in water oxidation. Fluorescence and time-resolved absorption spectroscopy provide evidence showing

that the charge separation is favorable in the case of the trimetallic UiO-66(Zr/Ce/Ti). In this way the photocatalytic activity for Overall Water Splitting for the trimetallic UiO-66(Zr/Ce/Ti) for the visible light increases about one order of magnitude with respect to the parent UiO-66(Zr). Overall, the experimental data are in general agreement with the theoretical prediction and illustrate the versatility and potential of MOFs as photo- catalysts.

3.3 Materials preparation

The materials under study, their preparation and the characterization data will be described in the first place, before commenting on their photocatalytic activity in Overall Water Splitting.

Five different UiO-66 containing either Zr or Ce and mixed bimetallic Zr/Ce, Zr/Ti and trimetallic Zr/Ce/Ti were prepared in the present study. Four of them, mono and bimetallic UiO-66(Zr), UiO-66(Ce), UiO-66(Zr/Ce) and UiO-66(Zr/Ti) materials have been already de- scribed in the literature and were prepared following the corresponding reported procedures, [44,51,59,60] while UiO-66(Zr/Ce/Ti) was synthesized for the first time in this work.

UiO-66

The synthesis of Zr-BDC MOF was carried out dissolving the metallic salt $ZrCl_4$ (0.053 g, 0.227 mmol) and the organic linker 1,4-benzene- dicarboxylic acid (H_2BDC) (0.034 g, 0.227 mmol) in *N,N'*-di-methyl formamide (DMF) (24.9 g, 340 mmol) at room temperature. The mixture was transferred in a Teflon-lined autoclave, sealed and placed in a pre-heated oven at 120 ℃ for 24 h. After cooling to room temperature, the resulting white solid was filtered and washed several times with DMF and dried at room temperature.

UiO-66(Zr/Ti)

UiO-66 (Zr/Ti) was synthetized following a post-synthetic method using $TiCl_4(THF)_2$ under inert atmosphere. Synthesized UiO-66 (0.45 mmol) and $TiCl_4$ (0.135

mmol) as Ti source were suspended in 2.5 mL DMF and incubated for 4 days at 120 °C. After cation exchange, the corresponding UiO-66 (Zr/Ti) solids were filtered, washed sequentially with DMF and MeOH and dried in vacuum at 40 °C for 24 h.

UiO-66(Zr/Ce)

UiO-66 (Zr/Ce) MOF was synthesized using Pyrex glass reaction tubes. H_2BDC (127.6 mg) was introduced into the glass reactor with DMF (3.6 mL) and aqueous solutions of cerium (IV) ammonium nitrate (0.533 M; 117 mg, 0.400 mL water), zirconium (IV) dinitrate oxide hydrate (0.533 M, 99.0 mg 0.800 mL) and concentrated formic acid (HCOOH, 100 %, 1.03 mL) were added. The suspension of the starting materials was heated under stirring for 15 min at 100 °C. The light-yellow precipitate was centrifuged in the mother solution and then it was decanted off. The solid was centrifuged twice in DMF (2 mL) and then, to remove DMF, the solid was washed and centrifuged with acetone (2 mL) four times. The resulting white solid was dried in air at 70 °C. Note that no cerium (IV) ammonium nitrate that could interfere in the photocatalytic Overall Water Splitting remains in the final solid.

UiO-66(Zr/Ce/Ti)

UiO-66(Zr/Ce) (0.45 mmol) and $TiCl_4(THF)_2$ (0.135 mmol) as Ti source were suspended in 2.5 mL DMF and incubated for 4 days at 120 °C. After cation exchange, the resulting UiO-66(Zr/Ce/Ti) solids were filtered, washed sequentially with DMF and MeOH and dried in vacuum at 40°C for 24h.

UiO-66(Ce)

H_2BDC (35.4 mg, 213 μmol) was introduced into the glass reactor with DMF (1.2 mL) adding an aqueous solution of cerium (IV) ammonium nitrate (0.400 mL, 0.5333 M). The glass reactor was heated under magnetic stirring for 15 min at 100 °C. The light-yellow precipitate was centrifuged in the mother suspension; then, the solid was centrifuged twice in DMF (2 mL). To remove DMF from the product, the solid was washed and centrifuged with acetone (2 mL) four times. The resulting

yellow solid was dried in air at 70 °C. Note that no cerium (IV) ammonium nitrate that could interfere in the photocatalytic Overall Water Splitting remains in the final solid.

Scheme S3.1 shows the route followed for the preparation of these five UiO-66 samples.

Three of them were prepared de novo in a single step using terephthalic acid and either $ZrCl_4$, Ce $(NH_4)_2(NO_3)_6$ or a mixture of both as described in the literature. [44,51,59,60] It should be noted that for the case of UiO-66(Zr/Ce), with Zr/Ce atomic ratio of 4, exhaustive characterization by elemental analysis and XPS has provided conclusive evidence supporting the location of the two metals at the nodes of the MOF. [59,61] The two Ti^{4+} containing samples were prepared by post-synthetic ion exchange in DMF as previously described, [44,50,60] starting either from UiO-66(Zr) or the bimetallic UiO-66(Zr/Ce) and using the $TiCl_4(THF)_2$ complex as Ti source in DMF at 120 °C.

Table 3.1 lists the samples under study and summarizes some of the relevant analytical and textural data obtained from ICP-AES, BET surface area and pore volume measurements (representative isotherm curves are shown in Figures S3.1-S3.3).

Table 3.1 List of the photocatalysts per formula, specific BET employed in this work indicating the metal content surface area and pore volume values.

MOF	Zr (mol)	Ti (mol)	Ce (mol)	Sum of moles	BET (m^2/g)	Pore Volume (cm^3/g)
UiO-66(Zr)	6.34	/	/	6.34	1258	0.75
UiO66 (Ce)	/	/	5.6	5.6	916	0.35
UiO-66(Zr/Ti)	4.82	0.84	/	5.66	974	0.78
UiO66 (Zr/Ce)	5.64	/	0.91	6.55	1297	0.69
UiO66 (Zr/Ce/Ti)	4.16	1.18	0.5	6.46	1019	0.65

The isomorphic crystal structure of the samples corresponding to the UiO-66 structure was confirmed by powder X-ray diffraction (PXRD). Supporting information presents the PXRD patterns recorded for the five samples (Figure S3.4-S3.5). Some small, but significant, shifts in the position of the lowest angle diffraction peak from 7.2° for UiO-66 (Ce) to 7.4° for UiO-66 (Zr) and UiO-66 (Zr/Ce) till 7.5° for UiO-66 (Zr/Ti) and UiO-66 (Zr/Ce/Ti) were observed. As a general trend, the replacement of Zr^{4+} or Ce^{4+} ions by smaller Ti^{4+} ones at the metal node causes some contraction of the unit cell, as confirmed by the crystallographic data shown in Figure S3.5. Comparison of the diffractograms b) and d) in Figure S3.5 shows for both MOFs containing Ti a shift of the peak at 7.4° to a value of 7.5°. This small shift in the position of the shortest angle diffraction peak has been already observed in the literature and attributed to the incorporation of Ti^{4+} having the small ionic radius to the nodes. [44] Similar observations have been previously reported in the literature and taken as evidence of the framework incorporation metals. [25,44,60,62,63]

Furthermore, the average size of the crystallites for the different UiO-66 materials under study was estimated using the Scherer's equation employing the most intense XRD peak at about 7.3 2 θ.

$$D = k \cdot \lambda / \beta \cos\theta$$

Where: D = crystallites size (nm); K = 0.9 (Scherer constant); λ =0.15406 nm (X-ray wavelength); β = FWHM (radiants); θ = peak position (radiants).

The calculation for the UiO-66 (Zr), UiO-66 (Zr/Ti), UiO-66 (Zr/Ce), UiO-66 (Zr/Ce/Ti) and UiO-66 (Ce) indicates average crystallite size of about 45, 30, 45, 39 and 34 nm, respectively. In the present cases, the smaller crystallite size of the different UiO-66 solids respect to the particle size obtained by FE-SEM measurements (see below) indicate that the particles are polycrystalline. Interestingly, the post-synthetic modification of UiO-66 (Zr) and UiO-66 (Zr/Ce) by Ti^{4+} ions result in a decrease of both the crystallite size and particle size as revealed by both XRD (Scherer equation) and FE-SEM measurements (see below).

The nature and content of the transition metals present in the material was determined by ICP-AES and the results obtained are listed in Table 3.1. The difference between the theoretical metal content of 6 mols of metal for the ideal formula $Zr6(\mu3\text{-}O)_4(\mu3{-}OH)_4(\mu4\text{-}BDC)_6]_n$ (BDC: benzene-1,4-dicarboxylate) and the experimental value (Table3. 1) is generally assumed as due to the presence of defects on the UiO-66 sample. [64] Importantly, the incorporation of Ti atoms on the UiO-66 (Zr) and UiO-66 (Zr/Ce) solids is accompanied by a decrease of Zr or Zr and Ce content of the materials. XRD and ICP-AES analysis agree with previous reports in the literature describing the partial replacement of Zr^{4+} or Ce^{4+} atoms present in the UiO-66 (Zr) [63] or UiO66 (Ce) solids [62], respectively, by Ti^{4+} atoms.

The density of defects in the series of UiO-66 was estimated by thermogravimetry, determining the residual remaining weight of the material after combustion of the organic linkers, corresponding to metal oxides, that was compared to the theoretical

amount according to the expected unit cell formula. Figure S3.6 contains the thermogravimetric profile of each of the different UiO-66 MOFs under study.

Surface area and porosity were determined by isothermal nitrogen adsorption at 77 K (Figures S3.1-S3.3). The data of all MOFs under study are presented in Table 3.1. It was found that UiO-66 (Zr) and UiO-66 (Zr/Ce) were the materials with the largest specific surface area above 1200 m^2/g. The smallest BET area corresponds to UiO-66 (Ce) that has a value of 916 m^2/g in good agreement with previous reports. [65] The two samples containing Ti^{4+} have an area that is in between these values. While the pore volume of four of the samples was about 0.7 cm^3/g, this value was about 0.4 in the case of UiO-66 (Ce), again in accordance with the data previously described in literature. [66] Analysis of these data shows that the surface area values of UiO-66 (Zr) and UiO-66 (Zr/Ce), both samples prepared by de novo synthesis, are comparable. This indicates that the presence of Ce^{4+} cation in the cluster of UiO66 (Zr/Ce) does not influence material porosity. This conclusion is in agreement with the coincidence of XRD patterns for UiO-66 (Zr) and UiO-66 (Zr/Ce). Particularly, the comparison of the diffractograms (a) and (c) in Figures S3.4 and S3.5 clearly indicates that the two MOFs are isostructural. In addition, the pore volume of the two materials is similar, going from 0.75 cm^3/g for UiO-66 (Zr) to 0.69 cm^3/g for UiO66(Zr/Ce). The small decrease of the pore volume could be related to somewhat larger metal nodes due to the larger cation radius of Ce^{4+} respect to Zr^{4+}. However, the fact that the Ce^{4+} percentage is less than 20 % does not cause large structural distortions. On the other hand, for UiO-66 (Ce), also prepared by de novo synthesis using a Ce^{4+} salt, the larger Ce^{4+} cation radius compared to Zr^{4+} is responsible for larger structural distortions reflected in the diffractogram of the samples (Figure S3.5) also causing a diminution of the BET surface area, 916 m^2/g, and the pore volume of the material, 0.35 cm^3/g, for UiO-66 (Ce).

Regarding Ti^{4+}, the partial replacement of Zr^{4+} and/or Ce^{4+} by Ti^{4+} cation is reflected in a substantial decrease in the surface area value of the material, but a constant pore volume size. These variations in the porosity indicate the formation of defects and distortions of the crystal structure.

IR spectroscopy shows some variation in the relative intensity of a specific peak of the terephthalate linker appearing at 1590 cm^{-1} and corresponding to the stretching vibration of the -C(O)O group, that depends on the nature of the transition metal at the node. This peak splits in two bands for UiO-66 (Zr/Ti) and shifts to higher wavenumber for UiO-66 (Zr/Ce/Ti) and UiO-66 (Zr/Ce). This variation in IR spectrum is in agreement with the replacement of Zr^{4+} in the inorganic node of bimetallic and trimetallic MOFs by Ti^{4+} and Ce^{4+} ions. Figure S3.7 in the supporting information contains the IR spectra of the five samples under study and the area where the previously mentioned variation of the peak can be observed has been marked.

The morphology of the particles was observed by field-emission scanning electron microscopy (FESEM), scanning transmission electron microscopy (STEM) and transmission electron microscopy (TEM) (Figures S3.8-S3.21 in supporting information). SEM and TEM images of UiO-66 (Zr) show the presence of nanocrystals of 248 nm in average (Figure S3.8) with cubic and octahedral morphology. The morphology of the UiO-66 (Zr) changes somewhat upon Ti^{4+} ion exchange accompanied by a decrease of the crystal size to about 173 nm in average (Figure S3.9), probably due to the occurrence of partial corrosion of the parent UiO-66 crystals as previously reported. [25] In the case of the UiO-66 (Zr/Ce) the morphology of the particles is quasi spherical with particle sizes 73 nm in average (Figure S3.10). The post-synthetic modification of the UiO-66 (Zr/Ce) by Ti^{4+} exchange also causes a decrease of the particle size to 62 nm and some deterioration of the quasi-spherical morphology of the parent bimetallic UiO-66 (Figure S3.11).

The UiO-66 (Ce) exhibits irregular spherical and octahedral shapes of about 72 nm (Figure S3.12). EDX elemental analysis of the particles shows the uniform distribution of the metals in the crystals. In particular, EDX elemental analysis of the trimetallic UiO-66 (Zr/Ce/Ti) MOF (Figure S3.17) shows somewhat higher titanium content than the value obtained by ICP analysis. In accordance with previous studies [25] the higher titanium content measured by EDX compared to ICP could be explained considering that the post-synthetic Ti exchange occur preferentially on the outermost shell of the MOF particles.
The series of the UiO-66 solids were also characterized by XPS. This technique reveals the presence and oxidation state of the atoms present in the solids. Some general XPS features for all the UiO-66 materials prepared can be drawn (Figures S3.22-S3.26 in supporting information). Thus, C1s XPS shows the presence of aromatic carbons (~284.4 eV), together with carboxylate carbon atoms (~288 eV) of the terephthalate ligands. The O 1s XPS band centered at about 532 eV is mainly due to the oxygens present at the carboxylate groups. The $Zr3d_{5/2}$ (182.5 eV) and 3 $d3/2$ (184.5 eV) are characteristic of the Zr^{4+} atoms present in the metal nodes. XPS Ti 2p confirms Ti^{4+} incorporation in the metal nodes as revealed by the XPS Ti $2p_{3/2}$ (~458 eV) and $2p_{1/2}$ (~464 eV). Regarding the characterization of Ce atoms in the UiO-66 solids, previous studies have reported the presence of Ce^{3+} atoms together with Ce^{4+} in the single-metal UiO-66 (Ce) material based on XPS. [51] The same mixed Ce^{3+}/Ce^{4+} valence state was also observed for mixed- metal UiO-66 (Zr/Ce) solids, where Zr^{4+} substitution at the nodes by $Ce^{4+/3+}$ was previously supported by X-ray absorption near edge structure spectroscopy. [51] In our study, the three XPS Ce 3d bands at 884, 901 and 917 eV can be attributed to Ce^{4+} ions at the metal nodes. [51,66]

One important issue to be addressed in mixed-metal MOFs is the location of metals in the secondary building units (SBUs). [67] One possibility is that the metals are arranged in different SBUs, while a second possibility is that the metals are randomly distributed sharing the same SBUs. Based on previous studies about mixed-metals, mixed- metal SBUs are more likely to be formed for metal ions of similar ionic radio and affinity to coordinate oxygen atoms. Thus, in principle the mixed-metal SBU would be more favorable when using Zr^{4+} and Ti^{4+} atoms, respect to Zr^{4+} and Ce^{4+}. In fact, previous reports using UiO-66 (Zr/Ce) have concluded that the more favorable configuration of this MOF would contain Zr_6 and Ce_6 nodes although mixed-metal SBU of $CeZr_5$ can be present.[68]

It was supposed, in the case of the UiO-66 (Zr/Ce/Ti) material, that the metal clusters could be constituted by one, two or three different metals. XPS has been reported as an appropriate technique to support the distribution of metals, depending on whether or no changes, in the binding energy and symmetry, of the XPS peaks corresponding to the different metal ions are observed. [67] Metal present in different SBUs should exhibit the same XPS peaks as those of single-metal MOFs since the interaction among these metal ions should be negligible because they are separated by the terephthalate units. In contrast, the presence of two or three different metals in the same SBU could be reflected in differences in the XPS spectra of the mixed-metal MOF compared to the monometallic MOF. Comparison of XPS Zr 2p peaks for the UiO-66 series (Figure S3.27) show a shift (0.32 eV) in the Zr binding energy in the case of UiO-66 (Zr/Ti) and UiO-66 (Zr/Ce/Ti) respect to the parent UiO-66 (Zr) that is not observed, as already reported, in the case of the UiO-66 (Zr/Ce). In contrast, the XPS Ti 2p peak of UiO-66 (Zr/Ti) and UiO-66 (Zr/Ce/Ti) are coincident in binding energy (Figure S3.27). These findings agree with the presence of mixed-metal SBUs of Zr and Ti atoms in the UiO-66 solids while Zr and Ce atoms should be located in isolated domains. Furthermore, XPS Ce 3d peak of UiO-66 (Ce) and UiO-66 (Zr/Ce) are very similar (Figure S3.27), as reported [61,68] while in the case

of UiO-66 (Zr/Ce/Ti) the binding energy for Ce decreases, indicating that Ce is sharing node with Ti as previously reported for the UiO-66 (Zr) partially exchanged with Ti^{4+} in the metal node. [62] In summary, XPS analysis of the samples are coincident with the literature in the case of UiO-66 (Zr/Ce) where separate Zr_6 and Ce_6 nodes are present but indicates that Ti shares nodes both with Zr and Ce.

Regarding the photocatalytic activity, one important information that indicates which are the photons absorbed by the material is the UV–vis absorption spectra. These absorption spectra recorded in the diffuse reflectance mode are presented in Fig. 3.1.

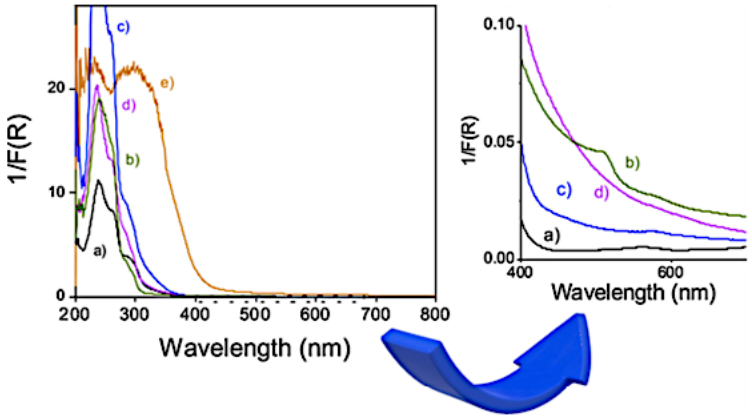

Fig. 3.1. Diffuse reflectance UV–vis spectra of a) UiO-66(Zr), b) UiO-66 (Zr/Ti), c) UiO-66(Zr/Ce), d) UiO-66(Zr/Ce/Ti), e) UiO-66(Ce). The inset (at right) corresponds to a magnification of the 400-650 nm region for plots a), b), c) and d).

It can be seen there that the sample absorbing at longer wavelength is the UiO-66 (Ce), in agreement with theoretical data that have predicted a narrowing of the HOCO/LUCO band gap for this material in comparison to UiO-66 (Zr).

In addition, as it can be, also, seen in Fig. 3.1, an expansion of the absorption spectrum onset shows that the introduction of titanium on the node produces a red shift of the onset respect to the parent UiO-66 (Zr) and the trimetallic UiO-66 (Zr/Ce/Ti) has an absorption tail that expands up to 600 nm into the visible zone.

The estimated band gap values from diffuse reflectance UV–vis spectroscopy (Figure S3.28) for UiO-66 (Zr), UiO-66 (Zr/Ce), UiO-66 (Zr/Ti), UiO-66 (Zr/Ce/Ti) and UiO- 66 (Ce) are 3.31, 3.25, 3.10, 3.05 and 2.60 eV, respectively. In particular, the band gap of UiO-66 (Zr/Ce) is close to that of UiO-66 (Zr) while UiO-66 (Zr/Ti) and UiO-66 (Zr/Ce/Ti) exhibit slightly smaller band gap values. According to previous studies [67] and in agreement with our XPS and XRD data it is proposed that the presence of Ti^{4+} in the same SBU as Zr^{4+} and $Ce^{4+/3+}$ is responsible of the band gap narrowing respect to the UiO-66(Zr) solid.[67]

3.4 Results and discussion

Photocatalytic activity

The samples under study were screened for their photocatalytic activity for Overall Water Splitting reaction upon irradiation with a xenon lamp (UV–vis) in the absence (Fig. 3.2a) or in the presence (Fig. 3.2b) of a cutoff filter ($\lambda > 450$ nm). The results obtained under these two conditions after 24 h irradiation is presented in Fig. 3.2.

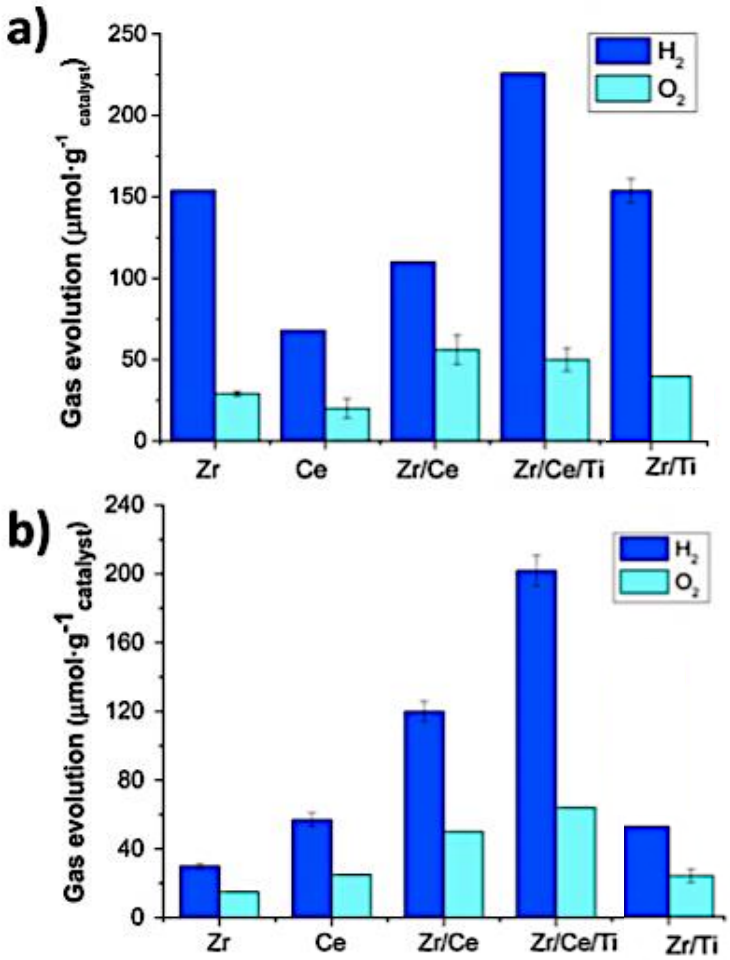

Fig. 3.2. Photocatalytic gas evolution using different UiO-66 as photocatalysts upon irradiation with UV–vis light (a) or exclusively with visible light (b) (λ > 450 nm). Reaction conditions: light source UV–vis xenon lamp (150 mW cm^{-2}) equipped or not with a filter (λ > 450 nm), photocatalyst 20 mg, H_2O (20 mL) photoreactor volume (51 mL), reaction temperature (35 °C).

As it can be seen in Figure 3.2, in all cases evolution of hydrogen and oxygen was observed. In general, the amount of oxygen was close to the expected stoichiometric amount according to the evolution of hydrogen. Similar lesser O_2 formation has been frequently observed in the literature and attributed to adventitious hole and/or

oxygen consumption. [56] This less than expected O_2 production is motivated by the high oxidation potential required in water oxidation and its slow kinetics. The lesser than expected O_2 evolution can be due to the partial consumption of holes causing some oxidation of metal sites of the photocatalyst, or the binding and consumption of some formed O_2 with metal nodes or photoreactor.

Several remarkable facts were observed when comparing the performance of the different samples. Thus, comparison of part a) and b) in Figure 3.2 shows that the photocatalytic activity of UiO-66 (Zr) derives mainly from the UV region, decreasing significantly when using exclusively visible light. This is in agreement with the poor photo response of UiO-66 (Zr) for most of the visible light photons. It is also remarkable that the photocatalytic activity of UiO-66 (Ce) remains almost the same when the sample is irradiated in the UV–vis or the visible region, meaning that in the case of UiO-66 (Ce) the photo response derives mainly from visible light, therefore contrasting with the behavior of UiO-66 (Zr). Similar performance of almost constant photocatalytic activity under UV–vis or visible light irradiation was also observed for other two samples, namely UiO-66 (Zr/Ce) and UiO-66 (Zr/Ce/Ti). The photocatalytic activity for Overall Water Splitting follows the order UiO-66 (Zr/Ce/Ti) > UiO-66 (Zr/Ce) > UiO-66 (Zr/Ti).

Overall, these photocatalytic data show the remarkable increase in visible light activity achieved by introduction of Ti^{4+} into the parent UiO-66 (Zr). As it can be seen in Figure 3.2b, the best performing UiO-66 was the trimetallic UiO-66 (Zr/Ce/Ti), showing the benefit on the photo-catalytic activity of introducing more than two metals. Overall, the photocatalytic activity of UiO-66 (Zr/Ce/Ti) is seven-time higher than that of UiO-66 (Zr). To put the obtained values into context, recently prof. Garcia's group has reported a hydrogen production from Overall Water Splitting using MIL-125(Ti)-NH_2 and MIL-125(Ti)-NH_2 simultaneously loaded with Pt and RuOx NPs as co-catalysts values of 48 and 218 μmol g^{-1} respectively, after 24 h under similar reaction conditions as there used in the parent

study. [56] The values presented in the Figure 3.2b) for UiO-66 (Zr/Ce/Ti) are similar to those reported by Pt, RuO_3-MIL 125 (Ti)- NH_2, but using exclusively visible light and in the absence of any precious metal. Thus, the results achieved in Figure 3.2 b) are remarkable and probably among the highest ever reported with visible light.

To better understand the reasons of the higher activity of the tri-metallic UiO-66 (Zr/Ce/Ti) with respect to the other related congeners, an additional experiment with monochromatic light at 400 nm was performed. This wavelength is at the limit of the visible region and corresponds to the onset of the absorption band for the four-zirconium containing UiO-66 (Figure 3.1) and the absorption intensity at this wavelength follows the same relative order as the photocatalytic activity measured for the full visible wavelength range. It is, therefore, proposed that light absorption is one of the main factors determining the relative photocatalytic activity order in the case of the Zr containing MOFs. However, the fact that UiO-66 (Ce) exhibits even higher visible absorption, but it is much less active indicates that the multi-metallic composition of the nodes should also play and important role.

In addition, the photo-response of UiO-66 (Zr/Ce/Ti) for Overall Water Splitting was measured for three specific wavelengths: 300, 400 and 500 nm (Figure 3.3), observing that the highest relative efficiency corresponds to 300 nm. The values of the apparent quantum yield (Φ) for Overall Water Splitting are given as numbers in the inset of Figure 3.3 a).

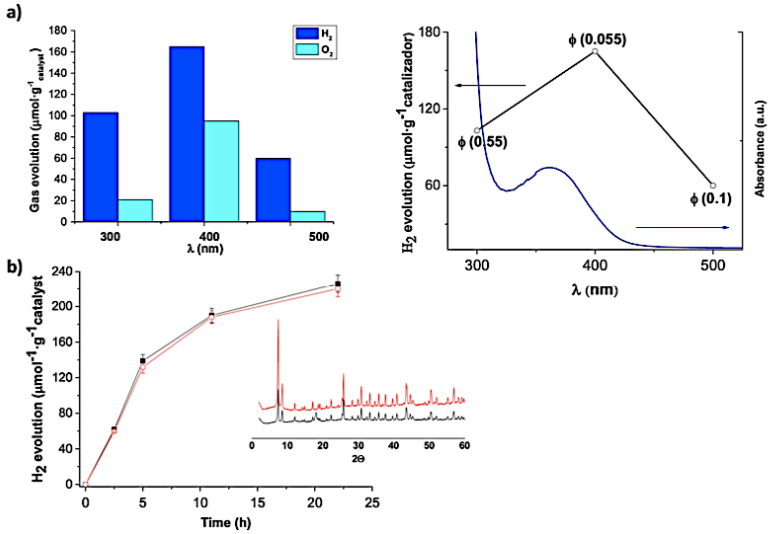

Figure 3.3: a) Overall water splitting using UiO-66 (Zr/Ce/Ti) under monochromatic irradiation (300, 400 or 500 nm). Inset: H_2 production upon monochromatic light irradiation and the corresponding UV–vis diffuse reflectance spectra of UiO-66 (Zr/Ce/Ti). The values of the apparent quantum yield for each wavelength, obtained by applying equation S1, are given as numbers in the graph for three wavelengths. Reaction conditions: UiO-66 (Zr/Ce/Ti) (10 mg), Milli Q-H_2O (10 mL), temperature (35 °C), and reaction time: 24 h. b) Photocatalytic H_2 evolution in the overall water splitting for two consecutive uses of UiO-66 (Zr/Ce/Ti): first use (■); second use (○). The inset shows the XRD of the fresh (black one) and two-times used (red one) UiO-66 (Zr/Ce/Ti) sample. Reaction conditions: catalyst (20 mg) light source UV–vis xenon lamp (150 mW cm-2) with a cut off filter (λ > 450 nm), H_2O (20 mL) photoreactor volume (51 mL), reaction temperature (35 °C).

As it can be seen in this inset, although H_2 production follows apparently the absorbance spectrum of UiO-66 (Zr/Ce/Ti), due to the higher light fluency, the highest Φ value is measured at 300 nm. Further knowledge on the photochemical processes is necessary to understand the reasons with Φ values do not follow the absorbance dependency of the UiO-66 (Zr/Ce/Ti), but they are higher at shorter wavelengths.

Regarding stability, the same sample of UiO66 (Zr/Ce/Ti) was submitted to two consecutive uses as photocatalyst under visible light irradiation (λ > 450 nm),

following the temporal profile of hydrogen and oxygen evolution (Figure 3.3b). A minor decrease in the initial reaction rate and final hydrogen production was observed that could be due to the incomplete recovery of the material after the run to be used as a photocatalyst in the subsequent reaction or to the analytical experimental error. In addition, XRD shows no change in the position or intensity of the diffraction peaks of the fresh and two times used samples.

The Overall Water Splitting reaction consists in the simultaneous production of hydrogen by conduction band electrons and the corresponding amount of oxygen by valence band holes. Typically, to increase the efficiency of a photocatalyst it is convenient to add a co-catalyst whose role is to facilitate interfacial electron transfer, and evolution of gases, increasing in this way the efficiency of the photocatalytic process. Typical co-catalysts are noble metals such as platinum, palladium and gold or critical metals such as ruthenium or cobalt. [9,56] It is important to note that in the present case, no co-catalysts are added, and that the overall splitting activity arises from the intrinsic efficiency of MOFs. Of the two simultaneously occurring reactions, i.e., hydrogen evolution and water oxidation, the latter is kinetically the most demanding reaction [69]. For this reason, it is a common practice to determine the photocatalytic hydrogen evolution in the presence of sacrificial electron donors that typically increase the efficiency of hydrogen generation by more than one order of magnitude [8]. In the present case, in the irradiation under UV–vis using UiO-66 (Zr/Ce/Ti) as photocatalyst addition of methanol as sacrificial electron donor increases the amount of hydrogen evolved by two-fold reaching a value after 24 h of 390 μ moles g^{-1} catalyst, particularly considering that methanol contributes also to H_2 evolution through photo reforming upon hole quenching. This modest influence of the presence of methanol on the photocatalytic hydrogen generation indicates that hole quenching by water with the evolution of oxygen production is, in the present case, a process that occurs at relatively high reaction rate compared to other photocatalytic systems. Therefore, that does not cause the expected slowdown

of the photocatalytic process. Since oxygen evolution by water oxidation is a four electrons-four protons process, it is proposed that the multi-metallic $M_6^{IV}O_4(OH)_4^{12-}$ clusters of UiO-66 are acting somehow similarly to the multi-metallic oxygen evolution center in the natural photosynthetic center II, cooperatively removing the electrons and protons required in the transformation of H_2O into O_2. In other words, the presence of three metals with different oxidation potentials in the same MOF could store in close spatial proximity more than one hole, while providing coordination sites for water, hydroxyl and other oxygen intermediates, making easier the formation of O_2.

Mechanism of the photocatalytic water splitting

To get more insights on the most photoactive material prepared in this work UiO-66 (Zr/Ce/Ti) the band energy was experimentally determined. In particular, a valence band energy vs. vacuum of -7.05 eV was estimated from XPS and the band gap of 3.10 eV was measured by diffuse reflectance UV–vis spectroscopy, resulting in a conduction band energy minimum vs. vacuum of 3.95 eV. These data confirm that the UiO-66 (Zr/Ce/Ti) band alignment is appropriate to promote Overall Water Splitting at pH 7 that requires CB of higher than -4.03 eV and VB lower than -5.26 eV for H_2 and O_2 evolution from water, respectively (Figure S3.29). Scheme S3.2 shows a proposed mechanism for the photoinduced charge separation in trimetallic UiO- 66 (Zr /Ce/Ti) MOF, where Ti is acting as a mediator in the electron migration, enhancing the efficiency of the photogenerated charge separation, able to generate H_2 and O_2, respectively.

To assess the occurrence of charge separation upon irradiation, an acetonitrile suspensions of mixed metal UiO-66 (Zr/Ce/Ti) in the presence of N, N, N', N'-tetramethyl-p-phenylene-diamine (TMPDA) and methyl viologen (MV^{2+}), two typical visual probes of photooxidation and photoreduction, [70,71] respectively, was carried out. As indicated in Scheme 3.1, upon excitation of the linker in UiO-66

(Zr/Ce/Ti) ligand-to-metal charge transfer should occur with the simultaneous generation of electrons in the LUCO and positive holes at the HOCO; these electrons and holes can be quenched by suitable electron acceptors (MV^{2+}) or electron donors (TMPDA).

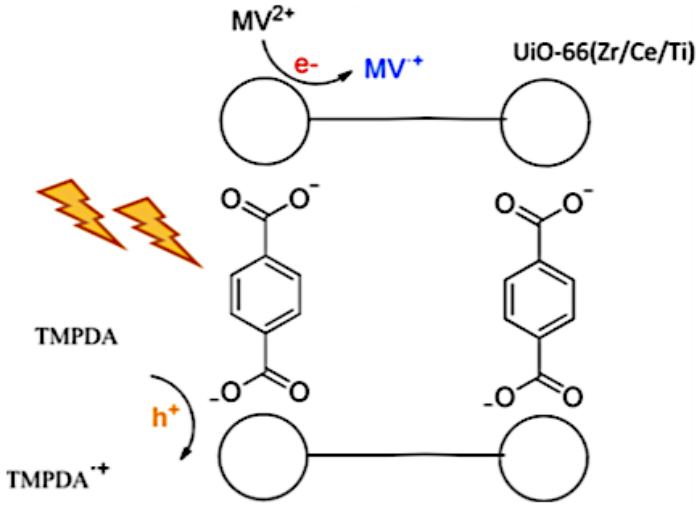

Scheme 3.1: Proposed photoinduced electron transfer process upon light excitation and generation of radical cation by MV^{2+} reduction and TMPDA oxidation.

The use of these quenchers in particular results in the generation of the corresponding radical cations that can be visually observed by their characteristic color and their generation can be conveniently followed by colorimetric techniques. These data could be also used to quantify the concentration of these radical cations. Figure 3.4 shows the absorption spectrum of an acetonitrile suspension of UiO-66 (Zr/Ce/Ti) containing TMPDA before and after irradiation. Upon irradiation the characteristic absorption band corresponding to $TMPDA^{\cdot+}$ radical cation, that exhibits an absorption band with fine structure centered at 590 nm, can be seen. [70,71]

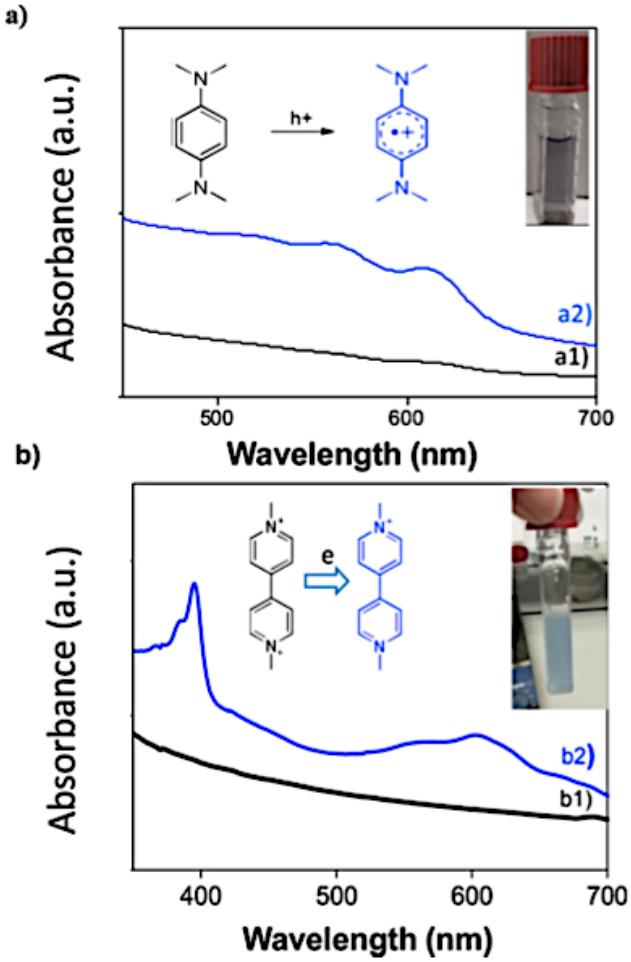

Figure 3.4. UV − vis absorption spectra of an acetonitrile suspension of the UiO-66 (Zr/Ce/Ti) MOF in the presence of: TMPDA as electron donor a), before a1) and after a2) solar simulator irradiation, and MV^{2+}, as electron acceptor b), before (b1) and after (b2) xenon lamp irradiation. The photographs of the insets show the visual appearance of the suspensions under each condition.

The inset in Figure 3.4 a) shows a photograph of the suspension upon irradiation showing the characteristic color of the photogenerated $TMPDA^{\cdot+}$.

While the use of TMPDA as probe shows the occurrence of oxidation upon simulated sunlight irradiation of UiO-66 (Zr/Ce/Ti) as photo-catalyst, an analogous

experiment was carried out with MV^{2+}, as electron acceptor. In this case the suspension becomes blue and optical spectroscopy shows the characteristic UV–vis spectrum of $MV^{\cdot+}$ radical cation that exhibits a sharp peak at 390 nm with a shoulder in the blue side and a much less intense broad peak with fine structure at 600 nm. Formation of $MV^{\cdot+}$ radical cation indicates the photogeneration of electrons upon irradiation of UiO-66 (Zr/Ce/Ti).

After having shown the occurrence of charge separation upon irradiation of UiO-66 (Zr/Ce/Ti) with generation of electrons and holes, it is of interest to determine the possible origin of the higher photocatalytic activity of trimetallic UiO-66 (Zr/Ce/Ti) in comparison with monometallic and bimetallic analogues. Towards this goal, emission spectra of the samples suspended in acetonitrile were recorded. The results are presented in Figure 3.5.

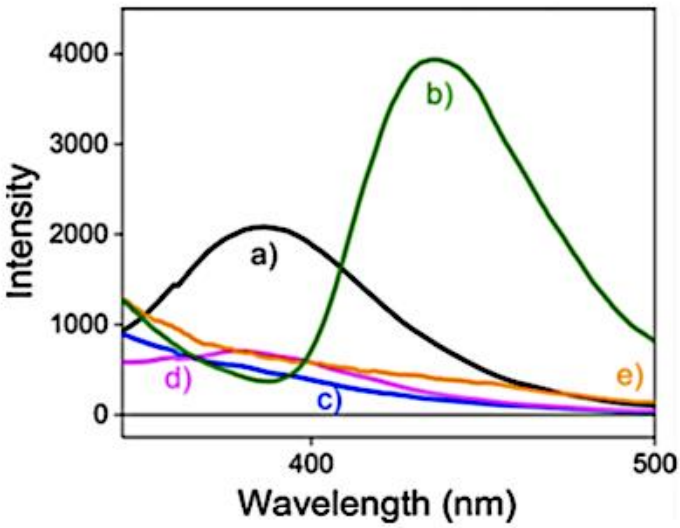

Figure 3.5. Emission spectra (λ_{exc}=266 nm) of acetonitrile suspensions of a) UiO-66 (Zr), b) UiO-66 (Zr/Ti), c) UiO-66 (Zr/Ce), d) UiO-66 (Zr/Ce/Ti), and e) UiO- 66(Ce).

As it can be seen there, two samples, UiO- 66 (Zr) and UiO-66 (Zr/Ti) exhibit emission in the range from 350−600 nm.

The emission intensity follows the order UiO-66 (Zr/Ti) > UiO-66 (Zr). Since the most removable origin of this emission is the energy dissipation of electron-hole recombination, the higher the emission intensity, the higher the electron-hole recombination. Therefore, the fact that trimetallic UiO-66 (Zr/Ce/Ti) does not emit indicates that, for this material, charge recombination occurs in much lesser extent than for the other samples. Charge recombination is an undesirable energy waste process, competing with photocatalyst.

This relative emission intensity is, therefore, compatible with the higher photocatalytic efficiency of UiO-66 (Zr/Ce/Ti) that should become favored as the percentage of charge recombination, related to the emission intensity decreases.

Transient absorption spectroscopy measurements were carried out to further understand the origin of the enhanced photocatalytic activity. In one of the series of the experiments, aqueous solution of the terephthalate ligand was irradiated with a nanosecond 266 nm laser pulse. A transient decay in the microsecond time scale, attributed to the photogeneration of the terephthalic triplet exited state, was recorded. The influence of the presence of the metals present in the nodes of UiO-66 to this transient excited state was studied by monitoring the transient signals at 330 nm. It was observed that the transient signal corresponding to the terephthalic triplet exited state is quenched by $Zr_6O_4(OH)_4^{-12}$, that was prepared previously to be used in the quenching experiment. Figure 3.6 shows the change in the terephthalate transient signal in the absence and in the presence of the $[Zr_6O_4(OH)_4]^{-12}$ cluster.

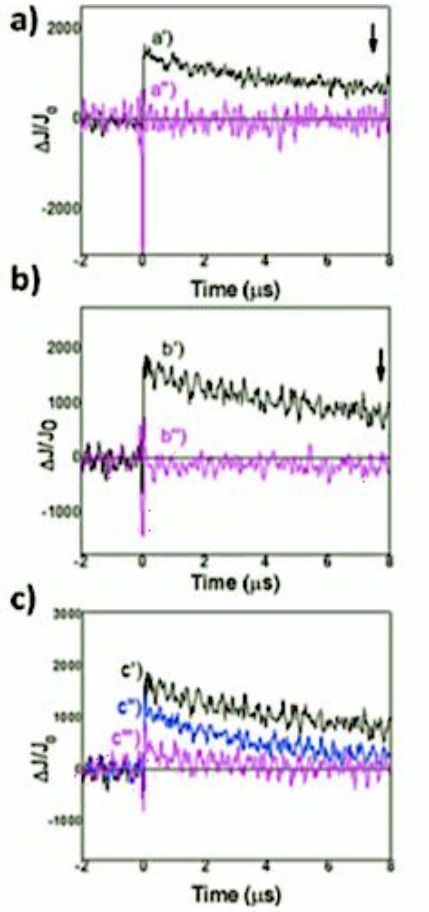

Figure 3.6. a) Temporal profiles of the transient signal monitored at 330 nm for an aqueous solution of the terephthalate ligand at pH 12: before a') and after a'') the addition of an aqueous solution of $Zr_6O_4(OH)_4$ (7.5×10^{-4} M); before b') and after b'') the addition of an aqueous solution of $TiCl_4$ (1.0×10^{-4} M) and before c') and after the addition of an aqueous solution of $Ce(NH_4)_2(NO_3)_6$ (0.5×10^{-4} M, c'') and 10.0×10^{-4}M c''')).

Similarly, terephthalate transient signal was quenched by the presence of $TiCl_4$ and Ce $(NH_4)_2(NO_3)_6$, although for these two cases the quenching rate constant was significantly lower than for the case of $Zr_6O_4(OH)_4^{12-}$ cluster (quenching rate constant values are k: $[Zr_6O_4(OH)_4]^{12-}$ = 71216 M^{-1}; k $TiCl_4$ = 45839 M^{-1}; k Ce

$(NH_4)_2(NO_3)_6$ = 48187 M^{-1}). Although the Ti^{4+} and Ce^{4+} species may not exactly correspond to the UiO-66 metal clusters, this quenching study in solution proves that the triplet excited state of the terephthalate linker can interact with the clusters or cations present in the UiO-66 (Zr/Ce/Ti) node.

Additional measurements were carried out with all the solid UiO-66 samples in acetonitrile suspensions. It has been reported in literature that photogenerated transients can be conveniently monitored using persistent suspensions of these semiconductors. [8] To address the nature of the transient signals, dichloromethane as electron quencher and methanol as hole quencher were employed. Upon excitation of acetonitrile suspensions of the five UiO-66 samples, transient signals spanning the whole range of UV and visible wavelengths were observed. The intensity of the absorbance increases toward the red region of the spectrum in three of the samples containing Zr and in UiO- 66 (Ce), while UiO-66 (Zr/Ti) presents a neutral absorbance intensity through the whole range of wavelength (Figure 3.7).

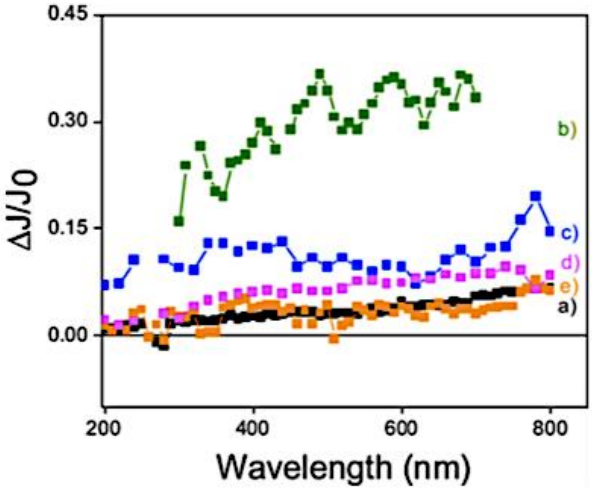

Figure 3.7. Transmission transient absorption spectra of a) UiO-66 (Zr), b) UiO-66 (Zr/Ti), c) UiO-66 (Zr/Ce), d) UiO-66 (Zr/Ce/Ti) and e) UiO-66 (Ce) MOF recorded 1.4 μs after 266 nm laser excitation under argon atmosphere for optically matched (absorbance 0.1) suspensions of the UiO-66 solids in acetonitrile.

Two different behaviors in the presence of quenchers were observed. In the case of monometallic UiO-66 (Zr), UiO-66 (Ce) as well as trimetallic UiO-66 (Zr/Ce/Ti) the transient signal is quenched both by addition of dichloromethane and methanol. This quenching behavior indicates that transient signals in the whole spectral range correspond to the combined absorption of electrons and holes. In agreement with the quenching, the signal monitored at 400 nm becomes faster in the presence of both quenchers. To illustrate this behavior Figure 3.8 shows the case of the most efficient trimetallic UiO66 (Zr/Ce/Ti) photocatalyst.

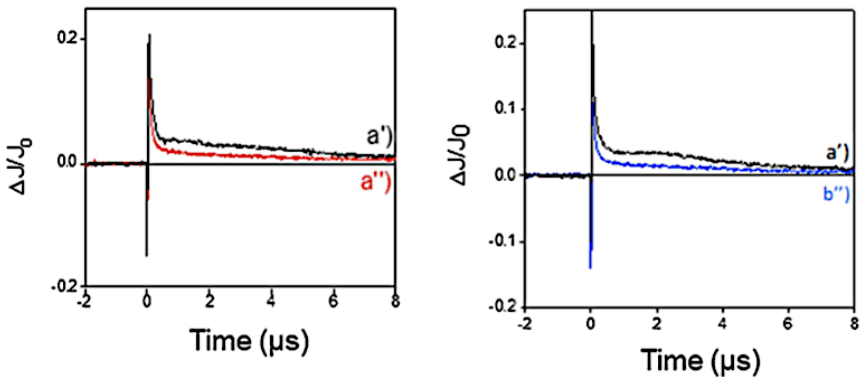

Figure 3.8. Temporal profile of the transient signals monitored at 400 nm for UiO-66 (Zr/Ce/Ti) recorded upon 266 nm laser excitation under argon atmosphere a'), and after addition of 300 μL of dichloromethane a'') and methanol b'').

The two bimetallic MOFs, UiO-66 (Zr/Ti) and UiO-66 (Zr/Ce) exhibit a contrasting behavior. The transient signals are quenched by the presence of methanol, but in the presence of dichloromethane, the intensity of the transient signals and the lifetime of the transient species increase for UiO-66 (Zr/Ti), while for UiO-66 (Zr/Ce) a moderate quenching in the intensity, but not in the lifetime can be seen. This indicates that for UiO-66 (Zr/Ti) the main component contributing to the monitored transient signals are photogenerated holes that disappear in the presence of methanol but increase in intensity in the presence of dichloromethane due to the lesser extent of electron-hole recombination, when an electron scavenger is present. Supporting information presents a more complete set of transient spectra in the presence of these

two quenchers (Figures S3.30-S3.33). Overall, the time resolved study agrees with the generation of a charge separated state decaying in a few μs with two kinetics (Figure 3.9): one fast that is complete in less than one microsecond corresponding to about 65 % of the total initial signal and another slower spanning a few microseconds.

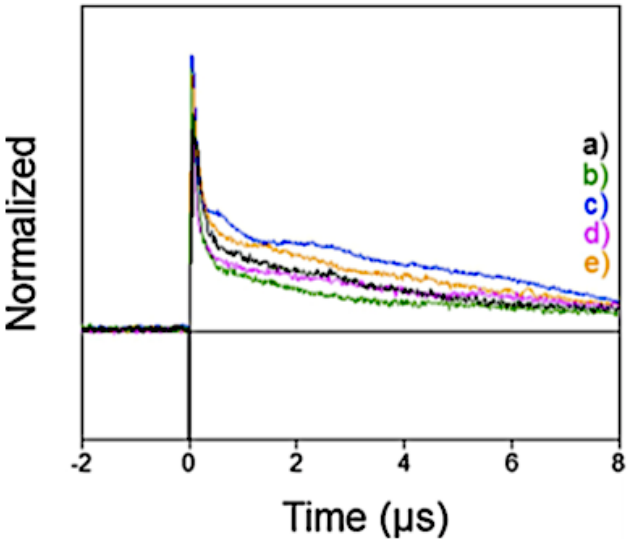

Figure 3.9. Temporal profile of the transient signals monitored at 400 nm recorded upon 266 nm laser excitation under argon atmosphere for a) UiO-66 (Zr), b) UiO-66 (Zr/Ti), c) UiO-66 (Zr/Ce), d) UiO-66 (Zr/Ce/Ti), e) UiO-66 (Ce) MOFs.

This temporal profile indicates the occurrence of a fast charge recombination of 50–70 % of the photogenerated electrons and holes in less than one microsecond and relocation of the remaining percentage of charge carriers resulting in a longer-lived charge separation state that finally disappears at a longer timescale. The presence of quenchers alters both the fast and the slower regime, indicating that both types of charge carriers are accessible to the quenchers. A summary of the kinetic data obtained from the time resolved measurements are summarized in Table S3.1 of the supporting information.

Importantly, the dynamic behavior of the trimetallic UiO-66 (Zr/Ce/ Ti) does not differ significantly from that of monometallic UiO-66 (Zr), since the transient

signals and the percentage of the slowest components are similar. Therefore, it is suggested that the higher efficiency observed in Overall Water Splitting is not related to thermodynamic considerations related to bandgap and HOCO-LUCO energy alignment, since H_2 and O_2 evolution is observed in all the materials, but to kinetic factors. In this way, the trimetallic UiO-66 (Zr/Ce/Ti) would exhibit the most efficient charge separation and the lesser degree of charge recombination. This would result in a higher density of electrons and holes available for water splitting. The charge separation state transients would have similar lifetimes and temporal decays in the five samples under study.

3.5 Conclusions

A computational study has suggested that UiO-66 (Ce) should be a suitable photocatalyst for Overall Water Splitting. However, the present study has provided experimental that, instead of monometallic MOFs, mixed metal UiO-66 are more efficient, particularly trimetallic UiO-66 (Zr/Ce/Ti). For this material a high percentage of the photocatalytic activity, over 40 %, derives from visible light photo-response. Photocatalytic experiments using methanol as sacrificial electron donor indicate that oxygen generation is considerably favored in trimetallic UiO-66, a fact that has been attributed to the collective cooperation of trimetallic clusters favoring the kinetics of the four electrons-four proton process resulting in oxygen evolution. Time resolved measurements in acetonitrile suspensions have allowed to detect the charge separation state in the microsecond time scale. The transient signals correspond to a combination of electrons and holes in the complete UV–vis wavelength range, both for UiO-66 (Zr) and UiO-66 (Zr/Ce/Ti), with similar kinetic behavior. In contrast with the similar charge separation state kinetics, photoluminescence measurements reveal much lesser emission intensity for trimetallic UiO-66 (Zr/Ce/Ti) than for monometallic UiO-66 (Zr), indicating that unfavorable charge recombination occurs for UiO-66 (Zr/Ce/Ti) in much lesser

extent than in the other UiO-66 congeners. Thus, the multi-metallic composition favors higher generation of charge separation, increasing the photocatalytic efficiency of this material. Overall, the present study shows the opportunity that MOFs offer to prepare efficient visible-light photo-catalysts for Overall Water Splitting, something that has been challenging for metal oxide semiconductors.

3.6 References

1. H. Li, M. Eddaoudi, M. O'Keeffe, O.M. Yaghi, *Nature*, **1999,** 402, 276–279.
2. G. Férey, C. Mellot-Draznieks, C. Serre, F. Millange, J. Dutour, S. Surblé, I. Margiolaki, *Science*, **2005**, 23, 2040–2042.
3. H. Furukawa, K.E. Cordova, M. O'Keeffe, O.M. Yaghi, *Science*, **2013**, 341, 1230444.
4. T. Devic, C. Serre, *Chem. Soc. Rev*., **2014**, 43, 6097–6115.
5. S. Kitagawa, R. Kitaura, S.-I. Noro, *Angew. Chem. Int. Ed*., **2004**, 43, 2334–2375.
6. O.M. Yaghi, M. O'Keeffe, N.W. Ockwig, H.K. Chae, M. Eddaoudi, J. Kim, *Nature*, **2003**, 423, 705–714.
7. H.-C. Zhou, J.R. Long, O.M. Yaghi, *Chem. Rev*., **2012**, 112, 673–674.
8. A. Dhakshinamoorthy, A.M. Asiri, H. García, *Angew. Chem. Int. Ed*., **2016**, 55, 5414–5445.
9. X. Li, J. Yu, M. Jaroniec, X. Chen, *Chem. Rev*., **2019**, 119, 3962–4179.
10. M. Cabrero-Antonino, S. Remiro-Buenamanaña, M. Souto, A.A. Garciá-Valdivia, D. Choquesillo-Lazarte, S. Navalón, A. Rodríguez-Diéguez, G. Mínguez Espallargas, H. Garciá, *Chem. Commun*.**2019**, 55, 10932–10935.
11. D. Mateo, A. Santiago-Portillo, J. Albero, S. Navalón, M. Alvaro, H. García, *Angew. Chem. Int. Ed*., **2019**,58, 17843-17848
12. H. García, S. Navalón, Metalorganic framework: application in separation and catalysis, *Wiley*, **2018**
13. I.I. Alkhatib, C. Garlisi, M. Pagliaro, K. Al-Ali, G. Palmisano, *Catal. Today*, **2020**, 340,209–224.
14. R. Li, W. Zhang, K. Zhou, *Adv. Mater.*, **2018**, 30, 1705512.
15. H. Luo, Z. Zeng, G. Zeng, C. Zhang, R. Xiao, D. Huang, C. Lai, M. Cheng, W. Wang, W. Xiong, Y. Yang, L. Qin, C. Zhou, H. Wang, Y. Zhou, S. Tian, *Chem. Eng. J.*, **2019**, 123196.
16. Y. Shi, A.-F. Yang, C.-S. Cao, B. Zhao, *Chem. Rev.*,**2019**, 390, 50–75.
17. C.G. Silva, I. Luz, F.X. Llabrés I Xamena, A. Corma, H. García, *Chem. Eur. J.*, **2010**, 11133–11138.
18. S. Wang, X. Wang, *Small*, **2015**, 26, 3097–3112.
19. H.-Q. Xu, J. Hu, D. Wang, Z. Li, Q. Zhang, Y. Luo, S.-H. Yu, H.-L. Jiang, *J. Am. Chem. Soc*., **2015**, 137, 13440–13443.
20. S.-N. Zhao, G. Wang, D. Poelman, P. Van Der Voort, *Molecules*, **2018,** 23, 2947.
21. A. Jamal Sisi, M. Fathinia, A. Khataee, Y. Orooji, *J. Mol. Liq*., **2020**, 308, 113018.
22. M.A. Nasalevich, C.H. Hendon, J.G. Santaclara, K. Svane, B. van der Linden, S.L. Veber, M. Fedin, A.J. Houtepen, M.A. van der Veen, F. Kapteijn, A. Walsh, J. Gascon, *Sci. Rep*., **2016**, 6, 23676.

23. M.A. Nasalevich, M. Van Der Veen, F. Kapteijn, J. Gascon, *CrystEngComm.*, **2014**, 16, 4919–4926.
24. J.G. Santaclara, F. Kapteijn, J. Gascon, M.A. Van Der Veen, *CrystEngComm*, **2017,** 19, 4118–4125.
25. A. Santiago-Portillo, H.G. Baldoví, M.T.G. Fernandez, S. Navalón, P. Atienzar, B. Ferrer, M. Alvaro, H. Garcia, Z. Li, *J. Phys. Chem. C*, **2017**, 121, 7015–7024.
26. L. Wang, P. Jin, S. Duan, H. She, J. Huang, Q. Wang, *Sci. Bull*., **2019**, 64, 926–933.
27. J. Qiu, X. Zhang, Y. Feng, X. Zhang, H. Wang, J. Yao, *Appl. Catal. B. Environ.*, **2018**, 231, 317–342.
28. F. Khodadadian, M. Nasalevich, F. Kapteijn, A.I. Stankiewicz, R. Lakerveld, J. Gascon, *Alternative Energy Sources for Green Chemistry*, **2016**, 227–269.
29. M. Shekofteh-Gohari, A. Habibi-Yangjeh, M. Abitorabi, A. Rouhi, *Crit. Rev. Environ. Sci. Technol*., **2018**, 48 806–857.
30. M. Salavati-Niasari, *Chem. Lett*., **2005**, 34, 1444–1445.
31. M. Pirhashemi, A. Habibi-Yangjeh, S. Rahim Pouran, *J. Ind. Eng. Chem*., **2018**, 62, 1–25.
32. M. Ghanbari, M. Salavati-Niasari, *Inorg. Chem*., **2018**, 57, 11443–11455.
33. P. Mehdizadeh, Y. Orooji, O. Amiri, M. Salavati-Niasari, H. Moayedi, *J. Clean. Prod*., **2020**, 252, 119765.
34. Y. Orooji, R. Mohassel, O. Amiri, A. Sobhani, M. Salavati-Niasari, *J. Alloys Compd.* **2020**,835, 155240.
35. Y. Orooji, Aa. Alizadeh, E. Ghasali, M.R. Derakhshandeh, M. Alizadeh, M.S. Asl, T. Ebadzadeh, *Ceram. Int.*, **2019**, 45, 20844–20854.
36. F. Mohandes, F. Davar, M. Salavati-Niasari, *J. Phys. Chem. Solids*, **2010**, 71, 1623–1628.
37. M. Salavati-Niasari, M.R. Loghman-Estarki, F. Davar, *Chem. Eng. J.*, **2008**, 145, 346–350.
38. M. Salavati-Niasari, *Microporous Mesoporous Mater.*,**2006**, 95,248–256.
39. M. Sabet, M. Salavati-Niasari, O. Amiri, *Electrochim. Acta*, **2014**, 117, 504–520.
40. L. Wang, S. Duan, P. Jin, H. She, J. Huang, Z. Lei, T. Zhang, Q. Wang, *Appl. Catal. B Environ*., **2018**, 239, 599–608.
41. M.A. Syzgantseva, C.P. Ireland, F.M. Ebrahim, B. Smit, O.A. Syzgantseva, *J. Am. Chem. Soc.*, **2019**, 141, 6271–6278.
42. X.-P. Wu, L. Gagliardi, D.G. Truhlar, *J. Am. Chem. Soc***., 2018**, 140 ,7904–7912.
43. X.-P. Wu, L. Gagliardi, D.G. Truhlar, *J. Chem. Phys*., **2019**, 150, 041701.
44. D. Sun, W. Liu, M. Qiu, Y. Zhang, Z. Li, *Chem. Commun.*, **2015**, 51, 2056–2059.
45. M. Salavati-Niasari, *Inorg. Chem. Commun.*, **2005**, 8, 174–177.
46. M.A. Nasalevich, M.G. Goesten, T.J. Savenije, F. Kapteijn, J. Gascon, *Chem. Commun*., **2013**, 49, 10575–10577.
47. M. Salavati-Niasari, A. Sobhani, F. Davar, *J. Alloys Compd*., **2010,** 507, 77–83.

48. J.H. Cavka, S. Jakobsen, U. Olsbye, N. Guillou, C. Lamberti, S. Bordiga, K. Lillerud, *J. Am. Chem. Soc*., **2008**, 130, 13850–13851.
49. L. Valenzano, B. Civalleri, S. Chavan, S. Bordiga, M.H. Nilsen, S. Jakobsen, K.P. Lillerud, C. Lamberti, *Chem. Mater.*, **2011**, 23, 1700–1718.
50. Y. Lee, S. Kim, J.K. Kang, C. S.M, *Chem. Commun*., **2015**, 51, 5735–5738.
51. F. Nouar, M.I. Breeze, B.C. Campo, A. Vimont, G. Clet, M. Daturi, T. Devic, R.I. Walton, C. Serre, *Chem. Commun*., **2015**, 51, 14458–14461.
52. K. Hendrickx, J.J. Joos, A. De Vos, D. Poelman, P.F. Smet, V. Van Speybroeck, P. Van Der Voort, K. Lejaeghere, *Inorg. Chem.*, **2018**, 57, 5463–5474.
53. A. Akhundi, A. Badiei, G.M. Ziarani, A. Habibi-Yangjeh, M.J. Muñoz-Batista, R. Luque, *Mol. Catal*., **2020**, 488, 110902.
54. P. Frontera, A. Macario, M. Ferraro, P. Antonucci, *Catalysts*, **2017**, 7, 59.
55. Y. An, B. Xu, Y. Liu, Z. Wang, P. Wang, Y. Dai, X. Qin, X. Zhang, B. Huang, *Chemistry Open*, **2017**, 6, 701–705.
56. S. Remiro-Buenamañana, M. Cabrero-Antonino, M. Martínez-Guanter, M. Álvaro, S. Navalón, H. García, *Appl. Catal. B. Environ.*, **2019** 677–684.
57. S. Gholamrezaei, M. Salavati-Niasari, *Ultrason. Sonochem.*, **2018**, 40, 651–663.
58. M. Ghasemi, A. Khataee, P. Gholami, R.D.C. Soltani, A. Hassani, Y. Orooji *J. Environ. Manage*., **2020**, 267, 110629.
59. M. Lammert, C. Glißmann, N. Stock, *Dalton Trans*., **2017**, 46, 2425–2429.
60. A. Santiago-Portillo, S. Navalón, M. lvaro, H. García, *J. Catal*., **2018**, 365, 450–463.
61. K.A. Lomachenko, J. Jacobsen, A.L. Bugaev, C. Atzori, F. Bonino, S. Bordiga, N. Stock, C. Lamberti, *J. Am. Chem. Soc*, **2018**, 140, 17379–17383.
62. Y. Zhang, H. Chen, Y. Pan, X. Zeng, X. Jiang, Z. Long, X. Hou, *Chem. Commun*., **2019**, 55, 13959–13962.
63. M. Kim, J.F. Cahill, H. Fei, K.A. Prather, S.M. Cohen, *J. Am. Chem. Soc*.**2012**, 134, 18082–18088.
64. A. De Vos, K. Hendrickx, P. Van Der Voort, V. Van Speybroeck, K. Lejaeghere, *Chem. Mater*., **2017**, 29, 3006–3019.
65. A. Buragohaina, S. Biswas, *CrystEngComm*, **2016**, 18, 4374–4381.
66. M. Lammert, M.T. Wharmby, S. Smolders, B. Bueken, A. Lieb, K.A. Lomachenko, D. De Vos, N. Stork, *Chem. Comm.*, **2015**, 51, 12578–12581.
67. Q. Liu, H. Cong, H. Deng, *J. Am. Chem. Soc*., **2016**, 138, 13822–13825.
68. F. Trousselet, A. Archereau, A. Boutin, F.-X. Coudert, *J. Phys. Chem. C*, **2016**, 120, 24885–24894.
69. Z. Wang, C. Li, K. Domen, *Chem. Soc. Rev*., **2019**, 48, 2109–2125.
70. M. Alvaro, E. Carbonell, B. Ferrer, F.X. Llabrés i Xamena, H. Garcia, *Chem. Eur. J*., **2007**, 13, 5106–5112.

71. M. De Miguel, F. Ragon, T. Devic, C. Serre, P. Horcajada, H. García, *ChemPhysChem*., **2012**, 13, 3651–3654.

3.7 Supporting information

Experimental procedure

All chemicals were obtained commercially from Sigma-Aldrich and used without further purification. ZrCl4 was purchased from Sigma Aldrich ≥99.5 % trace metals basis; Terephtalic acid was supplied by Sigma Aldrich; TiCl4 · 2THF was provided by Sigma Aldrich 97%; cerium ammonium nitrate was purchased from Sigma Aldrich ≥99.9 % trace metals basis; zirconium (IV) dinitrate oxide hydrate was bought from Sigma Aldrich 99%; Dimethylformamide was from Sigma for HPLC, ≥99.9%; Methanol was supplied by Sigma Aldrich for HPLC, ≥99.9%.

Material preparation

UiO-66: The synthesis of Zr-BDC MOF was carried out dissolving the metallic salt ZrCl4 (0.053 g, 0.227 mmol) and the organic linker 1,4-benzenedicarboxylic acid (H2BDC) (0.034g, 0.227 mmol) in *N,N`*-dimethylformamide (DMF) (24.9 g, 340 mmol) at room temperature. The mixture was transferred in a Teflon-lined autoclave, sealed and placed in a pre-heated oven at 220℃ for 12 hours. After cooling to room temperature, the resulting white solid was filtered and washed several times with DMF and methanol and dried at room temperature.

UiO-66(Zr/Ti): UiO-66 (Zr/Ti) was synthetized following a post-syntetic method using $TiCl_4(THF)_2$ under inert atmosphere. Synthesized UiO-66 (0.45 mmol) and $TiCl_4$(0,135mmol) as Ti source were suspended in 2.5 mL DMF and incubated for 4 days at 120 °C. After cation exchange, the corresponding UiO-66 (Zr/Ti) solids were filtered, washed sequentially with DMF and MeOH and dried in vacuum at 40 °C for 24 hours.

UiO-66(Zr/Ce): UiO-66 (Zr/Ce) MOF was synthesized using Pyrex glass reaction tubes. H_2BDC, (127.6 mg) was introduced into the glass reactor with DMF (3.6 mL)

and aqueous solutions of cerium (IV) ammonium nitrate (0.533 M; 117 mg, 0.400 mL water), zirconium (IV) dinitrate oxide hydrate (0.533 M, 99.0 mg 0.800mL) and concentrated formic acid (HCOOH, 100 %, 1.03 mL) were added. The suspension of the starting materials was heated under stirring for 15 min at 100 °C. The light-yellow precipitate was centrifuged in the mother solution and then it was decanted off. The solid was centrifuged twice in DMF (2 mL) and then, to remove DMF, the solid was washed and centrifuged with acetone (2 mL) four times. The resulting white solid was dried in air at 70 °C.

UiO-66(Ce): H_2BDC (35.4 mg, 213 μmol) was introduced into the glass reactor with DMF (1.2 mL) and an aqueous solution of cerium (IV) ammonium nitrate (400 μL, 0.5333 M). The glass reactor was heated under stirring conditions for 15 min at 100 °C. The light-yellow precipitate was centrifuged in the mother suspension; then, the solid was centrifuged twice in DMF (2 mL). To remove DMF from the product, the solid was washed and centrifuged with acetone (2 mL) four times. The resulting yellow solid was dried in air at 70 °C.

UiO-66(Zr/Ce/Ti): UiO-66(Zr/Ce) (0.45mmol) and $TiCl_4(THF)_2$ (0.135mmol) as Ti source were suspended in 2.5 mL DMF and incubated for 4 days at 120 °C. After cation exchange, the resulting UiO-66(Zr/Ce/Ti) solids were filtered, washed sequentially with DMF and MeOH and dried in vacuum at 40 °C for 24 h.

Photocatalytic reactions: The photocatalytic tests were performed using a concentration of catalyst (1 mg of photocatalyst per mL of Milli-Q water). Typically, measurements were carried out using 20 mg of photocatalyst in Milli-Q water (20 mL). Evolved gases were analyzed by injecting the head space gases into a calibrated micro-GC. The suspension was sonicated for 15 min to obtain a uniform, persistent dispersion. This dispersion was decanted in a quartz reactor and the system was purged for 1 h under argon atmosphere to remove the air. The suspension was stirred at room temperature and irradiated with a 300 W Xenon lamp, while maintaining stirring. For visible light irradiations, a cut off filter $\lambda > 450$ nm was coupled to the

Xenon lamp to ensure that no UV photons reach the irradiation vessel. The evolving gases were analyzed from the head space connecting directly the reactor to an Agilent 490 Micro GC system (Molsieve 5 Å column using Ar as carrier gas) without manual handling. Throughout the experiment the temperature of the system was monitor and the pressure was analyzed by the manometer adapted to the photoreactor.

Photocatalytic tests employing monochromatic light*:* The UiO-66(Zr/Ce/Ti) MOF was used as photocatalyst in these measurements. In detail 20 mg of MOF were suspended in Milli Q water (20 mL) and the suspension was subsequently excited with an output light of 150 W Xenon lamp through a Czerny Turner monochromator (PTI model 101). The power density was calculated with the use of a Newport (818- UV-L) calibrated photodiode. The sample was irradiated at the following wavelengths: 300 nm (0.47 W/m^2), 400 nm (5.66 W/m^2) and 500 nm (11.79 W/m^2).

Experimental Conditions for $MV^{\bullet+}$ Photogeneration. An acetonitrile suspension of UiO-66 (Zr/Ce/Ti) MOF (2 mg/mL, 200 μL) in 1.05 mL containing $MV(PF_6)_2$ 0.17 M was introduced in a 10 mm × 10 mm quartz cell. Additional acetonitrile was added in order to complete a total volume of 3 mL. The solution was purged for 15 min with argon and then irradiated for 10 min with a Xenon lamp through quartz.

Experimental Conditions for $TMPDA^{\bullet+}$ Photogeneration. An acetonitrile suspension of UiO- 66 (Zr/Ce/Ti) MOF (2 mg/mL, 200 μL) was added to an acetonitrile saturated solution of *N*,*N*,*N*′,*N*′- tetramethyl-*p*-phenylenediamine (TMPDA). The suspension was introduced in a 10 mm × 10 mm quartz cell, purged for 15 min with argon and then irradiated for 10 min with a solar simulator (525 W) through an AM1.5 filter.

Photophysical Measurements. Laser flash photolysis measurements were carried out using the fourth harmonic of a Q switched Nd:YAG laser (Quantel Brilliant, 266 nm, 10 mJ/pulse, 5 ns fwhm) coupled to a mLFP-122 Luzchem miniaturized detection equipment. This transient absorption spectrophotometer consists of a 300 W ceramic xenon lamp, 125 mm monochromator, Tektronix TDS-2001C digitizer, compact photomultiplier and power supply, liquid cell holder, fiber-optics connectors and computer interfaces. The software package was developed in the LabVIEW environment from National Instruments. The laser flash photolysis equipment supplies 5 V trigger pulses with programmable frequency and delay. The rise time of the detector/digitizer is ~3 ns up to 300 MHz (2.5 GHz sampling). The monitoring beam is provided by a ceramic xenon lamp and delivered through fiber-optic cables. The laser pulse is probed by a fiber that synchronizes the LFP system with the digitizer operating in the pre trigger mode. Transient spectra of the persistent suspensions were recorded using 10 × 10 mm quartz cells and were bubbled for 15 min with argon before data acquisition. Each decay or data point corresponds to the average of 5 signals to increase the signal to noise ratio.

Characterization of the materials. Powder X-ray diffraction (PXRD) patterns were recorded on a Philips XPert diffractometer equipped with a graphite monochromator (40 kV and 45 mA) employing Ni filtered CuKα radiation. N_2 adsorption isotherms at 77 K were recorded using a Micromeritics ASAP 2010 device. Thermogravimetric analyses were performed on a TGA/SDTA851e METTLER TOLEDO station. The different solids were analyzed by X-ray photoelectron spectra (XPS), the spectra were collected with a SPECS spectrometer equipped with MCD-9 detector using a monochromatic Al ($K\alpha$= 1486.6 eV) X-ray source calibrating the binding energy using the C 1s peak set at 284.4 eV as reference. CASA software has been employed for spectra deconvolution. Diffuse reflectance UV−visible spectra were recorded using a Cary 5000 Varian spectrophotometer having an integrating sphere; the sample as compressed powder

was placed in a sample holder. The morphologies and the compositions attributed to each MOFs were characterized using a SEM instrument (Zeiss instrument, AURIGA Compact) coupled with a EDX detector. ICP-AES analysis was used to determine the content of metals of each photo catalyst after dissolving them in concentrated nitric acid. ATR-FTIR spectra of the UiO-66 series were measured with a Bruker Tensor 27 instrument. Prior to ATR-FTIR measurements the solid samples were dried in an oven at 100 °C for 16 h to remove physisorbed water.

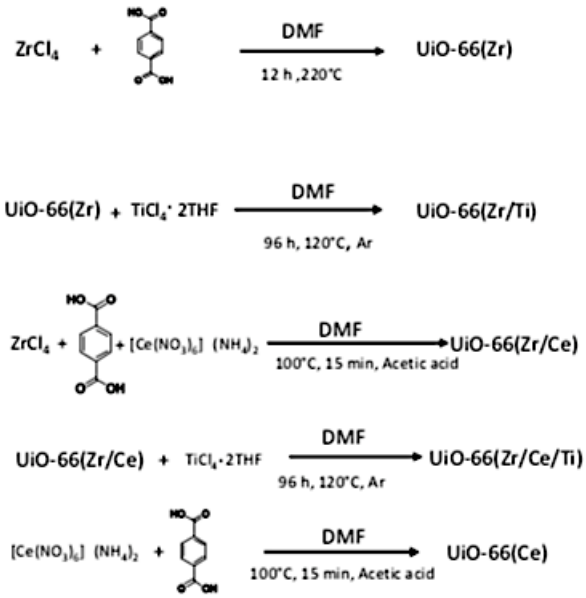

Scheme S3.1. Experimental procedure followed for the synthesis of the five UiO-66 MOFs.

$$\emptyset = \frac{number\ molecules\ H_2 x2}{number\ incidents\ photons} * 100$$

Where number incidents photons $= \frac{EX\lambda Radiated\ Area}{cXh}$ $Radiated\ Area = \pi X d^2/4$

Equation S3.1. Equation employed for the calculation of the energetic efficiency values for the overall water splitting process. Where E is the efficiency of the lamp, λ is the specific wavelength and c is the velocity of the light.

$$y = A_1 \cdot \exp\left(-\frac{x0}{t_1}\right) + y_0$$

Equation S3.2. Mono-exponential fit from Origin Pro 8 program.

$$y=(y_0 + A_1 \cdot \exp\left(-\frac{x-x_0}{t_1}\right) + A_2 \cdot \exp\left(-\frac{x-x_0}{t_2}\right);$$

Equation S3.3. Sum of two mono-exponential fit from Origin Pro 8 program.

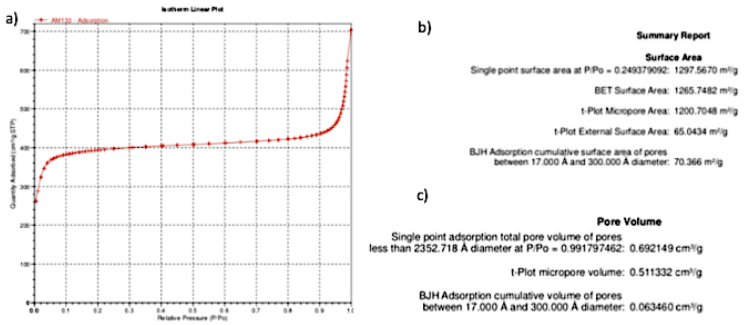

Figure S3.1: a) Adsorption isotherm of UiO-66(Zr/Ce); summary report of b) surface area and c) pore volume of UiO-66(Zr/Ce).

a)

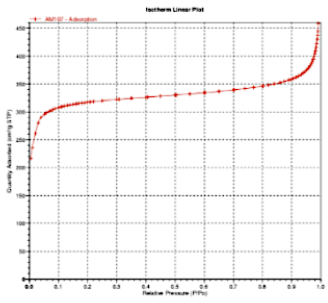

b)

Summary Report

Surface Area

Single point surface area at P/Po = 0.249879077: 1044.6538 m²/g

BET Surface Area: 1019.5435 m²/g

t-Plot Micropore Area: 948.1891 m²/g

t-Plot External Surface Area: 71.3544 m²/g

BJH Adsorption cumulative surface area of pores between 17.000 Å and 300.000 Å diameter: 72.158 m²/g

c)

Pore Volume

Single point adsorption total pore volume of pores less than 4012.192 Å diameter at P/Po = 0.995213880: 0.649614 cm³/g

t-Plot micropore volume: 0.259535 cm³/g

BJH Adsorption cumulative volume of pores between 17.000 Å and 300.000 Å diameter: 0.367124 cm³/g

Figure S3.2: a) Adsorption isotherm of UiO-66(Zr/Ce/Ti); summary report of b) surface area and c) pore volume of UiO-66(Zr/Ce/Ti).

a)

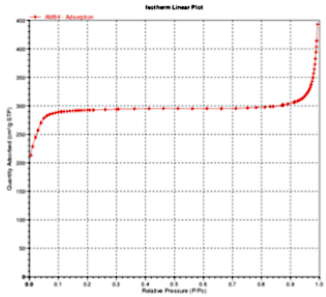

b)

Summary Report

Surface Area

Single point surface area at P/Po = 0.261476663: 943.3452 m²/g

BET Surface Area: 916.4476 m²/g

t-Plot Micropore Area: 915.9223 m²/g

t-Plot External Surface Area: 0.5253 m²/g

BJH Adsorption cumulative surface area of pores between 17.000 Å and 300.000 Å diameter: 11.357 m²/g

c)

Pore Volume

Single point adsorption total pore volume of pores less than 2373.962 Å diameter at P/Po = 0.991871714: 0.347706 cm³/g

t-Plot micropore volume: 0.239641 cm³/g

BJH Adsorption cumulative volume of pores between 17.000 Å and 300.000 Å diameter: 0.039833 cm³/g

Figure S3.3: a) Adsorption isotherm of UiO-66(Ce); summary report of b) surface area and c) pore volume of UiO-66(Ce).

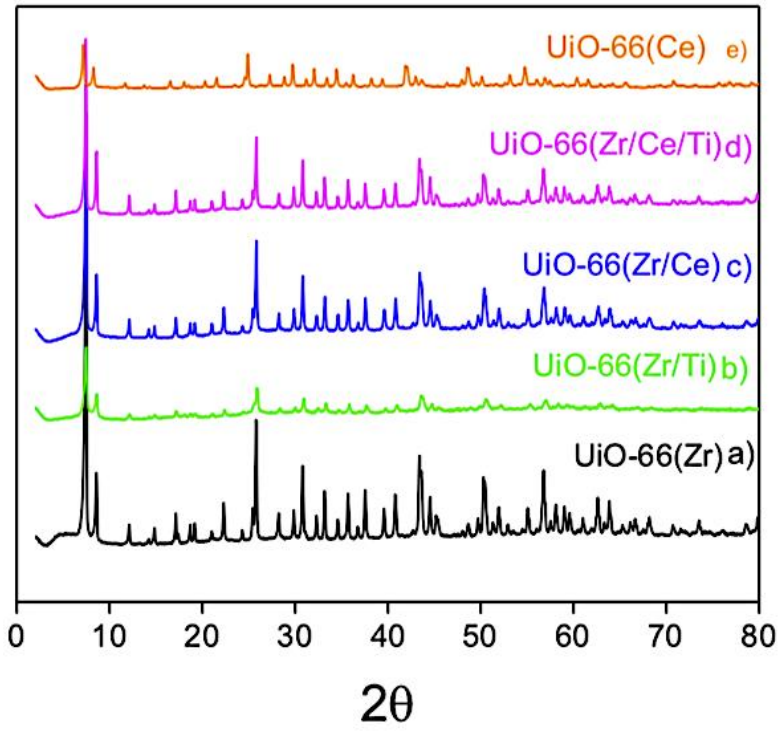

Figure S3.4. PXRD patterns of UiO-66 series: a) UiO-66(Zr), b) UiO-66(Zr,Ti), c) UiO-66(Zr,Ce), d) UiO-66(Zr/Ce/Ti) and e) UiO-66(Ce).

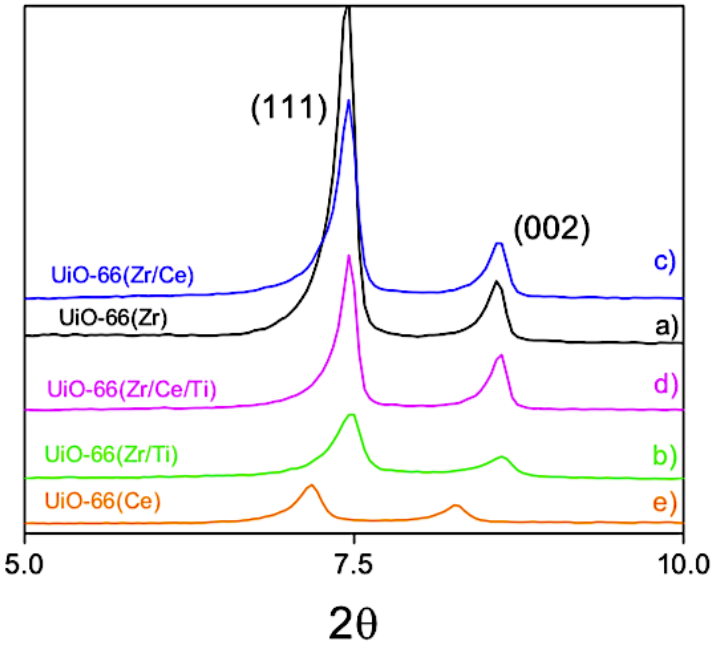

Figure S3.5. Expansion of the low angle region of Figure S1: a) UiO-66(Zr) b) UiO-66(Zr-Ti) c) UiO-66(Zr-Ce) d) UiO-66(Zr/Ce/Ti) and e) UiO-66(Ce).

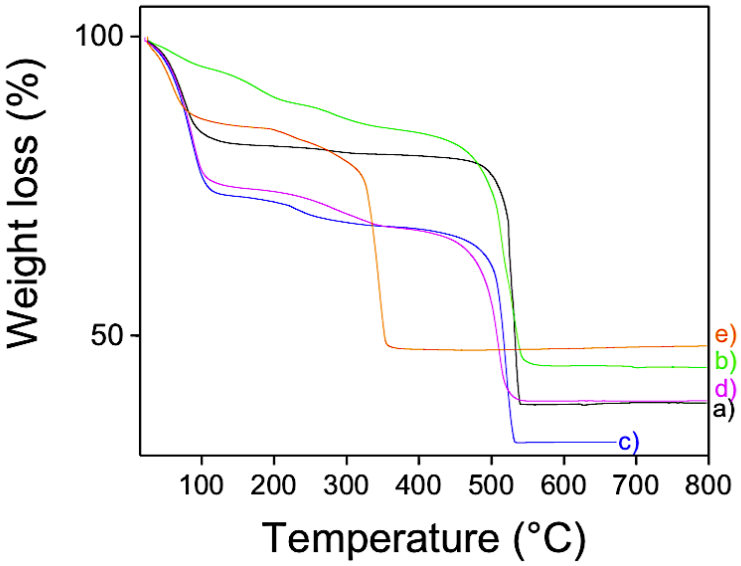

Figure S3.6. Thermogravimetric analysis of UiO-66 series: a) UiO-66(Zr) b) UiO-66(Zr/Ti) c) UiO-66(Zr/Ce) d) UiO-66(Zr/Ce/Ti) and e) UiO-66(Ce).

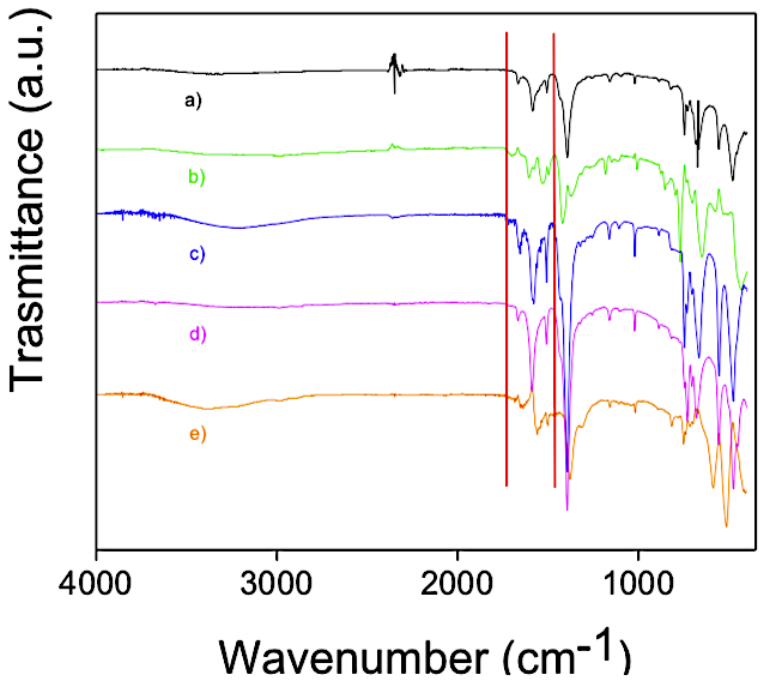

Figure S3.7. FT-IR spectra of UiO-66 series: a) UiO-66(Zr) b) UiO-66(Zr/Ti) c) UiO-66(Zr/Ce) d) UiO-66(Zr/Ce/Ti) and e) UiO-66(Ce). The red lines correspond to the stretching vibration of the carboxylic group and C-H.

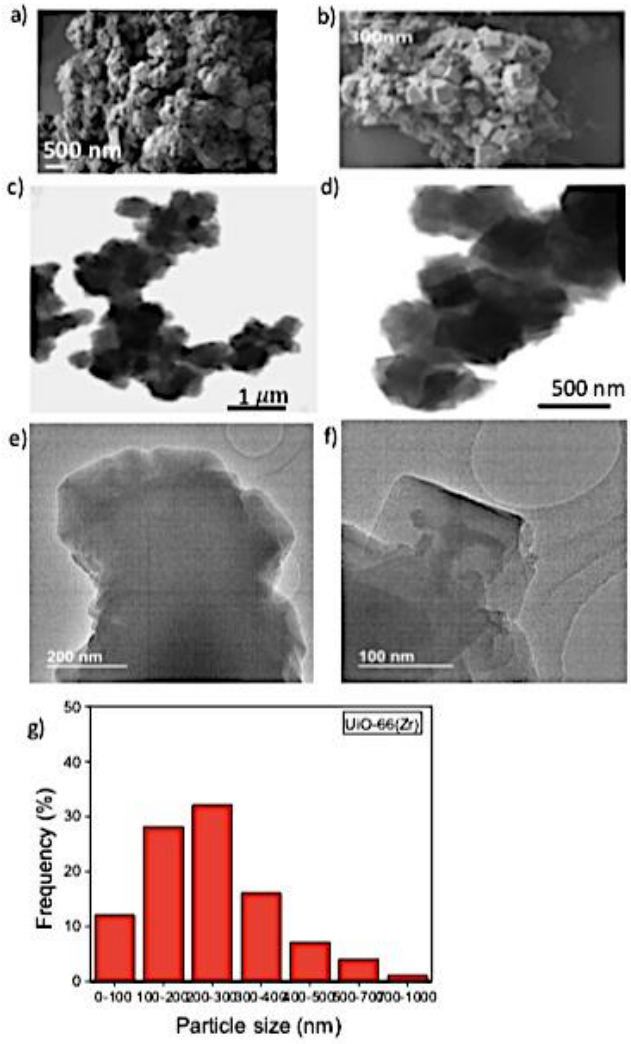

Figure S3.8. a) and b) FESEM image for UiO-66(Zr); c) and d) STEM images for UiO-66(Zr) e) and f) TEM for UiO-66(Zr) and g) histogram of particles size distribution.

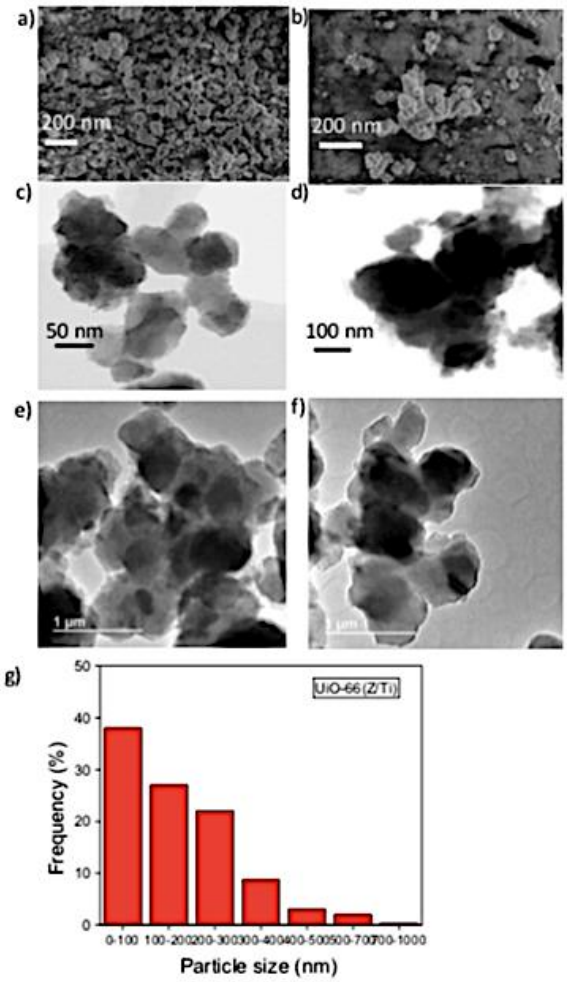

Figure S3.9. a) and b) FESEM image for UiO-66(Zr/Ti); c) and d) STEM images for UiO-66(Zr/Ti); e) and f) TEM for UiO-66(Zr/Ti) and g) histogram of particles size distribution.

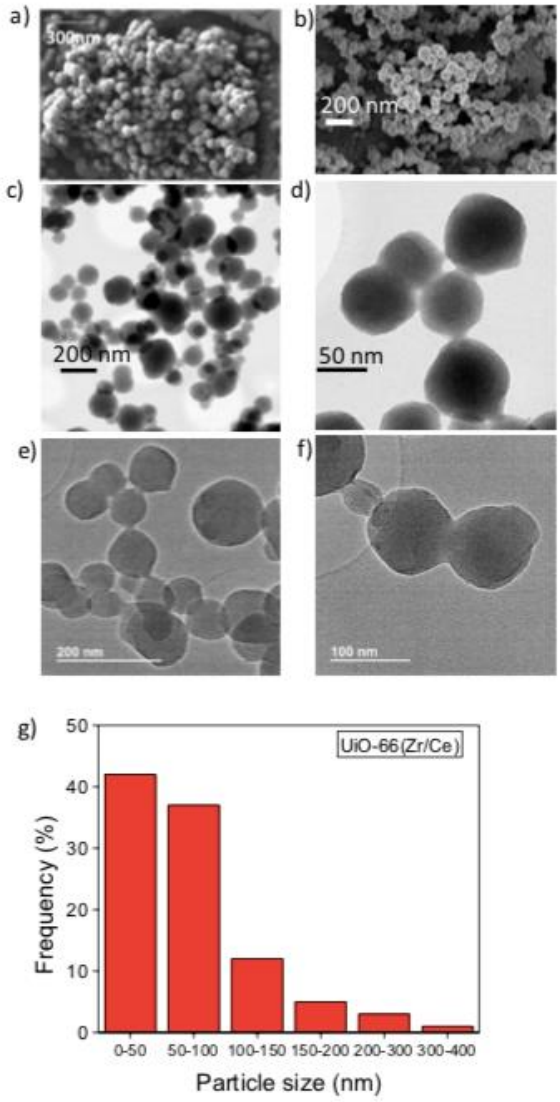

Figure S3.10. a) and b) FESEM image for UiO-66(Zr/Ce); c) and d) STEM images for UiO-66(Zr/Ce); e) and f) TEM for UiO-66(Zr/Ce) and g) histogram of particles size distribution.

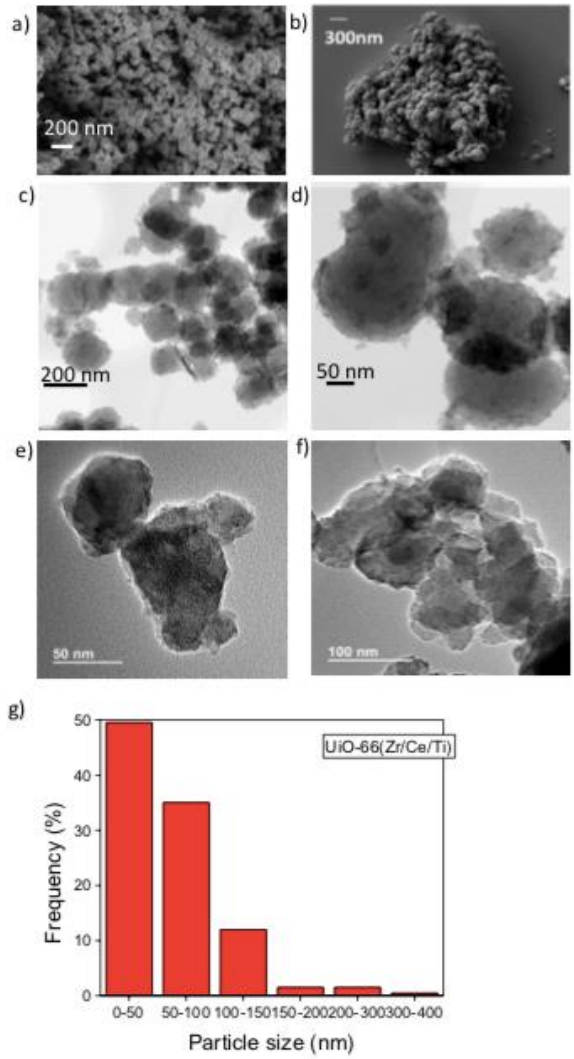

Figure S3.11. a) and b) FESEM image for UiO-66(Zr/Ce/Ti); c) and d) STEM images for UiO-66(Zr/Ce/Ti); e) and f) TEM for UiO-66(Zr/Ce/Ti) and g) histogram of particles size distribution.

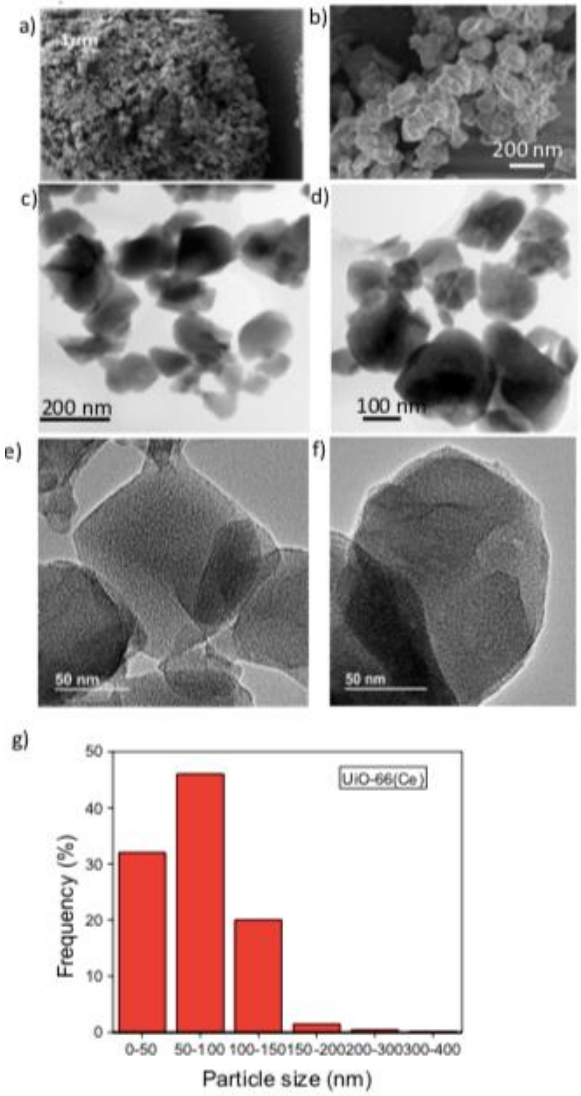

Figure S3.12. a) and b) FESEM image for UiO-66(Ce); c) and d) STEM images for UiO-66(Ce); e) and f) TEM for UiO-66(Ce) and g) histogram of particles size distribution.

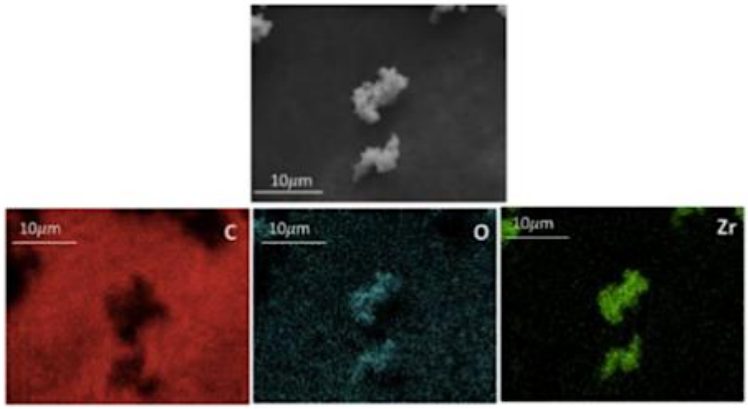

Figure S3.13. SEM image and elemental EDX mapping for UiO-66(Zr).

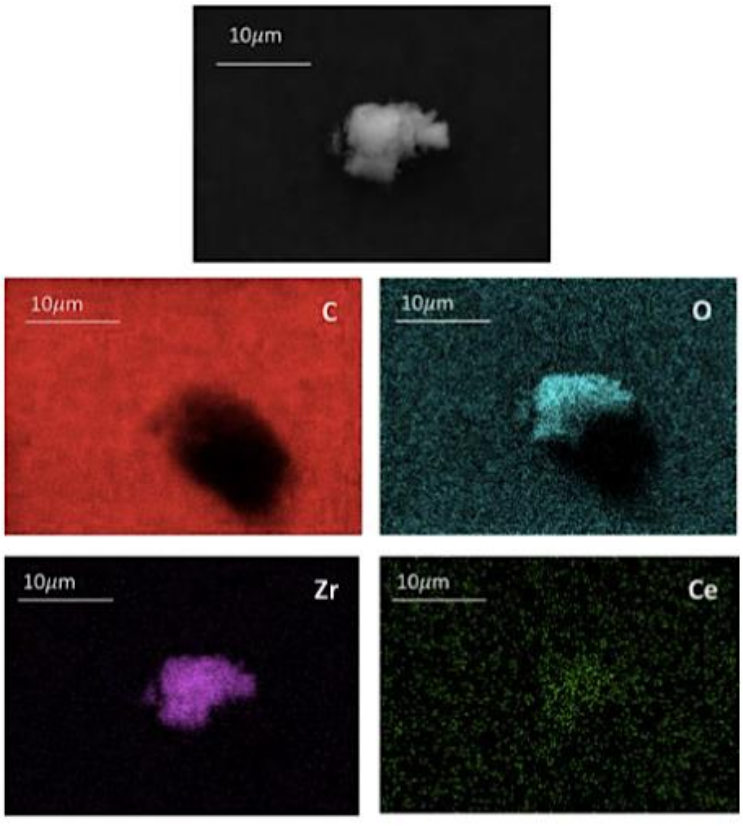

Figure S3.14. SEM image and elemental EDX mapping for UiO-66(Zr/Ce).

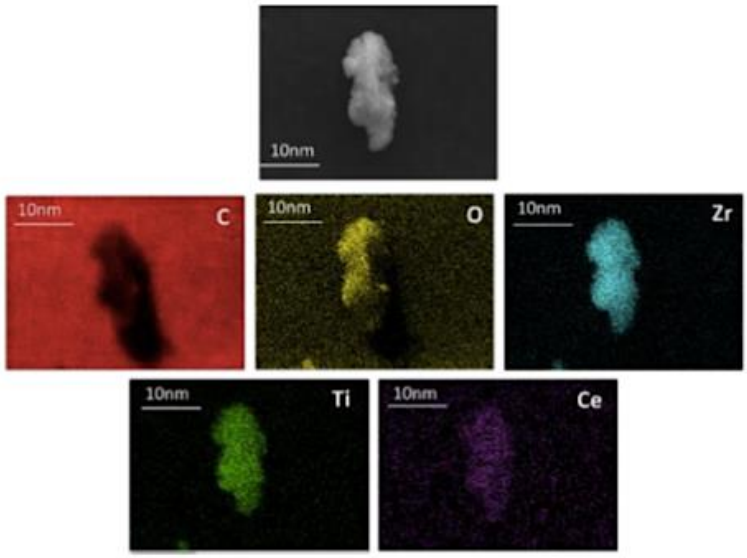

Figure S3.15. SEM image and elemental EDX mapping for UiO-66(Zr/Ce/Ti).

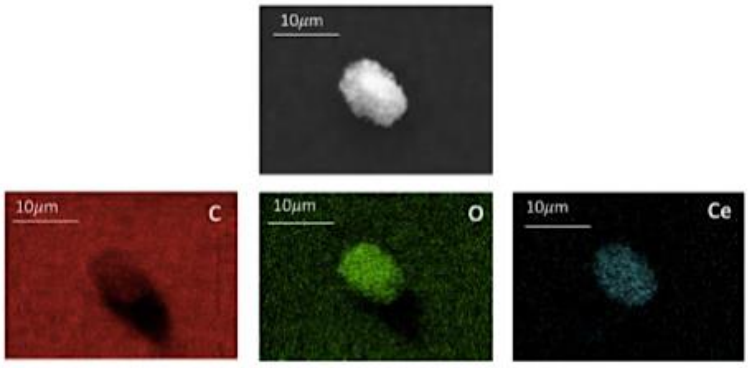

Figure S3.16. SEM image and elemental EDX mapping for UiO-66(Ce).

a)

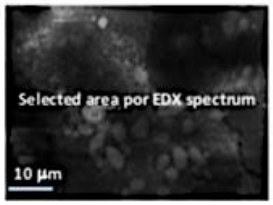

b)

Element	wt % EDX	wt % ICP
Zr	68.96	75.01
Ce	13.26	13.83
Ti	17.78	11.14

c)

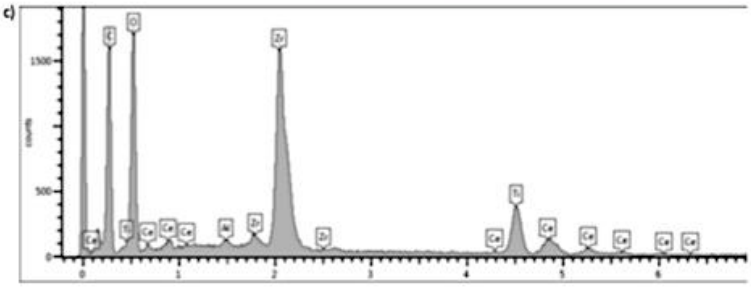

Figure S3.17. a) FESEM image for UiO-66(Zr/Ce/Ti); b) Table obtained from EDX scan of the constituent metals of the metallic clusters of the UiO-66(Zr/Ce/Ti) c) EDX scan of the constituent metals of the metallic clusters of the UiO-66(Zr/Ce/Ti).

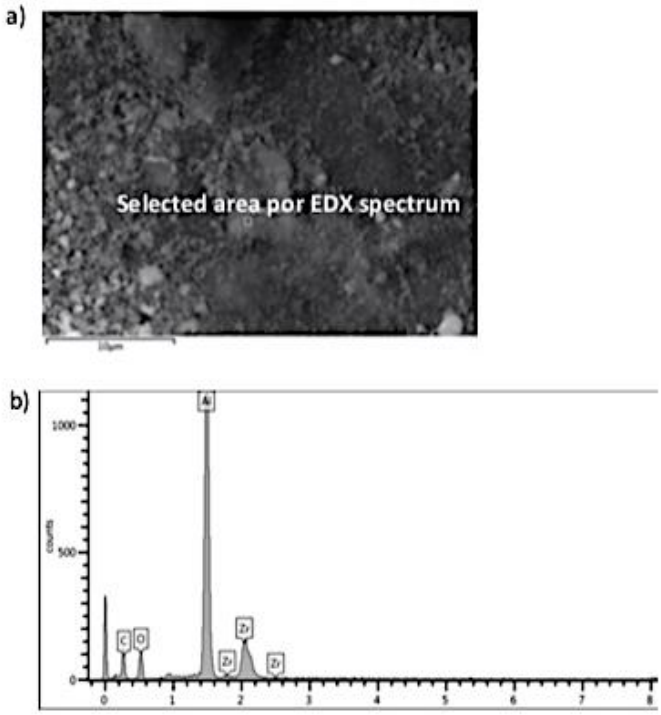

Figure S3.18. a) FESEM image for UiO-66(Zr); b) EDX scan of the constituent metals of the metallic clusters of the UiO-66(Zr).

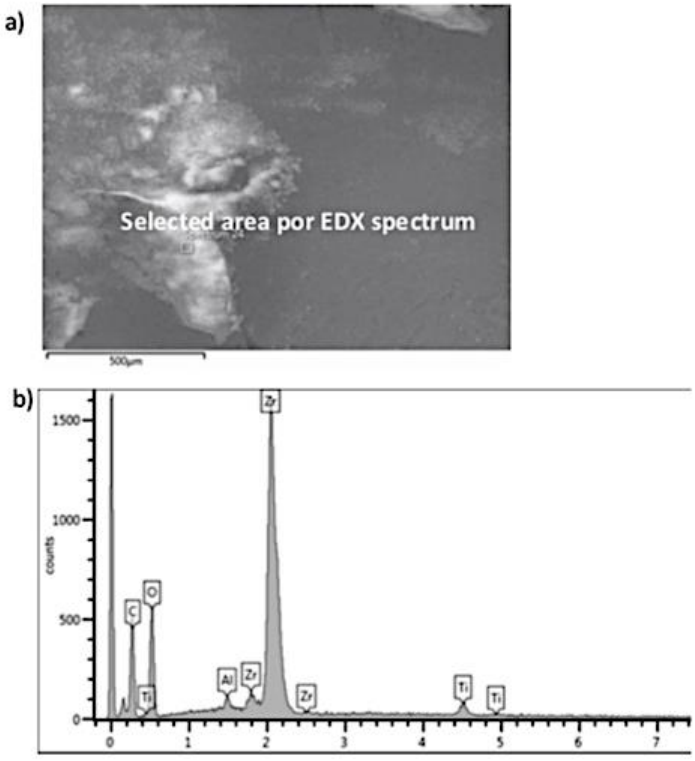

Figure S3.19. a) FESEM image for UiO-66(Zr/Ti); b) EDX scan of the constituent metals of the metallic clusters of the UiO-66(Zr/Ti).

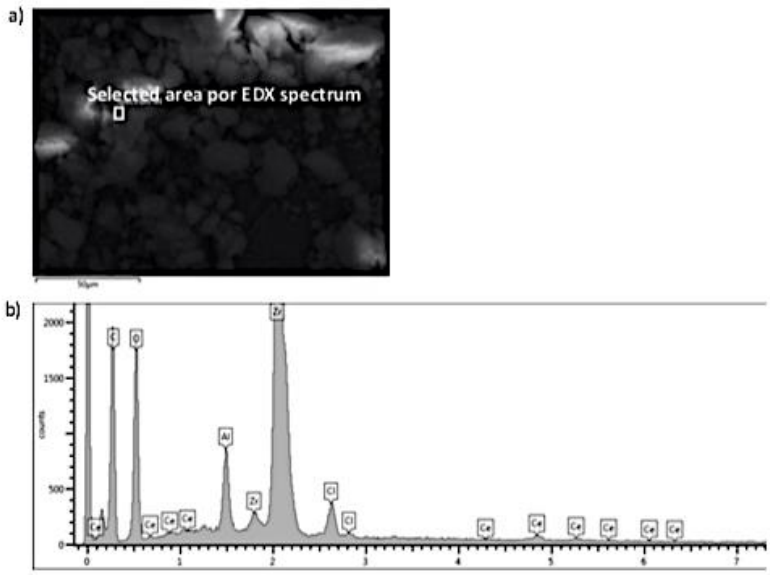

Figure S3.20. a) FESEM image for UiO-66(Zr/Ce); b) EDX scan of constituent metals of the metallic clusters of the UiO-66(Zr/Ce).

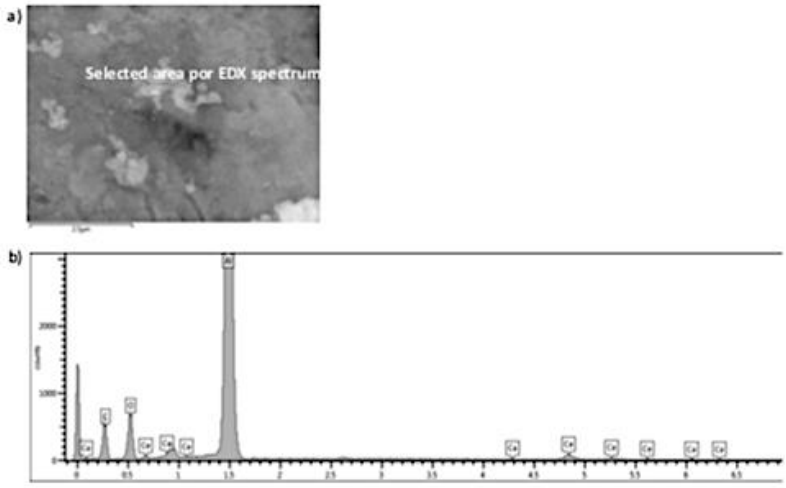

Figure S3.21. a) FESEM image for UiO-66(Ce); b) EDX scan of the constituent metals of the metallic clusters of the UiO-66(Ce).

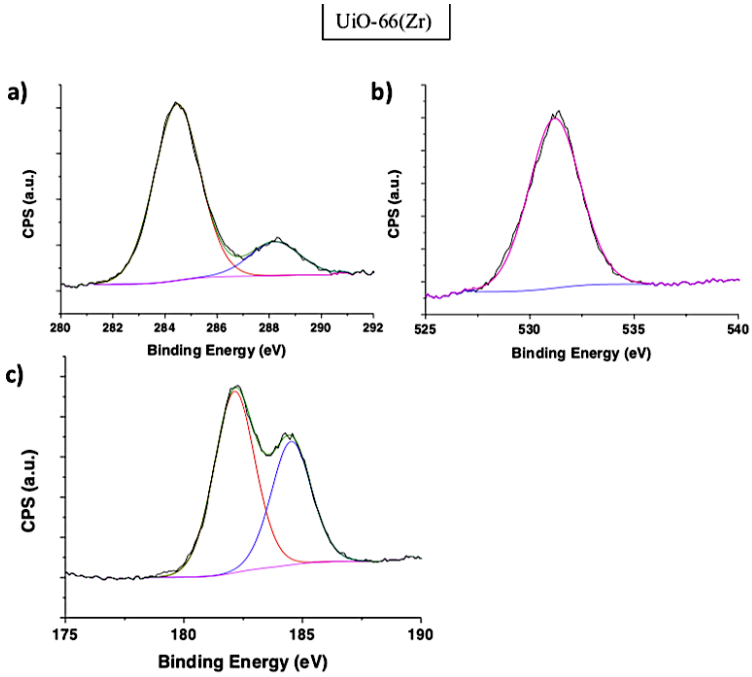

Figure S3.22. High resolution XPS peaks and the best deconvolution for the C 1s (a), O 1s (b) and Zr 2p (c) signals recorded for the UiO-66(Zr) sample.

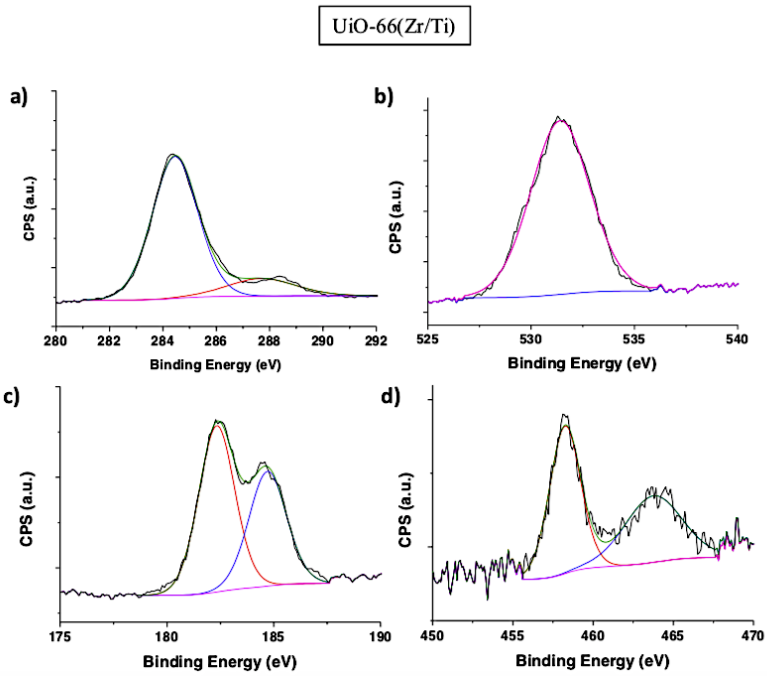

Figure S3.23. High resolution XPS peaks and the best deconvolution for the C 1s (a), O 1s (b), Zr 2p (c) and Ti 2d (d) signals recorded for the UiO66-(Zr/Ti) sample.

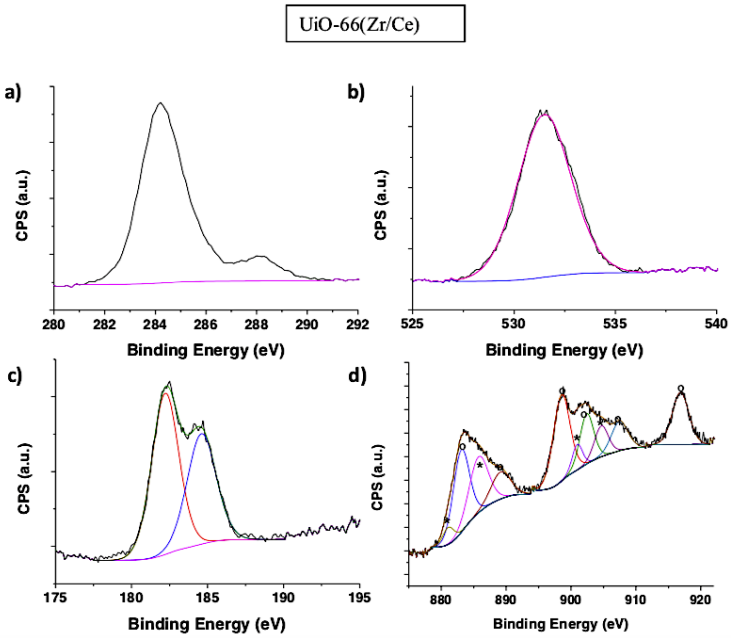

Figure S3.24. High resolution XPS peaks and the best deconvolution for the C 1s (a), O 1s (b) Zr 2p (c) and Ce 2d (d) signals recorded for the UiO-66(Zr/Ce) sample. Legend: Ce^{4+} (o), Ce^{3+} (*).

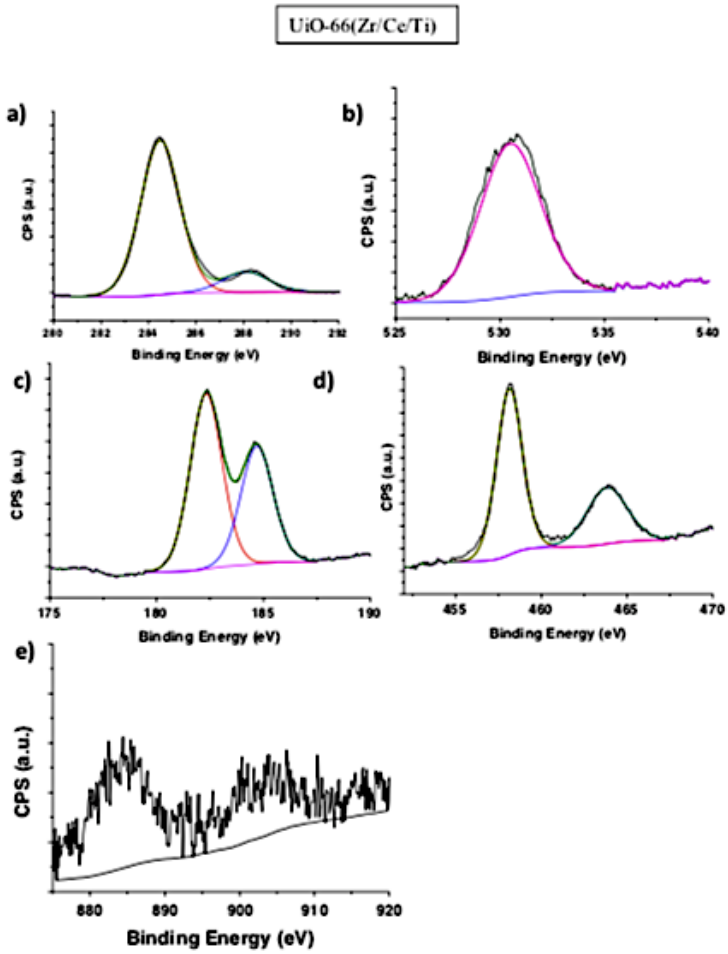

Figure S3.25. High resolution XPS peaks and the best deconvolution for the C 1s (a), O 1s (b), Ti 2d (c) Zr 2p (d) and Ce 2d (e) signals recorded for the UiO-66(Zr/Ce/Ti) sample.

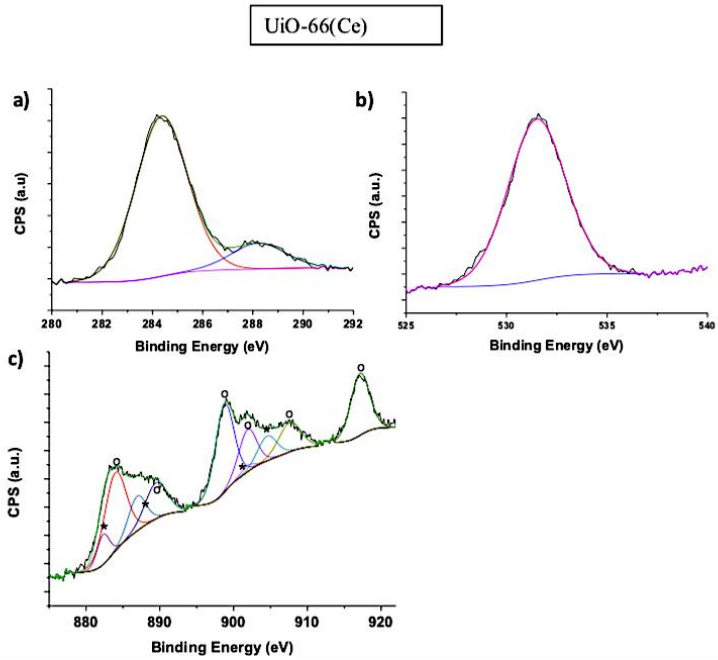

Figure S3.26. High resolution XPS peaks and the best deconvolution for the C 1s (a), O 1s (b) and Ce 2d (c) signals recorded for the UiO-66(Ce) sample. Legend: Ce^{4+} (o), Ce^{3+} (*).

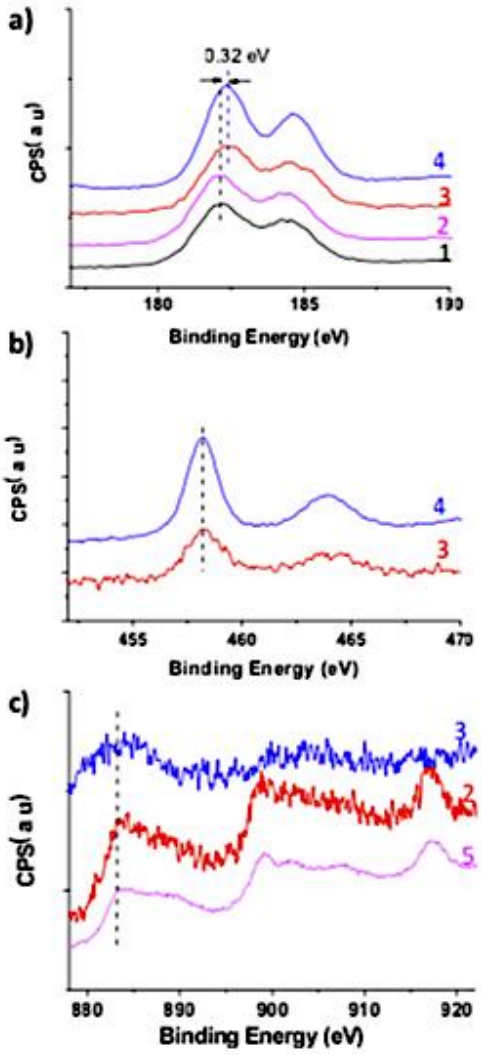

Figure S3.27. Comparison of the high resolution XPS Zr 2p (a), Ti 2p (b) and Ce 3d (c) peaks for the UiO-66(Zr) (1), UiO-66(Zr/Ce) (2), UiO-66(Zr/Ce/Ti) (3), UiO-66(Zr/Ti) (4) and UiO-66(Ce) (5) solids.

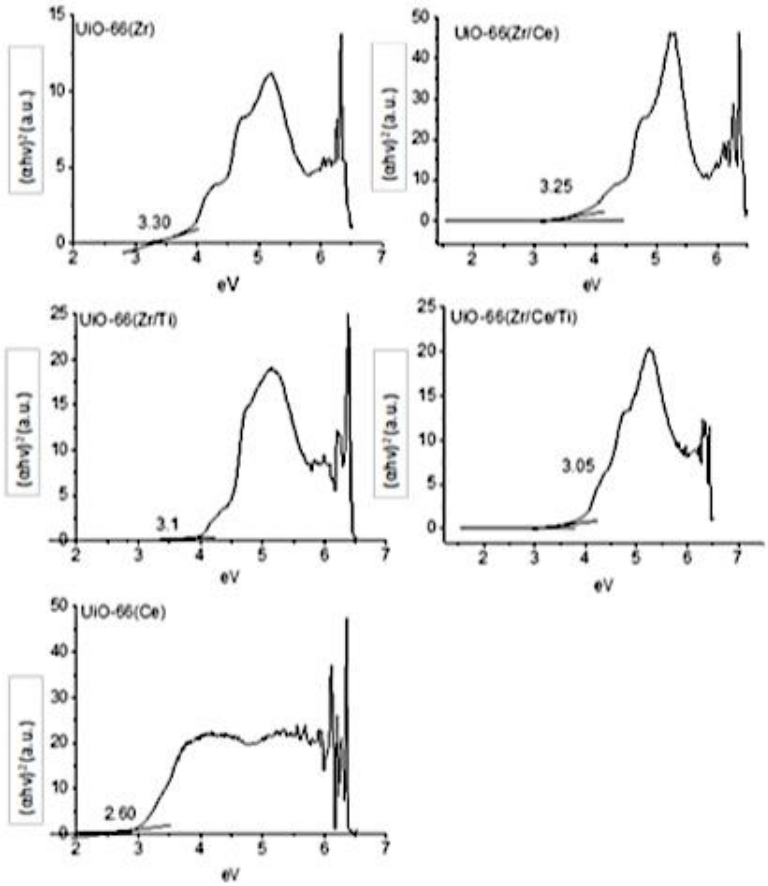

Figure S3.28. Tauc plot of UiO-66(Zr) (a), UiO-66(Zr/Ce) (b), UiO-66(Zr/Ti) (c), UiO-66(Zr/Ti/Ce) (d) and UiO-66(Ce) (e). The estimated band gap value is shown in each graph.

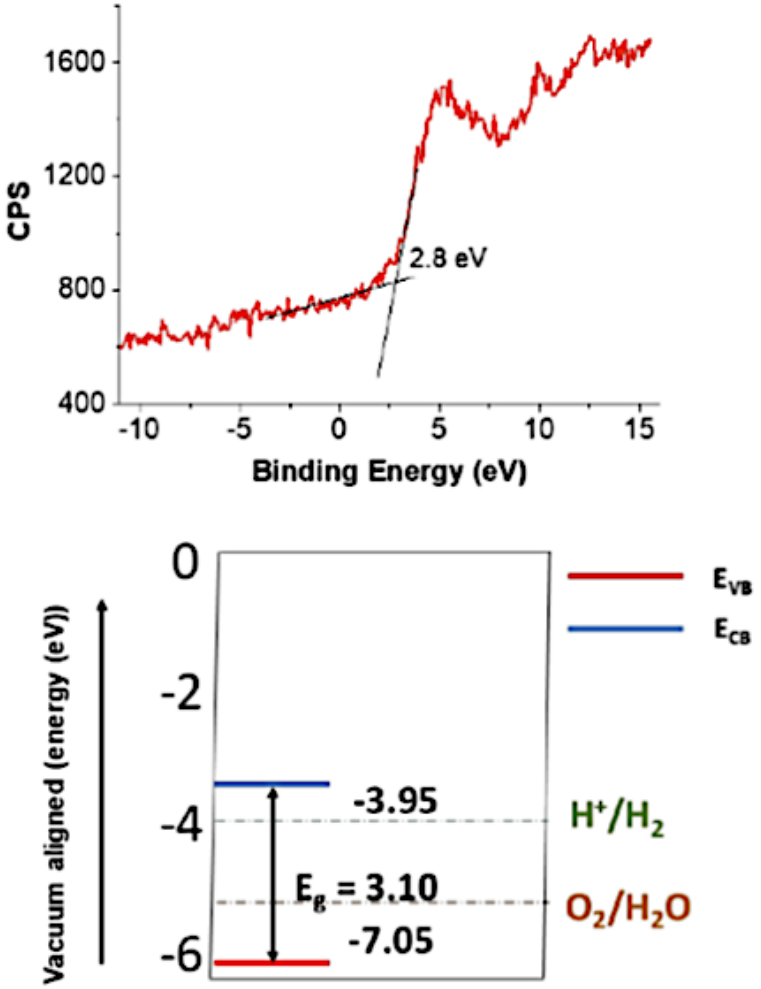

Figure S3.29. a) Valence band XPS and (b) band alignment for UiO-66(Zr/Ce/Ti) and positions of reduction potentials of H^+ to H_2 and O_2 to H_2O in the vacuum level (Valence band: VB; Conduction band: CB).

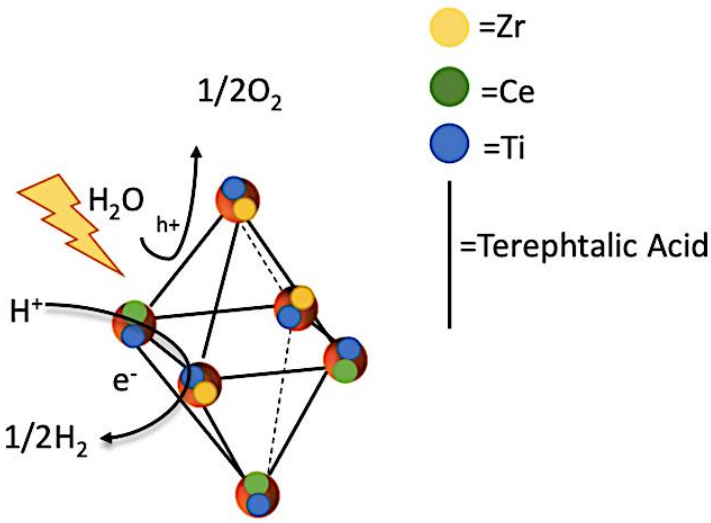

Scheme 3.2. Proposed mechanism on the role of Ti^{4+} as relay in the photoinduced electron transfer resulting in overall water splitting.

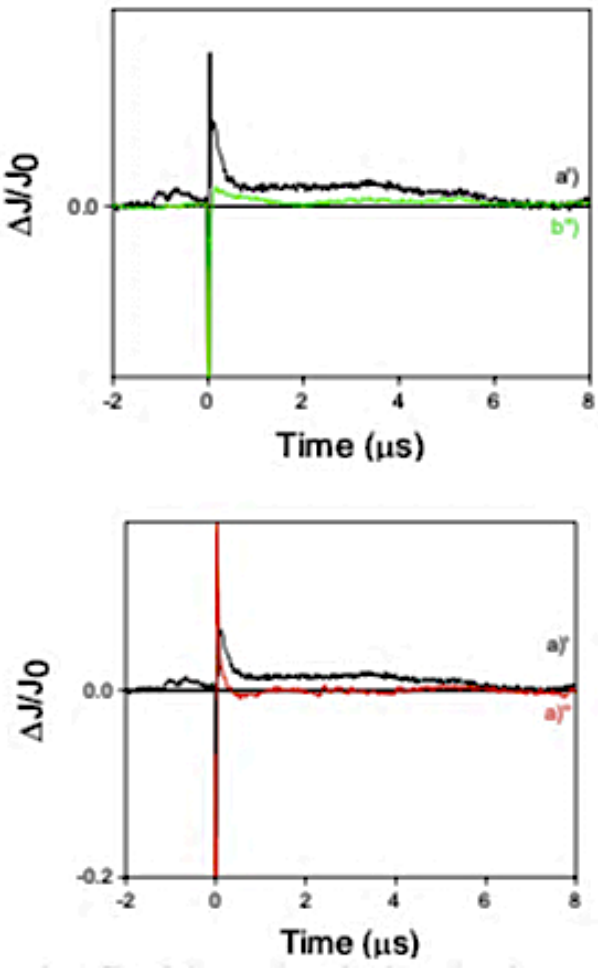

Figure S3.30. Temporal profile of the transient signal monitored at 400 nm for an acetonitrile suspension of UiO-66(Zr) recorded upon 266 nm laser excitation under argon atmosphere a'), upon addition of CH_2Cl_2 a"), and in the presence of CH_3OH b").

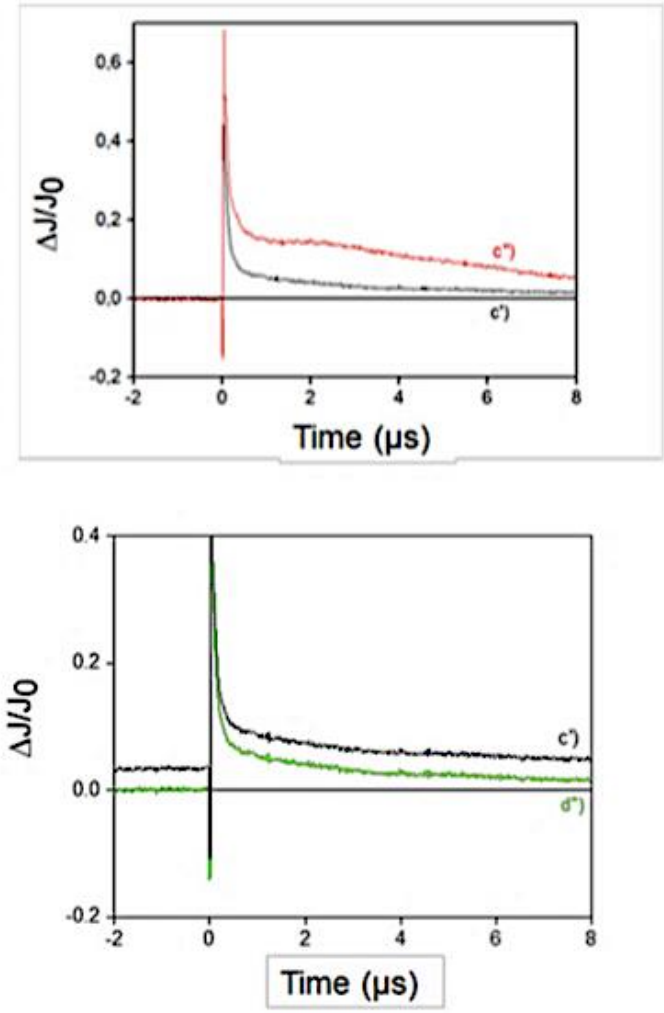

Figure S3.31. Temporal profile of the transient signal monitored at 400 nm for an acetonitrile suspension of UiO-66(Zr/Ti) recorded upon 266 nm laser excitation under argon atmosphere (c'), upon addition of CH_2Cl_2 (c"), and in the presence of CH_3OH (d").

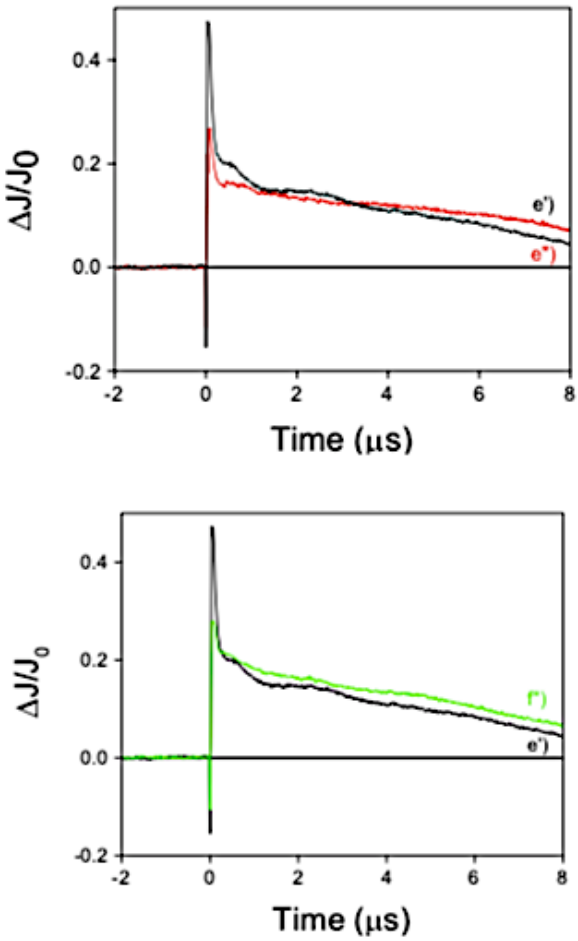

Figure S3.32. Temporal profile of the transient signal monitored at 400 nm for an acetonitrile suspension of UiO-66(Zr/Ce) recorded upon 266 nm laser excitation under argon atmosphere (e'), upon addition of CH_2Cl_2 (e"), and in the presence of CH_3OH (f").

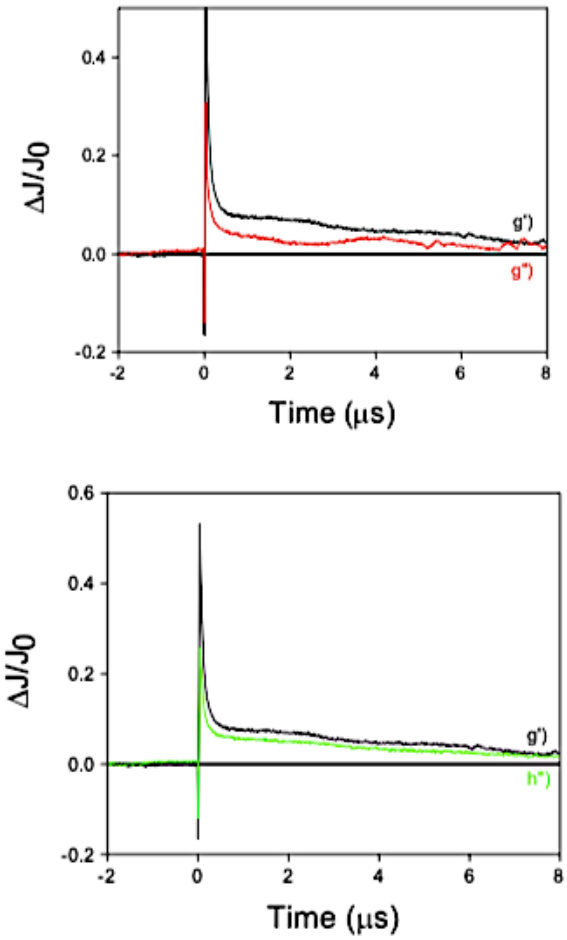

Figure S3.33. Temporal profile of the transient signal monitored at 400 nm for an acetonitrile suspension of UiO-66(Ce) recorded upon 266 nm laser excitation under argon atmosphere g'), upon addition of CH_2Cl_2 g"), and in the presence of CH_3OH h").

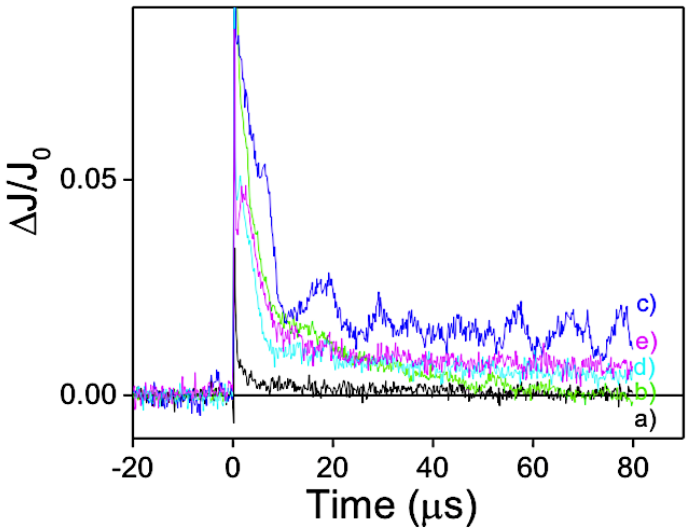

Figure S3.34. Temporal profiles of the transient signals monitored at 500 nm recorded upon 266 nm laser excitation under argon atmosphere for UiO-66(Zr) a), UiO-66(Zr/Ti) b), UiO-66 (Zr/Ce) c), UiO-66 (Zr/Ce/Ti) d) and UiO-66 (Ce) e) in a longer timescale (80 ms).

Table S3.1: Kinetic data of the transient signals recorded at long time scale (80 ms) (**Fig. S3.34**) for the series of UiO-66 solids obtaines from the best fit of the temporal profiles to a mono-exponential or a sum of two mono-exponential kinetics.

	t_1(μs)	E_1	A_1	t_2 (μs)	E_2	A_2
UiO-66(Zr)	0.67	0.04	0.05			
	19.41	2.98	0.004	0.40	0.02	0.06
UiO-66(Zr/Ti)	4.86	0.13	0.1			
	1.96	0.06	0.11	21.88	1.16	0.04
UiO-66(Zr/Ce) *	11.76	2.3	0.121			
	5.81	0.16	0.08	0.08	0.01	0.74
UiO-66(Zr/Ce/Ti) *	4.33	1.79	0.07			
	2.81	0.13	0.07	0.04	0.02	48.69
UiO-66(Ce) *	7.85	3.29	0.04			

t1 is the lifetime, E is the error of the t1 and A is the pre- exponential factor get from best fit of the temporal profiles to a mono-exponential or a sum of two mono-exponential kinetics given by the equations S2-S3. * In these cases, the temporal profiles do not decay completely in the 80 ms time scale.

Chapter 4.

Solar-driven photocatalytic overall water splitting using MOF-on-MOF heterojunctions based on UiO-66 topology

Arianna Melillo,[1,$] María Cabrero-Antonino,[1,$] Belén Ferrer,[1]

Herme G. Baldoví,[1,*] Sergio Navalón[1,*]

[1] Departamento de Química, Universitat Politècnica de València, C/Camino de Vera, s/n, 46022, Valencia, Spain

4.1 Abstract

There is a large interest for the sustainable conversion of H_2O into H_2 and O_2 assisted by sunlight. Recently, metal-organic frameworks have emerged as new type of photocatalysts for this purpose although their activities are still far from application. Herein, a series of novel MOF-on-MOF heterojunctions based on UiO-66 topologies have been developed and tested as photocatalysts for the Overall Water Splitting under simulated sunlight irradiation. The list of photocatalysts that have been prepared, through solvothermal synthesis, include UiO-66(Ce), UiO-66(Zr)-NH_2, UiO-66(Zr)-NH_2@UiO-66(Ce) and UiO-66(Ce)@UiO-66(Zr)-NH_2. Characterization data reveal that the developed MOF on MOF heterojunctions exhibit core-shell architecture with controllable layer thickness and unique electronic properties. The photocatalytic activity of MOF-on-MOF heterojunctions having a UiO-66(Zr)-NH_2 core and UiO-66(Ce) shell outperforms respect to their individual counterparts for the Overall Water Splitting under simulated sunlight irradiation. The achieved photocatalytic activity (540 and 267 μmol g^{-1} at 22 h for H_2 and O_2, respectively) with an optimized UiO-66(Zr)-NH_2@UiO-66(Ce) structure, in the absence of any co-catalyst, ranks among the most active MOF-based photocatalysts for this process. Characterization data suggest that the high photocatalytic activity of the optimized UiO-66(Zr)-NH_2@UiO-66(Ce) photocatalyst derives from the appropriate electronic interaction of its individual counterparts through a Type II heterojunction with enhanced absorption of visible light, appropriate band alignment and improved photoinduced charge separation respect to their individual MOFs. This chapter exemplifies for the first time the possibility of preparation MOF-MOF heterojunctions with better activity for the solar-driven photocatalytic Overall Water Splitting in the absence of sacrificial agents.

4.2 Introduction

Currently, fossil fuels are the primary source of energy to cover the increasing worldwide demand.[1-3] The main disadvantage that they present during their combustion is the emission of greenhouse gases such as CO_2 as well as polluting gases such as NO_x and SO_x with negative impacts on environment and the human health. In this context, hydrogen is considered the ideal energy vector to supply clean energy.[4] Hydrogen is expected to be the main energy vector in countries that aimed to reach zero neat emissions.[4] Therefore, there is a great interest on developing technologies for the sustainable production of green hydrogen. Nowadays, hydrogen is produced primarily by an unsustainable process called high-temperature steam reforming of natural gas that uses fossil fuels as secondary energy.[4,5] One of the most promising alternative strategies to produce green hydrogen is heterogeneous catalysis using H_2O and solar energy.[6-8] In 1972 Fujishima and Honda reported a seminal study on the use of TiO_2 photoelectrodes to produce H_2 from H_2O.[9] Since then, most of studies focused on the use of inorganic semiconductors as photocatalyst for the water splitting.[10-12] The target in this field for real applications would be to reach solar-to-hydrogen (STH) efficiency close to 10 %. In the area or inorganic semiconductors, the current state of the art shows that the current efficiencies of STH are mostly below 1 %.[11] The relatively low tunability of inorganic semiconductors hampers in large extent the development of the field. Therefore, there is a growing interest in the development of new alternatives for the preparation of efficient heterogeneous photocatalysts.

In this context, metal-organic frameworks (MOFs) have shown their potential use as photocatalysts.[13-15] MOFs, also known as porous coordination polymers, are a class of porous and crystalline materials composed by multitopic organic ligands containing electron donor atoms of functional groups coordinated to metal ions, metal oxo-clusters or metal-oxo chains.[16-21] MOFs are considered one of the most flexible materials to tune their physic-chemical and optoelectronic

properties. Thus, a vast number of studies have shown the possibility of using MOFs as photocatalysts for the hydrogen evolution reaction (HER) using sacrificial electron donors such as triethanolamine or methanol.[13,22] Recently, Kampouri et al have shown for the first time the possibility of construction a MOF/MOF heterojunction based on MIL-167(Ti)@MIL-125(Ti)-NH_2 enhanced photoactivity respect to its individual MOFs for the HER in the presence of methanol as sacrificial agent.[23] The increase of photoactivity, observed when using the MOF-MOF heterojunction, has been attributed to the appropriate band alignment of the MOFs, the enhancement of visible light absorption and increase of photoinduced charge separation. Regardless the advances made in the field of MOFs as photocatalysts for the HER, the use of TEOA or MeOH as sacrificial electron donors hampers the applicability of these systems. In this sense, Liu, Huang and co-workers reported in 2017 a pioneering work on the use of a MOF namely Ni^{2+}/MIL-53(Al)-NH_2 for the Overall Water Splitting in the absence of sacrificial agent. [24] Later, Garcia's group have shown the possibility of using MOF-based photocatalysts such as UiO-66[25] or MIL-125[26] among others for this purpose.[27,28]

With these precedents, the present study shows, for the first time, the preparation of novel and active MOF-on-MOF heterojunctions based UiO-66 topology for the photocatalytic Overall Water Splitting under simulated sunlight irradiation. Specifically, the most active heterojunction prepared in this chapter is composed by a UiO-66(Zr)-NH_2 core and UiO-66(Ce) shell. The improvement of photocatalytic activity of this heterojunction derives from its enhancement of visible light absorption, appropriate band alignment and efficient photoinduced charge separation respect to their individual parent MOFs. It is anticipated that this study will pave the way toward the development of efficient MOF-based photocatalysts for the solar-driven photocatalytic Overall Water Splitting.

4.3 Experimental section

Materials

All chemicals and solvents employed in this work were of analytical or HPLC grade and they are commercially available

Preparation of materials

UiO-66(Zr)-NH_2 was prepared according to previous reports.[29] Briefly, $ZrCl_4$ (0.466 g, 2 mmol) and 2-aminoterephthalic acid (0.362 g, 2 mmol) were added to *N',*-dimethylformamide (DMF, 6 mL) and the mixture sonicated for 20 minutes (450 W sonicator power). Then, the suspension was transferred in a Teflon-Line autoclave, sealed and placed in an oven at 100°C for 24 hours. Subsequently, the system was cool down to room temperature. The resulting yellow solid was recovered by filtration (0.22 μm Nylon filter) and washed three times with DMF at 60 ºC and, then, three more times with methanol (65 ºC). The solid was further washed in Soxhlet for 24 h using methanol as solvent. Finally, the solid was recovered by filtration (0.22 μm Nylon filter) and dried in an oven at 100 ºC for at least 24 h.

UiO-66(Ce) was synthetized according to previous reports.[30] Briefly, using a round-bottomed flask (25 mL), terephthalic acid (0.0354 g, 213 mmol) was dissolved in DMF (1.2 mL). A freshly prepared aqueous solution of cerium (IV) ammonium nitrate (0.400 mL, 0.5333 M) was added to the system. The reactor was magnetically stirred for 15 min at 100 ºC. Then, the system was cooled down to room temperature and the resulting pale-yellow solid recovered by centrifugation. This solid was washed first with DMF and then, with acetone at room temperature. The crystalline powder was further washed with acetone in a Soxhlet. The resulting solid was dried in an oven at 70 ºC for at least 24 h.

UiO-66(Zr)-NH_2/UiO-66(Ce) heterojunction preparation. In this case, a similar procedure to that of UiO-66(Ce) was employed, but in the presence of a certain amount of preformed UiO-66(Zr)-NH_2 (25 or 200 mg) prior heating. The resulting samples were labelled as UiO-66(Zr)-NH_2-25/UiO-66(Ce) or UiO-66(Zr)-NH_2-200/UiO-66(Ce).

UiO-66(Ce)/UiO-66(Zr)-NH_2 heterojunction preparation. In this case, a similar procedure to that of UiO-66(Zr)-NH_2 was employed, but in the presence of a certain amount of preformed UiO-66(Ce) (200 mg). The resulting sample was labeled as UiO-66(Ce)-200/UiO-66(Zr)-NH_2.

Characterization of the materials

Powder X-ray diffractograms (PXRD) were recorded on a Philips XPert diffractometer equipped with a graphite monochromator (40 kV and 45 mA) employing Ni filtered CuKα radiation. Diffuse reflectance UV−visible spectra of the MOF powders were recorded using a Cary 5000 Varian spectrophotometer having an integrating sphere. X-ray photoelectron spectra (XPS) of the solid samples were recorded using a SPECS spectrometer equipped with a MCD-9 detector using a monochromatic Al (Kα= 1486.6 eV) X-ray source calibrating the binding energy using the C 1s peak set at 284.4 eV as reference. CASA software has been employed for spectra deconvolution. ATR- FTIR spectra of the solids were measured with a Bruker Tensor 27 instrument. Prior to ATR-FTIR measurements the solid samples were dried in an oven at 100 °C overnight to remove physisorbed water. Isothermal N_2 adsorption measurements at 77 K were recorded using a Micromeritics ASAP 2010 device for N_2 adsorption isotherms at 77 K. Thermogravimetric analyses were performed on a TGA/SDTA851e METTLER TOLEDO station. The morphologies and the compositions of the MOF-based materials were characterized using a SEM (Zeiss instrument, AURIGA Compact) or TEM instrument (JEOL JEM-2100F

instrument operating at 200 kW) coupled with a EDX detector. The metal content of previously acid-digested MOF solids was determined by means of ICP-AES. MOF digestion was performed by suspending the MOF (10 mg) in concentrated HNO_3 (25 mL) and the system heated at 80 ºC for 24 h.

Photocatalytic experiments

All the photocatalytic experiments were carried out at least in duplicate. The presented data points correspond to the average of the independent measurements and the error bar corresponds to the standard deviation.

Photocatalytic Overall Water Splitting.

For these experiments a definite amount of MOF as photocatalyst (i.e. 10 or 20 mg) was dispersed in Milli-Q water (20 mL) using a quartz reactor (51 mL) and the system sonicated (450 W) for 20 min to obtain a good MOF dispersion. Then, this system was purged with argon for 15 minutes to remove the air from the system. The MOF suspension under stirring was irradiated with a UV-Vis Hg-Xe lamp (150 W). In some experiments a cut-off filter ($\lambda > 420$ nm) or AM 1.5 filter was employed to perform visible light or simulated sunlight irradiations, respectively. The evolving gases were analyzed from the head space connecting directly the reactor to an Agilent 490 Micro GC system (Molsieve 5 Å column using Ar as carrier gas) without manual handling. Throughout the experiment the temperature of the system was monitored, and the pressure was analyzed by the manometer adapted to the photoreactor

Photocatalytic hydrogen or oxygen evolution reactions. For those experiments that involve the hydrogen evolution reaction, a MOF suspension (10 mg) in a mixture of Milli-Q water (16 mL) containing methanol (4 mL) as electron donor was prepared in a quartz reactor (51 mL). In the case of the oxygen evolution reaction, a MOF suspension in Milli-Q water (20 mL) containing sodium persulfate (700 mg) as electron quencher was also prepared in a quartz reactor (51 mL). Then, each

system was sonicated (450 W) for 15 min to obtain a good dispersion and then, purged under Ar to remove the air. Each suspension was stirred at room temperature and irradiated under simulated sunlight irradiation (150 W Hg-Xe lamp equipped with AM 1.5 G filter). The evolving gases were analyzed from the head space connecting directly the reactor to an Agilent 490 Micro GC system (Molsieve 5 Å column using Ar as carrier gas) without manual handling. Throughout each experiment the temperature of the system was monitored, and the pressure was analyzed by the manometer adapted to the photoreactor.

Photocatalytic $MV^{\bullet+}$ generation. For each experiment an acetonitrile suspension of the MOF-based photocatalyst (2 mg/mL, 200 μL) in 1.05 mL containing $MV(PF_6)_2$ 0.17 M was introduced in a 10 mm × 10 mm quartz cell. Additional acetonitrile was added to achieve a total volume of 3 mL. The solution was purged with argon for 15 min. The cuvettes containing the MOF dispersions were irradiated, under Ar atmosphere, with a Xe lamp (150 W) for different times and measuring the UV/Vis absorbance with UV/Vis spectrophotometer. The photoinduced electron transfer measurements were followed by the increase of the absorption band centered at 390 nm corresponding to the $MV^{\cdot+}$. The concentration of $MV^{\cdot+}$ (C, M^{-1}) can be obtained applying the Lambert- Beer equation $A=\varepsilon \cdot l \cdot C$ where A is the absorbance at 390 nm, ε is the molar extinction coefficient of MV^{2+} at 390 nm (13900 M^{-1} cm^{-1}), l is the length of the cell (1 cm).

Photocatalytic $TMPDA^{\cdot+}$ generation. An acetonitrile suspension of each MOF (2 mg/mL, 200 μL) was added to an acetonitrile saturated solution of *N*,*N*,*N*′,*N*′-tetramethyl-*p*-phenylenediamine (TMPDA). The suspension was introduced in a 10 mm × 10 mm quartz cell, purged for 15 min with argon and then irradiated for several minutes with a Xe lamp (150 W). The course of the photocatalytic reaction was followed by the increase of the absorption band with fine structure centered at 590 nm. The concentration of the radical cation $TMPD^{\cdot+}$ can be obtained by applying the

Lambert- Beer equation $A=\varepsilon \cdot l \cdot C$ where A is the absorbance at 590 nm, ε is the molar extinction coefficient of $TMPDA^{\cdot+}$ at 590 nm (12200 M^{-1} cm^{-1}), l is the length of the cell (1 cm).

Photophysical measurements

Photoluminescence spectroscopy measurements. Firstly, a stock dispersion of each MOFs in acetonitrile (1 mg/mL) was prepared and the system sonicated for 20 min (450 W sonicator). Subsequently, 0.2 mL of each MOF dispersion was further diluted with acetonitrile until a total volume of 3 mL. Then, the suspensions were analyzed by UV-vis spectroscopy and diluted again with acetonitrile to obtain an absorbance, at 266 nm or 355 nm of 0.3. Finally, these MOF suspensions were purged in Ar for 10 min and, then, analyzed by fluorescence spectroscopy.

Laser flash photolysis measurements. A stock dispersion of 1 mg/ mL in acetonitrile was prepared for each catalyst; about 0.2 mL of this dispersion (approximately 0.3 optical density at 355 nm) was diluted with acetonitrile until a final volume of 3 mL and analyzed using the fourth harmonic of a Q switched Nd:YAG laser (Quantel Brilliant, 355 nm, 10 mJ/pulse, 5 ns fwhm) coupled to a mLFP-122 Luzchem miniaturized detection equipment. This transient absorption spectrophotometer consists of a 300 W ceramic xenon lamp, 125 mm monochromator, Tektronix TDS-2001C digitizer, compact photomultiplier and power supply, liquid cell holder, fiber-optics connectors and computer interfaces. The software package was developed in the LabVIEW environment from National Instruments. The laser flash photolysis equipment supplies 5 V trigger pulses with programmable frequency and delay. The rise time of the detector/digitizer is ~3 ns up to 300 MHz (2.5 GHz sampling). The monitoring beam is provided by a ceramic xenon lamp and delivered through fiber-optic cables. The laser pulse is probed by a fiber that synchronizes the LFP system with the digitizer operating in the pretrigger mode. Transient spectra of the persistent suspensions were recorded using 10 × 10 mm quartz cells and were bubbled for 15 min with argon before data acquisition.

Each decay or data point corresponds to the average of 5 signals to increase the signal to noise ratio.

4.4 Results and discussion

Material preparation and characterization

The series of MOF and MOF heterojunctions based on UiO-66 topologies were characterized by several techniques. PXRD measurements on the prepared UiO-66(Zr)-NH_2 and UiO-66(Ce) solids confirm the expected UiO-66 topology as previously reported (Figure 4.1). The lowest-angle diffraction peak of UiO-66(Ce) solid appears shifted to 7.2 º respect to UiO-66(Zr)-NH_2 at 7.4 º. This observation agrees with the higher ionic radius of Ce^{4+} respect to Zr^{4+} at the metal nodes that causes an expansion of the unit cell volume. PXRD of the synthetized UiO-66 heterojunctions show that they are isostructural respect to their individual UiO-66-(Ce) and UiO-66-(Zr)-NH_2 counterparts (Figure 4.1). The UiO-66(Zr)-NH_2-200@UiO-66(Ce) sample prepared using 200 mg of preformed UiO-66(Zr)-NH_2 is characterized by a main low-angle diffraction peak at about 7.4 º as in the case of the pure UiO-66(Zr)-NH_2 pattern. In the case of the UiO-66(Zr)-NH_2-25@UiO-66(Ce) sample prepared using only 25 mg of preformed UiO-66(Zr)-NH_2 solid two diffraction peaks at about 7.2 and 7.4 º can be observed and attributed to the UiO-66(Ce) and UiO-66(Zr)-NH_2 patterns, respectively.

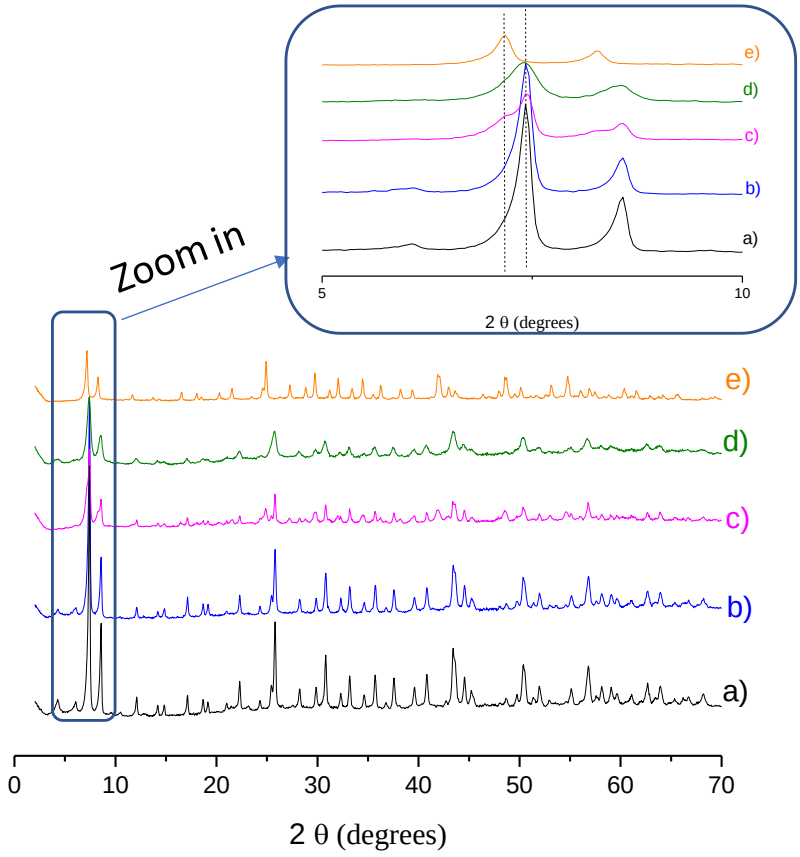

Figure 4.1: PXRD of UiO66-(Zr) (a), UiO66(Zr)-NH_2-200@UiO66(Ce) (b), UiO66-(Zr)-NH_2-25@UiO66(Ce) (c), UiO-66(Ce)-200@UiO-66(Zr)-NH_2 (d) and UiO-66(Ce) (e). The inset shows a zoon in in the low angle region.

In good agreement with previous studies,[25,31] isothermal N_2 adsorption experiments at -77 K using UiO-66(Zr)-NH_2 and UiO-66(Ce) solids allowed estimating their BET surface area with values of 923 and 906 m^2/g (Figures S4.1 and S4.2), respectively. In the case of UiO-66(Zr)-NH_2-200@UiO-66(Ce) and UiO-66(Zr)-NH_2-25@UiO-66(Ce) samples, the estimated BET values were 841 and 783 m^2/g, respectively (Figures S4.3 and S4.4). Attempts to prepare a UiO-66(Ce)@UiO-66(Zr)-NH_2 heterojunction using 200 mg of preformed UiO-66(Ce)

resulted in a crystalline solid (Figure 4.1d) with an estimated BET area of only 600 m^2/g. This lower specific BET area may reflect that UiO-66(Ce) is not completely stable in the presence of the acidic $ZrCl_4$ reagent during the preparation of the UiO-66(Ce)@UiO-66(Zr)-NH_2 heterojunction. In fact, this sample exhibited poor photocatalytic results for the Overall Water Splitting compared with the other two heterojunctions (data not shown). Therefore, we decide to continue the present study using the UiO-66(Zr)-NH_2@UiO-66(Ce) samples prepared by using two different amounts of preformed UiO-66(Zr)-NH_2 solid (200 or 25 mg).

HRSEM analysis of the UiO-66 samples under study revealed that UiO-66(Zr)-NH_2 (Figure S4.6) and UiO-66(Ce) (Figure S4.7) exhibited an average particle size and standard deviation of 133 ± 45 and 112 ± 46 nm, respectively. The preparation of the UiO-66(Zr)-NH_2-200@UiO-66(Ce) and UiO-66(Zr)-NH_2-25@UiO-66(Ce) samples from preformed UiO-66(Zr)-NH_2 (133 ± 45 nm) resulted in an increase of average particle size to 161 ± 80 and 142 ± 44 nm (Figures S4.8 and S4.9), respectively. The increase of particle size in the UiO-66s heterojunctions due attributed to the growth of the UiO-66(Ce) in the external part of the preformed UiO-66(Zr)-NH_2 solid. The UiO-66 samples under study were also analyzed by EDX mapping and observing the presence of all the expected elements in the sample (Figures S4.10 to S4.12). Interestingly, EDX mapping of the MOF-on-MOF UiO-66(Zr)-NH_2-@UiO-66(Ce) samples reveal the presence of a UiO-66(Zr)-NH_2 core surrounded by a UiO-66(Ce) shell (Figure 4.2 and S4.12).

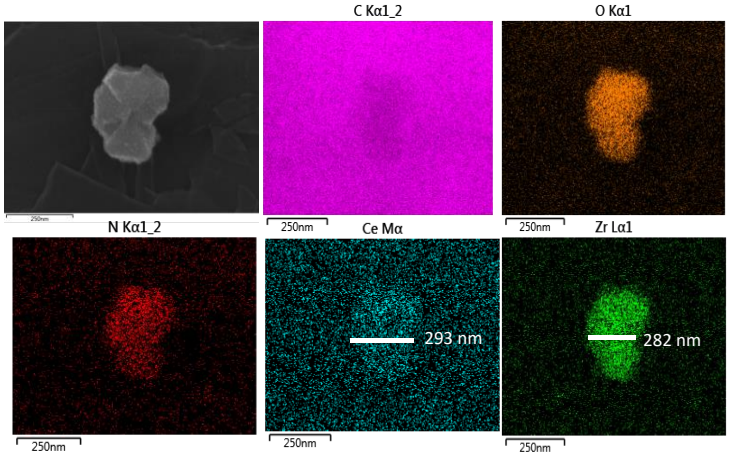

Figure 4.2. SEM image and elemental EDX mapping for UiO-66(Zr)-NH_2-25@UiO-66(Ce).

Interestingly, EDX line scanning across the MOF-on-MOF solids revealed that the use of higher (200 mg) or lower (25 mg) amounts of UiO-66(Zr)-NH_2 solid during the synthesis of the UiO-66(Zr)-NH_2@UiO-66(Ce) heterojunctions is accompanied by the presence of particles with core-shell architecture with higher or lower UiO-66(Ce) shell width, respectively. In good agreement with these observations ICP-AES analyses of the acid-digested samples revealed that the percentage of cerium respect to the total metal content (Zr+Ce) in weight present in the UiO-66(Zr)-NH_2-25@UiO-66(Ce) is higher (28.6 wt%) respect to that found in the UiO-66(Zr)-NH_2-200@UiO-66(Ce) (11.5 %). In good agreement with these observations. Besides, for the most photocatalytic active UiO-66(Zr)-NH_2-25@UiO-66(Ce) sample SEM-EDX analyses also confirms the core-shell structure of the sample.

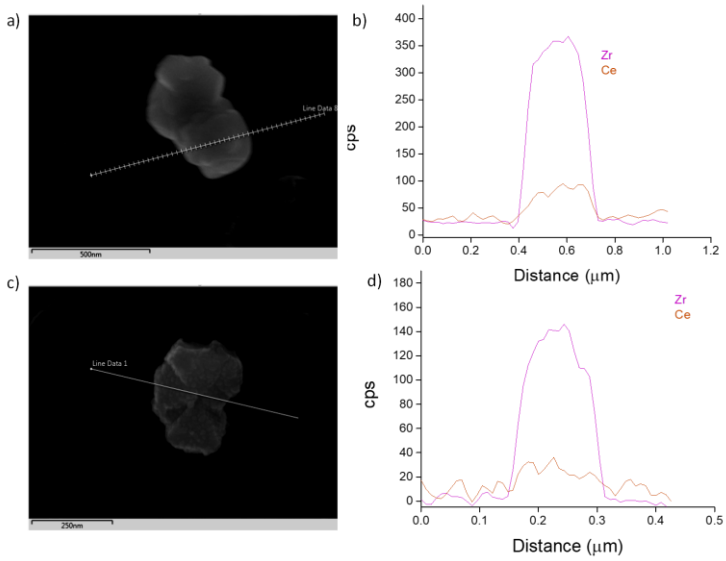

Figure 4.3. SEM images (a, c) and line scan EDX analysis (b, d) of UiO-66(Zr)-NH_2-200@UiO-66(Ce) (a, b) and UiO-66(Zr)-NH_2-25@UiO-66(Ce) (c, d)

ATR-FT-IR spectroscopy was also employed to characterize the samples under study. The UiO-66(Zr)-NH_2 solid is characterized by the presence of carboxylate (υ_{asymm}1585 and υ_{symm} 1384 cm-1) and amino (υ_{asymm} 3482 cm^{-1} and υ_{symm} 3386 cm^{-1}) functional groups together with the characteristic C-N stretching band (1595 cm^{-1}) as previously reported. The coordination of the carboxylate groups with Zr^{4+} ions is characterized by the vibration band at about 489 cm^{-1}. The UiO-66(Ce) solid is characterized by the vibrations bands of the carboxylate functional groups (υ_{asymm}1585 and υ_{symm} 1384 cm^{-1}) together with the carboxylate groups coordinated with Ce^{4+} ions at about 517 cm^{-1} (Figure S4.19).[32]

Thermogravimetric analyses show that UiO-66(Zr)-NH_2 and UiO-66-(Ce) solids are thermally stable up to about 300 ºC as previously reported. The combustion of the MOF organic ligand leads to a remaining weight that corresponds to the presence of metal oxides CeO_2 or ZrO_2. The UiO-66(Zr)-NH_2 solid the

experimental zirconium content determined by TGA (32.8 %) is analogous to that expected of the ideal solid (31.2 %) with neutral formula $Zr_6O_4(OH)_4(OOC\text{-}C_6H_3NH_2\text{-}COO)_6$. In the case of the UiO-66(Ce) material also a quite good coincidence between the experimental cerium content determined by TGA (42.9 %) and the cerium content present in the ideal formula $Ce_6O_4(OH)_4(OOC\text{-}C_6H_4\text{-}COO)_6$ was obtained. These small, but significant, differences between the experimental by TGA and theoretical metal content of these two MOFs is an indication of the presence of structural defects.[25] The UiO-66(Zr)-NH_2@UiO-66(Ce) heterojunctions prepared using two amounts of preformed UiO-66(Zr)-NH_2 exhibit a thermal stability intermediate between that of UiO-66(Ce) and UiO-66(Zr)-NH_2 counterparts (Figure S4.20).

The UiO-66(Zr)-NH_2@UiO-66(Ce) heterojunctions have also been characterized by XPS (Figure 4.4). C1s spectrum shows the characteristic signals of the aromatic sp^2 carbons (284.4 eV) together with the C-N (286 eV) and carboxylate carbon atoms (288 eV) of the terephthalate ligands. The O1s spectrum exhibits a main band at about 532 eV characteristic of the oxygen atoms present in the carboxylate groups. The N1s spectrum is characteristic of the C-N of the amino group present in the UiO-66(Zr)-NH_2. The Zr 3d spectrum shows two bands attributable to the $d_{5/2}$ (182.5 eV) and $d_{3/2}$ (184.5 eV) characteristic of the Zr^{4+} ions present in the metal nodes of UiO-66(Zr)-NH_2. The Ce 3d spectrum reveals the presence of both Ce^{4+} and Ce^{3+} ions in the metal nodes of UiO-66(Ce) in agreement with previous reports.[25]

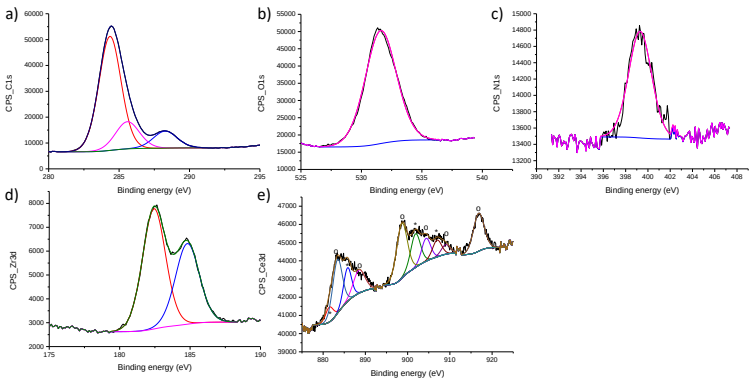

Figure 4.4. High resolution XPS peaks and the best deconvolution for the C 1s (a), O 1s (b), N1s (c), Zr 2p (d) and Ce 2d (d) signals recorded for the UiO-66(Zr)-NH_2-25@UiO-66(Ce) sample. Legend: Ce^{4+} (o), Ce^{3+} (*).

Other important feature of the UiO-66 solids under study for their use as photocatalysts for the Overall Water Splitting is their energy level diagram.[33] For this purpose, the optical band gaps of the UiO-66 materials were determined from their Tauc plots of absorption data spectra (Figure 4.5). The estimated band gaps for UiO-66(Zr)-NH_2 and UiO-66(Ce) were 2.81 and 2.99 eV in good agreement with previous results.[25] Importantly, the UiO-66 heterojunctions show lower band bap respect to their individual counterparts. Furthermore, their energy level of the valence band maximum was estimated from XPS from the intersection of a linear fit to the linear portion of the electron emission edge and the background. The obtained value corresponds to the valence band maximum energy versus the Fermi level (E^f_υ). The valence band position vs the NHE (E_υ^{NHE}) can be obtained from the following equation:

$$E_\upsilon^{NHE} = E_\upsilon^{f} + \phi_{sp} \text{ -4.44 where } \phi_{sp}$$

is the work function of the spectrometer with the value 4.244 eV. From this E_υ^{NHE} value and the band gap the conduction band energy minimum (E_c^{NHE}) can be determined. Figure 4.5 summarizes the energy level obtained for the UiO-66

heterojunctions and their individual counterparts.[25] The results indicate that the UiO-66 samples under study meet the thermodynamic prerequisites to be used as photocatalysts for the Overall Water Splitting into H_2 and O_2.

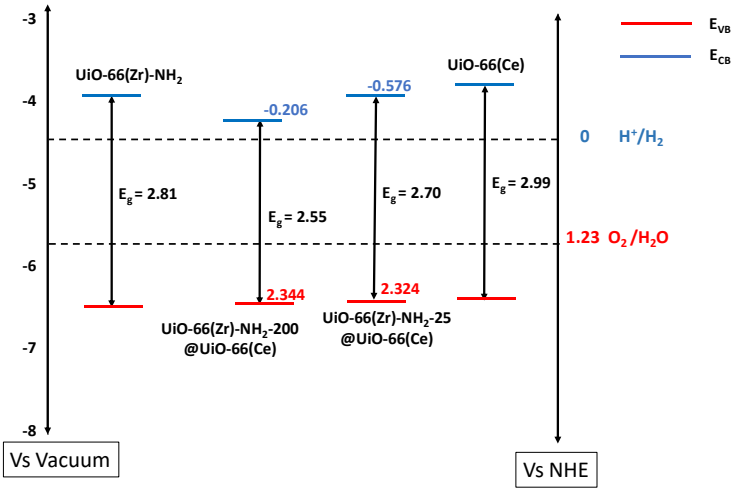

Figure 4.5. Energy band diagram of UiO-66(Zr)-NH_2, UiO-66(Zr)-NH_2-200@UiO-66(Ce), UiO-66(Zr)-NH_2-25@UiO-66(Ce) and UiO-66(Ce).

Photocatalytic results

The series of UiO-66 samples under study were initially evaluated for the photocatalytic Overall Water Splitting. In good agreement with the energy band diagram of the UiO-66 solids shown in Figure 4.5, all the four samples under study are active for this purpose under both UV-Vis and simulated sunlight irradiation. Importantly, the UiO-66(Zr)-NH_2@UiO-66(Ce) heterojunctions are more active than their individual UiO-66(Zr)-NH_2 or UiO-66(Ce) parts for the Overall Water Splitting into H_2 and O_2 under both UV-Vis or simulated sunlight irradiation. The somewhat lower oxygen content respect to the H_2O stoichiometry may be due to several reasons, including partial consumption of the photogenerated holes by spurious electron donor impurities or the in-situ reaction of O_2 evolved during the photocatalytic reaction. The most active sample UiO-66(Zr)-NH_2-25@UiO-66(Ce)

exhibits a H_2 and O_2 production as high as 375 and 170 μmol g^{-1} in 22 h under simulated sunlight irradiation (Figure 4.6). Additional experiments using exclusively visible light irradiation ($\lambda > 420$ nm) showed that a large part of the observed photocatalytic activity (277 μmol g^{-1} H_2 and 79 μmol g^{-1} of O_2 in 22 h) derives from its visible light response.

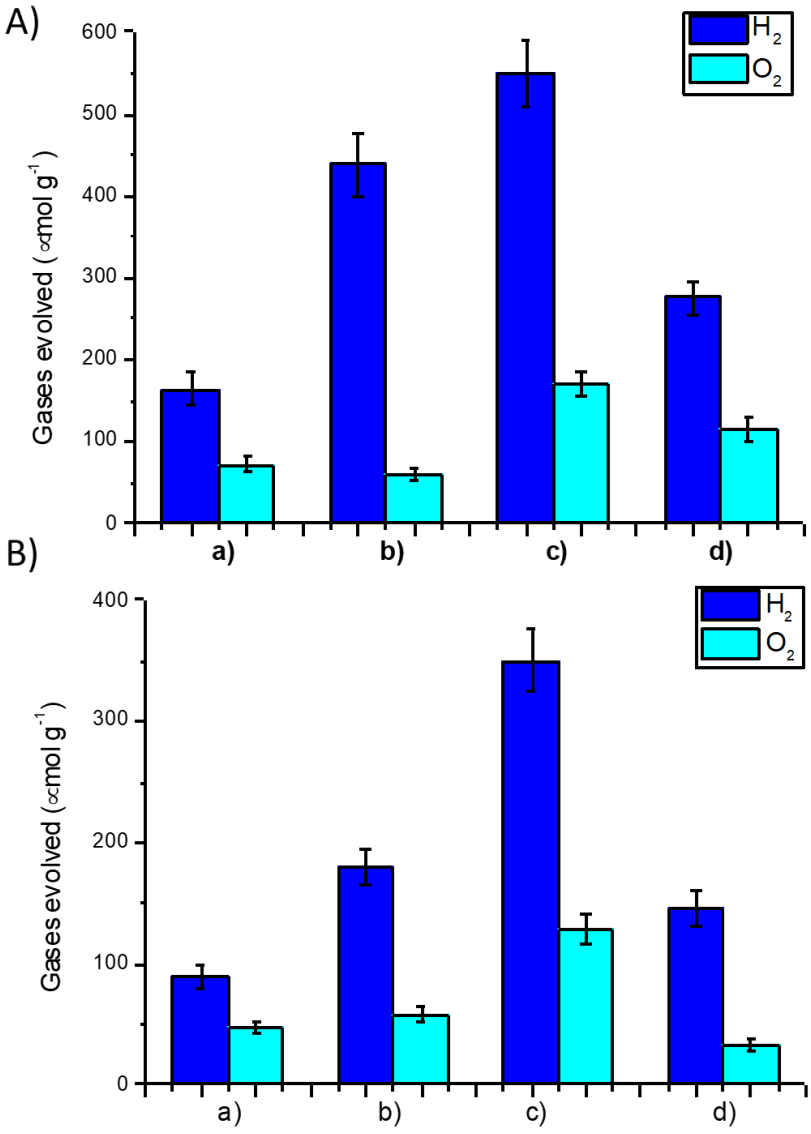

Figure 4.6. Photocatalytic overall water splitting using UiO-66(Zr)-NH_2 (a), UiO-66(Zr)-NH_2-200@UiO-66(Ce) (b), UiO-66(Zr)-NH_2-25@UiO-66(Ce) (c) and UiO-66(Ce) (d).

The photocatalytic activity of UiO-66(Zr)-NH_2-25@UiO-66(Ce) compares favorably with other MOF-based photocatalysts reported under similar conditions.[28] Specifically, Horcajada, García and co-workers have reported in 2021 one of the most active MOF photocatalysts for the Overall Water Splitting in the absence of any co-catalyst under simulated sunlight irradiation. In particular, using the same photocatalytic reaction conditions employed in this work (150 W Xe-He lamp, AM 1.5G filter, 10 mg of photocatalyst, 20 mL H_2O and 35 ºC) and the same photoreactor, a H_2 and O_2 production of 260 and 107 μmol g^{-1} h^{-1} in 22 h has been now achieved.[28] During photocatalyst amount optimization, the reported IEF-11 MOF achieved under the present reaction conditions, but using 5 mg of solid, a H_2 and O_2 productions of 540 and 267 μmol g^{-1} at 22 h, respectively[28]. In this work, the use of 5 mg of UiO-66(Zr)-NH_2@UiO-66(Ce) photocatalyst again overpasses this reported production with the values of 708 and 320 μmol g^{-1} at 22 h. Overall, this study shows for the first time the possibility of preparation MOF-on-MOF heterojunctions based on relatively simple UiO-66 solids to achieve one of the most active photocatalyst for the Overall Water Splitting under simulated sunlight irradiation until known.

The stability of the most active UiO-66(Zr)-NH_2-25@UiO-66(Ce) sample was tested during the reaction by performing several consecutive reuses. Figure 4.7 shows that the photocatalyst retains in large extent its initial photocatalytic activity after six consecutive uses. The PXRD of the six-times used sample reveals that the solid maintains most of its initial crystallinity. ICP-AES analysis of the liquid phase after three uses reveals the almost complete absence of zirconium leaching from the solid to the solution, while about 6 wt% of the initial cerium present in the sample leaches to the solution. Thus, the partial cerium leaching may be one of the reasons of the observed decrease of activity. In any case this study opens new avenues for the development of MOF-on-MOF heterojunctions with high photocatalytic activity and stability.

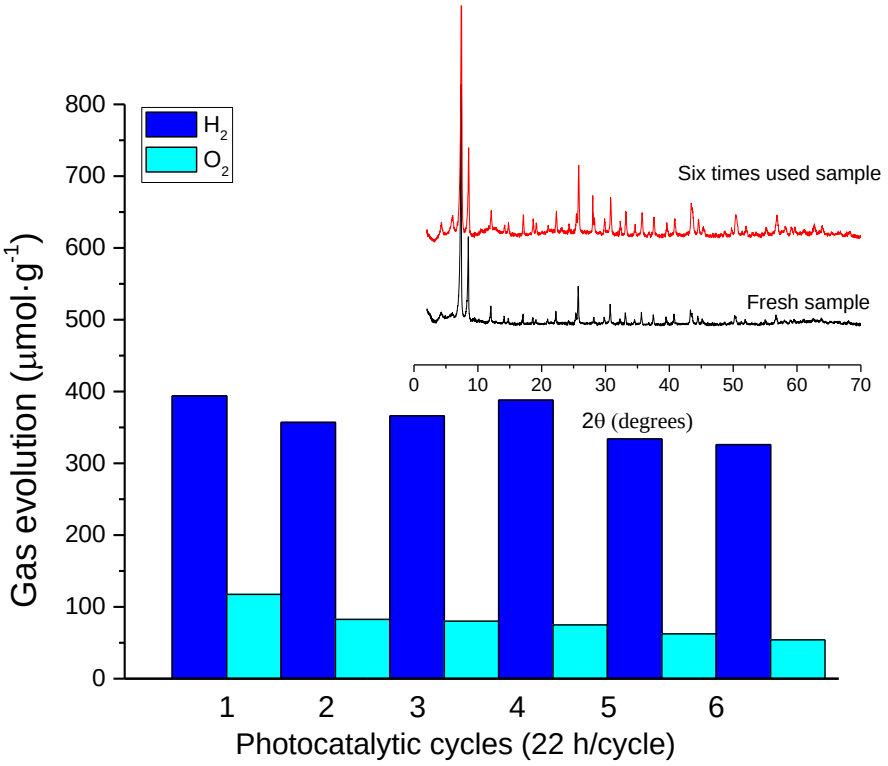

Figure 4.7. Photocatalytic overall water splitting for six consecutive cycles using UiO-66(Zr)-NH_2-25@UiO-66(Ce) under simulated sunlight irradiation. The inset shows the PXRD patterns of the fresh and six-times used sample. Reaction conditions: photocatalyst (10 mg), H2O (20 mL), simulated sunlight irradiation (Hg-Xe lamp 150 W through an AM 1.5G filter), 35 °C.

Reaction mechanism

To gain some insights on the high photocatalytic activity of UiO-66(Zr)-NH_2-25@UiO-66-(Ce) for the Overall Water Splitting additional experiments were carried out. Initially, the photocatalytic HER and OER in the presence of methanol or persulfate as sacrificial hole or electron scavengers, respectively, were performed. Figure 4.8 show that the order of activity for both photocatalytic HER or OER is the same than that observed for the Overall Water

Splitting. The most active photocatalyst for these processes is the heterojunction UiO-66(Zr)-NH_2-25@UiO-66(Ce). The observed order of photocatalytic activity for both HER and OER processes deserves some comments. The UiO-66(Zr)-NH_2 (-0.61 V) and UiO-66(Ce) (-0.8 V) have more negative LUCO values than UiO-66(Zr)-NH_2-25@UiO-66(Ce) (-0.576 V), but all of them meet the thermodynamic reduction potential required for the HER. In this case, the higher photocatalytic activity of UiO-66(Zr)-NH_2-25@UiO-66(Ce) may be at least attributed to higher visible light harvesting due to the differences in UV-Vis absorption spectra. At the same time, the UiO-66(Zr)-NH_2-25@UiO-66(Ce) sample with higher band gap (2.70 eV) than UiO-66(Zr)-NH_2-200@UiO-66(Ce) (2.55 eV) is also more active. In this case, the higher activity of UiO-66(Zr)-NH_2-25@UiO-66(Ce) respect to UiO-66(Zr)-NH_2-200@UiO-66(Ce) could be reflect the lower overpotential for HER since UiO-66(Zr)-NH_2-25@UiO-66(Ce) has a more negative LUCO (-0.576 vs -0.206 V). In the case of the photocatalytic OER all the samples under study exhibit similar HOCO values, while the most active UiO-66(Zr)-NH_2-25@UiO-66(Ce) sample exhibits an intermediate band gap value (2.70 eV) in the series. Therefore, the higher activity of the UiO-66(Zr)-NH_2-25@UiO-66(Ce) samples for the OER cannot simply explain based on its energy band diagram and other reasons should explain this behavior.

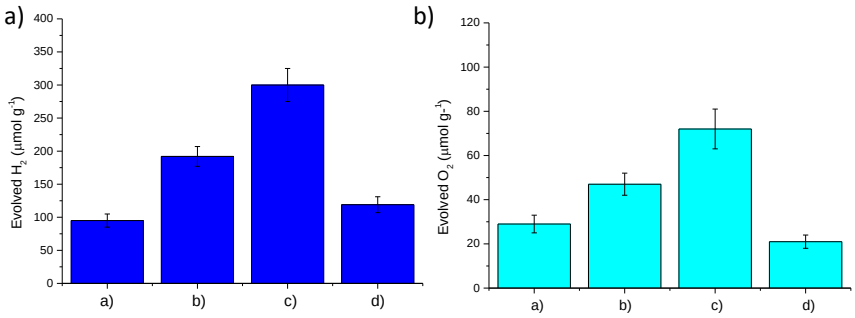

Figure 4.8. a) Photocatalytic H_2 (a) or O_2 (b) evolution reactions using UiO-66(Zr)-NH_2 (1), UiO-66(Zr)-NH_2-200@UiO-66(Ce) (2), UiO-66(Zr)-NH_2-25@UiO-66(Ce) (3) and UiO-66(Ce) (4) under simulated sunlight irradiation. Legend: Reaction conditions for panel a).

To further evaluate the possible origin of the high photocatalytic activity of the UiO-66(Zr)-NH_2-25@UiO-66(Ce) heterojunction, a comparative photoluminescence emission spectroscopy study with all the materials presented in this work was carried out. Photoluminescence spectroscopy is a useful technique to provide some insights about the occurrence of photoexcited charge transfer and recombination in photoresponsive MOFs.[34] It is worth commenting that the emission intensity of a specific sample after photoexcitation corresponds to its ability to undergo charge recombination, therefore, the higher the emission intensity, the higher the charge recombination. As it will be shown later, the photoexcitation of the UiO-66 materials under study results in the occurrence of photogenerated electron and hole pairs. Thus, the observed fluorescence emission of the UiO-66 samples here presented was attributed to the emission of photons due to the electron-hole recombination from the charge-separate state to the ground state.

Figure 4.9 shows the photoluminescence spectra of the UiO-66 series in acetonitrile suspension (about 0.2 $mg \times ml^{-1}$) after excitation at 266 or 355 nm. Similar results were observed for the two excitation wavelengths. The emission spectrum of UiO-66(Zr)-NH_2 upon 266 nm irradiation is dominated by two main bands centered at around 360 and 448 nm. In contrast, negligible photoluminescence (PL) was recorded for UiO-66(Ce). Interestingly the PL emission of the UiO-66(Zr)-NH_2-200@UiO-66(Ce) sample resembles to that of UiO-66(Zr)-NH_2 in the region around 448 nm. In the case of the UiO-66(Zr)-NH_2-25@UiO-66(Ce) sample, much lower PL intensity was recorded, indicating that charge recombination occurs in much lesser extent for this heterojunction in comparison to UiO-66(Zr)-NH_2-200@UiO-66(Ce) and the parent UiO-66(Zr)-NH_2. With these PL observations and the energy diagram of UiO-66(Ce) and UiO-66(Zr)-NH_2, it is likely to suppose that upon excitation at 266 nm the electrons present in the LUCO of either of UiO-66(Zr)-NH_2 or UiO-66(Ce) are injected into the less energetic conduction band of UiO-66(Zr)-NH_2@UiO-66(Ce) sample. It is important to highlight that a physical mixture of UiO-66(Ce) and UiO-66(Zr)-NH_2 does not result in the electronic interactions observed for the UiO-66(Zr)-NH_2-25@UiO-66(Ce) heterojunction.

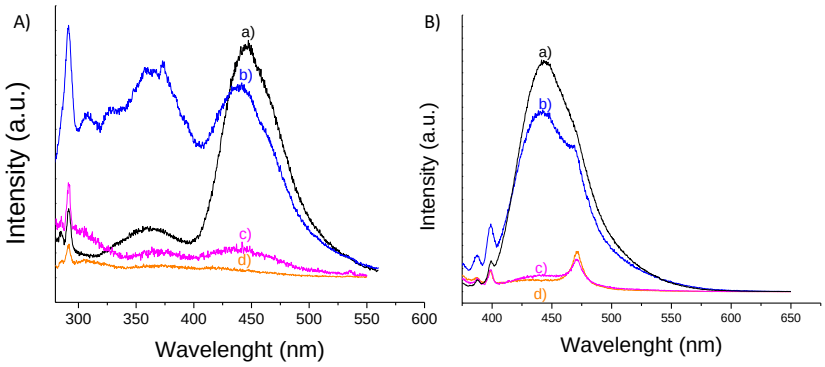

Figure 4.9): Emission spectra of acetonitrile suspension of a) UiO-66(Zr)-NH_2; b) UiO-66(Zr)-NH_2 200@UiO-66 (Ce); c) UiO-66(Zr)-NH_2-25@UiO-66(Ce); d) UiO66 (Ce) recorded at A) (λ_{exc}= 266 nm) and B) λ_{exc} = 355 nm.

Other important aspect from the PL study is the observation that the emission of the UiO-66(Zr)-NH_2-25@UiO-66(Ce) sample is much lower than that observed with the other heterojunction UiO-66(Zr)-NH_2-200@UiO-66(Ce) or the parent UiO-66(Zr)-NH_2, indicating that charge recombination occurs in much lesser extent in this heterojunction. Thus, the high photocatalytic activity of the UiO-66(Zr)-NH_2-25@UiO-66(Ce) sample respect to the other UiO-66(Zr)-NH_2-200@UiO-66(Ce) heterojunction or the UiO-66(Zr)-NH_2 can be attributed to the fact that the undesirable charge recombination takes place in much lesser extent. In the case of the UiO-66(Ce) sample that shows similar emission intensities at both 266 or 355 nm respect to the UiO-66(Zr)-NH_2-25@UiO-66(Ce) sample, its lower photocatalytic activity can be attributed at least partially to its lower ability to absorb visible light irradiation.

One common strategy to confirm the occurrence of photoinduced charge separation is the use of probe molecules that react with electrons or holes resulting in the formation of colored species. Among them, methyl viologen (MV^{2+}) is one of the preferred molecules employed as one-electron acceptor leading to the formation

of a visually observable blue colored radical cation ($MV^{\cdot+}$) under inert atmosphere.[35] Similarly, *N*,*N*,*N*',*N*'-tetramethyl-p-phenylenediamine (TMPDA) is commonly employed as one electron donor molecule rendering under inert atmosphere a visually observable blue-violet colored radical cation ($TMPDA^{\cdot+}$). In this study, it was observed that all the UiO-66 samples under study promote the photocatalytic one electron MV^{2+} reduction to $MV^{\cdot+}$ as well as the TMPDA oxidation to $TMPDA^{\cdot+}$. Furthermore, it is interesting to note that the order of photocatalytic activity of the UiO-66 samples for these two processes is the same than that observed for the Overall Water Splitting, HER and OER reactions: UiO-66(Zr)-NH_2-25@UiO-66(Ce) > UiO-66(Zr)-NH_2-200@UiO-66(Ce) > UiO-66(Zr)-NH_2 > UiO-66(Ce).

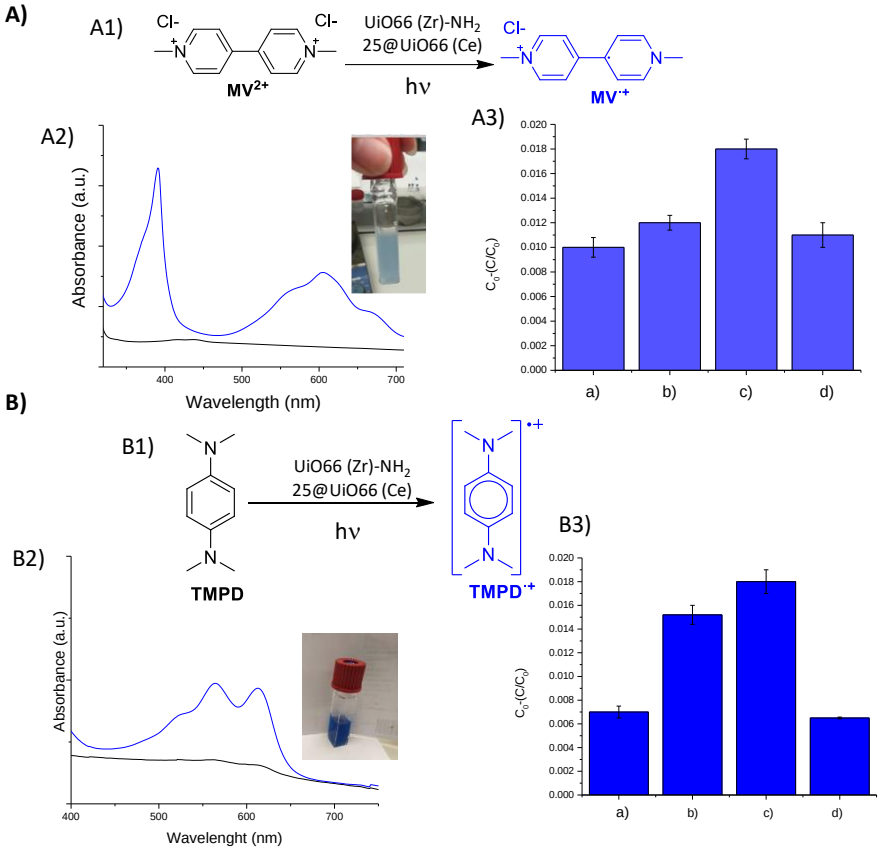

Figure 4.10. A) Photocatalytic one electron MV^{2+} reduction to $MV^{\cdot+}$ using UiO-66(Zr)-NH_2-25@UiO-66(Ce) (A1); UV-vis spectra before and after irradiation of an acetonitrile MV^{2+} solution containing the UiO-66(Zr)-NH_2-25@UiO-66(Ce) photocatalyst under Ar atmosphere and photograph of the resulting blue colored solution; Photocatalytic activity for MV^{2+} reduction to $MV^{\cdot+}$ using UiO-66(Zr) (a), UiO-66(Zr)-NH_2-200@UiO-66(Ce) (b), UiO-66(Zr)-NH_2-25@UiO-66(Ce) (c) and UiO-66(Ce) (d). B) Schematic illustration of the photocatalytic one electron TMPD oxidation to $TMPD^{\cdot+}$ using UiO-66(Zr)-NH_2-25@UiO-66(Ce) (A1); UV-vis spectra before and after irradiation of an acetonitrile TMPDA solution containing the UiO-66(Zr)-NH_2-25@UiO-66(Ce) photocatalyst and photograph of the resulting blue colored solution; Photocatalytic activity for TMPDA to $TMPDA^{\cdot+}$ under Ar atmosphere using UiO-66(Zr) (a), UiO-66(Zr)-NH_2-200@UiO-66(Ce) (b), UiO-66(Zr)-NH_2-25@UiO-66(Ce) (c) and UiO-66(Ce) (d).

In order to gain better insights into the observed photocatalytic activity and the occurrence of photoinduced charge separation observed by using probe molecules, the UiO-66 samples under study were further studied by means of microsecond transient absorption spectroscopy (TAS). For this purpose, optically matched (absorbance 0.3) acetonitrile suspensions of the four UiO-66 samples under study were prepared. Figure 4.11 shows the temporal profiles obtained for the UiO-66 samples upon laser excitation at 355 nm under Ar atmosphere and monitored at 340 nm. This selected wavelength is able to promote electrons from the HOCO to the LUCO of the UiO-66 materials under study. From the best fit of these temporal profiles to a monoexponential decay kinetics, lifetimes in the order of nanoseconds were obtained. Besides, it can be seen that all the transient signals shown in Figure 4.11 decay to the ground state in the time scale available for the measurement, indicating that no photoproducts are formed and the system decays to the initial ground state. Previous studies using defective UiO-66(Zr)-NH_2 samples as photocatalysts have described that the average decay lifetime obtained from femtosecond TAS can be used as indicator to evaluate the charge separation efficiency.[36] The somewhat faster decay lifetime obtained for the UiO-66(Zr)-NH_2-25@UiO-66(Ce) heterojunction respect to UiO-66(Zr)-NH_2-200@UiO-66(Ce), UiO-66(Zr)-NH_2 and UiO-66(Ce) can be attributed to the more efficient electron-hole separation.

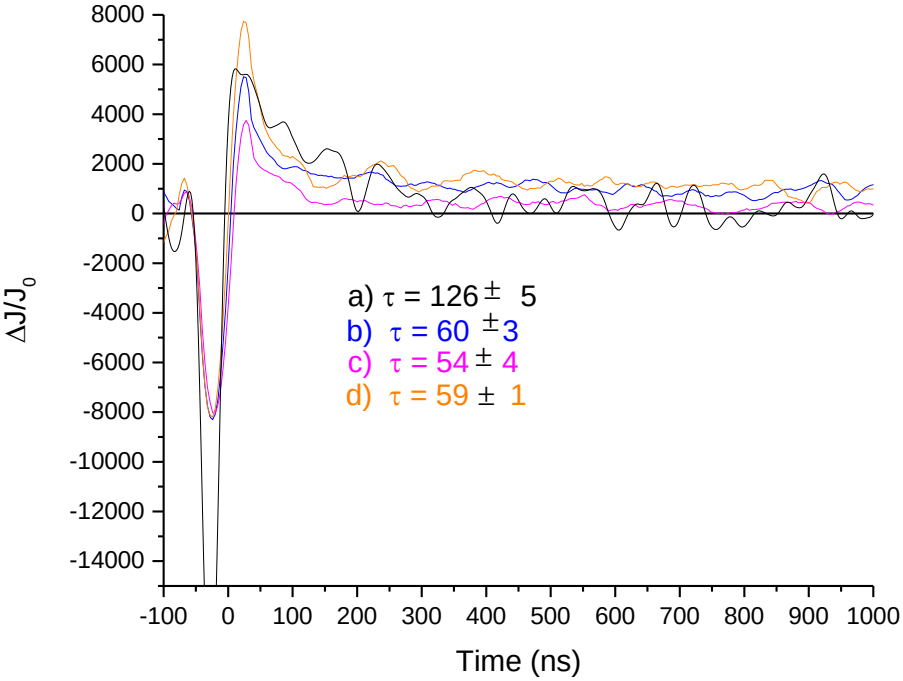

Figure 4.11: Temporal profiles of the transient signals monitored at 340 nm upon 355 nm laser excitation under argon atmosphere for a) UiO-66(Zr)-NH_2; b) UiO-66(Zr)-NH_2-200@UiO-66(Ce); c) UiO-66(Zr)-NH_2-25@UiO-66(Ce); d) UiO-66(Ce).

In the case of the most photo-catalytically active UiO-66(Zr)-NH_2-25@UiO-66(Ce) sample the nature of the photogenerated species was further evaluated by microsecond TAS performing selective electron and hole quenching experiments. In particular, N_2O was employed as electron quencher, while methanol was used as hole quencher. Figure 4.12 shows that the presence of both N_2O or MeOH quenches the transient signals monitored at 340 nm upon excitation at 355 nm. These observations are in agreement with the nature of the photogenerated transient species as being a contribution of electrons and holes. Figure 4.12 also shows that the presence of N_2O or MeOH quenches different regions of the transient absorption spectrum recorded under Argon. In particular, electrons have a larger contribution to the absorption from 300 to 700 nm, while positive holes are responsible in a larger proportion for the absorption between 260-575 nm. Overall, this behavior indicates that the species responsible for the absorption signal in the transient spectrum correspond to photogenerated electrons and holes.

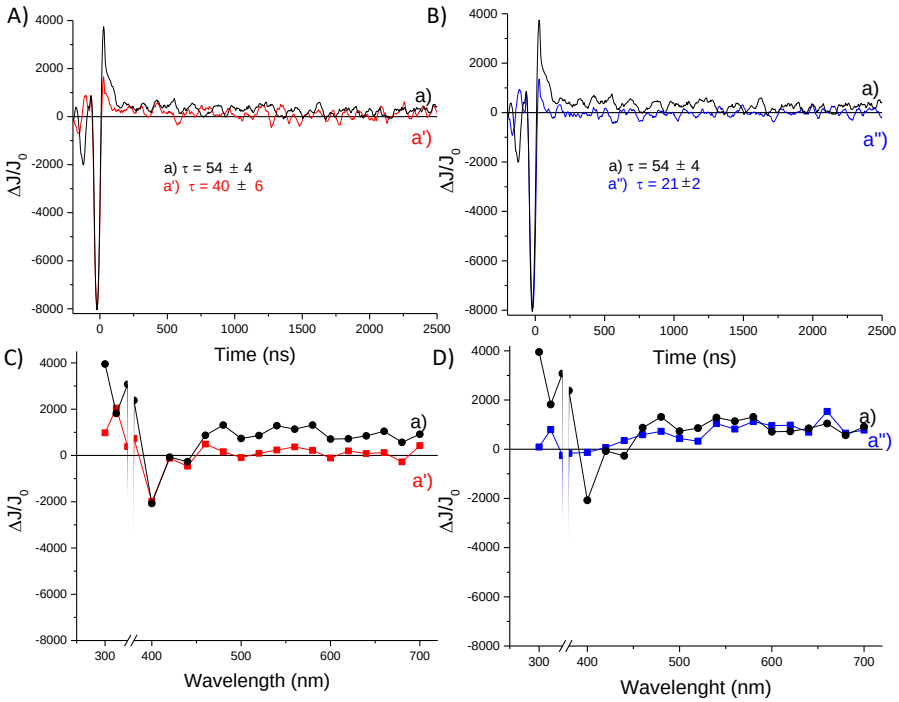

Figure 4.12: Temporal profile of the transient signals monitored at 340 nm recorded upon 355 nm laser excitation for UiO-66(Zr)-NH_2-25@UiO-66(Ce) sample (A, B) under argon atmosphere (a), N_2O atmosphere (a') and in the presence of methanol (a''). Transmission transient absorption spectra of UiO66 (Zr)-NH_2-25@UiO-66(Ce) sample (C, D) recorded at 10 ns after 355 nm laser excitation under argon atmosphere (a) or after the addition of 300 mL of dichloromethane (a') or methanol (a'') for optically matched (absorbance 0.3) suspensions of the heterojunction in acetonitrile.

So, the present results indicate that the UiO-66(Zr)-NH_2@UiO-66(Ce) materials operate under a Type II heterojunction scheme.

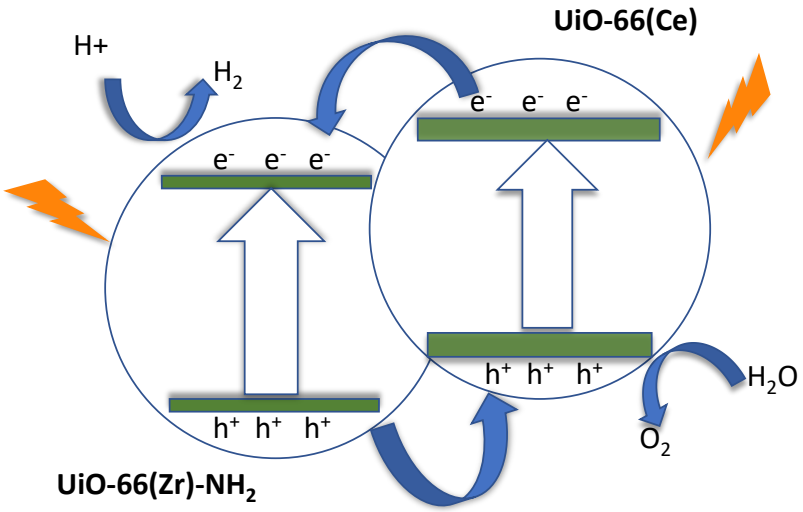

Scheme 4.1: Schematic representation of a type II heterojunction with UiO66 (Zr)-NH_2 and UiO66 (Ce)

In this way, the available data indicates that photoexcitation of the most active UiO-66(Zr)-NH_2-25@UiO-66(Ce) material tested in this study results in the photogeneration of charge-separated state, electrons and holes. The greater effectiveness for the photocatalytic Overall Water Splitting reaction employing the UiO-66(Zr)-NH_2-25@UiO-66(Ce) material could be explained by a lower emission intensity which corresponds to an unfavorable charge recombination process.

4.5 Conclusions

The present study shows the possibility of preparing novel MOF-on-MOF architectures based on UiO-66 topology and their use as superior photocatalyst for the Overall Water Splitting under simulated sunlight irradiation. Characterization data showed that the optimized UiO-66(Zr)-NH_2-25@UiO-66(Ce) sample exhibits a unique band diagram (2.70 eV, HOCO:2.234 eV and LUCO: -0.527 eV values) and favorable photoinduced charge separation for the photocatalytic water splitting respect to their individual parent MOFs. The photocatalytic activity of the optimized UiO-66(Zr)-NH_2-25@UiO-66(Ce) samples is about three times higher than that of

individual UiO-66(Zr)-NH_2 or UiO-66(Ce) for three related reactions including the HER, the OER as well as the Overall Water Splitting under simulated sunlight irradiation. The achieved photoactivity of UiO-66(Zr)-NH_2-25@UiO-66(Ce) without any co-catalyst for the Overall Water Splitting into H_2 (540 μmol g^{-1}) and O_2 (267 μmol g^{-1}) ranks among the most active MOF-based photocatalyst for this purpose. We are confident that this study will help to the development of novel MOF-based photo-catalysts with high activity for the solar-driven photocatalytic Overall Water Splitting.

4.6 References

(1) Li, X.; Yu, J.; Jaroniec, M.; Chen, X. *Chem. Rev.* **2019**, *119*, 3962−4179.

(2) Brockway, P. E.; Sorrell, S.; Semieniuk, G.; Heun, M. K.; Court, V. *Renewable and Sustainable Energy Reviews* **2021**, *141*, 110781.

(3) Shafiee, S.; Topal, E. *Energy Policy* **2009**, *37*, 181-189.

(4) Rissman, J.; Bataille, C.; Masanet, E.; Adene, N.; Morrow III, W. R.; Zhou, N.; Elliott, N.; Dell, R.; Heeren, N.; Huckestein, B.; Cresko, J.; Miller, S. A.; Roy, J.; Fennell, P.; Cremmins, B.; Blank, T. K.; Hone, D.; Williams, E. D.; de la Rue du Can, S.; Sisson, B.; William, M.; Katzenberger, J.; Burtraw, D.; Sethi, G.; Ping, H.; Danielson, D.; Lu, H.; Lorber, T.; Dinkel, J.; Helseth, J. *Appl. Energ.* **2020** *266*, 114848.

(5) Qian, J. X.; Chen, T. W.; Enakonda, L. R.; Liu, D. B.; Basset, J.-M.; Zhou, L. *Int. J. Hydrog. Energ.* **2020**, *45*, 15721-15743.

(6) Kim, J.; Hansora, D.; Sharma, P.; Jang, J.-W.; Lee, J. S. *Chem. Soc. Rev.* **2019**, *48*, 1908-1971.

(7) Lewis, N. S. *Chem. Rev.* **2015**, *115*, 12631-12632.

(8) Lewis, N. S. *Science* **2016**, *351*, 1920.

(9) Fujishima, A.; Honda, K. *Nature* **1972**, *238*, 37-38.

(10) Hisatomi, T.; Domen, K. *Nat. Catal.* **2019**, *2*, 387–399.

(11) Wang, Q.; Domen, K. *Chem. Rev.* **2020**, *120*, 919-985.

(12) Wang, Z.; Li, C.; Domen, K. *Chem. Soc. Rev.* **2019**, 2109-2125.

(13) Dhakshinamoorthy, A.; Asiri, A. M.; García, H. *Angew. Chem. Int. Ed.* **2016**, *55*, 5414-5445.

(14) Nasalevich, M. A.; Van Der Veen, M.; Kapteijn, F.; Gascon, J. *CrystEngComm* **2014**, *16*, 4919-4926.

(15) Qian, Y.; Zhang, F.; Pang, H. *Adv. Func. Mater.* **2021**, *31*, 2104231.

(16) Li, H.; Eddaoudi, M.; O'Keeffe, M.; Yaghi, O. M. *Nature* **1999**, *402*, 276-279.

(17) Férey, G. *Chem. Soc. Rev.* **2008**, *37*, 191-214.

(18) Férey, G.; Mellot-Draznieks, C.; Serre, C.; Millange, F.; Dutour, J.; Surblé, S.; Margiolaki, I. *Science* **2005**, *23*, 2040-2042.

(19) Kitagawa, S.; Kitaura, R.; Noro, S.-I. *Angew. Chem. Int. Ed.* **2004**, *43*, 2334-2375.

(20) Furukawa, H.; Cordova, K. E.; O'Keeffe, M.; Yaghi, O. M. *Science* **2013**, *341*, 1230444.

(21) Gropp, C.; Canossa, S.; Wuttke, S.; Gándara, F.; Li, Q.; Gagliardi, L.; Yaghi, O. M. *ACS Central Science* **2020**, *6*, 1255-1273.

(22) Nguyen, H. L. *Solar RRL* **2021**, *5*, 2100198.

(23) Kampouri, S.; Ebrahim, F. M.; Fumanal, M.; Nord, M.; Schouwink, P. A.; Elzein, R.; Addou, R.; Herman, G. S.; Smit, B.; Ireland, C. P.; Stylianou, K. C. *ACS Appl. Mater. Interfaces* **2021**, *13*, 14239−14247.
(24) An, Y.; Liu, Y.; An, P.; Dong, J.; Xu, B.; Dai, Y.; Qin, X.; Zhang, X.; Whangbo, M.-H.; Huang, B. *Angew. Chem. Int. Ed.* **2017**, *56*, 3036 –3040.
(25) Melillo, A.; Cabrero-Antonino, M.; Navalón, S.; Alvaro, M.; Ferrer, B.; García, H. *Appl. Catal. B. Environ.* **2020**, 278,119345
(26) Remiro-Buenamañana, S.; Cabrero-Antonino, M.; Martínez-Guanter, M.; Álvaro, M.; Navalón, S.; García, H. *Appl. Catal. B. Environ.* **2019**, 677-684.
(27) Salcedo-Abraira, P.; Vilela, S. M. F.; Babaryk, A. A.; Cabrero-Antonino, M.; Gregorio, P.; Salles, F.; Navalón, S.; García, H.; Horcajada, P. *Nano Res.* **2021**, *14*, 450–457.
(28) Salcedo-Abraira, P.; Babaryk, A. A.; Montero-Lanzuela, E.; Oscar R. Contreras-Almengor, O. R.; Cabrero-Antonino, M.; Grape, E. S.; Willhammar, T.; Navalón, S.; Elkäim, E.; García, H.; Horcajada, P. *Adv. Mater.* **2021**, *33*, 2106627.
(29) Sun, D.; Liu, W.; Qiu, M.; Zhang, Y., Li, Z. *Chem. Commun.* **2015**, *51*, 2056-2059.
(30) Lammert, M.; Glißmann, C.; Stock, N. *Dalton Trans.* **2017**, *46*, 2425-2429.
(31) Melillo, A.; García-Vallés, C.; Ferrer, B.; Álvaro, M.; Navalón, S.; García, H. *Org. Biomol. Chem.* **2021**, 19, 794-800
(32) Nagarjun, N.; Concepcion, P.; Dhakshinamoorthy, P. *Appl. Organometal. Chem.* **2020**, *34*, 5578.
(33) Peng, Y.; Rendón-Patiño, A.; Franconetti, A.; Albero, J.; Primo, A.; García, H. *ACS Appl. Energy Mater.* **2020**, *3*, 6623-6632.
(34) Xiao, Y.; Qi, Y.; Wang, X.; Wang, X.; Zhang, F.; Li, C. *Adv. Mater.* **2018**, 1803401.
(35) Striepe, L.; Baumgartner, T. *Chem. Eur. J.* **2017**, *23*, 16924 – 16940.
(36) Ma, X.; Wang, L.; Zhang, Q.; Jiang, H.-L. *Angew. Chem. Int. Ed.* **2019**, *58*, 12175 –12179.

4.7 Supplementary material

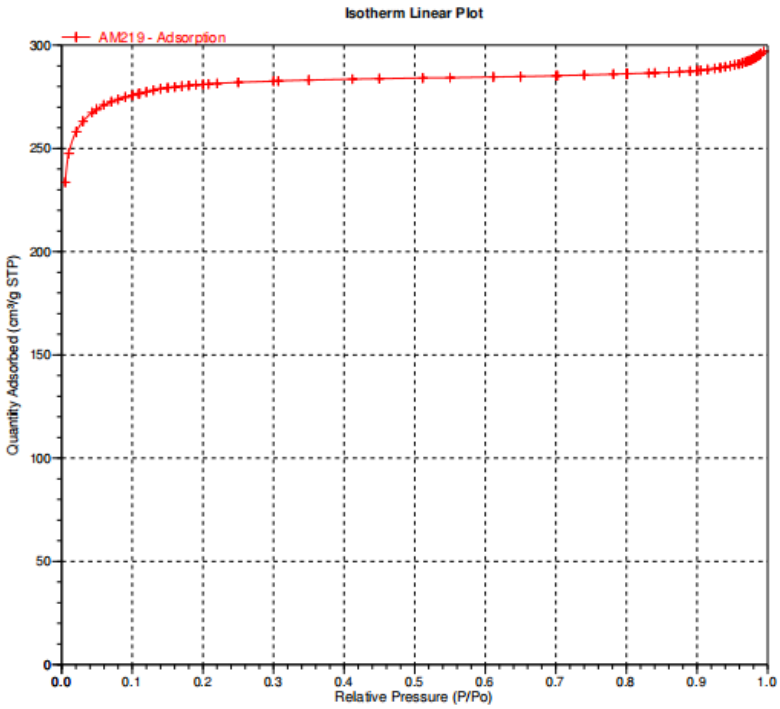

Figure S4.1. Isothermal N2 adsorption at 77 K for UiO-66(Zr)-NH_2

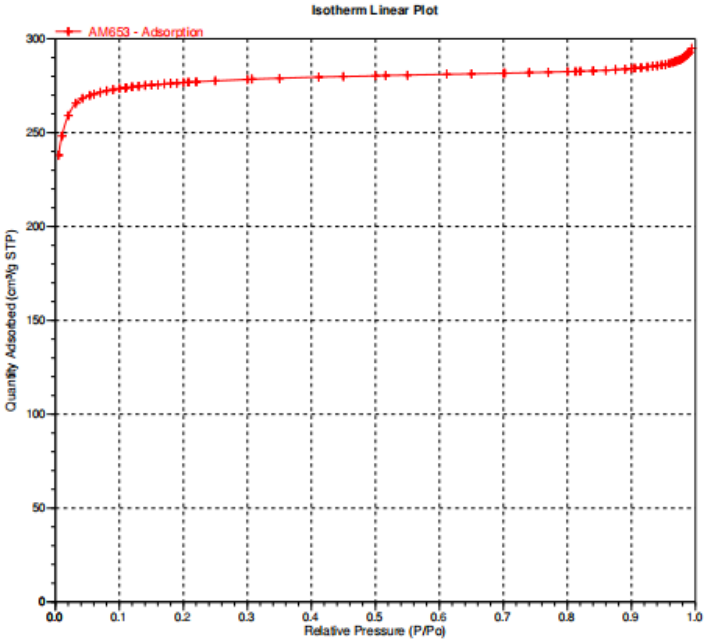

Figure S4.2. Isothermal N2 adsorption at 77 K for UiO-66(Ce).

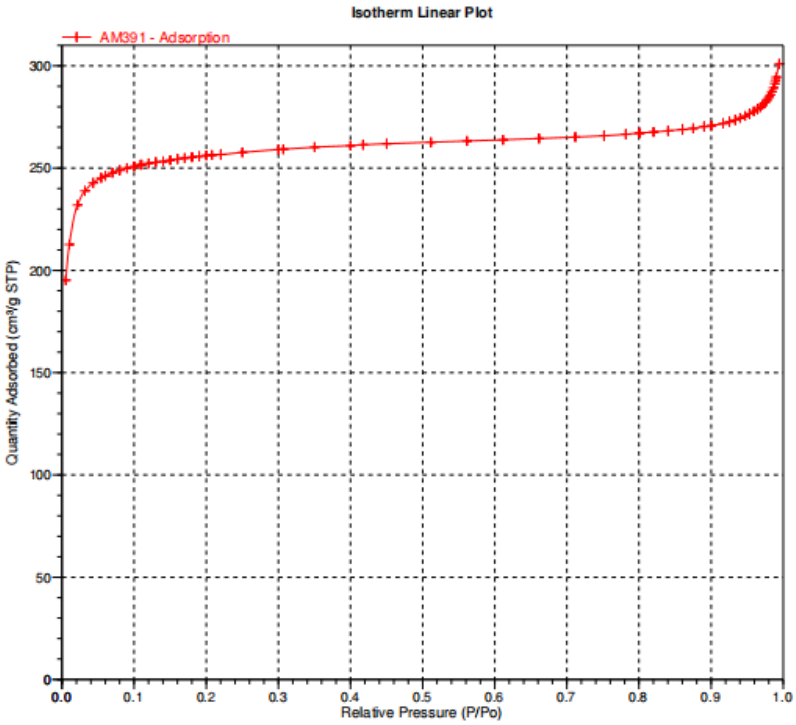

Figure S4.3. Isothermal N2 adsorption at 77 K for UiO-66(Zr)-NH_2-200@UiO-66(Ce)

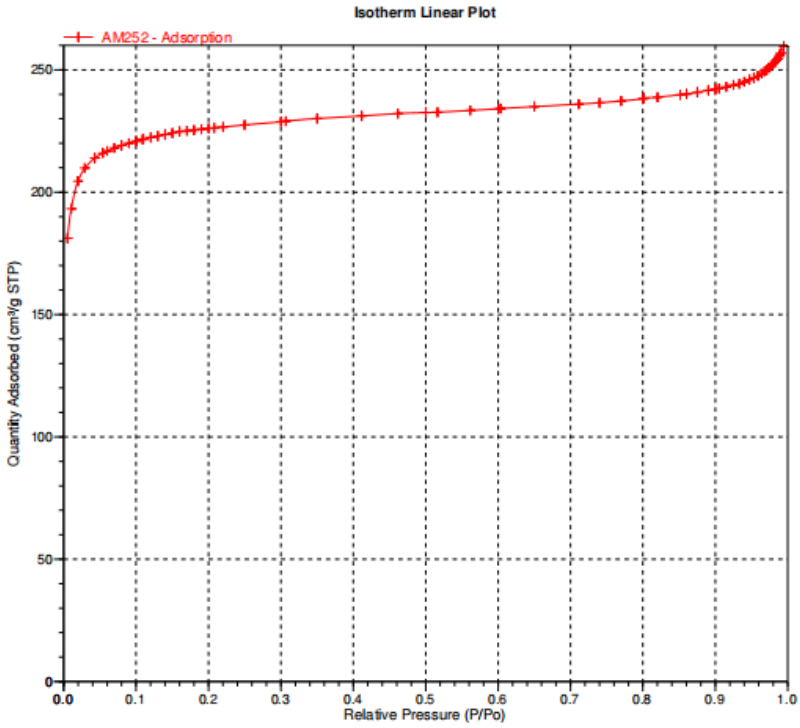

Figure S4.4. Isothermal N2 adsorption at 77 K for UiO-66(Zr)-NH_2-25@UiO-66(Ce)

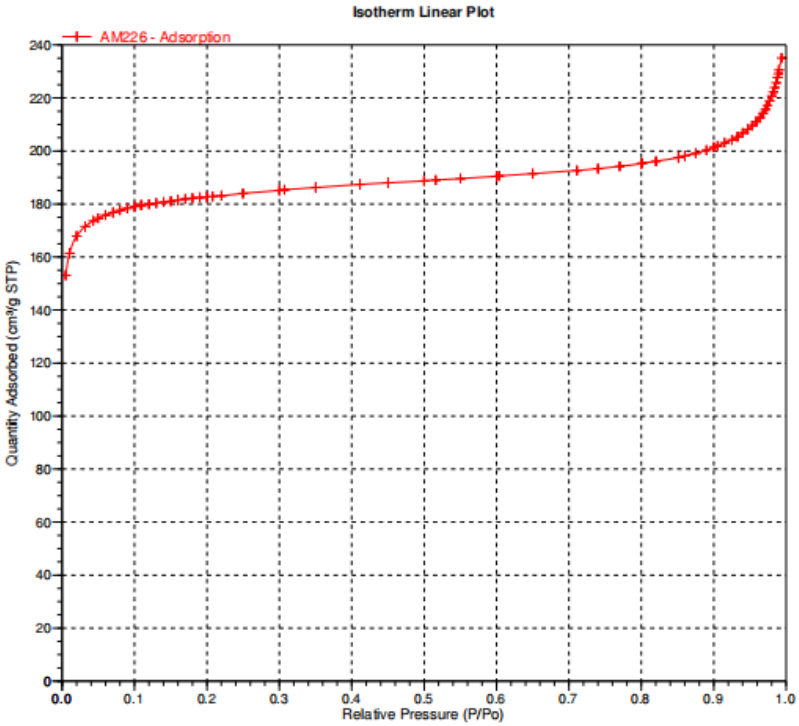

Figure S4.5. Isothermal N2 adsorption at 77 K for UiO-66(Ce)-200@UiO-66(Zr)-NH_2

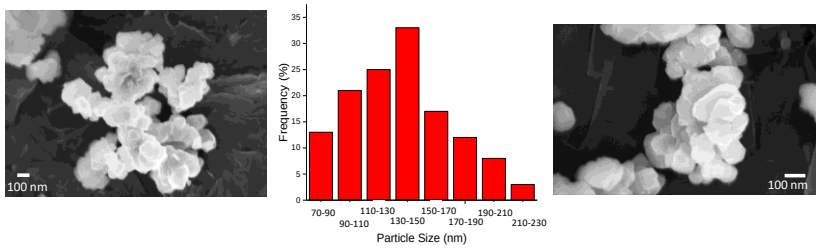

Figure S4.6. HRSEM images and particle size distribution for UiO-66(Zr)-NH_2. Average and standard deviation (nm): 133 ± 45.

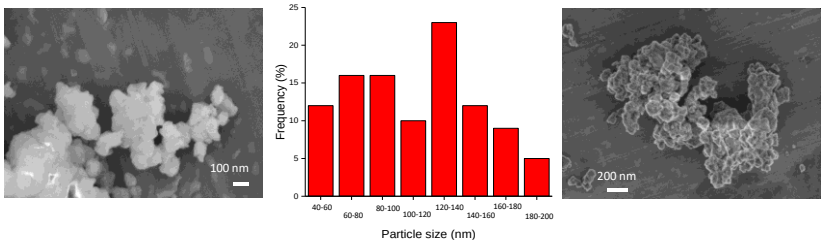

Figure S4.7. HRSEM images and particle size distribution for UiO-66(Ce). Average and standard deviation (nm): 112 ± 46

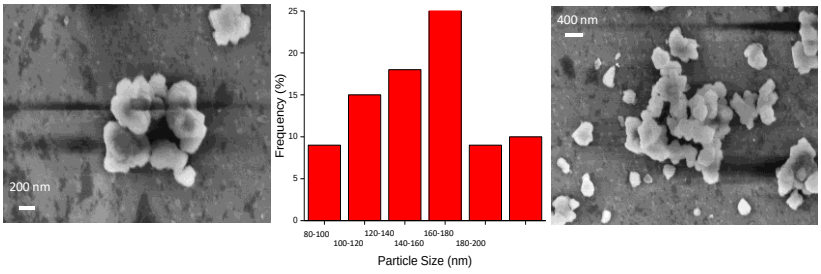

Figure S4.8. HRSEM images and particle size distribution for UiO-66(Zr)-NH_2-200@UiO-66(Ce). Average and standard deviation (nm): 161 ± 80.

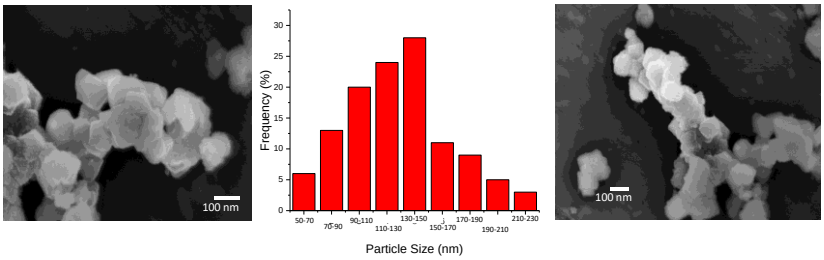

Figure S4.9. HRSEM images and particle size distribution for UiO-66(Zr)-NH_2-25@UiO-66(Ce). Average and standard deviation (nm): 142 ± 44

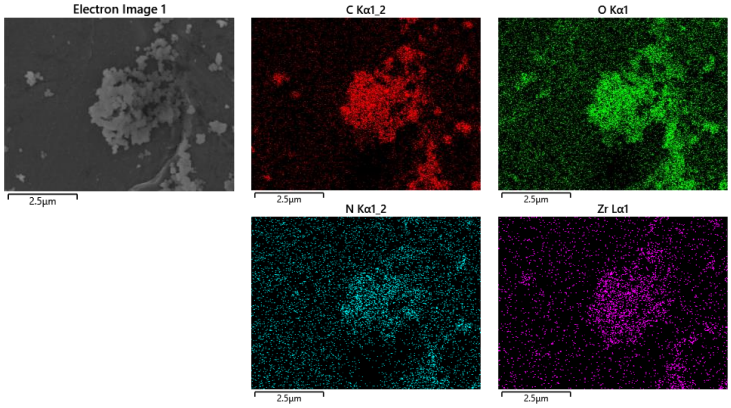

Figure S4.10. SEM image and elemental EDX mapping for UiO-66(Zr)-NH_2.

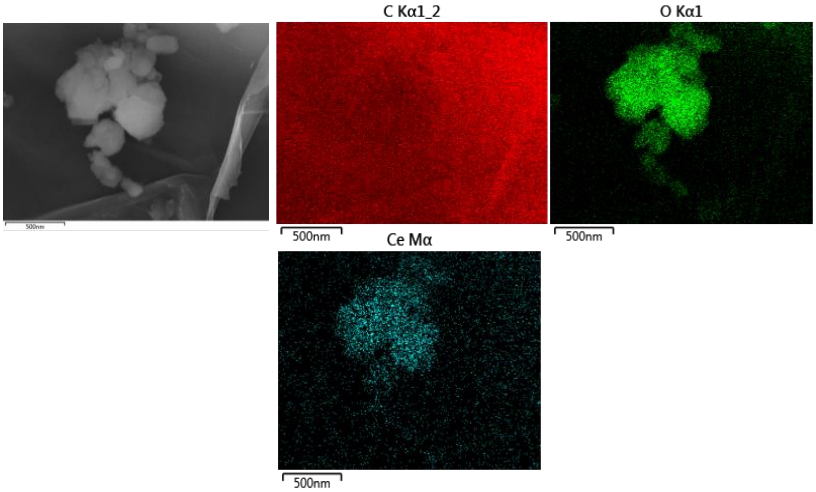

Figure S4.11. SEM image and elemental EDX mapping for UiO-66(Ce).

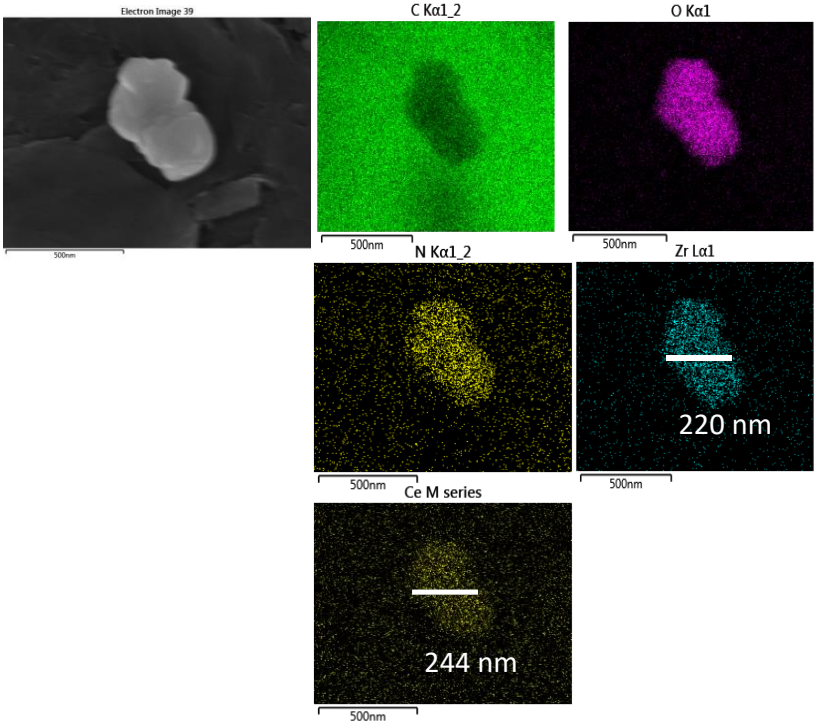

Figure S4.12. SEM image and elemental EDX mapping for UiO-66(Zr)-NH_2-200@UiO-66(Ce).

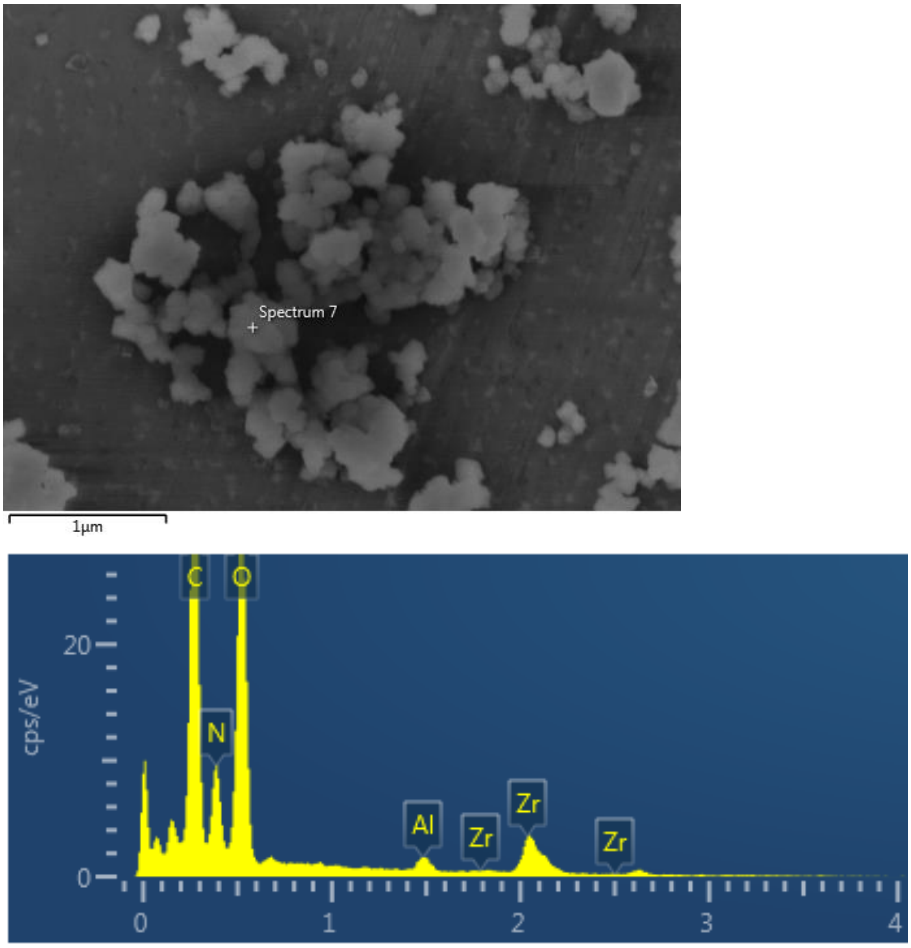

Figure S4.13. SEM image and EDX spectrum of UiO-66(Zr)-NH_2

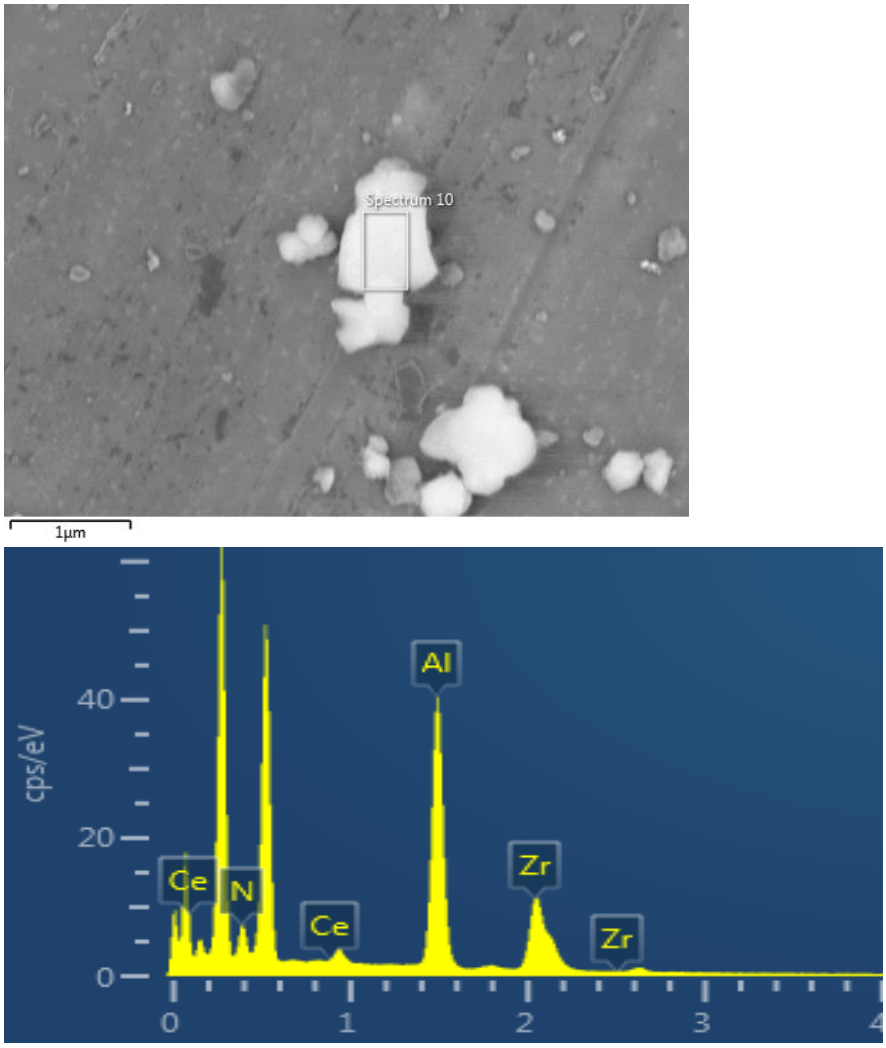

Figure S4.14. SEM image and EDX spectrum of UiO-66(Zr)-NH2-200@UiO-66(Ce)

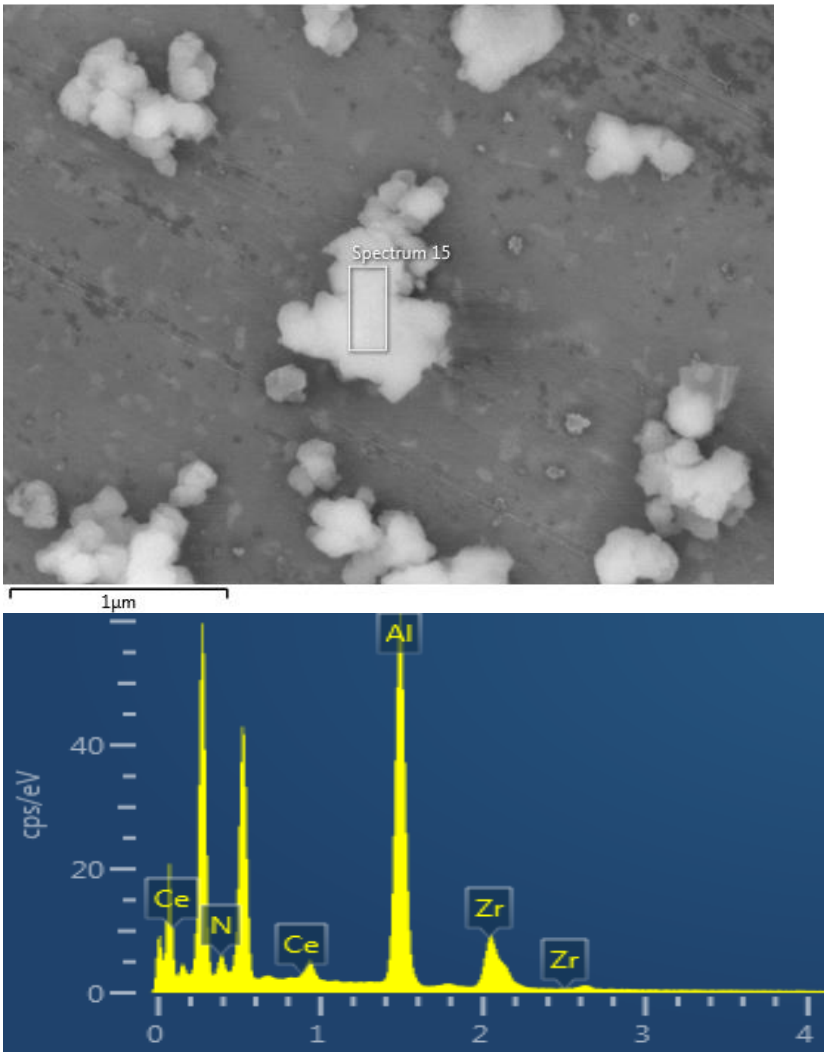

Figure S4.15. SEM image and EDX spectrum of UiO-66(Zr)-NH2-25@UiO-66(Ce)

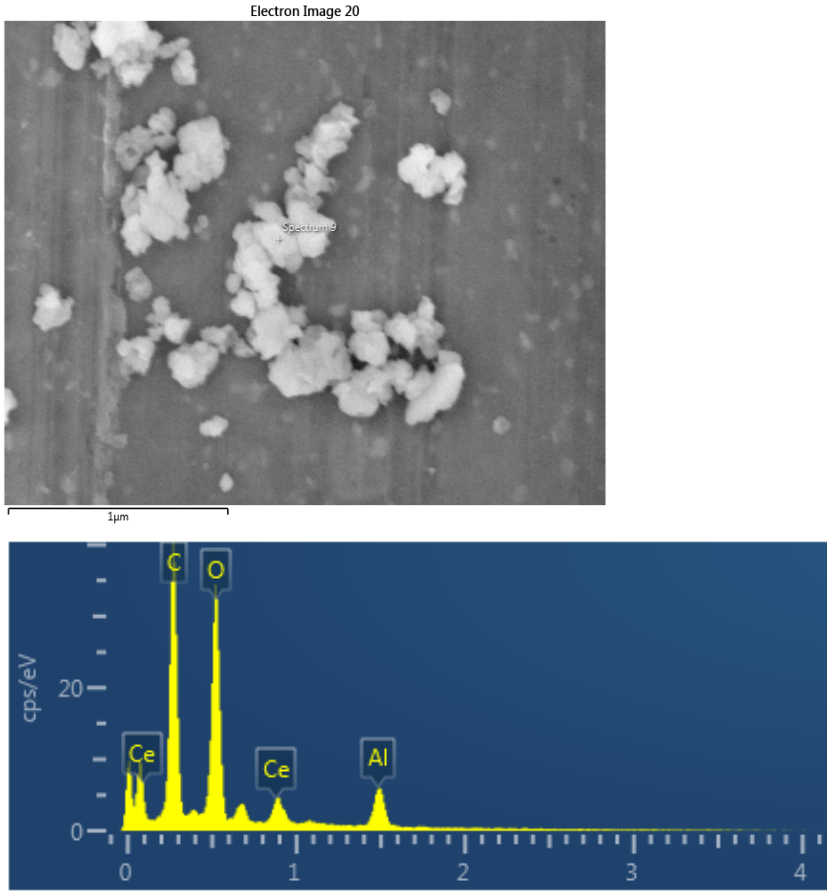

Figure S4.16. SEM image and EDX spectrum of UiO-66(Ce).

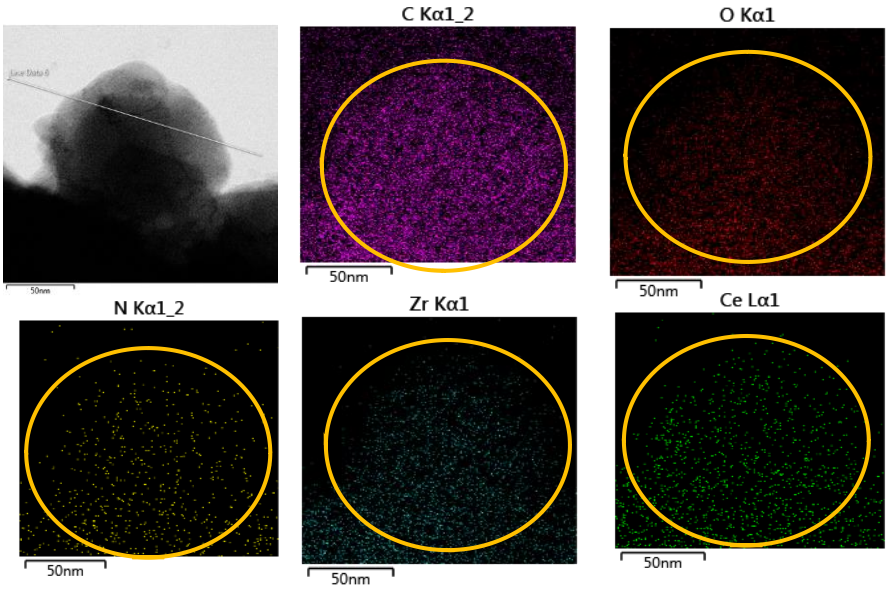

Figure S4.17. TEM images and elemental EDX mapping for UiO-66(Zr)-NH_2-25@UiO-66(Ce).

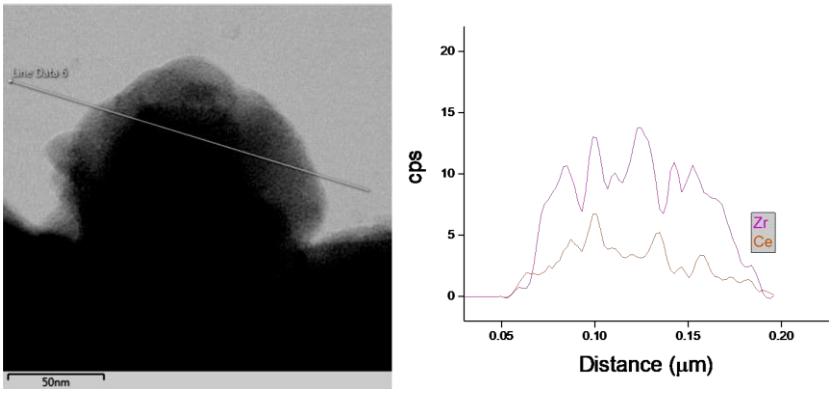

Figure S4.18. TEM image and line scan elemental EDX analyses for UiO-66(Zr)-NH_2-25@UiO-66(Ce).

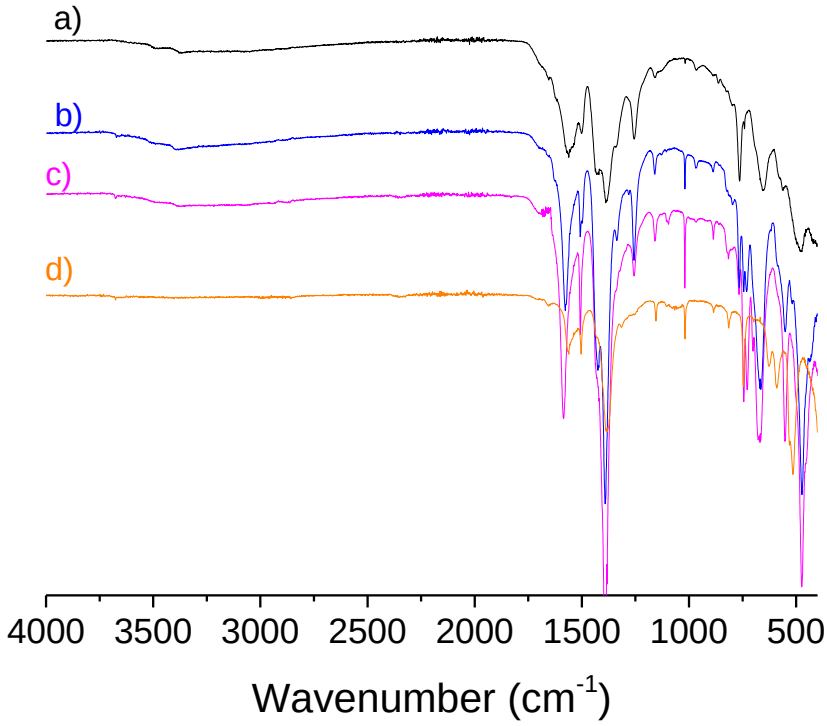

Figure S4.19. FT-IR spectra of UiO66-(Zr) (a), UiO-66(Zr)-NH_2-200@UiO66(Ce) (b), UiO-66(Zr)-NH_2-25@UiO66(Ce) (c) and UiO-66(Ce) (d).

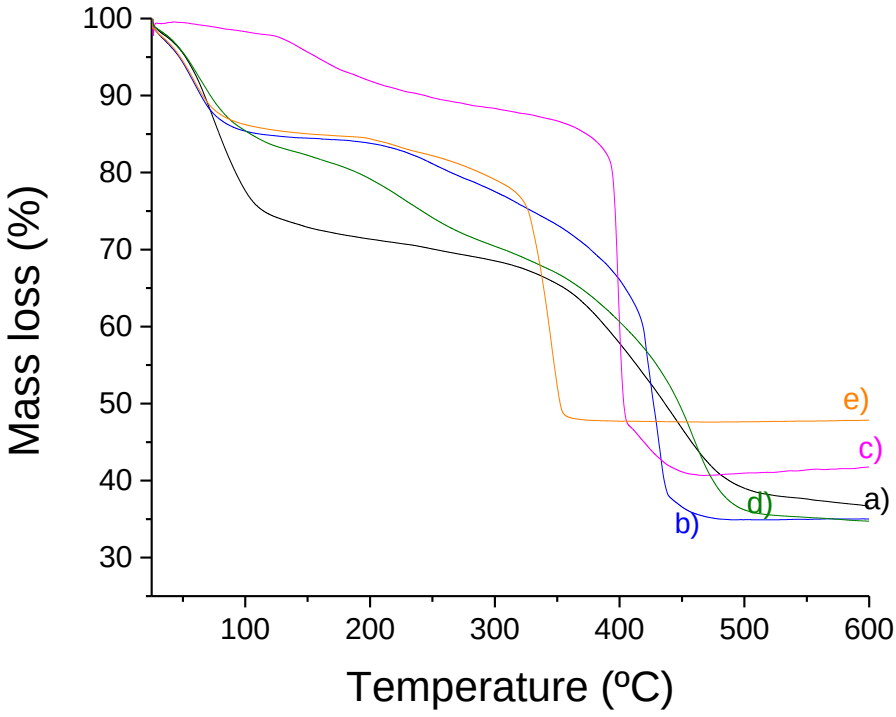

Figure S4.20. TGA analysis of UiO66-(Zr) (a), UiO-66(Zr)-NH_2-200@UiO66(Ce) (b), UiO-66(Zr)-NH_2-25@UiO66(Ce) (c) and UiO-66(Ce) (d).

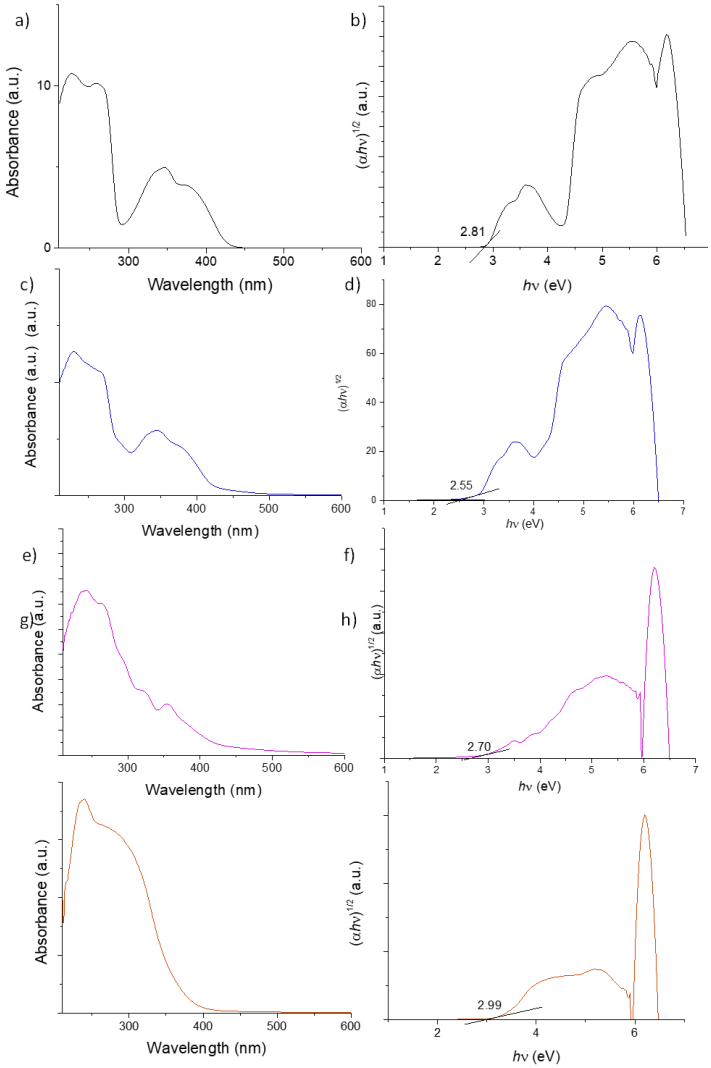

Figure S4.21. UV-Vis diffuse reflectance (a, c, e, g) and Tauc plot (b, d, f, h) of UiO66-(Zr) (a), UiO-66(Zr)-NH_2-200@UiO66(Ce) (b), UiO-66(Zr)-NH_2-25@UiO66(Ce) (c) and UiO-66(Ce) (d).

Chapter 5.

Bifunctional metal–organic frameworks for the hydrogenation of nitrophenol using methanol as the hydrogen source

Arianna Melillo,[a] Cristina García-Vallés,[a] Belén Ferrer,*[a] Mercedes Álvaro,[a] Sergio Navalón*[a] and Hermenegildo García

[a]Departamento de Química, Universitat Politècnica de València, Camino de Vera s/n, Valencia 46022, Spain. E-mail: sernaol@doctor.upv.es, hgarcia@qim.upv.es

[b]Instituto Universitario de Tecnología Química, CSIC-UPV, Universitat Politècnica de València, Av. de los Naranjos, Valencia 46022, Spain

Org. Biomol. Chem., 2021, 19, 794

5.1 Abstract

In this chapter it was reports the reduction of 4-nitrophenol to 4-aminophenol using UiO-66 (Zr) as a bifunctional photocatalyst using methanol as the hydrogen source. In particular, a series of UiO-66 (Zr)-X (X: NH_2, NO_2 and H) and MIL-125 (Ti)-NH_2 catalysts have been screened as bifunctional catalysts for this process. UiO-66 (Zr)-NH_2 was found to be the most active material to promote light-assisted nitro hydrogenation under both UV-Vis and simulated sunlight irradiation. The tandem reaction occurs via hydrogen generation from a water/methanol mixture in the first step and then, reduction of 4-nitro-phenol to 4-aminophenol. UiO-66 (Zr)-NH_2 acts as a truly heterogeneous catalyst and can be reused several times without significant loss of activity, maintaining its crystallinity. This work shows the possibility of using MOFs as solar-driven bifunctional catalysts to promote the hydrogenation of organic compounds using methanol as the hydrogen source.

5.2 Introduction

Metal–organic frameworks (MOFs), in which the lattice is defined by metal nodes held in place by rigid organic linkers forming a crystalline and porous solid, are among the preferred hybrid organic–inorganic catalysts. [1–5] MOFs offer a wide range of active sites including exchangeable coordination positions around the metal ions, acid or basic substituents on the organic linker or active guests incorporated within the empty voids. [6–12] In addition, MOFs may exhibit photo-response and they are among the most active photocatalysts for aerobic oxidations, [13–17] Overall Water Splitting [18–21] and CO_2 reduction [22–26] among other reactions. [27]

The presence of more than one active site makes MOFs very suitable hybrid catalysts to promote tandem reactions in which more than one elementary conversion occurs. [28–31] Included in the numerous examples of MOFs as catalysts for tandem reactions, one type that has received growing interest is those which are used in reactions combining a light-assisted transformation with a dark catalytic reaction. [32,33] One photo-catalytic reaction that is attracting considerable interest due to the possible role of hydrogen as an energy vector and the efficiency of MOFs in comparison to other semiconductors is the photocatalytic hydrogen generation.

In this context, inspired by literature that the ability of MOFs to generate in situ hydrogen could be combined with the use of hydrogen in a hydrogenation reaction, developing a so far unreported tandem reaction. The obvious advantage of this tandem photocatalytic H_2 generation–catalytic hydrogenation would be that no H_2 gas is needed, and the process is easily controlled by on–off switching of light.

In the present chapter, the concept of in situ photo-catalytic H_2 generation to carry out catalytic hydrogenation has been proved using a series of five MOFs with MIL-125 (Ti) and UiO-66 (Zr) structures that are among the most widely studied photocatalysts for H_2 generation. The photocatalytic activity of MIL-125 (Ti)-NH_2, UiO-66 (Zr)-H and UiO-66 (Zr)-NH_2 can be found in the literature. The light-

assisted H_2 generation is combined with frustrated Lewis's acid–base pairs in the MOFs to perform nitro aromatic hydrogenation to aniline that is a process of large industrial importance in the production of polyurethane monomers. It is shown that UiO-66 (Zr)-NH_2 is a reusable and stable heterogeneous catalyst for this light-assisted tandem reaction.

5.3 Experimental section

Materials

Zirconium tetrachloride (>99.5% trace metal basis), terephthalic acid (98%), 2-aminoterephthalic acid, 2-nitroterephthalic acid, 4-nitrophenol and titanium isopropoxide were purchased from Sigma-Aldrich; *N,N′*-dimethylformamide and methanol were supplied by Scharlab.

Catalyst preparation

The list of MOFs employed in this study includes UiO-66 (Zr)-X (X: NH_2, NO_2 and H) and MIL-125 (Ti)-NH_2 were been prepared following previously reported procedures. [20,34,35] The supplementary section reported below contains the detailed procedure for the solvothermal preparation of each solid.

Characterization of the materials

Powder X-ray diffraction (PXRD) patterns were recorded on a Philips XPert diffractometer equipped with a graphite mono- chromator (40 kV and 45 mA) employing Ni-filtered Cu Kα radiation. Isothermal N_2 adsorption measurements have been carried out at 77 K using a Micromeritics ASAP 2010 apparatus. The metal content of each MOF material was determined by ICP-AES analysis after digesting the solids in concentrated nitric acid at 80 °C for 24 h. ATR-FTIR spectra of MOFs were obtained with a Bruker Tensor 27 instrument. Prior to ATR-FTIR measurements, the MOF samples were dried in an oven at 100 °C for 24 h to remove physisorbed water.

Photocatalytic and thermocatalytic experiments

The light-assisted catalytic activity of UiO-66 (Zr)-X (X: NO_2, NH_2 or H) and MIL-125 (Ti)-NH_2 was evaluated for the reduction of 4-nitrophenol (NP) to 4-aminophenol (AP). Briefly, the required catalyst amount (i.e. 5 mg) was introduced into a quartz reactor with a total volume of 51 mL containing a pressure gauge at the outlet and one gas inlet. Figure S5.1 shows a photograph of the photoreactor. Then, a solution of 4-nitro- phenol (0.02 mmol) dissolved in a mixture of water (1.25 mL) and methanol (1.25 mL) was added, and the suspension was subjected to ultrasound for 20 min. Subsequently, the system was purged with Ar for 15 min. The reaction was irradiated by means of an optical fiber with the output of a Xe lamp (150 W) equipped or not with a 1.5 AM filter to simulate sunlight. The course of the reaction was followed by UV-vis spectroscopy (200–800 nm) analyzing diluted reaction aliquots (0.1 mL) in acetonitrile (2.9 mL). Prior to recording the UV-vis spectra, the suspension was filtered using a nylon filter (0.2 μm).

Photocatalytic hydrogen generation in the presence of the MOF was evaluated using the previous procedure described for the photocatalytic reduction using 5 mg of MOF, but in the absence of 4-nitrophenol. The evolving gases were analyzed from the head space, connecting the reactor directly to an Agilent 490 Micro GC system (Molsieve 5 Å column using Ar as the carrier gas) without manual handling. Throughout the experiment, the temperature of the system was monitored, and the pressure was determined by the manometer adapted to the photoreactor chamber.

Catalytic hydrogenation promoted by MOFs (5 mg) for 4-nitrophenol (0.02 mmol) hydrogenation was performed in water–methanol solution using a hydrogen atmosphere (1 bar) at 50 °C.

5.4 Results and discussion

Catalyst preparation

The MOFs under study were prepared by solvothermal synthesis following previously reported procedures. [20,34,35] Figure 5.1 (a1 and a2) compare the experimental PXRD patterns recorded for the UiO66 series and MIL-125 (Ti)-NH_2 with the simulated pattern showing the coincidence between the two. PXRD patterns confirm the successful formation of the crystalline MIL-125 (Ti)-NH_2 [36] material as well as that of isostructural UiO-66 (Zr)-H, UiO-66 (Zr)-NH_2 and UiO-66 (Zr)-NO_2 solids. (Figure 5.1a1 and a2). [37–39]

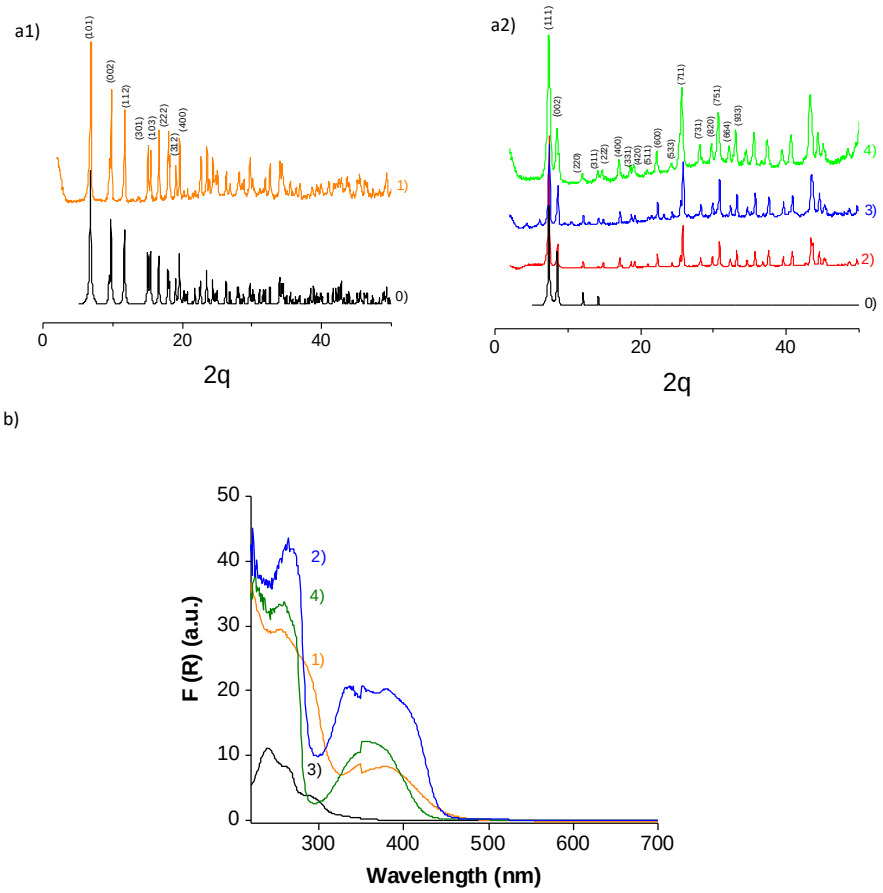

Figure 5.1: Simulated (0) and experimental PXRD (a1 and a2) and diffuse reflectance UV-vis spectra (b) of MIL-125 (Ti)-NH_2 (1), UiO-66 (Zr)-NH_2 (2), UiO-66 (Zr)-H (3) and UiO-66 (Zr)-NO_2 (4).

The difference of UIO-66, UiO-66 (Zr)-NH_2, UiO-66 (Zr)-H and UiO-66 (Zr)-NO_2 in the XRD patterns has been marked in Figure S5.2. As can be observed, the main peak is slightly shifted to the right for UiO-66 (Zr)-NH_2 and to the left for UiO-66 (Zr)-NO_2. Diffuse reflectance UV-Vis spectroscopy of the series of MOFs under study confirms the bathochromic shift in the absorption spectrum of the parent MIL-125 (Ti) and UiO-66 (Zr) materials due to the presence of $–NH_2$ or $–NO_2$ groups in the terephthalate linker (Figure 5.1b).[36–39] Tauc plots derived from optical

measurements allow the estimation of the values of 2.71, 3.11, 2.72 and 2.82 eV for the band gaps of MIL-125 (Ti)-NH_2, UiO-66 (Zr)-H, UiO-66 (Zr)-NH_2 and UiO-66 (Zr)-NO_2, respectively. These band gap values are in good agreement with the literature reported values (Figure S5.3). [20,21,40]

FT-IR spectroscopy reports the nature of the different functional groups present on the terephthalate ligand of the MOF samples by monitoring the characteristic vibrational peaks associated with COO– (1582 and 1391 cm^{-1}), –NH_2 (3482 and 3386 cm^{-1}) and –NO_2 (1500 and 1380 cm^{-1}) (Figure S5.4–7).

The BET surface area and pore volumes of the MOFs under study were determined by isothermal N_2 adsorption measurements at 77 K (Table 5.1 and Figure S5.8–S5.11).

Table 5.1 List of MOFs employed as bifunctional catalysts in this work together with some relevant porosity and analytical data

Entry	Theoretical MOF formula	BET surface area ($m^2 g^{-1}$)	Pore volume ($cm^3 g^{-1}$)	Theoretical (%)/experimental metal content (%)
MIL-125(Ti)-NH_2	$Ti_8O_8(OH)_4(C_6H_3C_2O_4NH_2)_6$	1200	0.57	23.0/21.7
UiO-66(Zr)-H	$Zr_6O_4(OH)_4(OOC\text{-}C_6H_4\text{-}COO)_6$	1368	0.80	32.8/31.6
UiO-66(Zr)-NH_2	$Zr_6O_4(OH)_4(OOC\text{-}C_6H_3NH_2\text{-}COO)_6$	923	0.91	31.2/30.9
UiO-66(Zr)-NO_2	$Zr_6O_4(OH)_4(OOC\text{-}C_6H_3NO_2\text{-}COO)_6$	903	0.66	28.2/27.4

These values are in general agreement with previous reports, indicating the porosity decrease due to the presence of the NH_2 or NO_2 substituents of the terephthalate ligand occupying some internal space in comparison to the values of the parent UiO-66 (Zr)-H. ICP-AES analyses of previously acid-digested MOFs are in good agreement with the theoretical Ti or Zr content, respectively, for the MIL-125 (Ti)-NH_2 or UiO-66 (Zr)-X materials under study. A summary of the characterization data is provided in Table 5.1 The morphology of the particles has been studied by HRSEM. Figure S5.12 shows the HRSEM images and particle size distribution obtained for the MOFs under study. The average particle size values obtained for the

different MOFs, summarized in Table S5.1, are in the same range. Therefore, it can be concluded that the particle size will not be a determining factor in the catalytic activity of the MOFs. The morphology of the particles has also been studied by TEM. Figure S5.13 shows the TEM images of the different MOFs.

Tandem light-assisted H2 generation-hydrogenation reaction

The activity of the MOFs under study as bifunctional catalysts in the tandem reaction was evaluated for the reduction of 4-nitrophenol to 4-aminophenol using methanol as the hydrogen source. The tandem process involves the photocatalytic H_2 generation from methanol and subsequent hydrogenation of the nitro group.

In the first step, light absorption leads to electron/hole separation in the conduction/valence bands, resulting in H_2 evolution from methanol as the sacrificial agent. Four materials, namely, MIL-125 (Ti)-NH_2, UiO-66 (Zr)-H and UiO-66 (Zr)-NH_2, have been reported as photocatalysts for H_2 generation from methanol. The second step, that make use of MIL-125 (Ti)-NH2 and UiO-66 (Zr)-X in the absence of any metal nanoparticles as the hydrogenation catalyst has not been previously disclosed.

Preliminary control experiments reveal that the photo-catalytic hydrogen generation from methanol or 4-nitrophenol hydrogenation does not occur in the absence of a MOF. An additional control experiment reveals that p-nitrophenol reduction to p-aminophenol does not occur upon MOF irradiation in the absence of methanol. This result agrees with the higher photocatalytic H_2 production using MOFs as photo-catalysts in the presence of electron donors such as MeOH as the sacrificial agent in comparison [13,41–45] to their photo- catalytic activity in pure water (Overall Water Splitting). [20,21] In contrast to the controls, UV-Vis irradiation of the MOFs in H_2O-CH_3OH solvent promoted in all cases the reduction of 4-nitrophenol to 4-aminophenol (Figure 5.2).

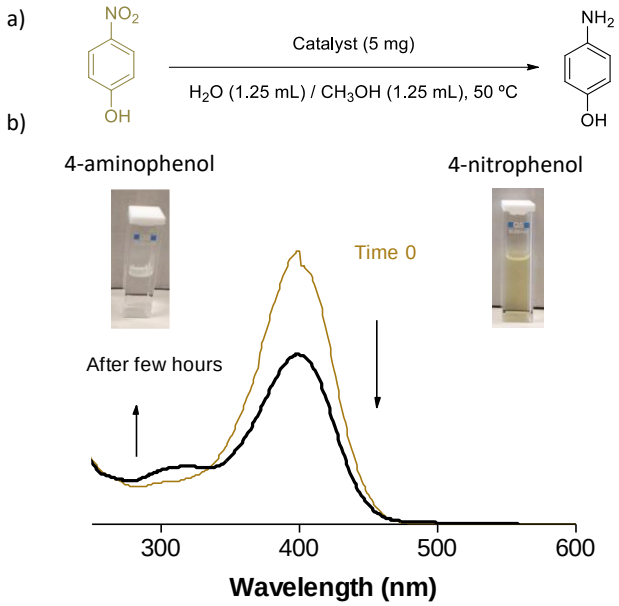

Figure 5.2 (a) Photocatalytic or thermocatalytic 4-nitrophenol reduction to 4-aminophenol using MOFs. (b) Changes in the transmission UV-vis absorption spectrum upon irradiation of 4-nitrophenol in water–methanol in the presence of MIL-125 (Ti)-NH_2. The insets correspond to the photographs of the cuvette before and after irradiation showing the variation of the visual appearance.

The temporal evolution of the light-assisted, tandem reaction depended on the nature of the MOF. The most active bifunctional catalyst in this study both under UV-Vis and simulated sunlight irradiation was UiO-66 (Zr)-NH_2 (Figure 5.3). An optimal amount of 5 mg of UiO-66 (Zr)-NH_2 was determined for 1.25 mL+ 1.25 mL H_2O-CH_3OH solution of *p*-nitrophenol (0.02 mmol) (Figure S5.14).

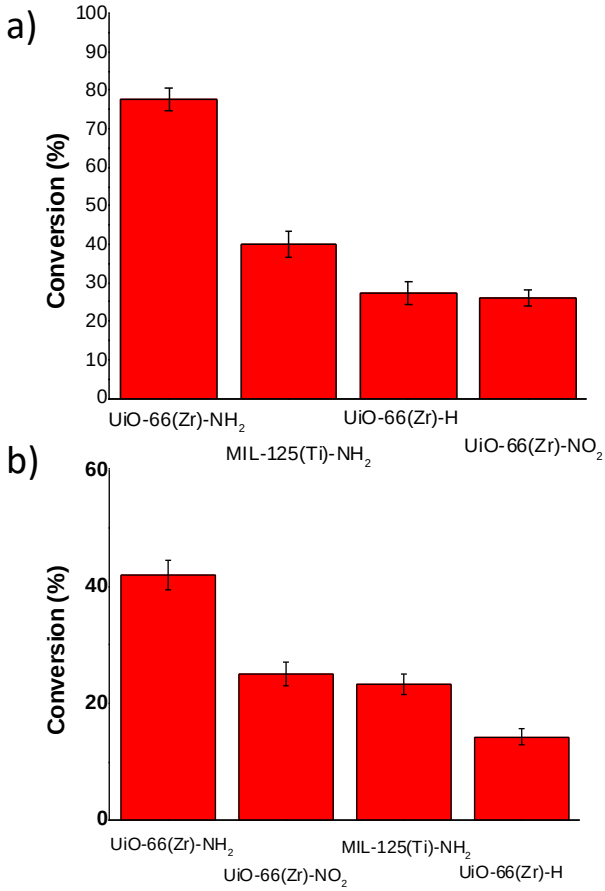

Figure 5.3 Light-assisted 4-nitrophenol hydrogenation to 4-aminophenol using methanol as the hydrogen source under UV-vis irradiation from a Xe lamp (a) or simulated sunlight irradiation (b) using MOFs. Reaction conditions: catalyst (5 mg), p-nitrophenol (0.02 mmol), solvent (H_2O: MeOH, 1.25 mL: 1.25 mL), photoreactor volume (51 mL), Xe lamp (150 W) with or without a 1.5AM filter, 50 °C.

A lower and higher catalyst amount either diminishes the number of active centers or increases the turbidity of the reaction medium hampering light penetration, respectively.

The higher efficiency of UiO-66 (Zr)-NH_2 as the bifunctional catalyst derives from its higher photocatalytic activity in H_2 generation under UV-Vis or simulated sunlight. This higher photocatalytic activity of UiO-66 (Zr)-NH_2 with respect to

UiO-66 (Zr)-H and UiO-66 (Zr)-NO_2 can be explained as a combination of enhanced visible-light absorption and its more negative lower unoccupied crystal orbital (LUCO) potential favoring H^+ reduction (Figure 5.4).[46,47]

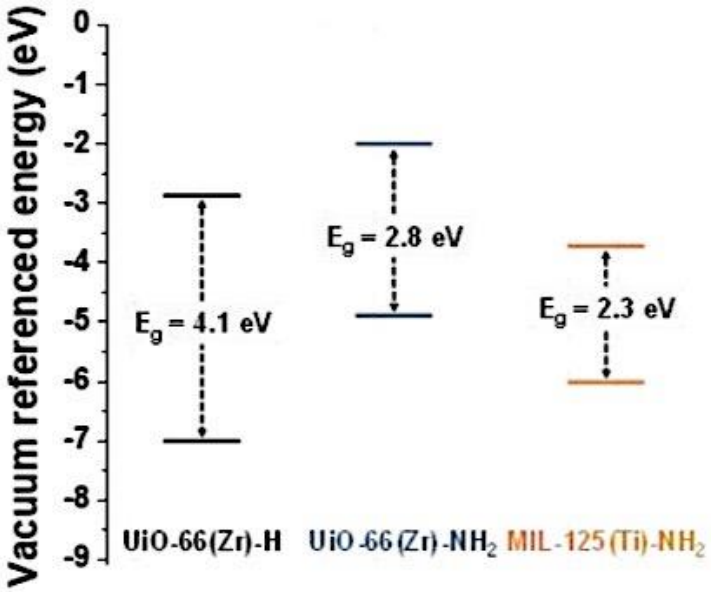

Figure 5.4 Energy band positions for MIL-125 (Ti)-NH_2, UiO-66 (Zr) and UiO-66 (Zr)-NH_2.

The higher photoactivity of UiO-66 (Zr)-NH_2 with respect to MIL-125 (Ti)-NH_2 can also be explained considering the lower LUCO value of the former (Figure 5.4).[46,47] Independent measurements of photocatalytic H_2 evolution in CH_3OH in the absence of 4-nitrophenol showed that the photocatalytic H_2 production by UiO-66 (Zr)- NH_2 (15.5 μmol g^{-1} h^{-1}) is higher than that by MIL-125 (Ti)- NH_2 (<5 μmol g^{-1} h^{-1}) upon UV-Vis irradiation for 5 h. These values agree with the relative activity order in the tandem p-nitrophenol reduction to p-aminophenol observed for UiO-66 (Zr)-NH_2 with respect to MIL-125 (Ti)-NH_2, both having amino substituents.

The variation in the relative activity order upon simulated solar light irradiation in favor of UiO-66 (Zr)-NO_2 with respect to UiO-66 (Zr)-H is due to the enhanced

visible light absorption of UiO-66 (Zr)-NO_2 derived from the presence of the NO_2 group (Figure 5.1).

The photocatalytic reaction of p-nitrophenol to p-amino- phenol using methanol as the hydrogen carrier is a tandem reaction that occurs in two steps. The first step is the photo-catalytic hydrogen generation upon MOF photoexcitation using methanol as the electron donor. Subsequently, H_2 should be activated by the MOFs. To study this step, additional experiments of 4-nitrophenol reduction were carried out, in the dark, using H_2 as the reagent at 50 °C. Figure 5.5 shows the relative catalytic activity of the series of the four MOF samples on the thermo catalytic 4-nitrophenol reduction to 4-aminophenol by H_2.

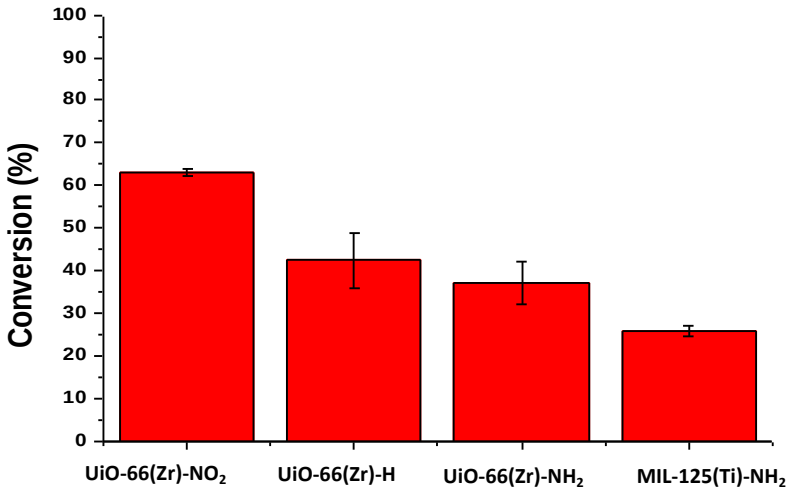

Figure 5.5 Catalytic hydrogenation of 4-nitrophenol to 4-aminophenol by molecular H_2 promoted by MOFs. Reaction conditions: catalyst (5 mg), *p*-nitrophenol (0.02 mmol), solvent (H_2O: MeOH, 1.25 mL: 1.25 mL), reactor volume (51 mL), temperature 50 °C.

Interestingly, all the MOFs exhibit catalytic hydrogenation activity, the most active MOF being the UiO-66 (Zr)-NO_2, followed by UiO-66 (Zr)-H and UiO-66 (Zr)-NH_2.

This trend in activity follows the order of Lewis acid strength of metal nodes in UiO-66 (Zr)-X (X: NO_2, H or NH_2) due to the inductive effect of substituents on the terephthalate linker that has been previously observed in Lewis's acid-catalyzed reactions. [48] Thus, catalytic data indicate that the higher the Lewis acidity of the metal nodes, the higher the hydrogenating activity. It is likely that a higher Lewis acid strength enhances H_2 polarization and, therefore, activates molecular H_2 towards the formation of metal-hydride species responsible for the reduction of 4-nitrophenol to 4-aminophenol. [49] Accordingly, it is proposed that frustrated Lewis's acid–base pairs in UiO-66 (Zr)- X (X: NO_2, H or NH_2) are the sites to activate H_2 molecules forming a metal hydride and protonating basic sites.

According to the relative reaction rates, it appears that photocatalytic H_2 evolution is the slowest elementary reaction controlling the overall efficiency of the bifunctional catalysts.

The most active UiO-66 (Zr)-NH_2 sample for the light- assisted reduction of 4-nitrophenol to 4-aminophenol was reused several times without a significant decrease of activity and maintaining its crystallinity as revealed by PXRD (Figure 5.6).

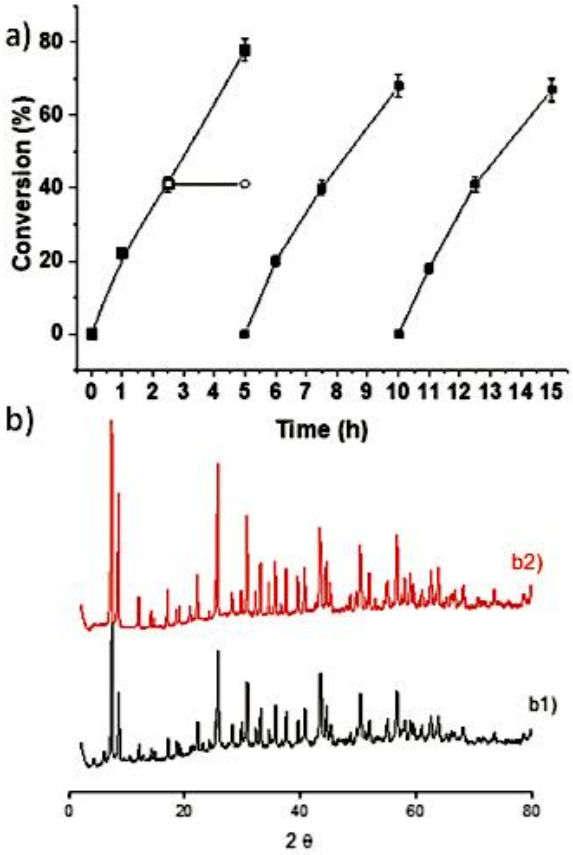

Figure 5.6 (a) Reusability of UiO-66 (Zr)-NH_2 as the solid catalyst for the UV-Vis light-assisted reduction of 4-nitrophenol to 4-aminophenol using methanol as the hydrogen source. The empty circle in the first run corresponds to an independent experiment in which the catalyst was filtered off at 2 h. (b) Comparison of the PXRD patterns of the fresh (b1) and three-times used (b2) UiO-66 (Zr)-NH_2 sample. Reaction conditions: catalyst (5 mg), p-nitrophenol (0.02 mmol), solvent (H_2O : MeOH, 1.25 mL : 1.25 mL), photoreactor volume (51 mL), Xe lamp (150 W), 50 °C.

Importantly, if the photocatalyst is removed once the reaction has started and the system allowed to react further under the same reaction conditions, but in the absence of any solid, 4-nitrophenol conversion stops. This observation indicates that the process is heterogeneous, ruling out the empty contribution of leached species to the tandem reaction. The BET surface area values of the tested MOFs after catalysis, calculated from the N_2 isotherms, are summarized in Table S5.2. No significant changes have occurred in the surface value of the MIL-125 (Ti)-NH_2 MOF during

the catalytic process. The decrease in the surface area for the UiO-66 (Zr) series MOFs after catalysis is more notable and probably indicates the strong adsorption of methanol oxidation products or phenolic compounds within the pores.

5.5 Conclusions

It has been shown that MOFs can promote the hydrogenation of *p*-nitrophenol using methanol as the hydrogen source. The tandem process requires light to promote the photocatalytic hydrogen generation, followed by frustrated Lewis's acid–base pair activation of molecular hydrogen. It has been found that while H_2 activation is enhanced by electron withdrawing substituents, the controlling step in the tandem reaction is the light-assisted hydrogen generation from methanol. Accordingly, the most efficient catalyst found was UiO-66 (Zr)- NH_2 that combines a more negative LUCO reduction potential and enhanced visible light absorption due to the bathochromic influence of the amino substituent. UiO-66 (Zr)-NH_2 was stable under the reaction conditions and can be reused without observing a loss of its catalytic activity. The present study shows the potential of photocatalytic H_2 generation under favorable conditions to perform the hydrogenation of organic compounds in the absence of molecular H_2 by developing a tandem process, requiring frustrated Lewis's acid–base pairs.

5.6 References

1. T. Devic and C. Serre, *Chem. Soc. Rev*., **2014,** 43, 6097–6115.
2. G. Férey, *Chem. Soc. Rev*., **2008**, 37, 191–214.
3. S. Kitagawa, R. Kitaura and S.-I. Noro, *Angew. Chem., Int. Ed*., **2004**, 43, 2334–2337.
4. H. Furukawa, K. E. Cordova, M. O'Keeffe and O. M. Yaghi, *Science*, **2013**, 341, 1230444.
5. H. García and S. Navalón, Metal-Organic Frameworks: Applications in Separations and Catalysis, *Wiley*, **2018**, ISBN: 978-3-527-80910-3.
6. S. M. Cohen, *Chem. Sci*., **2010**, 1, 32–36.
7. F. Vermoortele, M. Vandichel, B. V. de Voorde, R. Ameloot, M. Waroquier, V. Van Speybroeck and D. E. De Vos, *Angew. Chem., Int. Ed*., **2012**, 51, 4887–4890.
8. A. Santiago-Portillo, J. F. Blandez, S. Navalón, M. Álvaro and H. García, *Catal. Sci. Technol*., **2017**, 7, 1351–1362.
9. A. Santiago-Portillo, S. Navalón, P. Concepción, M. Álvaro and H. García, *ChemCatChem*, **2017**, 9, 2506–2511.
10. A. Dhakshinamoorthy, A. Santiago-Portillo, A. M. Asiri and H. Garcia, *ChemCatChem*, **2019**, 11, 899–923.
11. R. Zou, P.-Z. Li, Y.-F. Zeng, J. Liu, R. Zhao, H. Duan, Z. Luo, J.-G. Wang, R. Zou and Y. Zhao, *Small*, **2016**, 12, 2334– 2343.
12. Q. Sun, M. Liu, K. Li, Y. Han, Y. Zuo, F. Chai, C. Song, G. Zhang and X. Guo, *Inorg. Chem. Front*., **2017**, 4, 144– 153.
13. A. Dhakshinamoorthy, A. M. Asiri and H. García, *Angew. Chem., Int. Ed.,* **2016**, 55, 5414–5445.
14. J. Tu, X. Zeng, F. Xu, X. Wu, Y. Tian, X. Hou and L. Long, *Chem. Commun.*, **2017**, 53, 3361–3364.
15. S.-N. Zhao, G. Wang, D. Poelman and P. Van Der Voort, *Molecules*, **2018**, 23, 2947.
16. D. Sun, L. Ye and Z. Li, *Appl. Catal., B*, **2015**, 164, 428– 432.
17. A. Santiago-Portillo, H. G. Baldoví, E. Carbonell, S. Navalón, M. Álvaro, H. García and B. Ferrer, *J. Phys. Chem. C*, **2018**, 122(51), 29190–29199.
18. H. Luo, Z. Zeng, G. Zeng, C. Zhang, R. Xiao, D. Huang, C. Lai, M. Cheng, W. Wang, W. Xiong, Y. Yang, L. Qin, C. Zhou, H. Wang, Y. Zhou and S. Tian, *Chem. Eng. J*., **2019**, 123196.
19. Y. Shi, A.-F. Yang, C.-S. Cao and B. Zhao, Coord. *Chem. Rev*., **2019**, 390, 50–75.
20. S. Remiro-Buenamañana, M. Cabrero-Antonino, M. Martínez-Guanter, M. Álvaro, S. Navalón and H. García, *Appl. Catal., B*, **2019**, 254, 677–684.
21. A. Melillo, M. Cabrero-Antonino, S. Navalón, M. Álvaro, B. Ferrer and H. García, *Appl. Catal., B***, 2020**, 278, 1193452.

22. Y. Lee, S. Kim, J. K. Kang and S. M. Cohen, *Chem. Commun*., **2015**, 51, 5735–5738.
23. I. I. Alkhatib, C. Garlisi, M. Pagliaro, K. Al-Ali and G. Palmisano, *Catal. Today*, **2020**, 340, 209–224.
24. R. Li, W. Zhang and K. Zhou, *Adv. Mater*., **2018**, 30, 1705512.
25. X. Pan, H. Xu, X. Zhao and H. Zhang, *ACS Sustainable Chem. Eng*., **2020**, 8, 1087–1094.
26. H. Zhang, H. Xu, Y. Li and Y. Su, *Appl. Mater. Today*, **2020**, 19, 100609.
27. J. Wang, H. Xu, Ch. Ao, X. Pan, X. Luo, S. Wei, Z. Li, L. Zhang, Z. Xu and Y. Li, *Science*, **2020**, 23, 101233.
28. Y.-B. Huang, J. Liang, X.-S. Wang and R. Cao, *Chem. Soc. Rev*., **2017**, 46, 126–157.
29. C. Vallés-García, A. Santiago-Portillo, M. Álvaro, S. Navalón and H. García, *Appl. Catal., A*, **2020**, 590, 117340.
30. X. Liao, W. Wei, Y. Zhou, M. Zhang, Y. Cai, H. Liu, Y. Yao, S. Lu and Q. Haoa, *Catal.: Sci. Technol*., **2020**, 10, 1015– 1022.
31. Y. Hu, J. Zhang, H. Huo, Z. Wang, X. Xu, Y. Yang, K. Lin and R. Fan, *Catal.: Sci. Technol*., **2020**, 10, 315–322.
32. D. Wang and Z. Li, *Catal.: Sci. Technol*., **2015**, 5, 1623– 1628.
33. Y. Wang, S. Yuan, K. Y. Wang, J. L. Li, G. S. Day, D. Qiu, L. Cheng, W. M. Chen, S. T. Madrahimov and H. C. Zhou, *ACS Catal*., **2019**, 9(6), 5111–5118.
34. A. Santiago-Portillo, S. Navalón, M. Álvaro and H. García, *J. Catal*., **2018**, 365, 450–463.
35. J. F. Blandez, A. Santiago-Portillo, S. Navalón, M. Giménez- Marqués, M. Álvaro, P. Horcajada and H. García, *J. Mol. Catal. A: Chem*., **2016**, 425, 332–333.
36. M. A. Nasalevich, R. Becker, E. V. Ramos-Fernandez, S. Castellanos, S. L. Veber, M. V. Fedin, F. Kapteijn, J. N. H. Reek, J. I. van der Vlugt and J. Gascon, *Energy Environ. Sci*., **2015**, 8, 364–375.
37. L. Shen, R. Liang, M. Luo, F. Jing and L. Wu, *Phys. Chem. Chem. Phys*., **2015**, 17, 117–121.
38. M. Kandiah, M. H. Nilsen, S. Usseglio, S. Jakobsen, U. Olsbye, M. Tilset, C. Larabi, E. A. Quadrelli, F. Bonino and K. P. Lillerud, *Chem. Mater*., **2010**, 24, 6632– 6640.
39. D. Cunha, C. Gaudin, I. Colinet, P. Horcajada, G. Maurin and C. Serre, *J. Mater. Chem. B*, **2013**, 1, 1101–1108.
40. J. Qiu, X. Zhang, Y. Feng, X. Zhang and H. Wang, *Appl. Catal., B*, **2018**, 231, 317–342.
41. C. G. Silva, I. Luz, F. X. Llabrés, I. Xamena, A. Corma and H. García, *Chem. – Eur. J*., **2010**, 16, 11133–11138.
42. B. Yan, L. Zhang, Z. Tang, M. Al-Mamum, H. Zhao and X. Su, *Appl. Catal., B*, **2017**, 218, 743–750.

43. B. Zhang, J. Zhang, X. Tan, D. Shao, J. Shi, L. Zheng, J. Zhang, G. Yang and B. Han, *ACS Appl. Mater. Interfaces*, **2018**, 10, 16418–16423.
44. I. Majeed, M. A. Nadeem, A. Badshah, F. K. Kanodarwala, H. Ali, M. A. Khan, J. A. Stride and M. A. Nadeem, *Catal.: Sci. Technol*., **2017**, 7, 677–686.
45. Y. Shi, A.-F. Yang, C.-S. Cao and B. Zhao, *Coord. Chem. Rev*., **2019**, 390, 50–75.
46. J. G. Santaclara, A. I. Olivos-Suarez, A. Gonzalez-Nelson, D. Osadchii, M. A. Nasalevich, M. A. van der VeenO, F. Kapteijn, A. M. Sheveleva, S. L. Veber, M. V. Fedin, A. T. Murray, C. H. Hendon, A. Walsh and J. Gascon, *Chem. Mater*., **2017**, 29(21), 8963–8967.
47. M. A. Nasalevich, C. H. Hendon, J. G. Santaclara, K. Svane, B. van der Linden, S. L. Veber, M. Fedin, A. J. Houtepen, M. A. van der Veen, F. Kapteijn, A. Walsh and J. Gascon, *Sci. Rep*., **2016**, 6, 23676.
48. A. Santiago-Portillo, S. Navalón, P. Concepción, M. Álvaro and H. García, *ChemCatChem*, **2017**, 9, 2506–2511.
49. A. Kabadagi, S. Chikkamath, S. Kobayashi and J. Manjanna, *Appl. Clay Sci.*, **2020**, 189, 105518.

5.7 Supporting information

UiO-66 (Zr)-H: $ZrCl_4$ (0,466 g, 2mmol) and terephthalic acid (0,332 g, 2mmol) was dissolved in 6 ml of *N,N'*- dimethylformamide (DMF) and were introduced in a vial. The mixture was sonicated for 20 min. When a homogeneous suspension was formed, the mixture was transfer to a Teflon-lined autoclave, sealed and placed in a pre-heated oven at 220 °C, maintaining the temperature for 12 h. After this time, the resulting white solid was filtered and washed several times with DMF and methanol. The solid was dried under vacuum at 120 °C overnight.

UiO-66 (Zr)-NH_2: The synthesis of Zr-NH_2 MOF was carried out dissolving the metallic salt $ZrCl_4$ (0.466 g, 2 mmol) and the organic linker 2-amino-terephthalic acid (0.362g, 2 mmol) in *N,N`*- dimethylformamide (DMF) (6.0 mL, 340 mmol) at room temperature, sonicated for 20 min. The mixture was transferred in a Teflon-lined autoclave, sealed and placed in a pre-heated oven at 100℃ for 24 hours. After cooling to room temperature, the resulting yellow solid was filtered and washed several times with DMF and methanol and dried at room temperature.

UiO-66 (Zr)-NO_2: The material was synthetized dissolving, in a vessel vial, 0.466 g (2 mmol) of $ZrCl_4$, 0.422 g (2 mmol) of 2-nitroterephtalic acid in 6 mL of *N,N'*-dimethylformamide. The resulting mixed solution was sonicated for 20 minutes; subsequently the homogeneous system was transfer in a Teflon-line autoclave that was sealed and placed in a pre-heated oven at 220°C for 24 h. The resulting dark-yellow solid was collected by filtration and washed several times with DMF and methanol. The solid was dried at room temperature and characterized.

MIL-125 (Ti)-NH_2 was prepared following a previously reported procedure. In a 30 mL vessel vial was introduced a suspension of 2-aminoterephthalic acid (1.43 g, 7.9 mmol) in 20 mL of anhydrous DMF. Then, methanol (5 mL) was added to the flask and the system was sonicated for 20 min. Before transferred the mixture to a 50 mL Teflon-lined autoclave titanium isopropoxide (1.36 g, 4.8 mmol) was added. The

autoclave was sealed and heated up to 110 °C for 72 h. After cooling to room temperature, the product was obtained by filtration and in a second moment washed by suspending the powder in DMF for 12 h. Subsequently, the solid was washed with additional DMF at 60 °C for 12 h. This washing procedure was repeated using methanol as solvent to remove the DMF. The material was collected by filtration and dried overnight in an oven at 100 °C.

Figure S5.1. Photograph of the catalytic device employed for the tandem reaction.

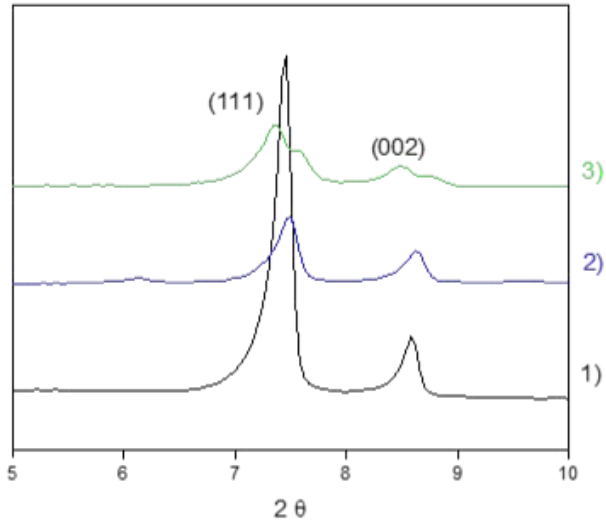

Figure S5.2. Magnification of the PXRD patterns of UiO-66 (Zr)-H (1), UiO-66 (Zr)-NH_2 (2), UiO-66 (Zr)-NO_2 (3) to mark the difference in the main peak.

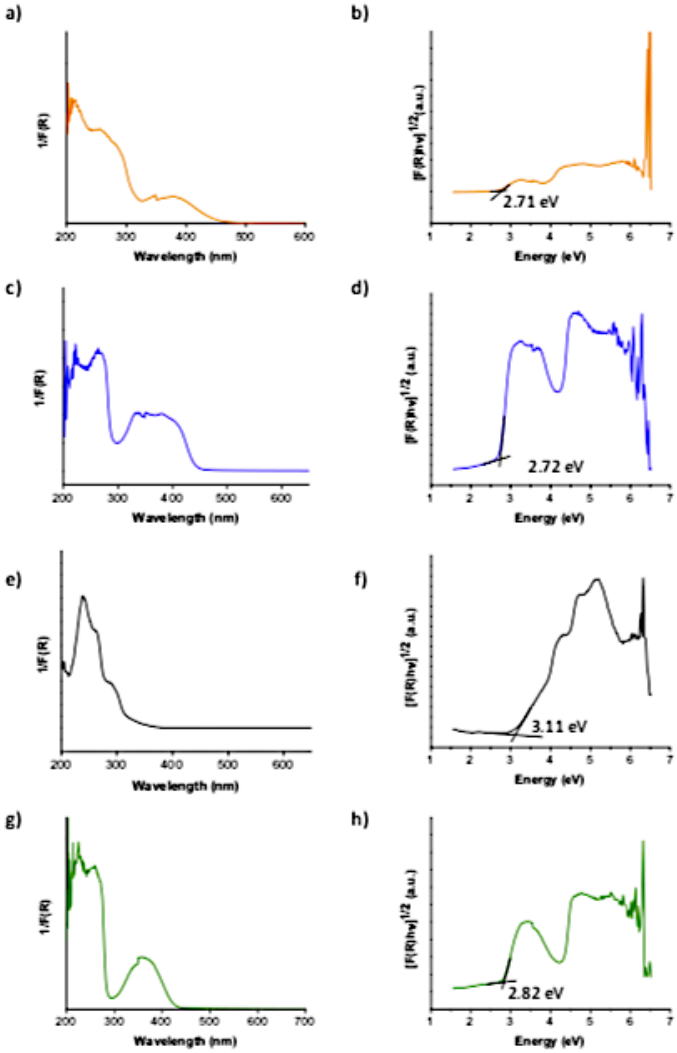

Figure S 5.3. Diffuse UV-Vis (a, c, e) and Tauc plot (b, d, f) for MIL-125 (Ti)-NH_2 (a, b), UiO-66 (Zr)-NH_2 (c, d), UiO-66 (Zr)-H (e, f) and UiO-66 (Zr)-NO_2 (g, h).

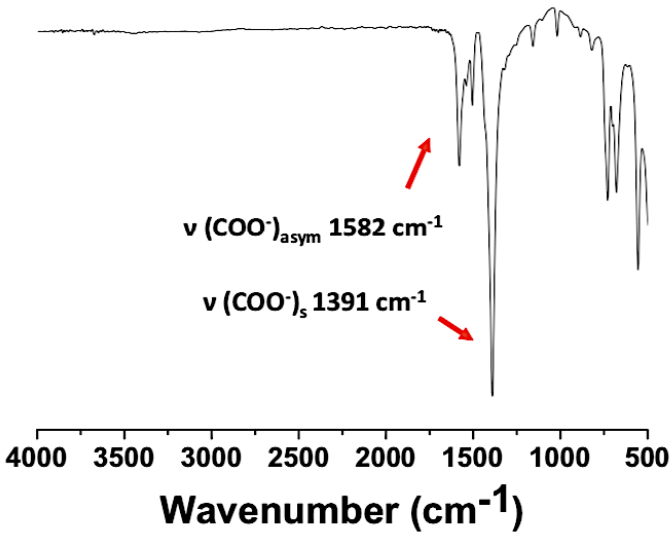

Figure S5.4. ATR-FT-IR spectrum recorded for UiO-66 (Zr)-H.

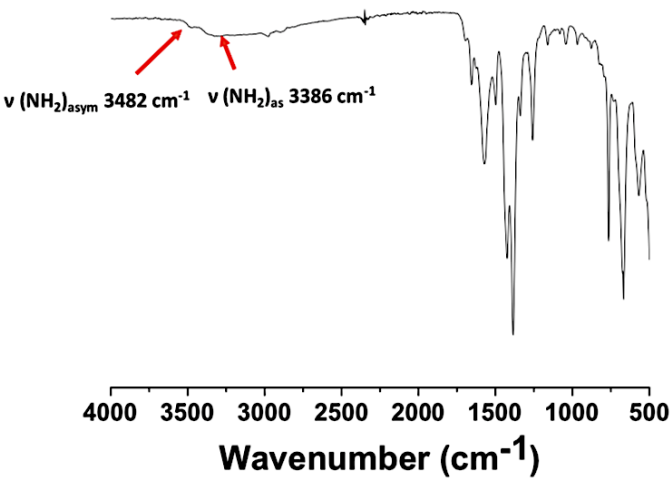

Figure S5.5. ATR-FT-IR spectrum recorded for UiO-66 (Zr)-NH_2.

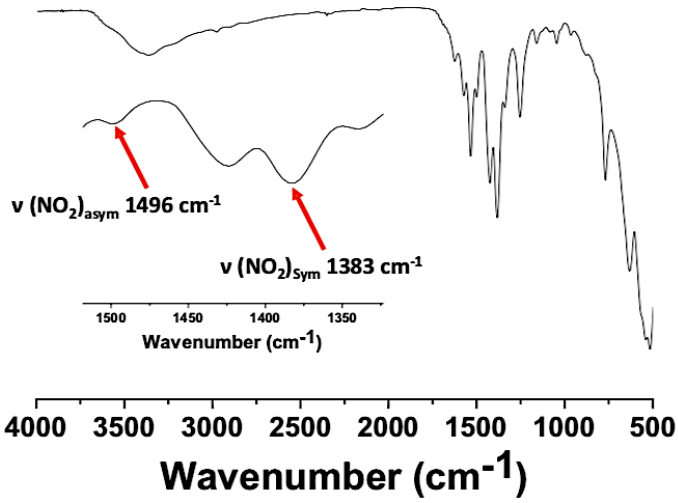

Figure S5.6 ATR-FT-IR spectrum recorded for UiO-66 (Zr)-NO_2. The inset shows an expansion of the 1575-1325 cm^{-1} region.

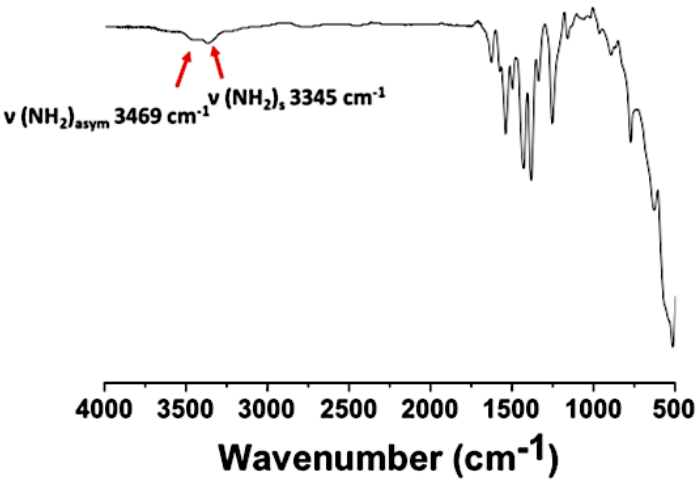

Figure S5.7. ATR-FT-IR spectrum recorded for MIL-125 (Ti)-NH_2.

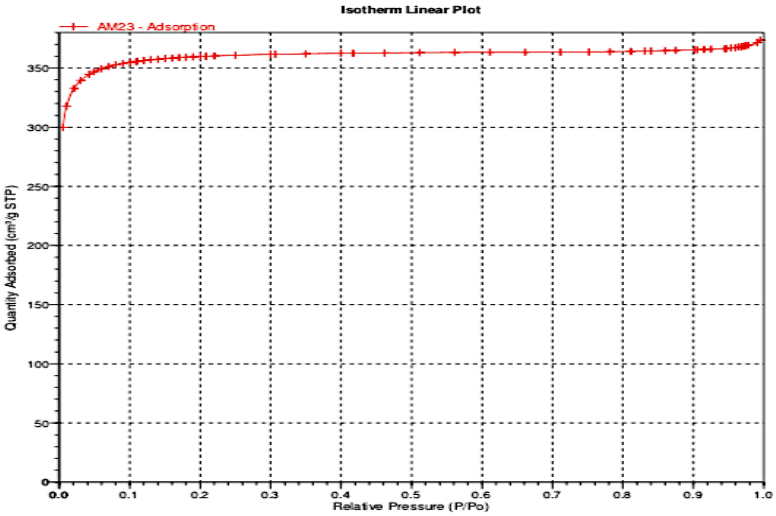

Figure S5.8. Isothermal N_2 adsorption at 77 K for MIL-125 (Ti)-NH_2.

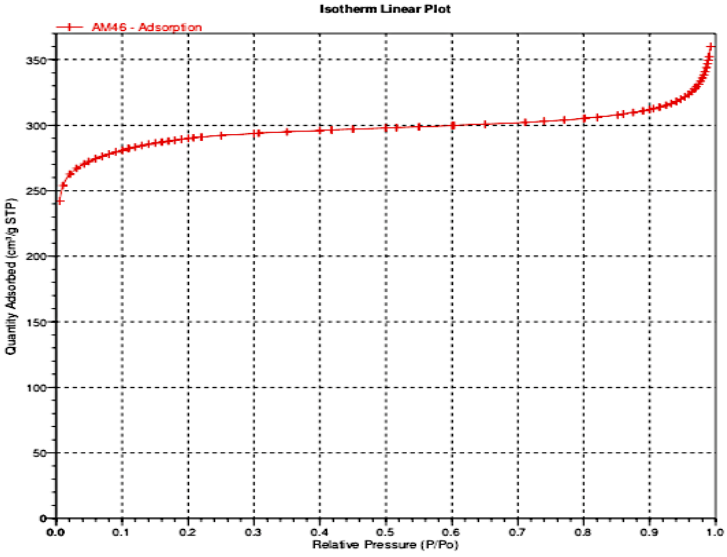

Figure S5.9. Isothermal N_2 adsorption at 77 K for UiO-66 (Zr)-NH_2.

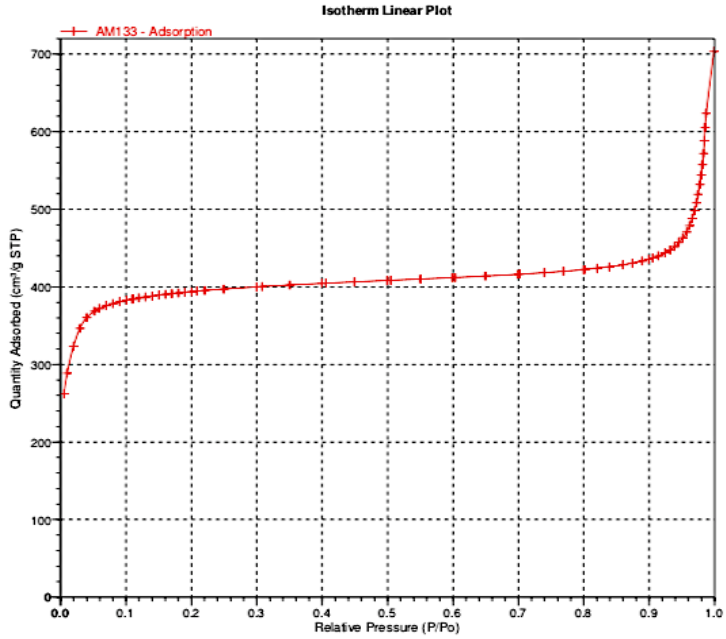

Figure S5.10. Isothermal N_2 adsorption at 77 K for UiO-66 (Zr)-H

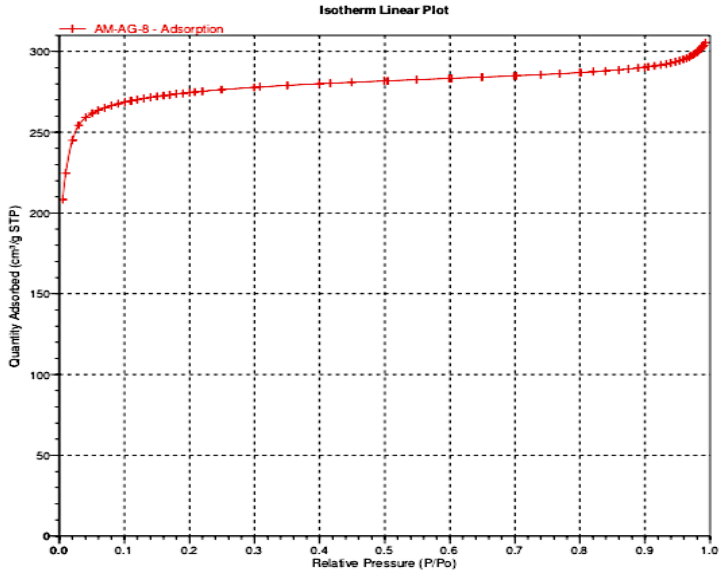

Figure S5.11. Isothermal N_2 adsorption at 77 K for UiO-66 (Zr)-NO_2

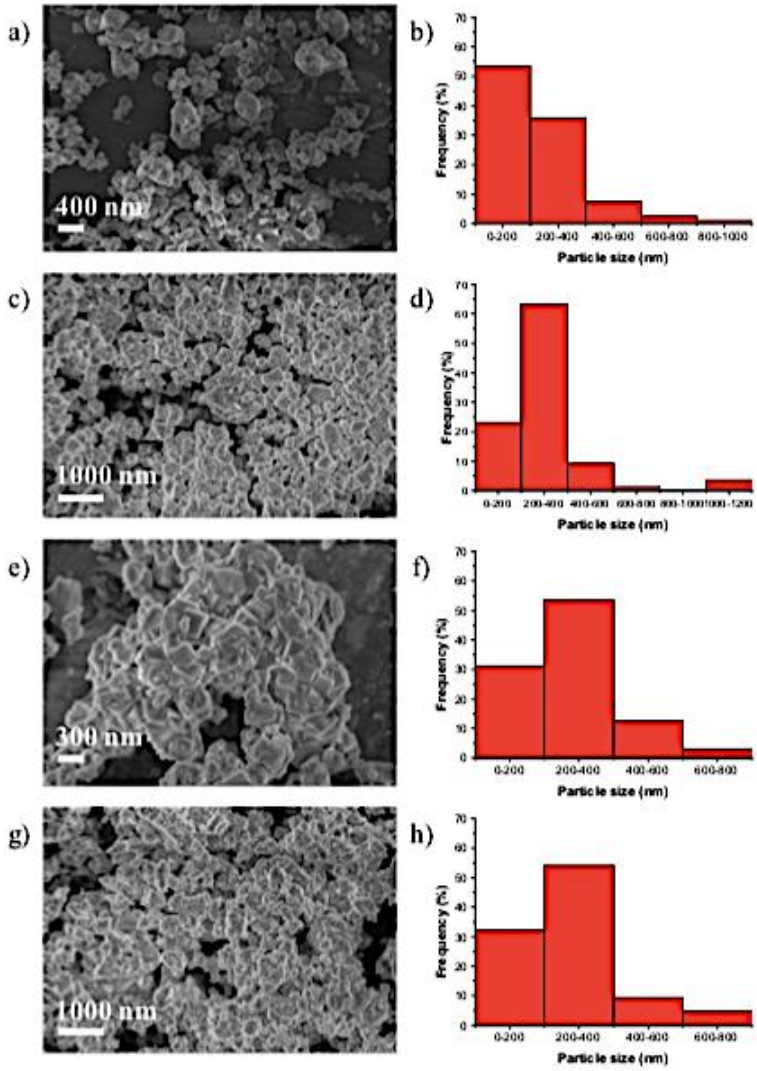

Figure S5.12. Representative HRSEM images and particle size distribution for MIL-125 (Ti)-NH_2 (a-b), UiO-66 (Zr)-NH_2 (c-d), UiO-66 (Zr)-H (e-f) and UiO-66 (Zr)-NO_2 (g-h) materials.

Table S1. Summary of the average particle size and standard deviation of the MIL-125(Ti)-NH_2, UiO-66(Zr)-NH_2, UiO-66(Zr)-H or UiO-66(Zr)-NO_2 materials.		
Entry	Catalyst	Average particle size distribution (nm)
1	MIL-125(Ti)-NH_2	225 ± 143
2	UiO-66(Zr)-NH_2	304 ± 178
3	UiO-66(Zr)-H	274 ± 112
4	UiO-66(Zr)-NO_2	272 ± 129

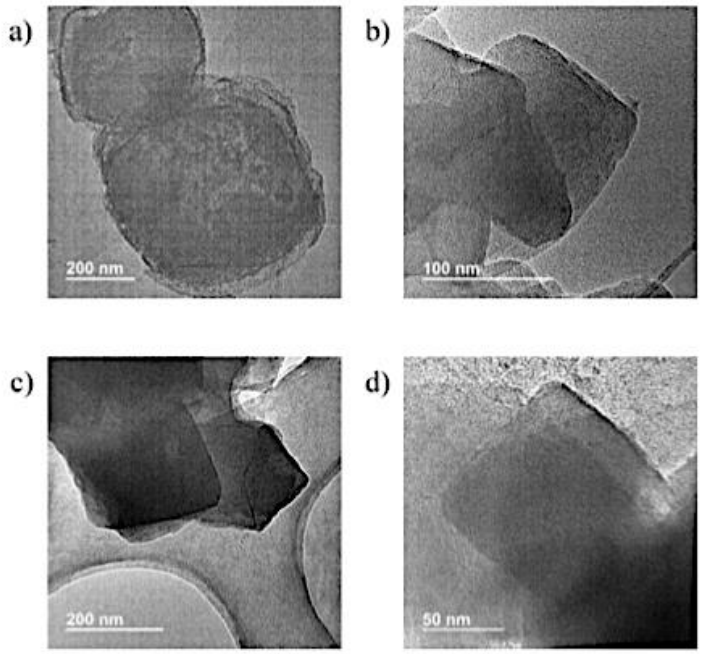

Figure S5.13. Representative TEM images of MIL-125 (Ti)-NH_2 (a), UiO-66 (Zr)-NH_2 (b), UiO-66 (Zr)- H (c) and UiO-66 (Zr)-NO_2 (d) materials.

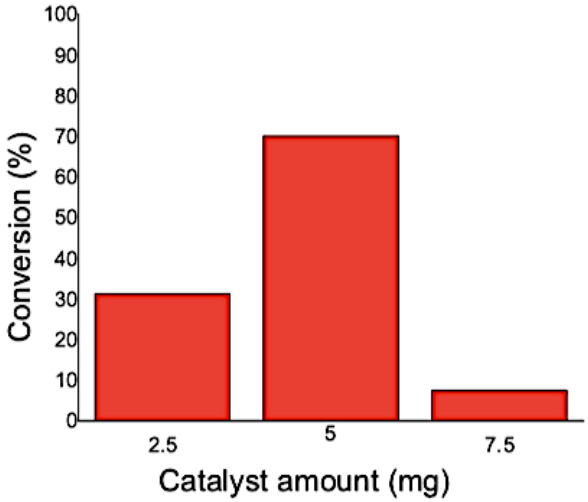

Figure S5.14. Photocatalytic reduction of 4-nitrophenol to 4-aminophenol under UV-Vis using different amounts of UiO-66 (Zr)-NH_2 solid. Reaction conditions: Catalyst amount as indicated, p-nitrophenol (0.02 mmol), solvent (H_2O :MeOH, 1.25:1.25 mL), photoreactor volume (51 mL), Xe lamp (150 W), 50 °C.

Table S2. Values of BET surface area before and after reaction of MOFs employed as bifunctional catalysts in this work.

Catalyst	Theoretical catalyst formula	BET surface area (m^2/g); before reaction	BET surface area (m^2/g); after thermal induced reaction	BET surface area (m^2/g); after photo induced reaction
MIL-125(Ti)-NH_2	$Ti_8O_8(OH)_4(C_6H_3C_2O_4NH_2)_6$	1200	1100	997
UiO-66(Zr)-H	$Zr_6O_4(OH)_4(OOC\text{-}C_6H_4\text{-}COO)_6$	1368	840	906
UiO-66(Zr)-NH_2	$Zr_6O_4(OH)_4(OOC\text{-}C_6H_3NH_2\text{-}COO)_6$	923	650	548
UiO-66(Zr)-NO_2	$Zr_6O_4(OH)_4(OOC\text{-}C_6H_3NO_2\text{-}COO)_6$	903	490	471

Chapter 6.

Metal Nodes of Metal Organic Frameworks Can Activate Molecular Hydrogen

Arianna Melillo, Belen Ferrer* and Hermenegildo Garcia*

Departmento de Química and Instituto Universitario de Tecnología Química, Universitat Politecnica de Valencia, Av. De los Naranjos s/n, 46022 Valencia, Spain.

Dedicated to Prof. Vincenzo Balzani, a visionary pioneer in chemistry, in the occasion of his 80th anniversary

6.1 Abstract

Hydrogenation of multiple bonds is one the most study organic reactions. Bibliography studies reported that this type of reaction can be given in present of heterogeneous catalysts. [1]

Typical heterogeneous catalysts are based on transition metal nanoparticles. [2] In this study it is reported the use of some of the most stable MOFs such as MIL-101 and UiO-66, that, in the absence of occluded metal nanoparticles can promote hydrogenation of polarized X=Y double bonds including nitro groups and carbonyl. It is proposed that the reaction mechanism is based on the operation of frustrated Lewis acid/base pair; in fact, it is know that, the catalytic activity of MOFs type materials can be explain as a function of the composition of the metal node and the organic linker.

It should be noted that the multiple bonds constitute the vast majority functional groups of various reagents useful for industry, therefore the catalytic hydrogenation reaction of these bonds is among the most requested from an industrial and synthetic point of view. [1,3] The reaction can be promoted using a large variety of homogeneous and heterogeneous catalysis.[4] Concerning the heterogeneous catalysts, supported transition metal nanoparticles, including noble metals, but also first raw transition metals are the most widely used and deeply studied. [5] Typical supports for these metal nanoparticles include active carbons, large surface area metal oxides and porous materials.[6]

Metal organic frameworks, constituted by metal nodes coordinated to rigid organic linkers defining a highly porous crystal lattice, have been also amply studied as supports of occluded metal nanoparticles with a remarkable activity in catalytic hydrogenation.[7] When MOFs are used as a matrix for active metal nanoparticles they play a passive role, just to host the catalytically active metal nanoparticle increasing its catalytic stability by impeding particle growth due to spatial

restrictions imposed by the MOF lattice.[8] In some cases, heterogeneous MOFs can be show a synergy with metal nanoparticles due to the cooperation of the adsorption capacity of MOFs and/or tuning the polarity of the internal voids in which the metal nanoparticles are accommodated. However, best of our knowledge, the active role of MOF lattice promoting hydrogenations has not been disclosed. Intrinsic catalytic hydrogenation activity of MOF would open new research aimed at a delineation of the scope, optimization of the metal/linker combination, deep understanding of the nature of the active sites and determination of the reaction mechanism.

6.2 Discussion

In this chapter, it is reported the use of UiO-66(X) and MIL-101(Cr) in the absence of any metal nanoparticle or any other additional component that are able to activate molecular hydrogen promoting hydrogenation of polar X=Y multiple bonds.

There are in the literature, some reports on the use of isopropanol and other alcohols to perform hydrogen transfer reduction of carbonyl groups [8,9] In this case the mechanism, however, involves hydride transfer of the hydrogen atom at the alpha position of the metal-alcoholate intermediate to the carbonyl group, but it is different from the more general direct activation of apolar molecular hydrogen.

As it is defended at the beginning of this chapter, the six samples used as catalysts correspond to two of the most robust and studied MOF structures, namely UiO-66[10] and MIL-101(Cr),[11] having large pores and high surface area. The four materials with UiO-66 structure differ on the composition of the metal node (Zr or Ce or bimetallic Zr-Ce)[12] and the substituent on the linker (terephthalate or aminoterephthalate).[13] This series lets define the role of the nodal metal composition and the basicity of the linker. The two MIL-101(Cr) materials, having terephthalate[11] or chloroterephthalate[14] as linkers, serve to generalize the H_2 activation process to metal-oxo clusters and the influence of the ligand inductive

effect on the metal node. Table 6.1 lists the samples studied, their composition and relevant textural parameters, including surface area and particle size. All the samples have been previously reported in the literature and were obtained directly from the corresponding metal salts and the corresponding terephthalic acid following reported solvothermal procedures.

Table 6.1: List of MOFs employed as catalysts in this work together with some relevant textural and analytical data.

MOF	% Zr teoric/% Zr experimental	% Ce teoric/% Ce experimental	% Cr teoric/% Cr experimental	Pore volumen (cm^3/g)	BET (m^2/g)
UiO66 Zr-H	32.8/31.6	/	/	0.8	1258
UiO66 Ce-H	/	25.3/21.2	/	0.35	916
UiO66 (Zr/Ce)-H	30.9/22.2	6.5/5.5	/	0.69	1297
UiO66 Zr-NH_2	31.2/30.9	/	/	0.91	923
MIL-101(Cr)-H	/	/	21.7/20	1.44	2690
MIL-101(Cr)-Cl	/	/	18.7/19.52	1.1	1199

The samples exhibit the expected XRD diffraction pattern according to the literature (Fig. S6.1) and the specific surface area is in the range of reported values for these materials, following the trend of lesser area for substituted terephthalate linkers and for UiO-66 Ce in comparison to the UiO-66 Zr analog. These characterization data confirm the successful preparation and the identity of the materials based on their coincidence with the reported values. The first catalytic hydrogenation reactions were carried out in acetonitrile solution using nitrobenzene as substrate under 3 bars H_2 pressure. Control experiments in the absence of any catalyst or in the presence of catalyst but in the absence of H_2 only resulted in barely detectable percentages of aniline, lesser than 3 %. Differently to the blank control, all the samples exhibit hydrogenation activity; aniline being the only product detected in almost complete selectivity. In Fig. 6.1, are reported the temporal profiles of nitrobenzene conversion.

As it can be seen there, the aniline yield at final reaction time follows the order: UiO-66(Zr/Ce)>MIL-101(Cr)-Cl>MIL-101(Cr), UiO-66(Zr)≈UiO-66(Ce)>UiO-66(Zr)-NH_2.

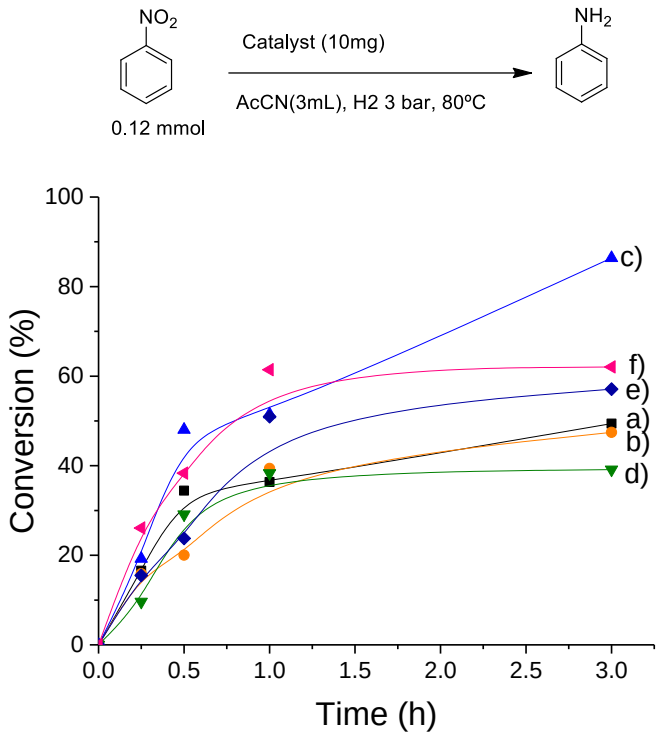

Fig. 6.1 Catalytic nitrobenzene reduction to aniline using UiO66 (Zr)-H (a, black), UiO66 (Ce)-H (b, orange), UiO66 (Zr/Ce) (c, blue), UiO66 (Zr)-NH_2 (d, green), MIL-101 (Cr)-H (e, dark blue) and MIL-101 (Cr)-Cl (f, pink). Reaction conditions: catalyst (0.010 g of MOF), nitrobenzene (37 µL, 0.12 mmol), acetonitrile (3 mL), 80 °C, 3 bar H_2.

Deep analysis of the temporal profiles of nitrobenzene conversion showed, however, that the initial reaction rates do not follow the same order than the final nitrobenzene conversion and that for some catalysts the reaction stops before nitrobenzene conversion was completed. A possible clarification of this behavior is that aniline, as it is being formed during the course of the reaction, acts as a poison of the active sites, slowing down the reaction rate and eventually stopping

completely the process. This poisoning effect would be apparently different depending on the MOF.

To confirm this aspect, two reactions were performed using UiO-66(Zr) as catalyst, under the same conditions, but adding since the beginning, aniline at two intermediate concentrations as those formed in the reaction. Measurements of the fresh UiO-66(Zr) in the absence and in the presence of aniline clearly show that the initial reaction rate decreases as the concentration of aniline increases, thus, confirming that aniline is blocking or deactivating the active sites. The results are presented in Fig. S6.2 in the supporting information.

The influence of H_2 pressure and the catalyst amount on the hydrogenation activity was determined in the range from 3 to 10 bars using 5 or 10 mg of catalyst. The temporal profiles of nitrobenzene conversion for these experiments, using UiO-66(Zr) as catalysts, are reported in Fig. 6.2. Rise up from the analysis of these data that the activity increased with the amount of UiO-66(Zr) and with H_2 pressure. A linear relationship between the initial reaction rate and initial H_2 pressure suggests that the reaction follows a first order kinetics respect to H_2 in the range of pressures under consideration (Fig. S6.3). Considering the best reaction conditions, a conversion of nitrobenzene of 90 % was achieved for 10 mg of UiO-66(Zr) catalyst after 3 h reaction time. It should be commented that blank controls in the absence of catalysts at increasing H_2 pressure showed that the uncatalyzed aniline formation increases with the H_2 pressure, but it always remained below 10 % at 3 h reaction time.

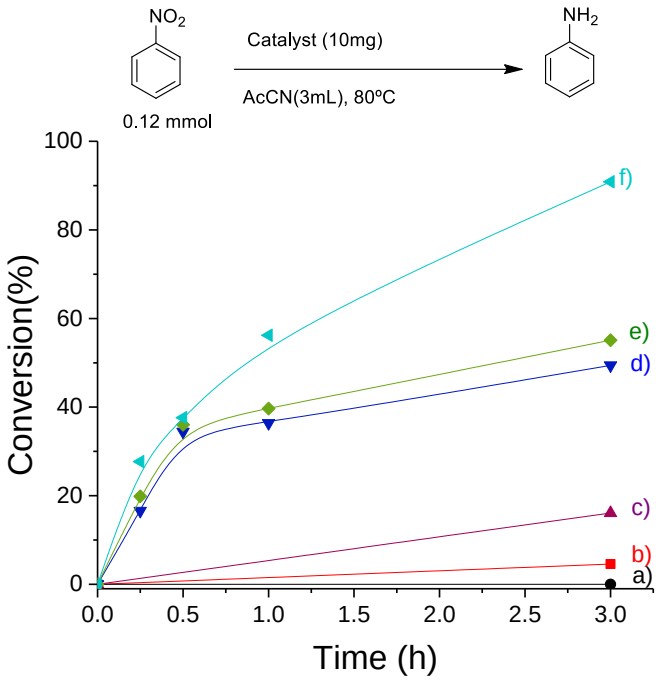

Fig. 6.2 Time-conversion plots of nitrobenzene using UiO66 (Zr)-H in different condition: 3 bar of H_2, 80 ºC, no catalyst (a), black), with 10 mg of catalyst, 80 ºC (b) red), : 5 bar of H_2, 80 ºC, no catalyst (c), dark pink), 3 bar of H_2, 80 ºC, 10 mg of catalyst(d), blue), 5 bar of H_2, 80 ºC, 10 mg of catalyst (e),green) and 10 bar of H_2, 80 ºC, 10 mg of catalyst (f), light blue). (Reaction conditions: catalyst (10 mg), nitrobenzene (37 µL, 0.12 mmol), CH_3CN (3 mL).

A series of experiments were performed to determine the reaction mechanism. In this case we focalized our attention on the most commonly studied UiO-66(Zr), although the results with nitrobenzene suggest that bimetallic UiO-66(Zr/Ce) could be even more efficient. Table 6.2 summarizes the results obtained using different substrates. In comparison to nitrobenzene, no conversion of 3-nitrostyrene was achieved in 3 h at 3 bars H_2 pressure, even at 130 ºC. A 3-nitrostyrene conversion of 77 % was, however, possible working at 10 bars H_2 pressure and 80 ºC. The only product formed was 3-aminostyrene, indicating that hydrogenation is selective for polarized multiple bonds, but no for C=C double bonds. Similar, but lower selectivity was reported using supported Au NPs as

catalysts, since C=C hydrogenation occurred in minute but detectable amounts.[15] The relative lesser reactivity of 3-nitrostyrene vs. nitrobenzene can be rationalized considering the hydrogenation reaction is sensitive to the molecular diameter of the substrate. Thus, the larger molecular diameter of 3-nitrostyrene in comparison to nitrobenzene will disfavor diffusion of the larger substrate inside the MOF pores and the approach of the encumbered molecule to the active metal nodes.

Table 6.2. Selective hydrogenation of different substrates catalyzed by different materials.

Entry	Substrate	Catalyst (10 mg)	H_2 pressure (bar)	Temperature (º C)	Time (h)	Conversion (%)
1	3-Nitrostyrene	UiO66 (Zr)-H	3	80	3	0
2	3-Nitrostyrene	UiO66 (Zr)-H	3	130	3	0
3	3-Nitrostyrene	UiO66 (Zr)-H	10	80	3	76.8
4	Nitrobenzene	UiO66 (Ce)-H	/	80	6	6.2
5	Nitrobenzene	UiO66 (Ce)-H	5	80	3	60.5
6	Nitrobenzene	UiO66 (Ce)-H	10	80	3	75.9
7	Benzaldehyde	UiO66 (Zr)-H	3	80	3	69.3
8	*P*-anisaldehyde	UiO66 (Zr)-H	3	80	3	76.1
9	*Trans*-cynnamaldehyde	UiO66 (Zr)-H	3	80	3	0
10	*Trans*-cynnamaldehyde	UiO66 (Zr)-H	3	100	5	0
11	*Trans*-cynnamaldehyde	UiO66 (Zr)-H	3	120	5	0
12	*Trans*-cynnamaldehyde	UiO66 (Zr/Ce)-H	3	80	3	55.5
13	cyclohexanone	UiO66 (Zr)-H	3	80	24	80.7
14	iso - octanal	UiO66 (Zr)-H	3	80	3	44.3
15	iso - octanal	UiO66 (Zr/Ce)-H	3	80	3	43.9
16	Cyclo-octanone	UiO66 (Zr)-H	3	80	3	40
17	Geranial	UiO66 (Zr)-H	3	80	3	0
18	Quinoline	UiO66 (Zr)-H	3	80	3	0
19	Acetophenone	UiO66 (Zr)-H	3	80	3	38.1
20	Benzaldehyde + Aniline	UiO66 (Zr)-H	3	80	6	92.9
21	Benzaldehyde + Aniline	/	3	80	6	0
22	1-octene	UiO66 (Zr)-H	3	80	3	67.4
23	Cyclohexanone oxime	UiO66 (Zr)-H	3	80	3	0
24	Styrene	UiO66 (Zr)-H	3	80	3	0
25	Cis-cyclooctene	UiO66 (Zr)-H	3	80	3	0
26	Trans-2-octene	UiO66 (Zr)-H	3	80	3	86

The ability of UiO-66(Zr) to catalyze hydrogenation of polar multiple bonds was also tested for benzaldehyde and anisaldehyde at 80 ºC. The corresponding benzylic alcohols were formed in both cases; however, benzaldehyde gave somewhat lower yield. In accordance with size restrictions to pore diffusion, *trans*-cinnamaldehyde does not undergo reduction under the same conditions. In the case of octanal, an aliphatic long chain aldehyde, the reaction undergo also hydrogenation

to the corresponding alcohol, but the yields at 3 h was lower than that of the benzaldehyde, due to the comparative unfavorable diffusion. Accordingly, geranial does not undergo hydrogenation at 3h under 3 bar H_2 pressure. Ketone groups can also undergo hydrogenation. Acetophenone can be reduced to 1-phenylethanol, although the yields were lower than those of benzaldehyde probably reflecting the unfavorable combination of steric encumbrance and lesser carbonyl reactivity. Small ketones like cyclohexanone could be reduced in high yields, although the reaction required longer times. Difficult diffusion is also the most likely reason of the lower reactivity of cyclooctanone compared to cyclohexanone.

So, the analysis of table 6.2 let to concluded that UiO-66(Zr) exhibits an intrinsic activity as hydrogenation catalyst for nitro and carbonylic group, while is not able, under the present conditions, to promote hydrogenation of C=C double bonds.

This hydrogenation reaction is expanded to a tandem catalyst by carrying out the condensation of aldehyde with primary amines, followed by hydrogenation of the resulting imine to a secondary amine. The results achieved using benzaldehyde and aniline as starting materials are presented also in Table 6.2. As it is possible to see there, benzaldehyde and aniline afford after 6 h reaction time the expected phenyl benzyl amine in very high yield. In contrast to the ability of UiO-66(Zr) to promote hydrogenation of imines, attempts to perform hydrogenation of a nitrogenated heterocycle such as quinoline were unsuccessful working at 80 ^{o}C and 3 bars H_2 pressure. Catalyst stability for nitrobenzene hydrogenation was evaluated using UiO-66(Zr)-H as MOF. At the end of the reaction, the solid was recovered, washed with acetonitrile and used in the subsequent run. A gradual catalyst deactivation was observed upon use, the final aniline yield at 3 h reaction time decreasing from 40 to 35 to 25 %. Figure S6.4 in supporting information provides the temporal profiles of the catalyst recycling test and the XRD pattern of the three-times used. Partially deactivated UiO-66(Zr)-H showed, however, that the materials

have preserved the crystallinity. It is proposed that this deactivation derives from the poison effect of aniline but attempts to reactivate the partially deactivated catalyst by a more exhaustive washing were unsuccessful.

To obtain some evidence of H_2 activation by UiO-66(Zr)-H, *in situ* IR spectra were acquired after exposure of UiO-66(Zr)-H to H_2 gas at 80 ºC. Figure 6.3 shows illustrative IR spectra of these analyses.

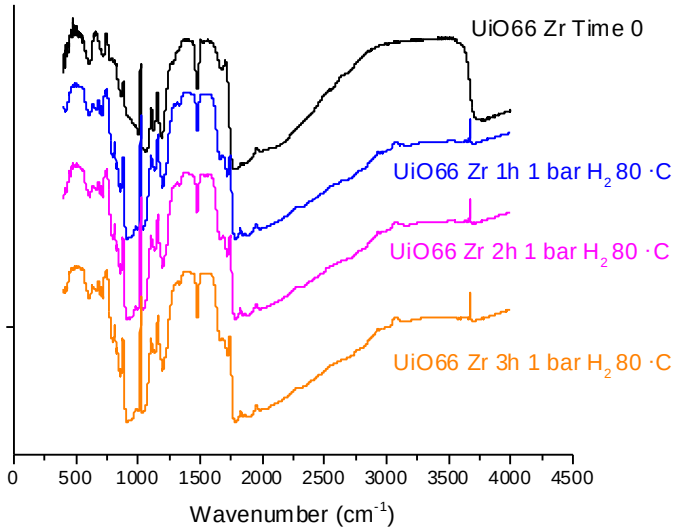

Figure 6.3: FT-IR spectra after adsorbing H_2 on UiO66(Zr)-H (a), UiO66(Zr)-H after 1h at 80 °C(b), UiO66(Zr)-H after 2h at 80 °C (c) and UiO66(Zr)-H after 3h at 80 °C(d). The peak at 3670 cm^{-1} is associated to the width of the generation of the O-H that correspond to the protonation of a nodal O atom.

The IR spectra clearly showed the appearance of a sharp O-H stretching peak at about 3670 cm^{-1}. The wavenumber and narrow width of the peaks indicates that they correspond to isolated OH that do not form hydrogen bridges. Although appearance of other peak was not observed, it is proposed that the generation of the O-H peak should correspond to protonation of a nodal O atom and it would be accompanied by the formation of Zr-H. However, the position of this proposed Zr-H

would appear at about 1600 cm^{-1} [16] and would be overlapped with the intense MOF vibrations and almost impossible to detect. Thus, based on the observation of the formation of O-H the following equation for H_2 chemisorption on UiO-66(Zr)-H is proposed:

$$M + x/2\ H_2 \leftrightarrow MH_X + \delta Q$$

The double arrow indicates the presence of a dynamic equilibrium between the two phases, that is the possibility of reversibly inverting reactants with products, simply by varying the reaction conditions. The presence of energy to the right of the equation indicates that the absorption process is exothermic, that is the release of energy during the hydrogenation of the metal and, at the same time, that the reverse process is endothermic. Since the reaction takes place at constant pressure, this energy also represents the enthalpy (or heat of formation) of the reaction.

6.3 Conclusions

In conclusion, in this chapter we have reported the hydrogenation reaction of multiple bonds X =Y of organic substrates, catalyzed by MOFs materials having UiO66(X) and MIL 101(Cr)-L structure, in the absence of any metal nanoparticle. The *in-situ* analysis, carried out in the presence of nitrobenzene as a substrate, clarified that the catalytic activity of the MOFs under examination follows a different order; in more detail it turned out that for some catalysts, the reaction does not reach a complete conversion of nitrobenzene to aniline such as aniline acts as a catalytic poison. The control reactions carried out in the absence of a catalyst but in the presence of 3 bar of hydrogen confirmed the active role of the catalyst; only 3% of nitrobenzene is, in fact, converted to aniline. On the other hand, rise up a linearity between the amount of H_2 introduced into the system and the conversion of the reagent into a product, similar to what happens with an increase of the amount of catalyst; thus, the greater the amount of H_2 and / or catalyst added to the system, the greater the percentage of reduction. The mechanistic study revealed that the

diffusion of the substrate within the MOF, an aspect that is directly related to the molecular diameter of the species under examination, plays a key role in the hydrogenation process. In fact, in the presence of 3 bar of H_2 and at 80 °C nitrobenzene gives greater conversion to the correspondent reduced compound than nitro-styrene when catalyzed by the well-known UiO66(Zr)-H. Under the same conditions, both benzaldehyde and anisaldehyde are reduced to give the corresponding alcohols; however, trans-cinnamaldehyde, due to its larger size, does not reach the active metal center of the catalyst and therefore is not reduced**.** In accordance with what has been described so far, it has been observed that the low diffusion of acetophenone within the pores of UiO66(Zr)-H is such as to allow only partial hydrogenation to 1-phenylethanol. The overall analysis of the reported results makes us to conclude that the catalytic activity is directed to polarized X=Y double bonds, however the reaction conditions defined here are not such as to favor the reduction of C=C bonds.

6.4 References

1. Stoffels, M. A.; Klauck, F. J.; Hamadi, T.; Glorius, F.; Leker, J.,Technology trends of catalysts in hydrogenation reactions: a patent landscape analysis, *Adv syn & cat* **2020,** *362*, 1258-1274.

2. L.Liu and A. Corma; Metal Catalysts for Heterogeneous Catalysis: From Single Atoms to Nanoclusters and Nanoparticles; *Chem. Rev.***2018**, *118(10), 4981*

3. Carruthers, W.; Coldham, I., *Some modern methods of organic synthesis*. Cambridge University Press: 1986.

4. Nishimura, S., *Handbook of heterogeneous catalytic hydrogenation for organic synthesis*. Wiley New York: 2001

5. Astruc, D.,Transition-metal nanoparticles in catalysis: from historical background to the state-of-the art, *Nano and cat* **2008,** *16*, 1-48.

6. Ndolomingo, M. J.; Bingwa, N.; Meijboom, R.,Review of supported metal nanoparticles: synthesis methodologies, advantages and application as catalysts, *J of Mat. Sci.* **2020,** *55*, 6195-6241.

7. Dhakshinamoorthy, A.; Garcia, H.,Catalysis by metal nanoparticles embedded on metal–organic frameworks, *Chem. Soc. Rev.* **2012,** *41*, 5262-5284.

8. Rojas-Buzo, S.; García-García, P.; Corma, A.,Catalytic Transfer Hydrogenation of Biomass-Derived Carbonyls over Hafnium-Based Metal–Organic Frameworks, *ChemSusChem* **2018,** *11*, 432-438.

9. Valekar, A. H.; Cho, K.-H.; Chitale, S. K.; Hong, D.-Y.; Cha, G.-Y.; Lee, U.-H.; Hwang, D. W.; Serre, C.; Chang, J.-S.; Hwang, Y. K.,Catalytic transfer hydrogenation of ethyl levulinate to γ-valerolactone over zirconium-based metal–organic frameworks, *Green Chem* **2016,** *18*, 4542-4552.

10. Kandiah, M.; Nilsen, M. H.; Usseglio, S.; Jakobsen, S.; Olsbye, U.; Tilset, M.; Larabi, C.; Quadrelli, E. A.; Bonino, F.; Lillerud, K. P.,Synthesis and stability of tagged UiO-66 Zr-MOFs, *Chem. Mat.* **2010,** *22*, 6632-6640.

11. Latroche, M.; Surblé, S.; Serre, C.; Mellot-Draznieks, C.; Llewellyn, P. L.; Lee, J. H.; Chang, J. S.; Jhung, S. H.; Férey, G.,Hydrogen storage in the giant-pore metal–organic frameworks MIL-100 and MIL-101, *Angewandte Chem. int.ed.* **2006,** *118*, 8407-8411

12. A.Melillo; M.Cabrero-Antonino; Sergio Navalón, Mercedes Álvaro, Belén Ferrer, Hermenegildo García Enhancing visible light photocatalytic activity by controlling metal-node composition, *Appl. Cat. b env*. **2020,** *278, 119345*

13. C. Loc Luu; T. Van Nguyen; T. Nguyen; T. Cuong Hoang, Synthesis, characterization and adsorption ability of UiO-66-NH_2, *Adv. Nat. Sci: Nanosci. Nanotechnol.* **2015,** *6- 025004*

14. A. Buragohain; Van Der Voort ; S. Biswas; Synthesis, characterization and sorption properties of functionalized Cr-MIL-101-X (X=–F, –Cl, –Br, $–CH_3$, $–C_6H_4$, $–F_2$, $–(CH_3)_2$) materials, *J. of sol. state chem.*, **2016**, *238*-
15. Corma, A.; Serna, P.,Chemoselective hydrogenation of nitro compounds with supported gold catalysts, *Sci.* **2006,** *313*, 332-334.
16. Lokshin, B. V.; Klemenkova, Z. S.; Ezernitskaya, M. G.; Strunkina, L. I.; Brainina, E. M.,Vibrational spectra of tris(cyclopentadienyl)zirconium and -hafnium hydrides and deuterides, Cp3MX (M= Zr, Hf; X = H, D), *J of Org. Chem.* **1982,** *235*, 69-75.

6.5 Supporting information

Experimental section:

All reagents used for the synthesis of the materials and for the catalytic reactions were purchased from Sigma Aldrich and are used without additional purification.

UiO66 (Zr)-H:

The synthesis of Zr-BDC MOF was carried out dissolving the metallic precursor $ZrCl_4$ (0.053 g, 0.227 mmol) and the organic linker 1,4-benzene- dicarboxylic acid (H_2BDC) (0.034 g, 0.227 mmol) in *N, N'*-di- methyl formamide (DMF) (24.9 g, 340 mmol) at room temperature. The transparent suspension was transferred in a Teflon-lined autoclave, sealed and placed in a pre-heated oven at 220℃ for 12 h. The resulting white solid was filtered and washed several times with DMF and Methanol and later, dried at room temperature.

UiO-66(Zr/Ce):

The catalyst was synthesized in a 25 mL Pyrex glass reaction tubes. H_2BDC (127.6 mg) was introduced into the glass reactor with DMF (3.6 mL) and aqueous solutions of cerium (IV) ammonium nitrate (0.533 M; 117 mg, 0.400 mL water), zirconium (IV) dinitrate oxide hydrate (0.533 M, 99.0 mg 0.800 mL) and concentrated formic acid (HCOOH, 100 %, 1.03 mL) were added. This suspension was heated and stirring for 15 min at 100 °C. The light- yellow precipitate was centrifuged in the mother solution and then it was decanted off. To obtain a pure UiO66 (Zr/Ce) solid, the suspension was centrifuged twice in DMF (2 mL) and then, to remove DMF, the solid was washed and centrifuged four times in acetone (2 mL). The resulting white solid was dried in air at 70 °C. Note that no cerium (IV) ammonium nitrate that could interfere in the photocatalytic overall water splitting remains in the final solid.

UiO-66 (Zr)-NH_2:

The preparation of Zr-NH_2 MOF was realized dissolving the metallic precursor $ZrCl_4$ (0.466 g, 2 mmol) and the organic linker 2-amino-terephthalic acid (0.362g, 2 mmol) in *N,N`*- dimethylformamide (DMF) (6.0 mL, 340 mmol) at room temperature, sonicated for 20 min. The yellow suspension was transferred in a Teflon-lined autoclave, sealed and placed in a pre-heated oven at 100℃ for 24 hours. After the system was cooling to room temperature, the resulting yellow solid was filtered and washed several times with DMF and methanol and dried at room temperature.

UiO-66(Ce):

To carry out the synthesis of UiO66(Ce) H_2BDC (35.4 mg, 213 μmol) was introduced into the glass reactor with DMF (1.2 mL) and an aqueous solution of cerium (IV) ammonium nitrate (400 μL, 0.5333 M). The 25 mL Pyrex glass reactor was heated under stirring conditions for 15 min at 100 °C. The light-yellow precipitate was centrifuged in the mother suspension; then, the solid was centrifuged twice in DMF (2 mL). To remove DMF from the porous of the MOF, the solid was washed and centrifuged with acetone (2 mL) four times. The resulting quite-yellow solid was dried in air at 70 °C.

Synthesis of MIL101(Cr)-L where L was: H or Cl:

The catalysts were synthetized starting from a mixture of a metallic precursor, CrO_3 (125 mg, 1.25 mmol), organic ligand H_2BDC-X (1.25 mmol), water (5 mL) and concentrated HCl (0.15 mL, 4.89 mmol), placed, after stirrer, in a 50 Teflon-lined autoclave and heated at 180°C for 144 h in a conventional oven. After cooling at room temperature, the green materials were collected by filtration; later, to remove the precursors it was washed with acetone (3 or 5 mL) and dried in air.

Catalytic activity:

The catalytic activity of UiO-66 (X) (X: Zr, Ce or Zr/Ce) and MIL-101 (Cr)-L, (L:H or Cl) was tested for the heterogeneous reduction of different organic substrates having industrial and/or pharmacological interest. Briefly, the required catalyst

amount (i.e. 10 mg) was introduced into a 10 mL Pyrex tube reactor containing a pressure gauge at the outlet and one gas inlet. Then, the specific reagent (0.12 mmol) was dissolved in acetonitrile (3 mL), and the suspension containing MOF, was subjected to ultrasound for 20 min. Subsequently, the system was purged with H_2 for 15 min until obtain the selected pressure for each reaction. The reaction was heated at different temperature. The course of the reaction was followed by GS chromatography analyzing diluted reaction aliquots (0.1 mL) in acetonitrile (0.5 mL) introduced an internal standard. Prior to analyzed the suspension, the mixture was filtered using a nylon filter (0.2 μm).

Characterization of the materials

Powder X-ray diffraction (PXRD) patterns were recorded on a Philips XPert diffractometer equipped with a graphite mono- chromator (40 kV and 45 mA) employing Ni-filtered Cu Kα radiation. Isothermal N2 adsorption measurements have been carried out at 77 K using a Micromeritics ASAP 2010 apparatus. The metal content of each MOF material was determined by ICP-AES analysis after digesting the solids in concentrated nitric acid at 80 °C for 24 h. ATR-FTIR spectra of MOFs were obtained with a Bruker Tensor 27 instrument. Prior to ATR-FTIR measurements, the MOF samples were dried in an oven at 100 °C for 24 h to remove physisorbed water.

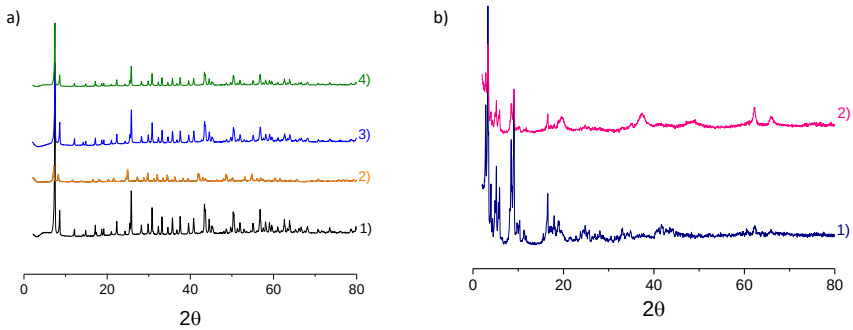

Figure S6.1: PXRD patterns of a): 1) UiO66(Zr)-H, 2) UiO66(Ce)-H, 3) UiO66(Zr/Ce)-H, 4) UiO66(Zr)-NH_2 and b) 1) MIL101 (Cr)-H, 2) MIL101 (Cr)-Cl.

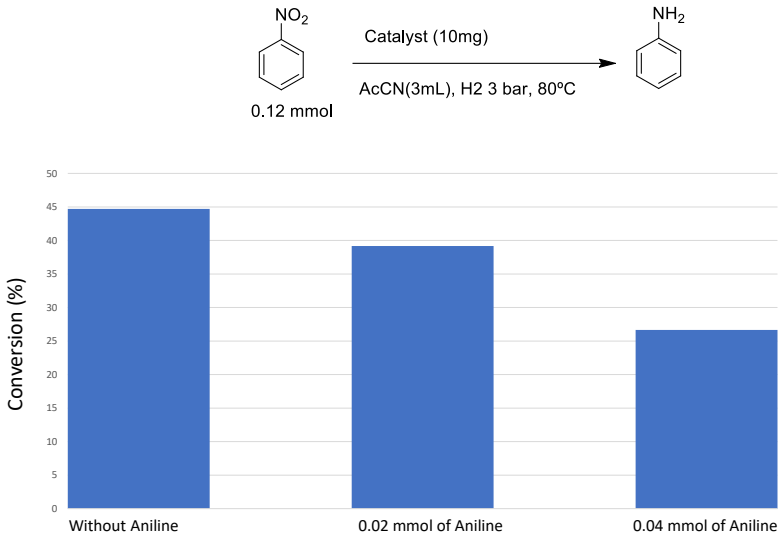

Figure S6.2. Evolution of nitrobenzene reduction catalyzed by UiO66-(Zr) (10 mg) using 3 bar of H_2 at 80 ° C with different quantities of aniline as possible catalytic poison.

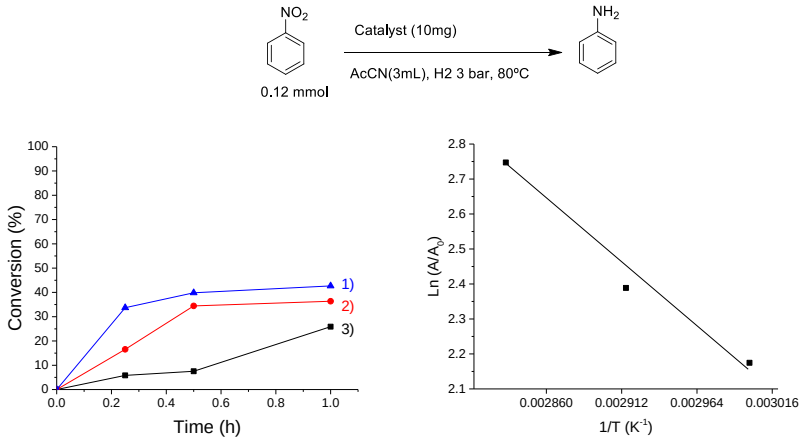

Fig.S6.3 a): Time conversion plot for the hydrogenation of nitrobenzene in the presence of UiO-66 (Zr) at different reaction temperature: 80 °C (1); 70 °C (2) and 60 °C (3) **b)** Arrhenius plot of the natural logarithm of the initial reaction rate obtained from panel a) vs 1/T (K^{-1}). Reaction condition: catalyst (10 mg), nitrobenzene (0.12 mmol), H_2 3 bar, acetonitrile (3mL); regression coefficient (R^2) 0.9741.

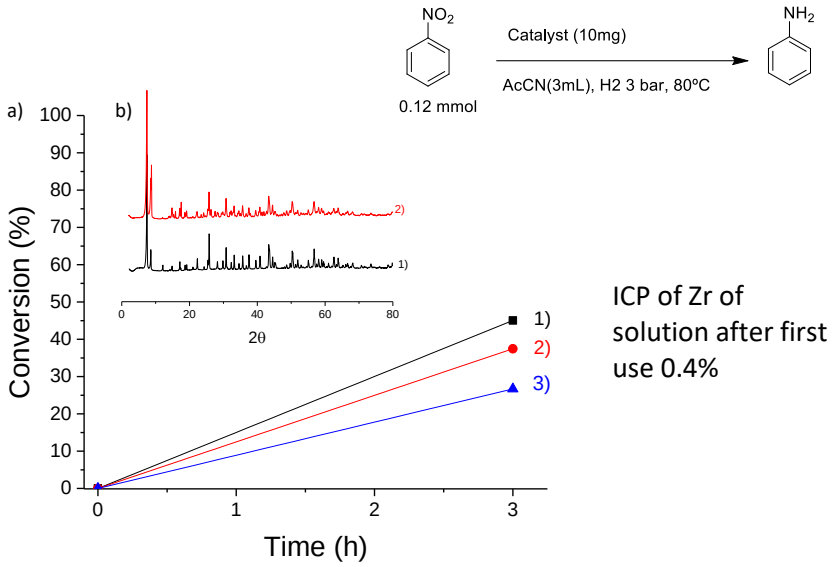

Fig S6.4.(a) Reusability of UiO-66(Zr) as the solid catalyst for the reduction of nitrobenzene to aniline using 3 bar of Hydrogen at 80ºC.1) in the first run corresponds to an independent experiment in which the catalyst was filtered off at 3 h. (b) Comparison of the PXRD patterns of the fresh (b1) and three-times used (b2) UiO-66/(Zr) sample. Reaction conditions: catalyst (10 mg), *nitrobenzene* (0.12 mmol), solvent (Acetonitrile 3 mL).

Chapter 7. Conclusions

From the analyses of the results presented in this doctoral Thesis it is possible to conclude that the new synthesized MOFs materials have shown a great potential in heterogeneous photocatalysis for the production of solar fuels starting from water and in the absence of metal nanoparticles. On the other hand, it has been shown that already known MOFs materials promote reduction reactions of polarized double bonds X=Y. The detailed conclusions of each chapter are described below:

i) The new MOF UiO66(Zr/Ce/Ti) obtained by post synthetic interchange of UiO66(Zr/Ce) with $TiCl_4$ showed a high photocatalytic activity for the Overall Water Splitting reaction when irradiated with visible light. The exchange of some Zr^{4+} and/or $Ce^{3+/4+}$ cations with Ti^{4+} is such as to reduce the HOCO-LUCO band gap and generate, under visible irradiation, 210 $\mu mol*g^{-1}$ of H_2 and 70 $\mu mol*g^{-1}$ of O_2 in 24 h. Photophysical studies, carried out on the suspensions of MOFs in acetonitrile, have shown an efficient (e^-/h^+) charge separation in the whole UV-Visible analyzed range.

ii) The photocatalytic activity of new core-shell MOFs materials obtained by heterojunction of the well-known UiO66(Zr)-NH_2 and UiO66(Ce) is reported. In the absence of metal nanoparticles, the best photocatalytic performance for the Overall Water Splitting reaction is shown by UiO66(Zr)-$NH_2$25mg@UiO66(Ce) which in water, when irradiated by UV-visible light, produces, in the absence of further electron donor, such as methanol or TEOA, 550$\mu mol*g^{-1}$ of H_2 in 24 h and in the presence of visible light and under the same reaction conditions, 350 $\mu mol*g^{-1}$ of H_2.The photocatalytic performance of the material is kept constant for 6 consecutive uses during which the material does not lose its crystallinity.

iii) The well-known UiO66(Zr)-X (X=H, NH_2, NO_2) and MIL-125(Ti)-NH_2 are used as photocatalysts in a tandem reaction, leading to the production of 4-aminophenol. The reaction is carried out in two steps: first of all, we observed the generation of

hydrogen starting from water, in the presence of UV-Visible light and/or solar radiation and using methanol as an electron donor; subsequently a reduction of 4-nitrophenol to give 4-aminophenol is given. It should be noted that the best photocatalytic yields must be attributed to UiO66(Zr)-NH_2, which turns out to be a valid heterogeneous catalyst since it can be reused 3 times without losing catalytic activity and preserving its crystallinity.

iv) UiO66(Zr), UiO66(Ce), UiO66(Zr/Ce), UiO66(Zr)-NH_2, MIL101(Cr)-H and MIL101(Cr)-Cl are efficient heterogeneous catalysts for the reduction of X=Y polarized double bonds. In the hydrogenation reaction of nitrobenzene to give the corresponding aniline it has been shown that the 6 materials under study follow a different reaction order and the conversion to aniline is not always complete as a consequence of the fact that aniline acts as a catalytic poison. The reduction reaction carried out in the presence of UiO66 (Zr)-H as heterogeneous catalyst has clarified that the greater the size of the substrate, the lower the conversion to the product. It should be due to a lower diffusion of the bigger reagents in the pores of the material. From the general analysis of the reported results, it emerges that, in the working conditions, in the absence of metal nanoparticles and in the presence of 3 bars of hydrogen, the MOFs materials employed act as heterogeneous catalysts and selectively reduce the polarized X=Y double bonds but disadvantaging the reduction reaction on C=C double bonds.

Chapter 8. Abstracts

8.1 Abstract

The present doctoral thesis has focused the attention on the synthesis of new MOFs materials obtained either by post-synthetic interchange of previously described MOFs or by heterojunction of stable MOFs having UiO66 structure.

These materials have been applied as photocatalysts for the promising Overall Water Splitting reaction which claims to obtain H_2 and O_2 stoichiometrically starting from water in the absence of sacrificial agents or deposited metals nanoparticles. The new material UiO66 (Zr/Ce/Ti) showed surprising results in both UV-Visible light and sunlight irradiation conditions.

Interesting results were also obtained in the case of the core-shell named UiO66(Zr)-$NH_2$25@UiO66(Ce) which, in the presence of water, when irradiated with both ultraviolet and solar light, allowed to obtain 550 $\mu mol * g^{-1}$ of H_2 and 350 $\mu mol * g^{-1}$ of H_2 in 24 h respectively, in the same working conditions defined for UiO66 (Zr/Ce/Ti).

In this thesis was presented, for the first time, the possibility of reducing 4NP through a tandem methodology which, first, involves the production of H_2 from water in the presence of methanol as a sacrificial agent and UiO66(Zr)-NH_2 as a photo-catalyst, and subsequent the 4 NP reduction to 4 AP.

On the other hand, it has been shown that defective materials with UiO66 structure can selectively reduce polarized X=Y double bonds in the presence of H_2 gas.

8.2 Resumen

La presente tesis doctoral ha centrado la atención en la síntesis de nuevos materiales MOFs obtenidos por intercambio post-sintético de MOFs descritos anteriormente o por heterounión de MOFs estables que tienen estructura UiO66.

Estos materiales se han aplicado como fotocatalizadores para la prometedora reacción de división completa del agua que pretende obtener H_2 y O_2 en forma estequiométrica a partir de agua en ausencia de agentes sacrificantes o nanopartículas metálicas. El nuevo material UiO66 (Zr/Ce/Ti) mostró resultados sorprendentes para la reacción general de división del agua en ambas condiciones de luz UV-Visible e irradiación solar.

También se obtuvieron resultados interesantes en el caso del nucleo-corteza UiO66(Zr)-$NH_2$25@UiO66(Ce) que, en presencia de agua, cuando se irradió con luz ultravioleta y con luz solar, permitió obtener 550 μmol∗g^{-1} de H_2 y 350 μmol∗g^{-1} de H_2 en 24 h respectivamente, en las mismas condiciones de trabajo definidas para UiO66(Zr/Ce/Ti).

En este trabajo de tesis se presentó por primera vez la posibilidad de reducir 4-NP a través de una metodología tándem que involucra primero la producción de H_2 a partir de agua en presencia de metanol, como agente de sacrificio, y UiO66(Zr)-NH_2, como fotocatalizador, y la posterior reducción de 4-NP a 4-AP.

Por otro lado, se ha demostrado que los materiales defectuosos con estructura de UiO66 pueden reducir selectivamente los dobles enlaces polarizados X=Y en presencia de gas H_2.

8.3 Resum

La present tesi doctoral ha centrat l'atenció en la síntesi de nous materials MOFs obtinguts per intercanvi post-sintètic de MOFs descrits anteriorment o per heterounió de MOFs estables que tenen estructura UiO66.

Estos materials s'han aplicat com fotocatalitzadors per a la prometedora reacció de divisió completa de l'aigua que pretén obtindre H_2 i O_2 en forma estequiomètrica a partir d'aigua en absència d'agents sacrificants o nanopartícules metàl·liques. El nou material UiO66 (Zr/Ce/Ti) va mostrar resultats sorprenents per a la reacció general de divisió de l'aigua en ambdós condicions de llum UV-Visible i irradiació solar.

També es van obtindre resultats interessants en el cas del core-shell UiO66 (Zr) - $NH_{2}25$@UiO66 (Ce) que, en presència d'aigua, quan es va irradiar amb llum ultravioleta i amb llum solar, va permetre obtindre 550 $\mu mol*g^{-1}$ de H_2 i 350 $\mu mol*g^{-1}$ de H_2 en 24 h respectivament, en les mateixes condicions de treball definides per a UiO66 (Zr/Ce/Ti).

En este treball de tesi es va presentar per primera vegada la possibilitat de reduir 4-nitrofenol a través d'una metodologia tàndem que involucra primer la producció de H_2 a partir d'aigua en presència de metanol, com a agent de sacrifici, i UiO66 (Zr) - NH_2, com fotocatalizador, i la posterior reducció de 4-NP a 4-AP.

D'altra banda, s'ha demostrat que els materials defectuosos amb estructura d'UiO66 poden reduir selectivament els dobles enllaços polaritzats X=Y en presència de gas H_2.

Annex I Research articles and conferences

I.1. Publications related with the Thesis report

1. Arianna Melillo, María Cabrero-Antonino, Sergio Navalón, Mercedes Álvaro, Belén Ferrer, and Hermenegildo García, Enhancing Visible Light Photocatalytic Activity for Overall Water Splitting in UiO-66 by Controlling Metal Node Composition, ***Appl. Cat. B env.*** 2020, **278,** 119345
2. Arianna Melillo, María Cabrero-Antonino, Belén Ferrer, Herme G. Baldoví, Sergio Navalón**.** Solar-Driven Photocatalytic Overall Water Splitting Using MOF-On-MOF Heterojunctions Based on Uio-66 Topology. Manuscript sends to **Appl. Cat. B env.** in January 2022
3. Arianna Melillo, Cristina Valles, Sergio Navalón, Mercedes Álvaro, Belén Ferrer, and Hermenegildo García, Bifunctional metal-organic frameworks for hydrogenation of nitrophenol using methanol as hydrogen source, ***Org. Biomol. Chem.***, 2021,**19**, 794-800
4. Arianna Melillo, Belen Ferrer, and Hermenegildo Garcia, Metal Nodes of Metal Organic Frameworks Can Activate Molecular Hydrogen. Manuscript in preparation.

I.2 Other publications

1. Arianna Melillo, Rocio García, Sergio Navalón, Pedro Atienzar, Belén Ferrer, Mercedes Álvaro and Hermenegildo García, Photoactive Zr and Ti Metal-Organic-Frameworks for solid-state solar cells. Accepted in *Chem.Phys.Chem* on march 2021.
2. Minoo Bagheri; Arianna Melillo; Belen Ferrer; Mohammad Yaser Masoomi; Hermenegildo García: "Enhanced catalytic performance of

Quasi-HKUST-1 for the tandem Imine Formation" accepted in Chemistry - A European Journal on august 2021

3. Minoo Bagheri; Arianna Melillo; Belen Ferrer; Mohammad Yaser Masoomi, Hermenegildo Garcia: Quasi HKUST Obtained via Post-Synthetic Defect Engineering for Extremely Improved Catalytic Hydrogen Release, accepted in ChemComm, on octuber 2021
4. Bagheri, Minoo; Melillo, Arianna; Ferrer, Belen; Masoomi, Mohammad; Garcia, Hermenegildo: Quasi-HKUST Prepared via Post-Synthetic Defect Engineering for Highly Improved Catalytic Conversion of 4-Nitrophenol" ACS Applied Materials & Interfaces, december 2021.
5. Arianna Melillo, Sergio Navalon, Belen Ferrer and Hermenegildo Garcia. Photocatalysis by Metal-Organic Frameworks. **Chapter 33**. ***Elsevier***, January 2021.
6. Arianna Melillo, J.Raoul Herance, Sergio Navalon and Hermenegildo Garcia. Photocatalysis by Graphene. **Photocatalysis using 2D nanomaterials, *Royal Society of Chemistry.*** October **2021**.
7. Tuğçe Günay Semerci, Arianna Melillo, Yasemin Çimen Mutlu and Hermenegildo Garcia, Band alignment of PCN-222 via selection of the metal porphyrin linker for sunlight driven photocatalytic overall water splitting, submitted to *ACS Applied Materials & Interfaces.*
8. Maria Novoa Cid, Arianna Melillo, Hermenegildo Baldovi and Hermenegildo Garcia: Influence of ultrasound treatment time on the amount of hydrogen in the head space, manuscript in preparation**.**
9. Maria Cabrero Antonino, Arianna Melillo, Eva Montero Lanzuela, Hermenegildo Baldovi, Belen Ferrer and Sergio Navalon: Ru

Nanoparticles: Synthesising, Characterizing and Photocatalyst uses of UiO-66 materials, Manuscript in preparation.

10. Arianna Melillo; Ruben Ramirez Grau; Belen Ferrer; Ana Primo and Hermenegildo Garcia: Enhancing photocatalitic activity of MXene Quantum dots. Manuscript in preparation

I.3 Participation in conferences

1. **World Congress on Chemistry 24 th -25 th October 2019** Olympia Hotel**,** Alboraya, Valencia, Spain, Oral presentation
2. **XVI SYMPOSIUM OF YOUNG RESEARCHERS OF THE REAL SPANISH SOCIETY OF CHEMISTRY, RSEQ - Sigma Aldrich (Merck)**, 4 **th** November 2019 to 7 **th** November 2019, Flash presentation
3. **INTERNATIONAL SOLAR FUELS CONFERENCE 2021,** 26th-29th July 2021, Online, poster session
4. **E-MRS 2021 FALL MEETING,** 20th-23rd September 2021, Online, oral presentation